VASCULARIZATION OF BIOENGINEERED FAT WITH TUNABLE MATRIX PROPERTIES FOR MACRO-PERFUSION AND SOFT TISSUE RECONSTRUCTION

A Dissertation

Presented to the Faculty of the Graduate School

of Cornell University

In Partial Fulfillment of the Requirements for the Degree of

Doctor of Philosophy

by

Chelsea Jane Stephens

August 2024

VASCULARIZATION OF BIOENGINEERED FAT WITH TUNABLE MATRIX PROPERTIES FOR MACRO-PERFUSION AND SOFT TISSUE RECONSTRUCTION

Chelsea Jane Stephens, Ph.D.

Cornell University 2024

Deep, chronic wounds are a prevalent clinical concern caused by injury or trauma to the skin and underlying soft tissues such as fat, vasculature, fascia, muscle, and even bone. Fat is one of the most abundant and key tissue types necessary for soft tissue reconstruction (STR) and is harvested via autologous fat transfer (AFT), which is the resection and reallocation of adipose tissue from a healthy donor region to the defect site. While these procedures are effective, they are limited by donor-site morbidity, post-operative debilitation, risk of infection and necrosis, and donor tissue availability. 3D-bioprinting and tissue engineering strategies provide a promising solution to address these shortcomings. However, in order to adequately fabricate tissues for regenerative medicine, perfusable and hierarchical vasculature must be incorporated. Additionally, a more robust understanding of matrix mechanics, such as stiffness and viscosity, is crucial to recapitulating the material properties that support fat and vascular formation. Thus, there is a need to establish a tunable system capable of bioengineering fat and other clinically relevant tissues with patent vasculature as an alternative to AFT and other STR procedures. The objective of this work was to examine the vascular and adipogenic potential of endothelial and adipose stem cells within a tunable matrix for macro-perfusion and STR. First, we synthesized and utilized a

mechanically tunable bioink, gelatin methacryloyl, to examine the role of matrix stiffness and viscosity on adipogenesis and vasculogenesis. Next, we developed a macro-perfusion bioreactor (MPB) system that can support the fabrication of large constructs with patent and high-throughput lumen geometry (the *Squiggle*). Finally, we build upon our MPB system, harboring the *Squiggle* channel design, to elucidate the impact of hemodynamic shear stress and vorticity on bulk diffusion and endothelium maturation, which will eventually serve as a platform to study the effects of hemodynamic flow on angiogenesis. Altogether, the hope is that the knowledge gained from this work and the establishment of a model MPB system can be adapted to engineer fat and other heterogenous tissues with patent and hierarchical vasculature for STR and regenerative medicine.

BIOGRAPHICAL SKETCH

Chelsea Jane Stephens, a Los Angeles, California native, fell in love with STEM after she and her friend (or lab partner) won their middle school science fair with a simple project on a candle vacuum. While she probably could not fully understand or articulate the scientific and engineering principles at play, she would continue to pursue her curiosity in STEM across the country in New York for the next decade. In 2010, Chelsea graduated from William Howard Taft High School and traveled to Syracuse, NY at the tender age of 17, leaving all her family and childhood friends behind. By 2015, she received her B.S. in Bioengineering from Syracuse University (SU) and graduated magna cum laude. Chelsea often describes her choice to attend SU as the best decision she ever made. Not only did she continue to study biomedical science and engineering while at SU, but she also got the opportunity to discover who she truly was – a problem solver, educator, activist, and lifelong learner. With this newfound knowledge of herself, she went on to explore scientific research in a post-baccalaureate research education program at the University of Michigan under the mentorship of Dr. Rhima Coleman (2015-2017), where she continued to study cartilage tissue engineering and regenerative medicine. After the completion this program, Chelsea moved back to the northeast for graduate school at Cornell University, where she received her Master's in Biomedical Engineering in 2021 and also completed her doctoral dissertation research with the Cardiovascular Developmental Bioengineering Laboratory, led by Dr. Jonathan T. Butcher. During her tenure at Cornell, Chelsea has been the recipient of numerous awards and fellowships including, the Provost Diversity Fellowship for Advanced Students, the Social Justice Award, the Change Agent Award, Diversity Programs in Engineering Graduate Student of the Year, the NYSTEM Cornell Training Program in Stem Cell Research Fellowship, and the Dean's

Excellence Fellowship. Additionally, Chelsea has presented her work at numerous international and domestic conferences and symposiums, including *Tissue Engineering & Regenerative Medicine International Society*, *Biomedical Engineering Society Annual Conference*, and *Stem Cell Program Symposium*. As a PhD candidate, she also mentored multiple students and worked on several published papers, as both a first author and contributing author. Her work is published in peer-reviewed journals including *Tissue Engineering, Part A*, *Translational Research: The Journal of Laboratory and Clinical Medicine*, and *Journal of Magnetic Resonance Imaging*. Lastly, while Chelsea was not in the lab, she served as a prominent leader in various school organizations (*Building Allyship Series* and *Black Graduate and Professional Student Association*), startup ventures (*Gutsy*, Cornell eLab Start-up Accelerator Program, *Black Entrepreneurship and Reform*, and *Vinstinct*), and educational programs in the community (Cornell *Splash!* and *Graduate Student Outreach Program*).

For my inner child

ACKNOWLEDGEMENTS

Firstly, I would like to acknowledge the faculty and staff at **Syracuse University College of Engineering and Computer Science**, specifically Dr. Julie Hasenwinkel, Sarah Mack, Karen Davis, and Ms. Tamara Hamilton. Thank you for mentoring and encouraging me throughout my time at SU as a young, naïve, and sometimes obnoxious bioengineering student. I always felt supported and protected by you all and I believe my education at SU set as strong foundation for my success thus far and my continued journey ahead. Attending SU for undergraduate school was truly the best decision I ever made.

Next, I would like to acknowledge my mentors and advisors from the Post-Baccalaureate Research Education Program (PREP) at **The University of Michigan**, including Dr. Kate Barald, Dr. Rhima Coleman, and Dr. Biming Wu. My time at UofM was pivotal in my scientific research career and without this experience, I would not be the confident researcher that I am today. I especially want to thank my PREP advisor, Dr. Coleman, for teaching me how to be a thorough, critical, and assured scientist. I would also like to thank Dr. Biming Wu for the extensive education and training that you provided me with in Dr. Coleman's lab. Lastly, I would like to thank Dr. Kate Barald for the mentorship, letters of recommendation, and additional support that ultimately helped me get into graduate school.

I would also like to thank my advisor **Dr. Jonathan Butcher and committee members**, Dr. Daniel Berry, Dr. Claudia Fischbach, and Dr. Jason Spector for your guidance and support during the completion of my degree. Through your mentorship I have continued to develop my skills as

a critical thinker, problem solver, and researcher. I would also like to express my gratitude for Dr. Martin Prince whom I had the privilege of shadowing and conducting clinical research with during my time in the **Summer Immersion** program.

As for my friends in the broader **Cornell BME community** and the **Black graduate student and professional community**, I would also like to thank you for the support, laughs, memories, adventure, growth, and love that you have given me throughout my doctoral journey and time in Ithaca. I would like to specifically acknowledge the many lab mates and friends whom I have had the privilege of working with, learning from, and celebrating with over the last 7 years. Thank you to my previous lab mates who were present and helpful at the beginning of PhD career, including Daniel Cheung, David Bassen, Ablajan Mahmut, Duc Pham, Benjamin Albert, Katherine Driscoll, and Minghkun Wang. I would also like to give a special thanks to my lab mates who joined the Butcher Lab after me. You really helped me towards the middle and end of my PhD tenure by boosting lab moral and improving the overall culture. Thank Alex Cruz, Shuofei Sun, Steve Poon, Kenny Nguygen, Janani Guru, and John Toftegaard. To my undergraduate and Masters student mentees, Reina Kobayashi, Shivashki Gupta, Emma Stowe, and Yashi Sanghvi, it has been a pleasure working with you and mentoring you over the years. I am extremely thankful for your help and very much proud of your success and achievements.

As for ***Team Flow***, which includes Yahav Rave, Aminat Ibrahim, and Gening Dong, words cannot express my gratitude and appreciation for your support, hard work, knowledge, and expertise during the last two years of my PhD. I truly believe I would have not been able to finish this degree

without you. It has been an honor to work with you and learn from you and I hope you have benefited from me in the same capacity that I have benefited from you.

In regard to my entrepreneurial journey at Cornell, I would also like to thank my **eLab** mentors and advisors, Ken Rother, Alex Meyers, Kristen McClellan, John Balen, Steven Gal, Richard Patrina, and Andrea Ippolito. Entrepreneurship has had such a positive impact on my life and has expanded my world to include more creative opportunities that are in better alignment with who I am, not just as a scientist or engineer, but as a holistic person. To my **Vinstinct** team members, Taylor Walker, Apriele Minott and Tiffany Agard, and **ESINL** cofounder, Timothy Thompson, you absolutely changed my life for the better. You taught me how to be a better leader, communicator, partner, teammate, and friend. I only want to be the best version of myself with you. Thank you for always supporting me and being patient with me as I was developing my new entrepreneurial skills on the fly. **(SN: I'm listening to *For You to Love* by Luther Vandross while writing this. That's why it's so mushy! Lol**)

I would also like to thank the Cornell **Counseling & Psychology Services (CAPS)** team for providing amazing mental and physical healthcare during the last 7 years. I would especially like to give a special thanks to my therapists, Dr. Nadia Abdo and Dr. Susan Wiser, who helped me overcome my issues with disordering eating early in my PhD tenure, and Jake Carver and Dr. Sheila Singh, who helped me improve my relationship with alcohol and substance misuse at the end of my PhD tenure.

As for my lifeline during graduate school, I want to give a special thanks to **Uber, Tompkins Consolidated Area Transit (TCAT), and my close friends** who always gave me a ride and made sure I got home safely, especially after late nights in the lab. I would also like to thank **DoorDash** and the staff and owners at ***The Watershed***, ***Monks on the Commons***, ***Nowhere Special***, ***Taverna Banfi***, ***The Regent Lounge***, **and** ***Northstar Public House*** for keeping me well-fed and nourished when I did not have the capacity or bandwidth to cook for myself.

I would also like to thank **The Joe Budden Podcast (JBP)** for keeping me thoroughly entertained while performing tedious lab task, such as data analysis, graphic design, cell culture, immunohistochemistry, confocal imaging, and mechanical testing. I have been an avid listener of the JBP since 2018 and I hope I have the privilege of being interviewed by Joe Budden in the future when I'm wealthy and famous. Other shows, podcast, and streaming services with an honorable mention include: *The Walking Dead*, *The Last of Us*, *The View*, *The Majority Report*, *Dance Moms*, *South Park*, *Game of Thrones*, *House of Dragon*, *La Casa De Papel*, *Elite*, and *TikTok*.

Finally, I would like to acknowledge that this work was funded by several sources, including the: Dean's Excellence Fellowship for Early PhD Students (2017-2018), NYSTEM Fellowship for Cornell Training Program in Stem Cell Research (2018-2020), and Provost Diversity Fellowship for Advanced PhD Candidates (2024). The research materials and laboratory infrastructure were supplied by Dr. Jonathan T. Butcher, which were funded by grants from the National Institutes of Health (R21AR070408 and R01HL143247). The instruments needed to acquire data for confocal imaging, mechanical testing, and ^{1}H NMR analysis were provided by the Biotechnology Resource

Center, Cornell Center for Materials Research, and the Cornell NMR and Chemistry Mass Spectrometry facilities, respectively. Conference travel stipends for the presentation of this research were additionally funded by the Cornell Graduate School.

TABLE OF CONTENTS

LIST OF FIGURES

CHAPTER 1

CHAPTER 2

CHAPTER 3

CHAPTER 4

CHAPTER 5

LIST OF TABLES

LIST OF ABBREVIATIONS

3-isobutyl-1-methylxanthine (IBMX)
4',6-diamidino-2-phenylindole (DAPI)
Acetylated low-density lipoprotein (acLDL) expression
Adipose-derived stem cells (ADSC)
Adipose microvascular endothelial cells (AMvECs)
Alkaline Phosphatase Activity (ALP)
Alpha smooth muscle actin (aSMA or αSMA)
Antibiotic antimycotic (AA)
Arterial insufficient ulcers (AIU)
Articular fat pads (AFPs)
Angiopoietin-1 (Ang1)
Angiopoietin-2 (Ang2)
Basic fibroblast growth factor (bFGF)
Beige adipose tissue organoids (BAO)
Beige adipose tissue (BeAT)
Brown adipose tissue (BAT)
Cadherin 5 or vascular endothelial (VE)-cadherin (Cad-5)
Collagen Type 1 (Col 1)
Deep inferior epigastric perforator (DIEP)
Dedifferentiated fat (DFAT)
Dexamethasone (DEX)
Dulbecco's Modified Eagle Medium: Nutrient Mixture F-12 (DMEM-F12)
Diabetic foot ulcer (DFU)
Endothelial cells (EC)
Epidermal growth factor (EGF)
Endothelial growth medium-2 (EGM2)
Epidermal stem cells (EpSC)
Ethidium homodimer-1 (EthD-1)
Extrusion-based bioprinting (EBB)
Extracellular matrix (ECM)
Fatty acid binding protein receptor 4 (FABP4)
Fetal bovine serum (FBS)
Fetal calf serum (FCS)
Gelatin (Gel)
Gelatin methacryloyl (GelMA)
Gelatin with 40% degree of methacrylation (GelMA40, G40)
Gelatin with 60% degree of methacrylation (GelMA60, G60)
Gelatin with 100% degree of methacrylation (GelMA100, G100)
Glycosaminoglycan (GAG)
Green fluorescent protein-human umbilical vein endothelial cells (GFP-HUVEC)
Growth factor therapy (GFT)
Heparan (Hep)

Hepatocyte growth factor (HGF)
Human adipose-derived mesenchymal stem cells (hAdMSC)
Human bone marrow-derived mesenchymal stem cells (hBM-MSC)
Human dermal fibroblasts (HDF)
Human microvascular endothelial cells (HMVEC)
Human muscle progenitor cells (hMPC)
Human neonatal dermal fibroblast (HNDF)
Human umbilical vein endothelial cells (HUVEC)
Hyaluronic acid or hyaluronan (HA)
Hypoxic inducible factor (HIF-1a or HIF-1α)
Integrated tissue-organ printing (ITOP)
Interferon-gamma (INF-γ)
Interleukin (IL)
Irgacure 2959 (IRG)
Insulin-transferrin-selenium (ITS)
Lithium phenyl-2,4,6-trimethylbenzoylphosphinate (LAP)
Laponite-alginate-methylcellulose (LAM)
Latissimus dorsi (LD)
Lysine (Lys)
Macro-perfusion bioreactor (MPB)
Matrix metalloproteinases (MMP)
Mesenchymal stem cells (MSC)
Methacrylic anhydride (MAA)
Minimally manipulated extracellular matrix (MA-ECM)
Muscle-tendon unit (MTU)
Penicillin-Streptomycin (PS)
Osteocalcin (OC)
Osteopontin (OP)
Paraformaldehyde (PFA)
Pentraxin 3 (PTX3)
Phosphate buffered solution (PBS)
Platelet-derived growth factor (PDGF)
Platelet/endothelial cell adhesion molecule-1 (PECAM-1)
Polycaprolactone (PCL)
Polyethylene glycol (PEG)
Polyethylene glycol dimethacrylate (PEGDMA)
Proliferator-activated receptor gamma (PPARg or PPARγ)
Proton nuclear magnetic resonance (^{1}H NMR)
Serpin E1
Skin decellularized extracellular matrix (S-dECM)
Smooth muscle cells (SMC)
Soft tissue reconstruction (STR)
Sphingosine-1-phosphate (S1P)
Stem cell therapy (SCT)
Stromal vascular fraction (SVF)

Superficial inferior epigastric artery (SIEA)
Transforming growth factor beta-1 (TGFß-1)
Transverse rectus abdominis myocutaneous (TRAM)
Uncoupling protein 1 (UCP1)
Unidirectional and pulsatile (UNP)
Ultraviolet (UV)
Vascular endothelial growth factor A (VEGFA)
von Willebrand factor (vWF)
Wall shear stress (WSS)
Weight percentage (%wt)
Weight per volume (w/v)
White adipose tissue (WAT)

LIST OF SYMBOLS

p-value < 0.05 (*)
p-value < 0.01 (#)
p-value < 0.001 (**ζ**)

PREFACE

BACKGROUND AND SIGNIFICANCE

Large, gaping wounds, caused by injury or infection, are complicated by deranged wound bed vasculature and lack the capacity to properly heal on their own. (1) Immediate and proper care of these chronic wounds are required to reduce a patient's risk of permanent disfigurement, debilitation, or death. (2) Autologous "flaps", which are tissues equipped with their own hierarchical vascular supply, can be harvested from one region of the patient and transplanted to the wound where it is reperfused upon microsurgical anastomosis to appropriate recipient vessels. (3) Despite the success of autologous flap transfer, these procedures are extremely invasive, incur obligatory donor-site morbidity, require sufficient donor-tissue availability as well as microsurgical expertise and specialized equipment. (4) Therefore, there is a need for an alternative tissue engineering approach to address the limitations of autologous pedicle transfer procedures. Yet, meaningful progress towards the clinical application has been limited by the lack of vascularization requirements that are necessary to meet the nutrient and oxygen demands of clinically relevant tissue volumes.

Extrusion-based bioprinting (EBB) is a growing advancement in tissue engineering that offers a cost-effective and minimally invasive alternative to autologous flap transfer. In general, EBB technology can fabricate geometrically precise and heterogenous biological constructs equipped with viable cells, structural matrix proteins, and bioactive morphogens to guide tissue-specific cell behavior. (5) However, these biofabrication methods are restricted to the development of only thin tissue-engineered constructs capable of facilitating the diffusion of oxygen, which are not suitable for treating large tissue defects. (4,6,7) To address this limitation, the incorporation of multiscale

vasculature within voluminous bioprinted tissues is required to ensure that healthy tissue-specific function is achieved and maintained upon implantation. Bioprinted constructs must be equipped with patent macro-vessels that can anastomose with the host vasculature and withstand physiological perfusion pressures. Additionally, hierarchical vascular organization within organ-level tissues is required to support adequate nutrient transfer, oxygen diffusion, and waste removal throughout voluminous structures. Although these advances in tissue engineering have been made, it is crucial that the bulk material surrounding the fabricated lumen is not only mechanically robust enough to withstand long-term perfusion but also implantation into the wound site. These bioengineered tissues must also be compliant enough to support varied cell behavior response, including angiogenic sprouting, adipogenesis, and myogenesis. Therefore, there is a need to develop a tunable bioink that supports tissue-specific maturation, long-term perfusion, and neovascularization.

Gelatin methacryloyl (GelMA) is a photo-crosslinkable polymer that serves as an ideal bioink for EBB and tissue engineering. Due to its biocompatible (8), thermo-reversible (9), and mechanically tunable(8–11) properties, GelMA bioinks can be used to print cellularized constructs of varying substrate mechanics with high shape fidelity and fine spatial resolution. (8,12) Previous studies have shown that GelMA constructs containing bioprinted lumens were not only capable of withstanding perfusion, but also capable of supporting the adhesion, survival, and proliferation of various perivascular cell types, including HUVEC, human neonatal dermal fibroblast (HNDF), and mesenchymal stromal cell (10T1/2 cells). (13) It has also been demonstrated that a dual hydrogel system, containing GelMA and polyethylene glycol dimethacrylate (PEGDMA), can support the endothelialization of PEGDMA, the vascularization of GelMA, and molecular diffusion under pulsatile flow. (14) In addition to supporting 2D microvessel formation and lumen

vasculogenesis upon perfusion, GelMA has also been shown to promote adipogenesis and myogenesis of MSC-laden constructs. When adipose-derived stem cells (ADSC) were encapsulated in 3D GelMA-hyaluronic acid (HA) composite materials, adipogenic differentiation of ADSCs was achieved after 21 days.(15) In muscle fabrication studies, alterations to GelMA mechanics and geometric confinement supported myogenesis, myotube alignment, and 3D muscle network formation. (16,17) Despite GelMA's potential to support angiogenesis, adipogenesis, and myogenesis separately, these tissue engineering strategies are limited by the nutritive and oxygen demands of cells within the bulk material, making these systems ill-suited for clinical translation. Thus, there is a need to incorporate hierarchical and patent vasculature within these bioengineered tissues in order to maintain robust cell viability and functionality within the core of these voluminous constructs. The overall goal of this thesis is to elucidate the effects of GelMA mechanics (*stiffness, viscosity*) and hemodynamics (*shear stress, vorticity*) on the vascularization of bioengineered fat. This research will allow for the biofabrication of highly vascularized neo-pedicle tissues suitable for *in vivo* studies and will provide potential insight on engineering other highly vascularized tissues for regenerative medicine.

INNOVATION

The work presented in this thesis is innovative for three major reasons: (1) it utilizes a tunable, 3D-bioprinting material, GelMA, to elucidate the independent role of matrix stiffness and viscosity on adipogenesis and vasculogenesis; (2) it sheds light on the regulatory influence matrix stiffness and viscosity on driving white versus thermogenic fat lineage potential; and (3) it further investigates the impact of hemodynamic shear and vorticity on local angiogenesis using high-throughput lumen geometry in a voluminous and perfusable GelMA construct. In terms of the first

innovation, research regarding the role of biomechanics on fat and vascular formation has historically prioritized the study of matrix stiffness. However, tissues are viscoelastic materials, harboring an instantaneous elastic response and time-dependent viscous response to deformation. While much work has been done to uncover the role of matrix stiffness on cell behavior and fate, additional knowledge on the impact of matrix viscosity on these phenomena is necessary and this work aims to achieve that.

In addition to establishing a tunable GelMA polymer with adjustable stiffness and viscous parameters, the thermo-reversible properties of GelMA make it suitable for 3D-bioprinting, which is necessary for fabricating heterogeneous tissues. Traditionally, the field of tissue engineering uses either native biological materials (e.g., collagen, hyaluronan, fibrin, or Matrigel) or synthetic materials (e.g., PEG) to study fat and vascular formation. However, these materials are limited in their ability to fabricate large, hierarchical and functional tissues, which can be achieved through advanced technology, such as 3D-bioprinting. In this study, we successfully use the GelMA, a biocompatible, mechanically tunable, and thermo-reversible bioink, study the role of matrix mechanics on fat and vascular formation.

In terms of the second innovation, this work also contributes to the knowledge of distinguishing between various types of fat tissue. It is well understood that there are different types of fat, namely metabolic (or white) and thermogenic (or brown and beige) fat, which have very different functions. However, the field of adipose tissue engineering is primarily focused on the regeneration of white fat and are now beginning to prioritize brown fat, as it has shown great relevance in obesity, diabetes, and cancer research. Alternatively, while the field of adipose biology has been able to uncover the biochemical factors that govern brown versus white fat differentiation, there is less work on the role that mechanics plays in this phenomenon. In our work, we not only study the

effects of viscosity and stiffness on fat formation but also investigate how these mechanical features of the matrix push adipose stem cells down either a metabolic or thermogenic fat lineage pathway.

Lastly, in terms of the third innovation, this work also examines the role of hemodynamic shear stress and vorticity on local angiogenesis in a voluminous and perfusable GelMA system. The novelty of this system is the creation and use of high-throughput lumen geometry to generate a variety of hemodynamic regimes in a large GelMA construct. In the field of vascular tissue engineering, research studies have traditionally relied on the use of microfluidic devices, bidirectional flow systems, and simple flow platforms to study the effects of shear stress on angiogenesis. While these systems are useful in adding meaningful insight on vascular formation, they do not adequately recapitulate the native hemodynamic properties of microvascular networks. Additionally, there are few studies in the literature that highlight the impact of vortical flow on these phenomena. In this work, we fabricate voluminous GelMA constructs that support complex, perfusable, and high-throughput lumen geometry to ascertain the effects of hemodynamic shear stress and vorticity on angiogenesis.

Through this research, our lab is at the forefront of developing voluminous GelMA constructs that support flow-induced hierarchal vascularization, and subsequent adipogenic differentiation of adult stem cells**.** Close work with my thesis advisor, committee members, and other biomedical engineering student and faculty allowed me to receive the proper guidance and mentorship in carrying out the work for my thesis. Additionally, with the combined and interdisciplinary expertise in vascular tissue mechanics and engineering (*Butcher*), adipose cell biology (*Berry*), biomaterials (*Fischbach*), and reconstructive surgery (*Spector*), I was able to develop a

mechanically tunable GelMA platform that can support microvascularization and bioengineered adipose tissue for reconstructive surgery.

RESEARCH AIMS

Aim 1. Synthesize Biomaterials with Tunable Matrix Stiffness and Viscosity

Soft tissue defects caused by burns, trauma, congenital anomalies, or infection are prevalent concerns that require large volumes of subcutaneous fat equipped with vasculature for full restoration. While tissue engineering strategies can serve as a clinical alternative to current reconstructive procedures, further elucidation on the role of matrix mechanics, such as stiffness and viscosity, on adipose and vascular stem cell behavior is necessary. Tunable polymers, such as gelatin methacryloyl (GelMA), serve as an ideal biomaterial for examining the role of matrix stiffness and viscosity on cell behavior. In this work, GelMA was fabricated with varying degrees of methacrylation (DoM) and photo-crosslinked at 5% and 10% (w/v) to elicit variations in its mechanical properties. In cellular studies, human adipose-derived mesenchymal stem cells (HAdMSCs) were encapsulated in 5% and 10% (w/v) GelMA polymers with a DoM of 40% and 100% and underwent adipogenic conditioning for 21 days. Additionally, human umbilical vein endothelial cells (HUVEC) were cocultured with HAdMSCs under the same hydrogels conditions and induced in vasculogenic medium for 10 days. The results from this work revealed that matrix stiffness depended on both the DoM and weight percentage of GelMA polymers, while its viscosity relied solely on the latter. When cells were encapsulated in GelMA hydrogels and cultured in either adipogenic or vasculogenic media, cell behavior was characterized by viability, circularity, and hydrogel compaction. In regard to adipose studies, cell viability, circularity, and hydrogel compaction were neither stiffness- nor viscous-dependent. However, the compaction of GelMA

proved to be DoM-dependent, where hydrogels with lower DoM experienced the greatest reduction in surface area in comparison to hydrogels with higher DoM. Alternatively, in vascular studies, cell viability depended on matrix viscosity, while cell circularity and hydrogel compaction were influenced by matrix stiffness. Altogether, these results demonstrate that while matrix stiffness, viscosity, and crosslinking efficiency have unique influences on adipose and vascular stem cell behavior, elucidating the effects of these mechanical parameters on adipogenesis and vasculogenesis offer invaluable insight for engineering voluminous soft tissues.

Aim 2. Elucidate the Role of Matrix Stiffness and Viscosity on Adipogenesis and Vasculogenesis

Aim 2a. The role of matrix stiffness and viscosity on lipid phenotype and fat lineage potential

Autologous fat transfer is a common procedure that patients undergo to rejuvenate large soft tissue defects. However, these surgeries are complicated by limited tissue sources, donor-site morbidity, and necrosis. While the biofabrication of fat tissue can serve as a clinical option for reconstructive surgery, the influence of matrix mechanics, specifically stiffness and viscosity, on adipogenesis requires further elucidation. Additionally, the effects of these mechanical parameters on metabolic and thermogenic fat potential have yet to be investigated. GelMA polymers with varying DoM were fabricated to create matrices with different stiffnesses and viscosities. Human adipose-derived mesenchymal stem cells were then encapsulated in mechanically tunable GelMA and underwent adipogenesis to investigate the effects of matrix mechanics on lipid phenotype and fat potential. Mechanical testing confirmed that GelMA stiffness was regulated by DoM and weight composition, while viscosity was determined by the latter. Further work revealed that while lipid phenotype became more enriched as matrix stiffness and viscosity declined, the potential towards

metabolic and thermogenic fat appeared to be more viscous-dependent rather than stiffness-dependent. Additionally, FABP4 and UCP1 gene expression exhibited viscous-dependent behavior despite comparable levels of PPARg. However, despite the superior role of viscosity, lipid quantity and mitochondrial abundance demonstrated stiffness-dependent behavior. Overall, this work revealed that matrix viscosity played a more superior role than stiffness in driving adipogenesis and distinguishing between metabolic and thermogenic fat potential. Ultimately, this differentiation in fat production is important for engineering ideal adipose tissue for large soft tissue defects.

Aim 2b. The role of matrix stiffness and viscosity on microvascular formation

Deep, chronic wounds are highly prevalent and require surgical intervention for full restoration. Neo-pedicle flap transfer, or the resection and relocation of heterogenous, autologous, and vascularized tissues from a healthy donor region to the deranged site, is a promising solution for treating these wounds. However, these procedures are extremely invasive, increase donor-site morbidity, and exacerbate post-operative debilitation. The biofabrication of heterogenous tissues equipped with patent and hierarchical vasculature can serve as clinical alternative to these surgeries. In order to achieve this, the biomechanical and biophysical matrix properties, such as stiffness, viscosity, and crosslinking efficiency, must be fine-tuned to support microvessel formation. Although the effect of stiffness on vasculogenesis has been well studied, less is known about the role of viscosity and crosslinking efficiency on this phenomenon. In this study, we used GelMA as a tunable material to study the effects of matrix stiffness, viscosity, and crosslinking efficiency on vasculogenesis. GelMA was fabricated with 40% and 100% DoM and polymerized at 5% and 10% (w/v) to achieve variations in these matrix properties. HUVEC and hAdMSCs

were then co-cultured in these tunable GelMA hydrogels to examine the role matrix stiffness, viscosity, and crosslinking efficiency on microvascular formation. The findings from this work ultimately revealed that various matrix properties regulate distinct characteristics of microvascular formation. Specifically, optimal matrices for invoking vasculogenesis have moderate stiffness, low viscosity, and low DoM, such as the material properties achieved by the 10%G40 matrix composition. It was shown that microvessel density and αSMA expression were inversely related to each other and regulated by stiffness with some influence due to DoM, demonstrating that soft and low-DoM matrices significantly augment microvessel formation. Additionally, it was shown that matrix stiffness and viscosity both increased during vasculogenesis and directly regulated the formation of microvascular junctions and branches. Although matrices with low stiffness and high viscosity enhanced the presence of junctions and branches, additional microvessel characteristics, such as vessel thickness, were dependent on matrix DoM, where low DoM matrices were a able to produces thicker vessels. Overall, the findings of this work offer valuable insight on how the modulation of specific biomechanical and biophysical matrix features can regulate distinct characteristics of microvasculature.

Aim 3. Establish a macro-perfusion bioreactor to examine the combinatorial role of hemodynamic shear stress and vorticity on angiogenesis in a mechanically tunable matrix for fat vascularization

Aim 3a. Establish a macro-perfusion bioreactor that can support long-term, unidirectional, and pulsatile flow through a high-throughput channel geometry

The biofabrication of thick tissues for regenerative medicine require patent and hierarchical vasculature to ensure cell survival and function. It is well understood that fluid shear stress plays a significant role developing and maintaining the necessary vasculature for large tissues. However, current systems used to examine the role of fluid shear stress on angiogenesis are typically low-throughput, small in size, use bi-directional flow, and neglect the role of other hemodynamic parameters, such as vorticity. In this study, we developed a high-throughput channel to establish variations in hemodynamic shear stress and vorticity at distinct regimes of the design. We also fabricated thick and acellular GelMA hydrogels equipped with our patent and high-throughput channel geometry to determine if our macro-perfusion bioreactor system can support long-term, unidirectional, and pulsatile flow. ANSYS simulations performed on this channel geometry (the *Squiggle*) revealed that significant variations in shear stress and vorticity were established at distinct regions, including the arch, plenum, and elbow of the channel. After characterizing the flow profile, voluminous GelMA constructs containing a patent *Squiggle* were fabricated using a new polymer composition of 6% GelMA60. Attempts to prepare the macro-perfusion bioreactors with either 5%G40 or 5%G100 hydrogel compositions failed due to poor crosslinking efficiency, low mechanical robustness, and the inability to support perfusion. Additionally, the use of 10%G40 and 10%G100 hydrogel compositions for macro-perfusion studies were ruled out due to

its limited polymer supply and unfavorable material properties for vasculogenesis, respectively. While these limitations were present, 6% GelMA60 was found to be mechanically robust with limited polymer usage for long-term, unidirectional, and pulsatile macro-perfusion for up to 24 hours with no perturbations in the channel or hydrogel integrity. Further investigation into the native mechanical properties of 6%G60 revealed that it bears also moderate stiffness and low viscosity, which closely resembles the biomechanical properties of 10%G40 and the biophysical properties of 5%G100. Altogether, these findings demonstrate that a macro-perfusion model can be developed to support long-term, unidirectional and pulsatile flow and can be used to study the combinatorial role of hemodynamic shear stress and vorticity on angiogenesis.

Aim 3b. Examine the combinatorial role of hemodynamic shear stress and vorticity on angiogenesis in a mechanically tunable matrix

The physical forces generated from hemodynamic flow play a significant role in initiating endothelial cell migration and establishing mature microvascular networks. Various studies have emphasized the importance of dynamic shear stress on microvessel formation, maturation, and maintenance. However, many of these systems designed to investigate the role of shear stress on angiogenesis are either low throughput or too small, such as microfluidic devices, which are not ideal for engineering large vascularized tissue with macro-vessels. Not to mention, there are additional physical forces caused by blood flow, such as vorticity, that contribute to the angiogenic behavior of endothelial cells. Despite this understanding, the role of vorticity on angiogenesis is far understudied and currently limited to either basic *in vitro* systems or complex *in vivo* models. Therefore, a more thorough understanding of the influence of various hemodynamic flow parameters on angiogenesis is beneficial in fabricating highly vascularized tissues for regenerative

medicine. The goal of this work was to elucidate the role of hemodynamic shear stress and vorticity on angiogenesis within a mechanically tunable macro-perfusion bioreactor. First, we characterized microvessel phenotype in 6%G60 hydrogels to validate its use for perfusable angiogenic studies. This work demonstrated that while 6%G60 exhibited comparable native properties to 10%G40 (moderate stiffness, low viscosity), it invoked similar vascular network structures and endothelial behavior as in 5%G100 (moderate stiffness, high viscosity), making is a suitable polymer composition to study angiogenesis with our macro-perfusion bioreactor. Perfusable GelMA, with patent, high-throughput *Squiggle* geometry, was then either left acellular or endothelialized with GFP-HUVEC and perfused with unidirectional and pulsatile flow for 2 days to examine the effects of shear stress and vorticity on lumen closure and permeability. These studies revealed that our macro-perfusion system can be seeded with endothelial cells and perfused up to 48 hours under constant pulsatile flow to generate a complete endothelium. After 2 days of perfusion, particulate diffusion through acellular and cellular constructs were analyzed to assess lumen permeability at distinct regions of the *Squiggle* under steady-state flow. This work revealed that regions of low or intermediate shear stress and vorticity contributed to the greatest diffusion in acellular constructs, while areas of high shear stress and vorticity resulted in diminished diffusion throughout the surrounding matrix. However, when *Squiggle* channels were endothelialized, the flow regions that initially supported robust diffusion exhibited diminished particle displacement, due to cell blockage, regardless of hemodynamic shear stress and vorticity. Despite these findings, continuous optimization of our system is necessary to truly ascertain the effects of shear stress and vorticity on lumen maturation and angiogenesis. Overall, these studies not only provide a model platform that can be adapted to engineer a variety of thick tissues equipped with hierarchical vasculature

for regenerative medicine, but also helps elucidate the combinatorial role of hemodynamic shear stress and vorticity on angiogenesis.

CHAPTER 1. BIOFABRICATION OF THICK VASCULARIZED NEO-PEDICLE FOR RECONSTRUCTIVE SURGERY

This chapter was adapted and expanded on from the following publication:

Stephens CJ, Spector JA, Butcher JB. Biofabrication of Thick Vascularized Neo-Pedicle Flaps for Reconstructive Surgery. Transl Res. 2019; 211:84-122. doi: 10.1016/j.trsl.2019.05.003

INTRODUCTION

Chronic, large wounds following infection, severe burns and trauma, diabetes, or tumor resection can cause permanent disfigurement and have a limited capacity to restore functional tissue. Nearly 6.5 million Americans are burdened by the chronicity of non-healing, cutaneous wounds, with an annual cost of $25 billion dollars for treatment. (18) Unlike acute wound healing, which spontaneously restores injured tissue within a predictable timeframe, chronic lesions are complicated by a severely compromised wound bed, limiting the successful implantation and revascularization of transplanted tissue grafts and adjunctive therapies for tissue rejuvenation. Delivery of an autologous flap of tissue, with intact and patent vascular networks, to the wound site provides a reliable solution for the reconstruction of full-thickness tissue wounds. However, these highly invasive surgical procedures have obligatory donor-site morbidity, which can exacerbate patient debilitation post-operatively, and may require a large supply of unavailable donor tissue. Novel tissue engineering strategies coupled with stem cell therapy can be used to address this clinical concern through the biofabrication of functional and vascularized tissue flaps.

In native tissues, defined vascular organization exists to ensure that organ viability and functionality are achieved. Tissue flaps used for autologous transplantation maintain distinct layers

of healthy skeletal bone, muscle, and/or subcutaneous fat and skin equipped with its own vasculature, regardless of size. Importantly, this vasculature is hierarchical, and the flap is harvested with an intact pedicle comprised of an arterial inflow vessel and at least one venous outflow vessel which are micro-surgically anastomosed to recipient vessels at the recipient site. Establishment of tissue-specific properties will be necessary for the replacement of deranged tissues with a viable alternative. However, variations in niche specificity and cell occupancy of distinct tissue limits the ability to engineer a flap with tissue-specific properties. 3D-bioprinting has been investigated as a prospective strategy for the development of cellular scaffolds with precise vascular design and geometry, biological and mechanical properties, and robust structural integrity and architecture. (19) Common modalities of 3D-bioprinting vascularized constructs are categorized as laser-assisted, inkjet, and extrusion-based. However, the successful use of bioprinting technology to fabricate cellularized full-thickness constructs are highly dependent on bioink composition, crosslinker method, substrate stiffness, bioink rheology, cell source, and construct preconditioning. Thus, identification and exploitation of the key biomolecular and biophysical regulators that support hierarchical neovascularization of distinct tissues can inspire innovative approaches to engineer a functional full-thickness tissue flap for chronic wound repair.

Noteworthy factors that facilitate angiogenic sprouting in the perivascular niche are attributed to mural support cells, extracellular matrix (ECM) stiffness and composition, and acute microenvironmental stresses to local regions of the vascular endothelium. Mesenchymal stromal cells and other support mural cells (e.g. pericytes, smooth muscle cells, and adipose progenitor cells) have been shown to promote microvessel formation of endothelial cells (ECs) via enhanced paracrine signaling in 2D and 3D co-culture systems. (20–23) When ECs are subjected to local

microenvironmental stresses, such as hypoxia, hemodynamic flow, and inflammation, capillary network formation, structure, and integrity are improved. (24,25) Additionally, the formation and patency of endothelial microvasculature is highly regulated by the stiffness and composition of the ECM that ECs and other mural support cells reside in. (26) In this review, we will briefly discuss the current applications used to treat deep cutaneous wounds and highlight key 3D-bioprinting modalities used to prepare vascularized constructs. We will also summarize the microenvironmental nuances that prime neovascularization and feature the key biological and biophysical factors that must be considered when 3D-bioprinting cellularized constructs with tissue-specific functionality for wound healing.

CLASSIFICATION AND CONTRIBUTING FACTORS OF CHRONIC WOUND REPAIR

Wound repair involves an intricate and highly coordinated series of events that enable lesion closure and tissue regeneration within a predicted timeframe (**Fig. 1.1A**). The general mechanisms that govern acute wound healing are categorized into the following four stages: hemostasis, inflammation, proliferation, and remodeling. (27) In brief, damage of the skin prompts vasoconstriction of leaky microvessels to reduce blood flow and trigger fibrin clot formation at the injury site to mitigate excessive blood loss. (28,29) Proinflammatory cytokines released from platelet granules of the fibrin clot and resident macrophages attract circulating neutrophils, macrophages, and T-lymphocytes to the wound bed for the removal of cell debris, infection, and necrotic tissue, while stimulating the anti-inflammatory response to promote angiogenesis, dermal tissue regeneration, and wound closure. (27,29–35) Although the native response to acute injury is finely tuned, this phenomenon may be disrupted due to complications accompanied by metabolic syndromes, radiation therapy, infection, ischemia, and prolonged inflammation, leading to chronic

wound development (**Fig. 1.1B**). Erroneous response to native wound healing processes can extend recovery time, resulting in the development and expansion of chronic, non-healing ulcers, which are further distinguished as pressure-induced, diabetic, venous, or arterial-insufficient wounds (**Table 1.1**).

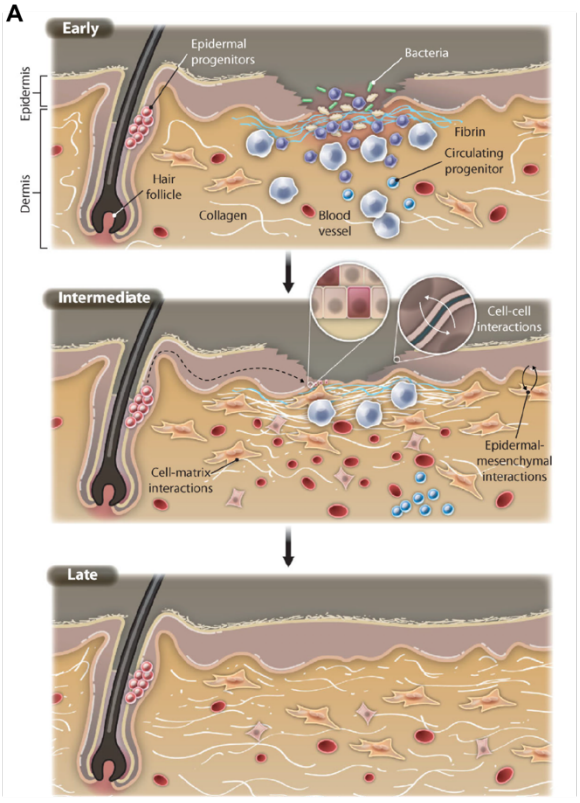

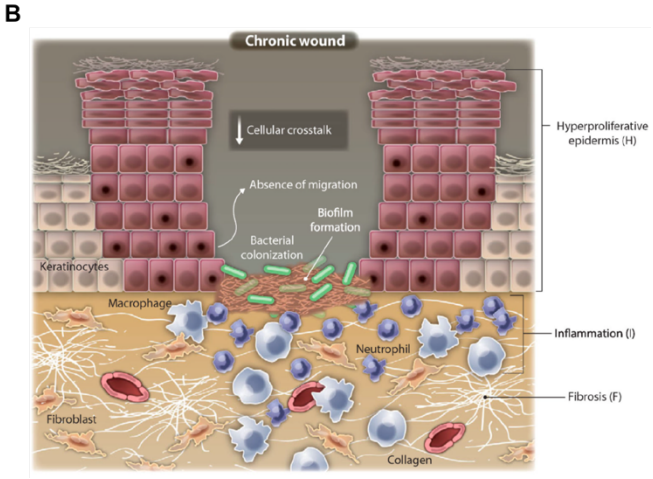

Figure 1.1 Wound Healing Physiology and Pathology. During (A) acute wound repair, injured microvessels constrict and induce fibrin clot formation to prevent excessive blood loss. The combination of leaky blood vessels and pathogenic breach of the skin barrier elicits inflammation, triggering the recruitment and infiltration of immune cells, which support the removal of cell debris and microbes, while promoting neoangiogenesis in the developing tissue and re-epithelialization over the defect site. However, if inflammation persists for an extended period of time, chronic wounds may form, increasing susceptibility to infection and tissue degeneration (B). The key cell players and cytokine regulators present during wound repair are indicated by the legend (C). (Eming et al., 2014)

Continuous tissue compression, particularly at highly-sensitive pressure points or bony protuberances, can disrupt blood flow and nutrient transfer to local subcutaneous regions, increasing the risk of pressure ulcer formation and growth (**Fig. 1.2A**; 19). Pressure ulcers can present as acute, non-blanchable erythema with skin intact and vasculature or manifest into full-thickness tissue loss and derangement of the underlying muscle, fascia, bone and connective tissue. (36–38) Current preventative strategies to mitigate the occurrence of pressure-induced wounds in immobilized or heavily debilitated patients require the use of soft pads and frequent repositioning of the patient to ameliorate prolonged periods of pressure. (39) However, when a pressure ulcer has developed, standard wound care procedures, including pressure offload, selective gauze and topical treatment, necrotic tissue debridement, infection minimization, supplemented with adjunctive pressure removal techniques, such as negative wound pressure therapy, are used to heal severe pressure ulcers.

Similar to PIU, diabetic foot ulcer (DFU) typically develop in regions of high pressure such at the plantar metatarsal heads of the foot and are induced due to neuropathy, peripheral ischemia, and irregular foot biomechanics (**Fig. 1.2B**; 23–25). In general, large vessels above the ankle remain healthy and viable in patients with diabetes mellitus; however, the microvasculature below the ankle can become severely compromised and irreparable. In neuropathic-related DFU development, the loss of pain sensation compromises the loaded regions ability to detect aversive stimuli caused by gait abnormalities, allowing it to undergo repetitive pathological stresses and subsequent ulceration. (40,41,43–45) DFU are also acquired by DM patients with peripheral vascular diseases. In these cases, inadequate microvessel perfusion at local regions of high pressure can impede adequate nutrient diffusion and barrier protection, which subsequently induce tissue

necrosis and defective infection clearance, respectively. (40,41,43) Adjunctive therapies supplemented with necrotic tissue debridement, pressure alleviation, infection mitigation, and vascular reconstruction in appropriate candidates. (42,43) However, persistent ulcer infection can develop into a limb and/or life-threatening gangrene requiring amputation to appropriately treat the infection.

Venous perforator incompetence due to sustained hypertension, particularly in the lower extremities between the midcalf and the ankle, contributes to the development of venous ulcerations, which are characterized by hyperpigmented tissue granulation surrounded by eczematous skin (**Fig. 1.2C**; 29–33). Expansion of the venous walls allows excess fluid and sera proteins to enter the surrounding interstitium, causing edema, and triggers capillary deposition of a fibrin cuff and entrapment of leukocytes. This increases proinflammatory cytokines secretion and chronic inflammation, while preventing adequate diffusion of oxygen and proteins to the subcutaneous tissue, leading to tissue necrosis and ulceration. (48–51) Venous incompetence is exacerbated by immobility, deranged calf muscle pumping, congenital defects or valvular dysfunction; and patients afflicted by old age, obesity, deep vein thrombosis, or previous leg injuries are at high risk for developing lower extremity venous ulcers. (49) Current treatment options, including compression therapy or endo-venous procedures, are aimed at maintaining a moist environment for the healing wound, while minimizing infection and alleviating edema about the injury.

Although the characteristics of arterial and venous ulcers are comparable, arterial insufficient ulcers (AIU) are distinguished from venous ulcers due to the presence of pain and lack of edema

at the lesion site. Arterial ulcers commonly develop in the lower extremities of patients with significant lower extremity peripheral vascular disease; however, they can occur in local regions subjected to repetitive trauma or induced pathological pressure. (46,52) AIU is caused by chronic ischemia of tissue are distinguished as painful, demarcated, "punched out" wounds of necrotic tissue, slough, and minimal exudate (**Fig. 1.2D**; (46). In general, aberrant perfusion of the peripheral arteries caused by macrovessel restriction damages capillary function, depriving the skin and subcutaneous tissues from adequate oxygen and nutrients. (46,52,53) Persistent low blood supply at local tissue regions contributes to necrosis, ulceration, and infection. Interventional strategies implemented to mitigate ulcer expansion and tissue loss are centered around improving tissue perfusion via (endo)surgical revascularization, nutrition, pain management, patient education, infection clearance, and topical treatment. (46,54,55)

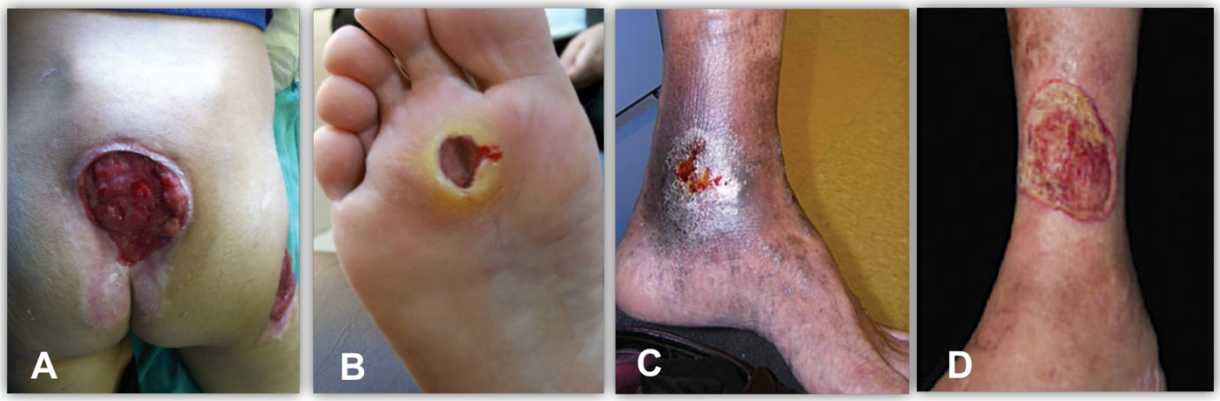

Figure 1.2 Chronic Wound Classification. Chronic wounds are classified into 4 major categories: (A) Pressure ulcers, (B) diabetic foot ulcer, (C) venous ulcers, and (D) arterial-insufficient ulcers. (Duci et al., 2013; Besse et al., 2011; Werchek et al., 2010; Grey et al., 2006)

TISSUE-SPECIFIC FLAPS FOR FULL-THICKNESS WOUNDS

The emergence of advanced therapies supplemented with standard wound care procedures have been implemented to promote chronic lesion closure within a timely manner. Growth factor

therapy (GFT) accelerates the healing of deranged tissues through local or topical delivery of restorative factors in the lesioned area. (56,57) However, there is a high cost associated with growth factor usage, and the external application of these reparative cytokines is limited by the swift degradation rate, high dose requirement and reapplication, and low permeation through the wound (58). In stem cell therapy (SCT), autologous mesenchymal stem cells (MSCs) derived from bone marrow or adipose lipoaspirates has been shown to improve wound granulation, lesion closure, and tissue restoration in chronic, non-healing wounds. (59–65) However, patients with severe microvascular deficiencies and chronic inflammation may not support cell-based treatment to repair chronic wounds in a time- and cost-efficient manner. (66–68) Lastly, artificial skin substitutes with decellularized or cellularized matrices can be used to promote host cell infiltration, proliferation, differentiation, and matrix remodeling for adequate wound closure. (56,57,66,69,70) However, these options are limited by the host immunological response to allogeneic and xenogeneic materials, degradation rate of biological matrices, cell type source, isolation and seeding methods, and compromised biofunctionality of soluble and insoluble ECM constituents. (57,70) Wound bed vasculature of late-stage chronic ulcers may also be too deranged to support revascularization of transplanted matrices or skin substitutes. In this case, surgical procedures involving the transfer of a tissue flap will be required to reconstruct the wound.

Autologous tissue flap transfer relies on the successful resection and transplantation of a vascular pedicle derived from a healthy, autologous source either adjacent or distant to the defect site to repair the wound. (71,72) Tissue flaps are equipped with their own hierarchical vasculature and do not require vascular ingrowth from the underlying wound bed to receive adequate nutrients and oxygen because they already contain adequate perfusion. (73,74) Tissue flaps that restore the

anatomical and physiological integrity of severely compromised tissue are beneficial to patients who suffer from microvascular inadequacies and advanced ulcers that penetrate the subcutis. It should be noted that the injured tissue will not achieve the same properties and appearance as the native tissue upon transplantation; therefore, the essential requirements for donor-site flap selection must prioritize optimal tissue aesthetics and functionality. (75) Distinct vascular properties of potential donor sites also dictate its use for sufficient wound repair. Thus, full-thickness tissue flaps are classified by donor site proximity, structure and composition, and origin of blood supply**.** Tissue flaps identified by donor site proximity can be local, regional, or distal. Autologous local and regional flaps are derived from anatomical locations adjacent to and near the defect site, respectively, and maintain their original source of blood supply. (73) However, distant flaps are harvested from a different location of the body, and the vascular pedicle, which contains the feeding artery and draining veins are micro-surgically anastomosed to recipient vascular supply at the defect site. (73) Tissue flaps can contain a variety of tissues including skin-only and muscle-only, or the underlying musculocutaneous, fasciocutaneous, and osteocutaneous regions of donor tissue, or any combination thereof. (74,76–78) Tissue flaps can also be categorized as random or axial depending on their origin of blood supply. In random pattern skin flaps, the dermal-subdermal plexus is harvested from a local donor site and transplanted to the wound bed to replenish the health skin and subcutaneous fat via small, unnamed blood vessels. (79,80) Axial tissue flaps, however, may contain skin, subcutaneous fat, muscle or bone, and can either be transplanted regionally connected to its original vascular source, or distally, as a free flap, reconnected to the new blood vasculature near the wound. (79,80)

Candidate regions for autologous donor tissue must meet a set of criteria to repair the functional and aesthetic needs of tissue-specific wounds with severely compromised vasculature. As previously described, deep cutaneous wounds are slow healing and require interventional methods for full recovery. Wound chronicity can cause any combination of subcutaneous fat, muscle, or bone to be exposed, increasing the patients' susceptibility to infection if left untreated. Therefore, adequate tissue reconstruction through surgical methods requires knowledge regarding the properties of the specific donor-site tissue in relation to the native tissue properties at the recipient site. This is not only crucial for the successful transplantation an autologous flap, but also for the biofabrication of full-thickness tissues using tissue engineering strategies. The biostructural and mechanical properties of bone, muscle, fat, skin, and relevant connective tissue (tendon and ligaments) are important considerations that must be accounted for when treating full-thickness wounds (**Fig. 1.3**). Insight on these parameters streamlines the selection process of potential donor tissues that will recapitulate the former properties and mechanics of the defective tissue. For instance, subjects afflicted by craniofacial congenital defect, such as oral clefts, require local flaps for proper palate reconstruction to improve speech, realign soft palate muscles, and minimize maxillary disturbances. (81) On the other hand, breast cancer patients who have undergone a mastectomy, require the transplantation of fleshy and fatty tissue from the abdomen or buttock to reestablish the original aesthetic and contour of breast tissue. (82) Therefore, tissue engineers can benefit from the understanding of autologous donor-tissue flap properties when fabricating constructs that are capable for rejuvenating specific full-thickness wounds (**Table 1.2**).

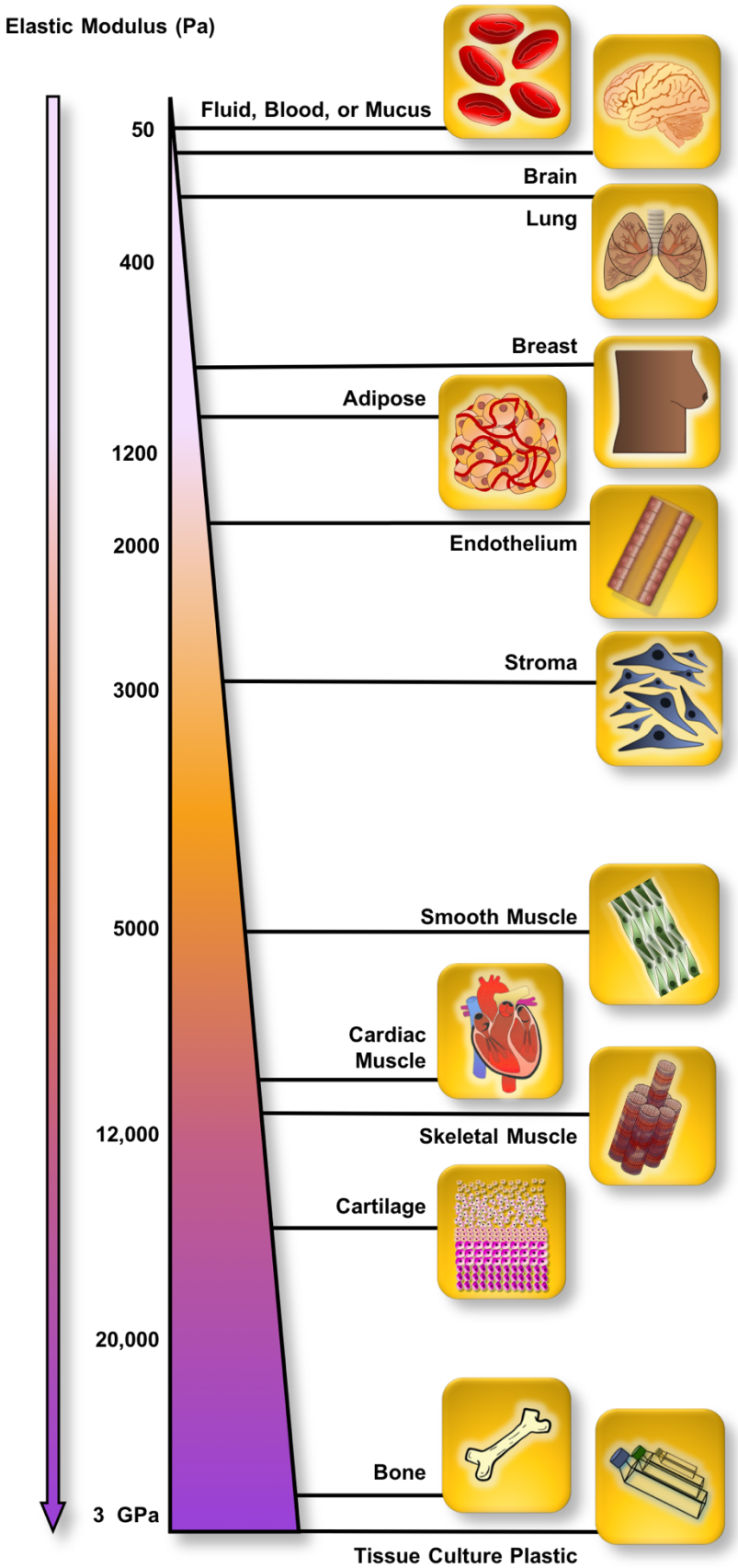

Figure 1.3 Tissue-Specific Mechanics. Distinct tissues acquire unique mechanical properties that contribute to their overall function. Compliant tissues (e.g., brain and lungs) exhibit a lower elastic modulus, indicative of tissue stiffness, whereas rigid tissues (e.g., bone) demonstrate a greater elastic modulus (Cox TR and Erler, 2011)

3D-BIOPRINTING OF ANATOMICALLY PRECISE VASCULARIZED TISSUES

Autologous flap transfer procedures have demonstrated the capacity to restore the function and appearance of chronic wounds with compromised vasculature; however, these strategies are not only limited by donor tissue availability, but also increase donor-site morbidity and infection susceptibility post-operatively. Stem-cell based therapies supplemented with protective bio-scaffold design can be implemented to overcome these hurdles. 3D-bioprinting is a growing advancement in tissue engineering that offers a cost-effective and minimally invasive alternative to autologous flap transfer. In general, 3D-bioprinting fabricates geometrically-precise and heterogenous biological constructs equipped with viable cells, structural matrix proteins, and bioactive morphogens to guide tissue-specific cell behavior. (83,84) The combined use of adult autologous progenitor cells, readily available biomaterials with low immunogenicity, pro-angiogenic stimuli, and extrusion-based 3D-bioprinting (EBB) can produce organ-specific constructs with anatomical precision, replacing autologous flaps for chronic wound repair.

Microvessels

Guided by computer-aided designs or medically acquired images, EBB technology utilizes pressure or mechanically driven dispensing systems to fabricate 3D cellular constructs with high shape fidelity, spatial resolution, and reproducibility. (**Fig. 1.4A**; 2,68–70) In EBB, cylindrical filaments of bioink are deposited in a layer-by-layer fashion to generate mechanically robust and cell-compatible constructs that recapitulate the native structure and organization of healthy tissues. (85,87) Despite these advances, biofabrication methods are restricted to the development of thin tissue-engineered constructs that can facilitate the diffusion of oxygen, which falls between 100 and 200 microns. (88,89) To address this concern, the incorporation of multiscale vasculature

within voluminous bioprinted tissues is required to ensure that healthy tissue-specific function is achieved and maintained upon implantation. Bioprinted constructs must be equipped with macro-vessels that can anastomose with the host vasculature and withstand physiological perfusion pressures (**Table 1.3**). Additionally, hierarchical vascular organization of large vessels to microscopic capillaries within organ-level tissues can support optimal nutrient transfer, oxygen diffusion, and waste removal through the bulk of voluminous biostructures. (**Fig. 1.4B-G**; 71) Macro-channels that are embedded in the bulk and mimic native vessel geometry can be fabricated, endothelialized, and anastomosed to the host vasculature, where upon perfusion, vasculogenesis and subsequent angiogenesis can occur through indirect, direct, or a combination of both strategies. (91)

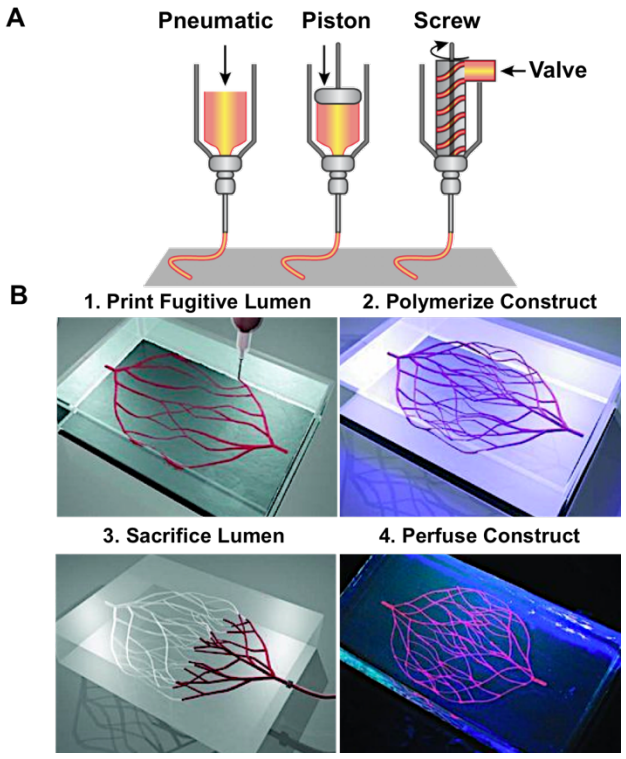

Figure 1.4 Extrusion-Based Bioprinting to Fabricate Hierarchical Vascularized Constructs. General schematic of pressure or mechanically driven EBB (A) and omnidirectional 3D-printing of bifurcated micro-channels within a hydrogel reservoir (B-G). (Murphy and Atala., 2014; Wu et al., 2011)

Skin

The stability of implanted biomaterials into the wound bed of injured tissues is highly dependent on its ability to adjoin with the host vascular supply, as well as support host vascular integration. Thus, the development and implementation of 3D bioprinting strategies to engineer multi-level vascularized flaps is of increasing interest to tissue engineers for chronic wound recovery. Previous studies have verified that hierarchical and permeable vasculature within voluminous tissue is feasible and can support adequate cell survival and activity throughout the bulk of tissue-engineered constructs. (**Table 1.4**; **Fig. 1.5**; (89–95)) However, it is crucial that the bulk material surrounding the fabricated lumen is mechanically robust to withstand implantation and complaint enough to facilitate tip and stalk cell activation and angiogenic sprouting to establish bifurcated microvasculature for adequate cell survival. Dermal tissue biofabrication for full-thickness wound therapy has also made great strides in using EBB to produce avascular or pre-vascularized skin bio-constructs for tissue repair. (**Table 1.5**; **Fig. 1.6**; (96–98)) Despite these findings, 3D-bioprinting methods for generating vascularized hypodermal tissue and subcutaneous fat for the complete rejuvenation of full-thickness tissue defects remains an untapped area of research.

Fat

EBB technology can also be used to construct fat with vasculature for tissue engineering applications, *in vitro* disease models, and wound healing therapies. In regard to tissue engineering applications, Colle et al. established a 3D-bioprinted GelMA scaffold containing ASC spheroids as a potential platform for breast reconstruction and demonstrated that the deposition of ASC spheroid laden GelMA supported cell viability, adipogenesis, and microtissue self- assembly after 14 days (**Fig. 1.7A**). (99) Further studies performed by Zhou et al. revealed that the mechanical

properties, rather than the lattice architecture, of a bioprinted fat scaffold had a greater influence on host acceptance and integration, where softer scaffolds supported greater adipose survival, increased vascularization, and milder fibrosis when transplanted (**Fig. 1.7B**). (100) Additionally, EBB technology has been implemented to study cancer progression using an *in vitro* disease model. Xue et al. established a system for engineering human WAT (eWAT) through bioprinting to simulate cancer-associated cachexia (CAC) *in vitro* (**Fig. 1.7C**). (101) When eWAT constructs were printed, vascularized *in vitro,* and conditioned with pancreatic cancer cell medium, angiogenesis, fat retention, inflammation, and ECM accumulation all improved in comparison to non-vascularized (**Table 1.6**; (99–101)).

In addition to developing adipose tissue engineering applications and *in vitro* disease models with EBB, bioprinting technology has also been used to successfully fabricate fat for chronic wound treatment. Schmitt et al. established a 3D-bioprinted microfat construct, with ASC- and EC-laden methacrylated collagen, as a viable option to improve microfat retention and engraftment for non-healing chronic wounds. In this work, bioprinted microfat clusters were capable of maintaining high cell viability, metabolic activity, and pro-inflammatory signaling, an indication of a supportive wound healing environment (**Fig. 1.7D**). (102) Additional work in this area has also examined the potential use of minimally manipulated ECM (MA-ECM) prepared from 3D-bioprinting autologous adipose tissue for the treatment of DFU in clinical patients. (103,104) When MA-ECM scaffolds were printed and grafted on to the injury site of patients with DFU, clinicians observed graft acceptance, complete closure and re-epithelialization of the wound, and limited infection (**Table 1.6**; **Fig. 1.7E-F;** (102–104)**)**. While the above studies demonstrate the advancement of EBB technology and its ability to 3D-bioprint fat for tissue engineering

applications, *in vitro* disease models, and chronic non-healing wound treatment, there is still a need to develop fat equipped with hierarchical vasculature in order to generate and sustain larger tissue constructs.

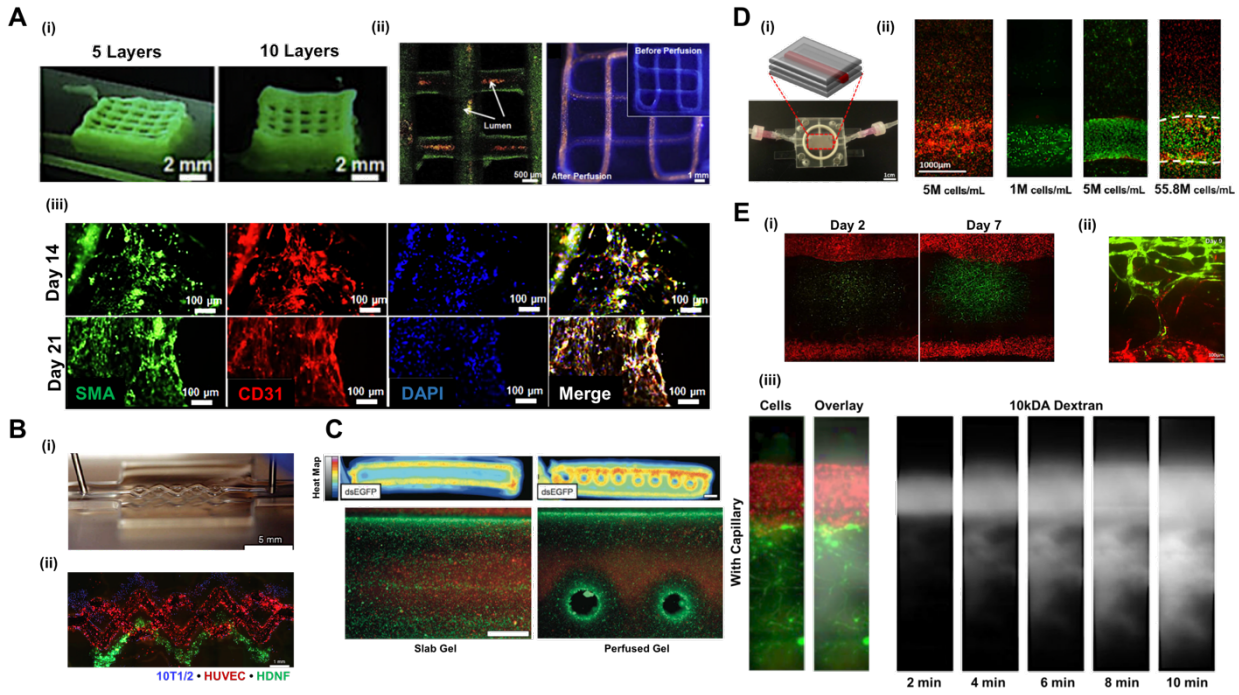

Figure 1.5 Vascular Biofabrication Using EBB. (A) Schematic of bioprinted PEGTA/GelMA tubular constructs with multiple layers (i). A single, ten-layered tubes bioprinted with green fluorescent microbeads supports perfusion along a continuous lumen (ii). Fabricated lumens support colocalization of **α**SMA+-MSCs and CD31+-HUVEC after 14 (top) and 21 (bottom) days of culture (iii). (B) Optical image of bioprinted GelMA construct with interwoven channels upon sacrificing fugitive bioink (i). Cellularized channels containing bioprinted 10T1/2 fibroblasts –based GelMA (blue), HDNF-based GelMA (green) and endothelialized lumen with HUVEC (red) (ii). (C) Schematic of perfusion systems with (right) and without (left) lumen fabrication (i). Heat map depicting cell activity within each PEG-based construct (ii). Live/Dead analysis on bulk stromal fibroblasts within slab (left) or perfusable (right) agarose-based construct indicate perfusion support enhanced cell viability. (D) Schematic (top) and optical image (bottom) of a collagenous biofabricated construct within a custom-designed flow chamber (i). Live/Dead analysis of hepatocytes within the bulk of hydrogel indicate that confluency of the endothelial barrier at the lumen wall perturbs cell viability after 3 days (ii). (E) De novo formation of capillary networks between two parental channels after 2 (left) and 12 (right) days (i). Depiction of lumen HUVEC sprouting upon perfusion and inosculation with bulk material forming sprouts after 9 days (ii). Formation of patent capillary networks connected to larger parental channels as demonstrated by the 10kDa dextran diffusion through the fibrin bulk material (iii). (Jia et al., 2016; Kolesky et al., 2013; Miller et al., 2012; Lee et al., 2014)

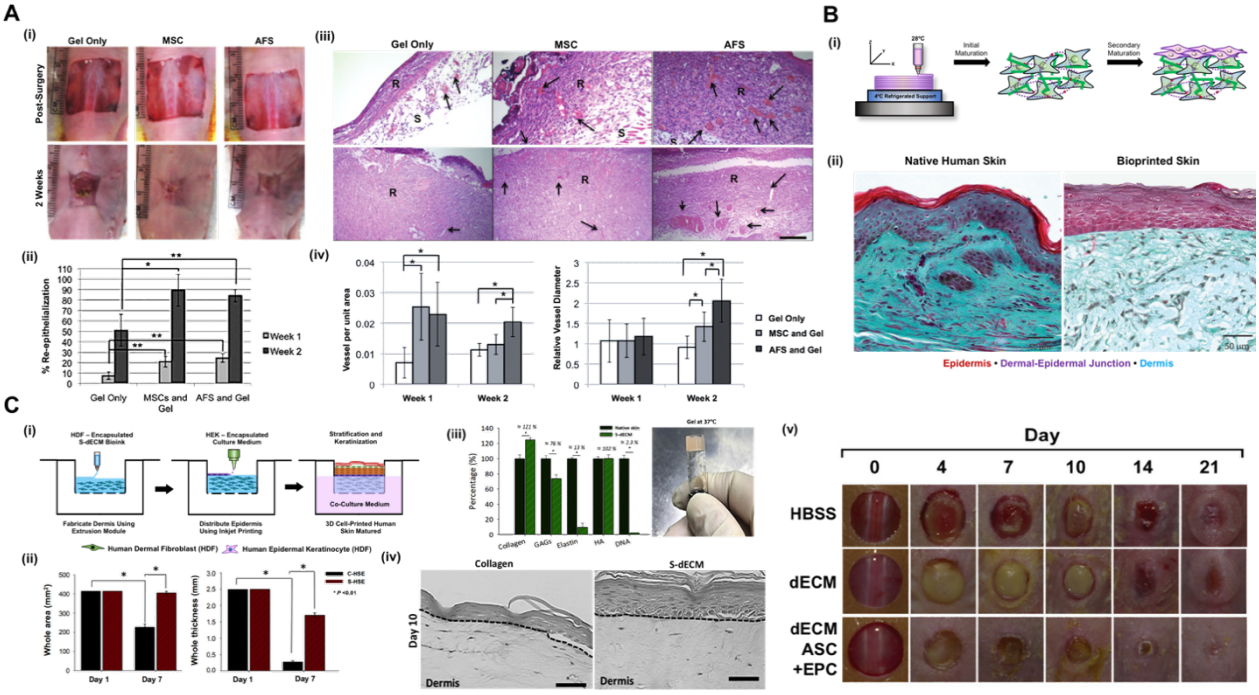

Figure 1.6 Skin Biofabrication Using EBB. (A) Supplementation of fibrin-collagen bioink with MSCs or AFSCs alone augment wound closure rate (i), re-epithelization (ii), tissue thickening (iii), microvessel density and vessel diameter (iv). (B) Schematic of the maturation process of skin tissue (i). This biofabrication method for producing fibroblast-laden alginate-gelatin-fibrinogen hydrogels with a superficial keratinocyte monolayer recapitulates the native morphology of human skin tissue as depicted by the organized epidermis (red), dermal-epidermal junction (purple), and dermis (blue) (ii). (C) ECM structural ligands (collagen, glycoaminoglycans (GAGs), and hyaluronan) are maintained upon porcine dermal tissue decellularization and are capable of forming a bioink at 37C (i). Schematic of 3D-bioprinted human skin model construct (ii). Quantitative analysis depicting S-dECM retained significantly greater area and thickness of the original structure in comparison to collagen gels (iii). D10 histological images of epidermal thickening of collagen- or s-dECM-fabricated constructs (iv). Prevascularization of S-dECM skin patches using ASC s and EPCs accelerates wound closure with near native skin tissue aesthetics (v). (Skardal et al., 2012; Pourchet et al., 2017; Kim et al., 2018)

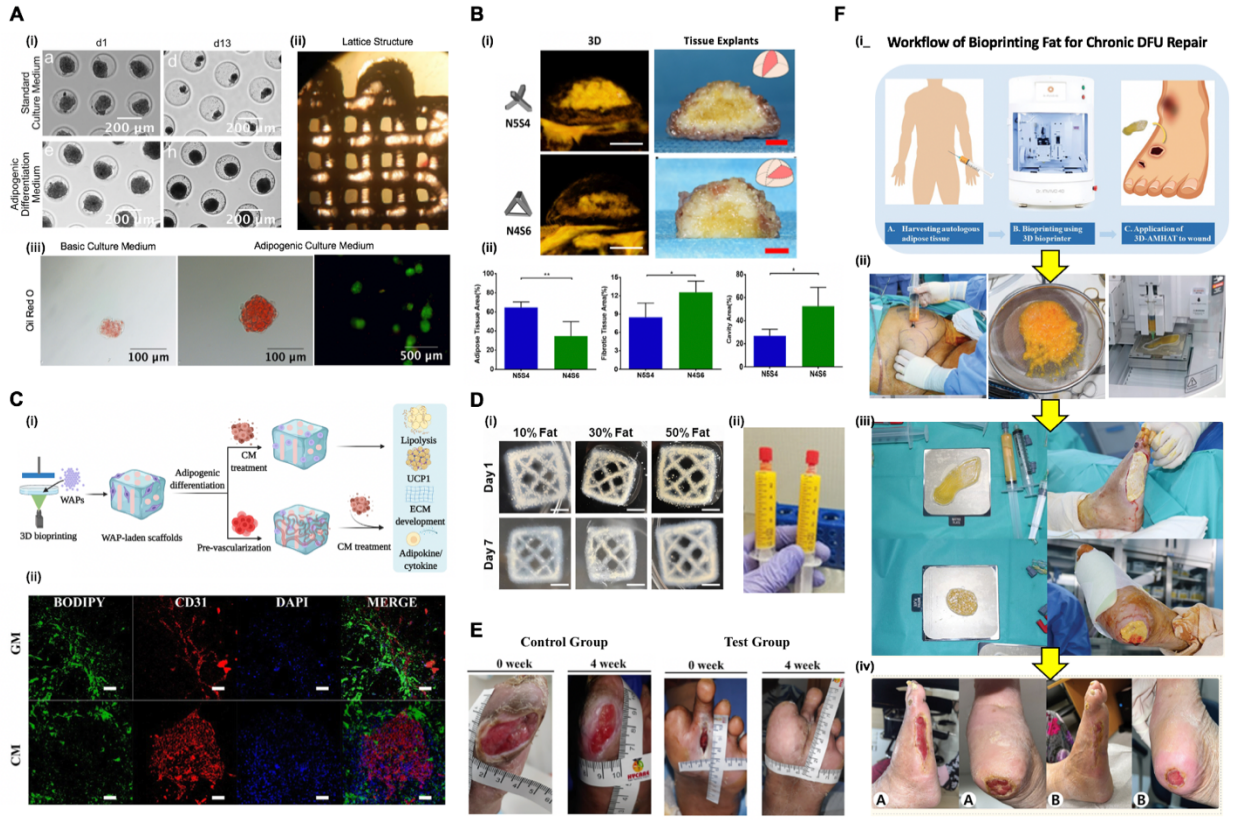

Figure 1.7 Fat Biofabrication Using EBB. (A) Images of ASC spheroids treated with standard or adipogenic media at D1 and D13 timepoints (i). Images of 3D-bioprinted scaffolds (13 x 13 x 1mm) photo-polymerized with UV light for 15 minutes after physical gelatin at 4ºC for 30 minutes (ii). Oil red O images of ASC spheroids after treatment with basic culture medium (left) and adipogenic culture medium (center), as well as Live/Dead images of ASC spheroids treated with adipogenic medium only (left) (iii). (B) MRI of tissue-engineered breasts fabricated with N5S4 (soft) and N4S6 (stiff) scaffolds after 12 weeks of implantation in rats (i). Quantitative analysis of adipose tissue volume, fibrotic tissue area and cavity area (ii). (C) Schematic of experimental design and workflow. White adipose tissue (WAT) was 3D-bioprinted, induced with adipogenic medium, vascularized with ECs, and treated with pancreatic cancer cell conditioned medium (i). Immunofluorescent stains of fat (green; BIODIPY), vessels (red; CD31), and nuclei (DAPI; blue) in vascularized WAT after treatment with general and conditioned medium (ii). (D) Images of 3D-bioprinted collagen with 10%, 30%, and 50% micro-fat encapsulation at D1 and D7 timepoints (i). Syringes of ready to use micro-fat derived and processed from a patient. (E) Re-epithelialization and healing of chronic DFU wounds in patients treated with standard wound care (control group) versus 3D-bioprinted MA-ECM (test group). (F) Workflow schematic of using 3D-bioprinted fat to treat chronic DFU (i). Autologous adipose tissue harvested from the abdomen, processed, and printed in the shape of the patient defect (ii). Transplantation of the 3D-bioprinted fat construct to the DFU sites at the lateral aspect and base of the foot (iii). Postoperative image of the patient's DFU after 6 (A) and 12 (B) weeks. (Colle et al., 2022; Zhou et al., 2019; Xue et al., 2022; Schmitt et al., 2021; Kesavan et al., 2021; Yoon and Song, 2024)

Muscle and Fascia

In addition to the biofabrication of fat, chronic tissue wounds may also require restoration of musculocutaneous defects. Integrated tissue-organ printing systems have shown a promising capacity to fabricate concentric layers of tightly-packed and organized engineered myofibers and muscle-to-tendon units to achieve the native contractile properties of skeletal muscle (**Table 1.7**; **Fig. 1.8**; (105–107) Although these studies demonstrate that printed muscle constructs can attain mechanical robustness and structural integrity to support neural and vascular network integration by the host, there is a lack of research on the biofabrication of muscle tissue, equipped with its own hierarchical vascular supply using EBB technology. Lastly, chronic osteocutaneous defects may also arise if deep wounds manifest to the underlying bone. Much work has been done to 3D-bioprint biomimetic and perfusable bone-like structures that support cell proliferation and differentiation for bone defect repair; however, various 3D-bioprinting modalities may be necessary to accomplish this goal (**Table 1.7**; **Fig. 1.8**; (108–110)).

Bone

Biofabrication of functional tissues relevant to chronic defects require sufficient knowledge on the local regions of intended repair. The specific biological and mechanical demands of bone, muscle, fat, skin, and connective tissue must be considered when generating functional bio-constructs (**Table 1.8).** Bone composition, in particular, varies in strength and toughness depending on its classification, location, and cortical-to-trabecular bone ratio (**Table 1.9**). Tissue engineers must consider these differences for osteocutaneous wound repair as it would be important to distinguish the structural and mechanical properties that, for example, differentiate the sacrum from the sternum. Additionally, information on the cell types that reside in defined niches can help tailor

tissue engineering approaches to coax targeted stem cell behavior and function (**Table 1.10**). 3D-bioprinting applications provides a tool to produce tissue-specific heterogeneity with hierarchical vascular networks in engineered neo-pedicles, which require the fine manipulation of perivascular cell type.

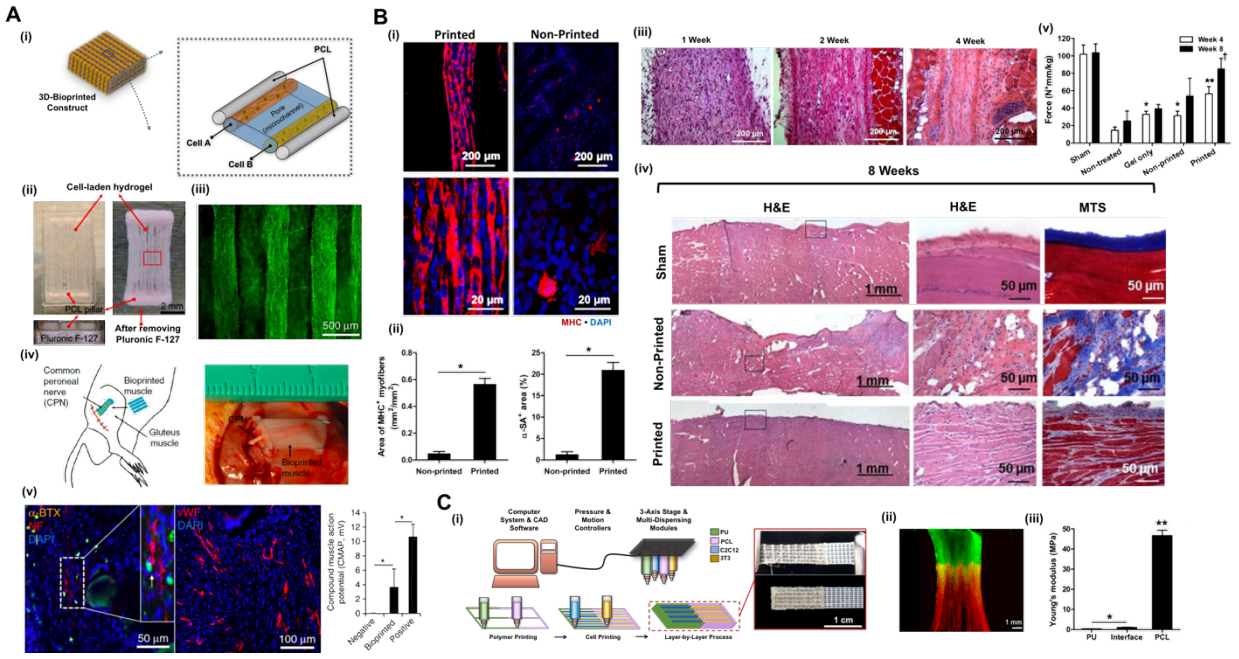

Figure 1.8 Muscle Biofabrication Using EBB. (A) Schematic of 3D-bioprinted cell-laden hydrogels flanked by PCL polymer support filaments (i). Optical image of 3D bioprinted muscle before (left) and after (right) the removal of fugitive ink, Pluronic F127 (ii). D7 live/dead analysis of myoblasts encapsulated in a composite fibrinogen-gelatin-hyaluronan structure, demonstrating cell alignment along the length of the printed fiber direction (iii). Subcutaneous implantation of bioprinted muscle facilitates host innervation, vascularization, and partial restoration of muscle-generated action potentials (iv-v). (B) D7 immunohistochemical images of myofiber formation depict that bioprinted muscle constructs enhance myoblasts alignment and increase myogenic-specific marker (□-sarcomeric actin and myosin-heavy chain) expression in comparison to nonprinted muscle constructs (i-ii). Histological analysis of muscle construct explants after 2 weeks demonstrates an increase in cell density overtime (iii). H&E and MTS analysis on muscle construct explants after 8 weeks reveals comparable muscle volume retention and morphology in bioprinted tissues and sham models in relation to non-printed tissue (iv). Tetanic force of bioprinted muscle construct displayed the greatest recovery in muscle function in comparison to non-printed muscle constructs (v). (C) Schematic of 3D muscle-tendon unit printing system and optical images of the fabricated structure under tension (top) and at rest (bottom) (i). Fluorescently labelled NIH/3T3 fibroblasts (red) and C2C12 myoblasts (green) imaged after 7 days in culture presenting a well-defined intermediate zone (yellow) between fabricated muscle and tendon (ii). Mechanical properties of distinct acellular MTU regions under tension (iii). (Kang et al., 2018; Kim et al., 2018; Merceron et al., 2015)

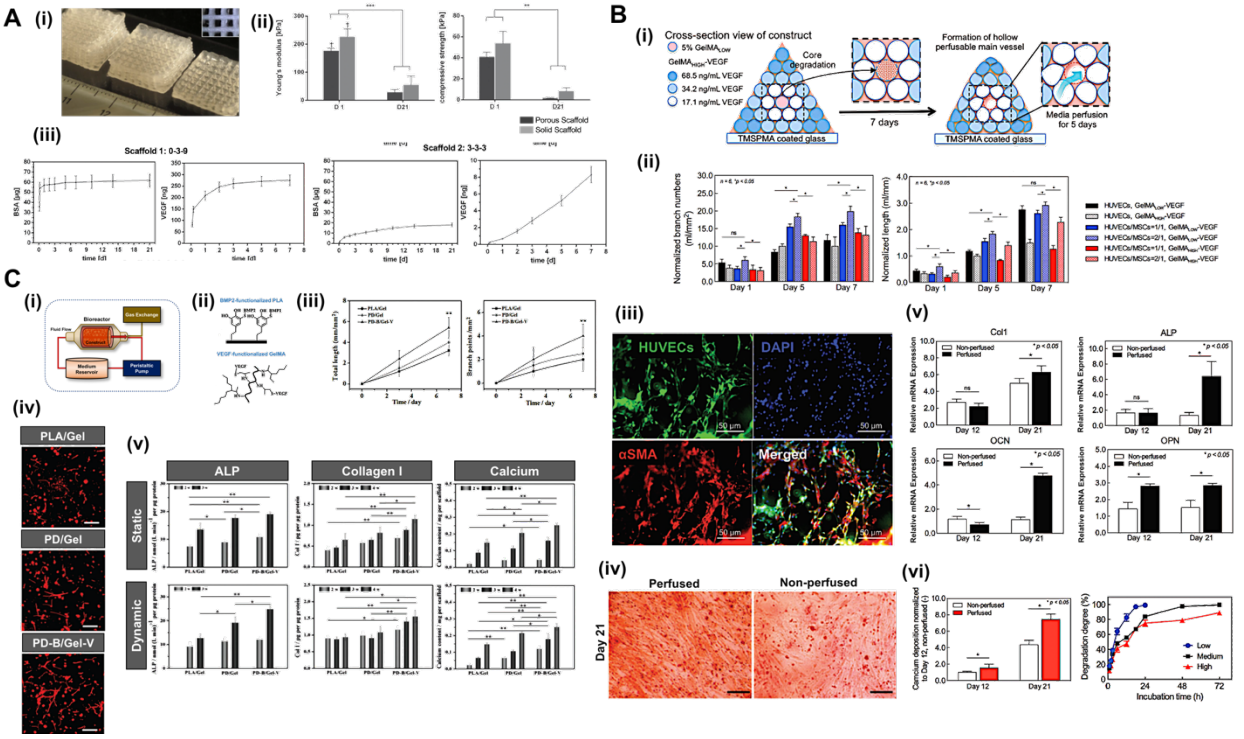

Figure 1.9 Bone Biofabrication Using EBB. (A) Cubic scaffolds of composite Laponite-alginate-methylcellulose (LAM) bioink with increasing layers of polymer maintain high shape fidelity upon printing (i). Release profiles of BSA and VEGF from different scaffolds designs over 7 days indicate that tunable cytokine liberation from LAM scaffolds can be achieved for specific application (ii). Mechanical properties of LAM scaffolds decrease within 3 weeks in cell culture conditions. (B) Schematic of computer-aided bioprinting procedure for producing cylindrical filaments of tissue-engineered bone with complex structure, a perfusable lumen, and an increasing VEGF gradient from the outer lumen to the construct perimeter (i-ii). 5% (w/v) GelMA with a low degree of efficiency (34.1%) and VEGF functionalization enhances angiogenic sprout length and branch points (v) in and colocalization (iv) of luminal MSC and ECs in co-culture. Upon perfusion, the mineralization of biofabricated bone (v) and osteogenic-specific markers (collagen type I (col1), alkaline phosphatase activity (ALP), osteocalcin (OC), osteopontin (OP); vi) is enhanced comparison to static controls after 21 days. Degradation rate of GelMA with varying degrees of methactylation over 3 days. (C) Schematic of the biofabrication process for printing bone tissue with native structural architecture using EBB and laser-assisted bioprinting (i) Functionalized GelMA and polydopamine with VEGF (left) and BMP-2 (right), respectively (ii). Schematic of perfusion bioreactor system (iii). Dynamic flow enhances angiogenic sprouting and branching (iv), and osteogenic differentiation in HUVEC/hMSC cocultures encapsulated in biphasic materials (v). (Ahlfeld et al., 2017; Byambaa et al., 2017; Cui et al., 2016)

BIOLOGICAL CONSIDERATIONS FOR VASCULAR CONSTRUCTS USING EBB

Replication of the native tissue at the recipient site is crucial for the retention and bio-integration of specific tissues. Thus, stem cell regeneration of targeted phenotypes will require more complex microenvironmental control to relevant cell morphogenesis and their spatial boundaries. Strategic selection of biological agents (e.g., cell type, polymer selection, and pro-angiogenic cytokines) for printing vascularized tissue constructs, requires a thorough understanding of the cellular, mechanical, and biological components that regulate neoangiogenesis (**Table 1.11**).

Endothelial Cells

Microvessel formation and maturation occurs through three major processes: (1) vasculogenesis, the *de novo* formation of macrovessels from angiogenic progenitor cells; (2) angiogenesis, the sprouting of microvessels from preexisting blood vessels; and (3) pruning, the regression of excessive angiogenic sprouts that are no longer needed. These phenomena are crucial for the survival and function of cells that reside within voluminous tissue. Peripheral vasculature is subdivided into arterial and venous systems, by which the arterial circulation is highly pressurized for adequate nutrient and oxygen delivery and waste removal to distal organs, whereas venous vasculature functions to transport large volumes of blood from the periphery to the heart under lower pressures (111). The anatomical structure of both arterial and venous vasculature is arranged in concentric, cylindrical sheets of tunica intima, media, and adventitia. The innermost tunica intima consists of a polarized monolayer of endothelial cells (ECs) bound to basement membrane structural ligands, including collagen, laminin, and proteoglycans (91,112). Vascular ECs are directly exposed to the cellular, protein, and mineral components of circulating blood, controlling cell infiltration and soluble ligand diffusion (91,113). Alternatively, the tunica media surrounds

the intima and consists of multiple layers of tightly packed smooth muscle cells (SMCs), innervated by neurons to facilitate vessel contraction and dilatation in response to changes in physiological demands (91,113). The tunica adventitia, or outermost vessel layer, contains fibroblasts embedded in a dense collagenous matrix to stabilize peripheral vasculature and maintain blood vessel functionality (91,113). Pro-angiogenic stimuli deposited from the perivascular and extravascular niche, activates luminal ECs to degrade the underlying matrix and invade the media and adventitia strata, initiating tip and stalk cell activation and neovessel elongation along chemotactic gradient to distal regions (112). Crosstalk between ECs and mural support cells (e.g. pericytes, SMCs, fibroblasts, adipocytes, and MSCs) is not only crucial for tubule formation, but also vessel inosculation and stabilization for adequate blood vessel functionality and tissue survival (25,112).

Pericytes

Colocalization of pericytes to vascular endothelium is necessary to support capillary maturation and stabilization during development and wound healing. Neovascularization occurs in a stepwise process by which endothelial sprouting and migration are followed by pericyte recruitment and colocalization to the abluminal surface of newly-formed vasculature (114). Pericyte secretion of vascular endothelial growth factor A (VEGFA) guides EC sprouting and *de novo* tubule formation through bidirectional, angiopoietin (Ang)/Tie2-mediated pathways (115–117). Co-presentation of both ligands induces pro-angiogenic activity of Ang2, supporting EC proliferation and migration, basal lamina remodeling (118,119). Recent studies also reveal that the expression of the Tie2 is not only specific to ECs but is also minimally expressed in pericytes, contributing to vascular maturation (120). Upon tubulogenesis, neovessel inosculation and pericyte recruitment to the

vascular endothelium are required to modulate proper lumen geometry and stability through EC/pericyte interactions; however, VEGF signaling is not sufficient to support these phenomena alone (114,121). Endothelial secretion of platelet-derived growth factor (PDGF) and epidermal growth factor (EGF) activate the motility, proliferation, and recruitment of pericyte progenitors to the vascular lumen surface for neovessel maturation (122). These paracrine mediators also facilitate robust secretion of the basal lamina structural proteins, collagen, laminin, and fibronectin to support sufficient cell-ECM interactions (23,122,123). Although VEGFA is known to support EC proliferation and migration during angiogenesis, its role in pericyte functionality offers deleterious effects on vessel maturation (124). In vascular pruning, EC apoptosis must occur to finalize the maturation process of nascent microvessels via anti-angiogenic, Ang2-mediated vessel regression and weakened endothelial/pericyte interactions (117,125,126). Endothelial lumen diameter and permeability to soluble ligands require direct contact between ECs, pericytes, and ECM structural ligands to support favorable lumen morphology, constriction, and barrier function through tightly-regulated VEGFA and transforming growth factor beta-1 (TGF-β1)/SMAD-signaling signaling (114,121,122,127–130). Although restricted lumen permeability is important for microvessel maintenance, an influx of circulating pro-inflammatory cytokines, a key feature of wound healing, increases vessel dilation and leakiness through interfering with pericyte behavior and supports angiogenesis via Notch/Jagged1 signaling (131,132). Overall, these studies indicate that finely tuned crosstalk between ECs, pericytes, and the surrounding matrix is required for supporting proper tubulogenesis, matrix deposition, neovessel stabilization, and maturation through lumen diameter and permeability restrictions; and that inflammatory mediators can reverse this process by interfering with pericyte functionality and cell-cell interactions to support adequate wound healing.

Smooth Muscle Cells

Smooth muscle cells also maintain the capacity to support microvessel maturation and stability through enhancing endothelial migration, barrier permeability, and network formation via VEGFA, PDGF, and TGF-β1 activity (133). HUVEC/SMCs 3D-cocultures exhibit improved endothelial tight junctions, cytoskeletal organization, and EC/SMC colocalization, preventing leakage of high molecular weight proteins from *de novo* sprouts (134–136). ECs seeded onto the surface of fibrin-encapsulated SMC aggregates facilitated unidirectional invasion and superior sprout length and density in relation to endothelial-coated acellular aggregates (137). *In vivo* studies further demonstrate that co-transplantation of spatially-arranged ECs and SMCs into an ischemic animal model enhances secretion of VEGFA, impedes necrotic tissue progression, and improves neovascularization, cell migration, blood vessel patency, and tissue regeneration (136,138,139). Despite these findings, recent work demonstrates that tissue-specific SMC derivation regulates endothelial sprouting and maturation differently (140). Additional paracrine mediators have also shown to support the formation, organization and stabilization of neovasculature. EC/SMC spheroids spontaneously reorganize to recapitulate the structural organization of native lumen structure, forming cell aggregates arranged as an SMC-core pellet surrounded by an EC monolayer in the presence of VEGFA and Ang 2 (141). Further investigation revealed that pharmacological inhibition of Ang-2 disrupts the EC/SMC dissociation mechanisms crucial for angiogenesis, impeding vessel destabilization and subsequently, VEGFA-induced endothelial sprouting (142). Previous work has also shown that microvessel formation and stabilization is regulated by sphingosine-1-phosphate (S1P)-induced EC angiogenesis and Notch3/Jagged1-mediated SMC phenotype switching, indicating that paracrine interactions

between endothelial and smooth muscle cells support the differentiation and maintenance of both cell types for microvessel formation and maturation. (143–148).

Fibroblast

Fibroblasts can also facilitate neovascularization by modulating EC behavior, tubule formation, and vessel regression. In 3D-cocultures, HMVEC overlaid with collagen-encapsulated human dermal fibroblasts (HDF) facilitated robust capillary network formation through enhanced EC survival, migration into the overlying matrix, and tubulogenesis via fibroblastic-mediated VEGFA/VEGFR2 signaling (149). Additionally, co-encapsulation of cardiac fibroblast and aortic ECs in fibrin-spheroid model demonstrates superior EC proliferation, sprout extension, and vessel density in relation to EC/MSC constructs (150). Not only are biomolecular ligands involved regulating neoangiogenesis, but also biostructural ligands play a significant and synergistic role in regulating endothelial and fibroblastic cell behavior. The combinatorial effects of bioactive BG ions and nanofibrous ligand structure and orientation supports robust VEGFA secretion from HDFs and endothelial tubule formation in 3D cocultures (151). This work further confirmed that cocultured bio-scaffolds, with combined structural and chemical features, enhanced wound closure, neo-epidermis formation, and neovascularization in a chronic wound healing murine model, indicating the significance of these synergistic properties in potential skin tissue engineering strategies. These phenomena demonstrated by both *in vitro* and *in vivo* work can be attributed to the enhanced expression of genes and proteins critical to the development of functional blood vessels. Microarray analysis of EC/fibroblast cocultures revealed an upregulation in over 300 uniquely expressed genes, namely pro-angiogenic factors and receptors required for mural cell recruitment and vessel stabilization, αβ-integrins that support vessel wall integrity

through cell and basement membrane adhesive interactions, and blood coagulation factors necessary for downstream maturation and functionality of developing neovessels (152). Further investigation of this work demonstrated that EC/fibroblast paracrine mechanisms upregulates these genes via Notch/Jagged1 signaling, suggesting that tightly regulated crosstalk between ECs and fibroblasts is crucial for the proper formation and function of blood vessels. Although paracrine interactions between ECs and fibroblasts strengthen vessel integrity, variations in sera source, cell derivation, and culture conditions evoke differences in neovessel development and maturation (153,154). Overall, these studies conclude that a universal strategy cannot be applied to promote angiogenesis *in vitro*, and that precise culture systems and cytokine cocktails must be considered to optimize this phenomenon.

Adipocytes

Crosstalk between adipocyte and ECs is not only important for durable vascular formation and maintenance but also for healthy fatty acid metabolism in adipose tissue. (155,156) In regard to vasculogenesis, previous studies have demonstrated that pro-angiogenic factors, such as VEGFA, basic fibroblast growth factor (bFGF), interleukin-6 (IL-6), angiogenin, and adiponectin, can be secreted by adipocytes to support healthy endothelial function and vascular development. (155,157,158) When human microvascular endothelial cells (mvEC) were treated with a defined endothelial/ adipocyte coculture medium, mvEC maintenance and microvascular structures were enhanced, as determined by increased CD31, von Willebrand factor (vWF), and acetylated low-density lipoprotein (acLDL) expression, in comparison to mvECs treated with either endothelial- or adipocyte-monocultured media. (159) Further analysis revealed that endothelial-adipocyte communication drives several signaling pathways that regulate endothelial function and

maturation. When adipose microvascular endothelial cells (AMvECs) were incubated in the presence of adipocytes, pro-angiogenic pathways involved in endothelial cell differentiation as well as blood vessel and aorta and mitral valve development were upregulated. (160) It has also been shown that adipocytes have the potential to encourage the pro-angiogenic activity of other cell types that reside in the stromal vascular fraction (SVF) niche, such as immune cells. Adipocytes co-cultured with THP-1 macrophages stimulated the expression of angiogenic factors, such as VEGFA, IL-8, matrix metalloproteinase 9 (MMP9), pentraxin 3 (PTX3), and serpin E1, enhancing endothelial tube formation *in vitro*. (161) Lastly, it has been discovered that mature adipocytes derived from dedifferentiated fat (DFAT) cells also have the capacity to secrete VEGFA and hepatocyte growth factor (HGF) in the presence of vascular ECs, differentiate into pericytes via TGF-ß1/ Smad2/3 signaling, and promote fat graft survival and vascularization *in vivo*. (162,163)

Further *in vivo* analysis validated the significance of EC and adipocyte communication in establishing healthy microvascular formation and integration between host defects and soft tissue transplants. Previous work by Yu et al. showed that their ASC spheroids-sheet coculture system augmented CD31, VEGFA, and HGF expression, improved endothelial tube formation in EC monocultures, and increased capillary density and branch points in an *in vivo* chick chorioallantoic membrane assay. (164) Additional work by Muller et al. revealed that ASC-EC spheroids derived from the SVF of white adipose tissue (WAT) promoted the self-assembly of highly organized endothelial networks with mature unilocular lipid droplets. Additional *in vivo* studies demonstrated that when differentiated spheroids were transplanted in immune-deficient mice, endothelial cells

derived from the spheroids anastomosed with the recipient vasculature, becoming fully integrated within the host. (165)

In addition to the pro-angiogenic role of adipocytes, it should also be noted that the presence of ECs is critical for healthy adipocyte function and fatty acid metabolism. (155,156) Work by Volz et al. further revealed that ASCs treated with adipocyte/endothelial cell cocultured medium, in comparison to EC-monoculture medium, experienced more robust adipogenesis, as determined by increased perilipin A expression, lipid accumulation, and leptin release. (159) Further work revealed that presence of mature vasculature stimulated more robust lipid accumulation, increased adipogenic gene expression, and faster ASC maturation. (166) In addition to these studies, work by Chaurasiya et al. continued to reveal that EC-adipocyte communication not only stimulated pro-angiogenic signaling pathways but also pro-adipogenic pathways, particularly those involved in fatty acid metabolism. (160) Overall, these findings highlight the symbiotic relationship of adipocytes and endothelial cells within the adipose niche and reveal the importance of adipocyte-endothelial crosstalk on healthy adipogenesis and vasculogenesis.

Mesenchymal Stromal Cells

MSCs can easily be harvested from a variety of tissues and maintain their innate proliferative, migratory, multipotent, and immunoregulatory capacity outside their native niche, making them an ideal cell source for regenerative medicine. These distinct features encourage neovascularization and subsequent vessel stabilization through endothelial/MSC interactions, making MSCs suitable for chronic wound healing therapies. Global gene expression analysis of human BM-MSCs (hBM-MSCs) cocultured with ECs demonstrated an upregulation of the pro-

angiogenic factors, cadherin-5 (Cad-5), Ang-4, CD34, platelet/endothelial cell adhesion molecule-1 (PECAM-1) and vWF, and robust expression of Ang proteins, suggesting that ECs play a potential role in mediating MSC behavior and differentiation (167,168). When BM-MSCs were cocultured with HUVEC in 3D-fibrin matrices, Ang-1 stimulation supported vasculature with restricted lumen diameter, and coaxed MSC differentiation down a mural support cell lineage, as demonstrated by increased αSMA expression and EC/MSC colocalization (169). In 3D-collagenous cultures of MVEC and adipose-derived stromal cells (ASC), disruption of Notch/Jagged1 signaling attenuated the expression stromal ligands, VEGF-A/B, and endothelial receptors, VEGFR1/3, but supported robust angiogenic behavior of MVEC under native conditions (170). Additionally, HUVEC/hMSC cocultures in 3D collagen-fibronectin matrices prompted stable vascular network architecture and cell-cell contact, yet immature plexus formation, via mesenchymal secretion of Ang-1/2 cytokines and HGF, a known regulator of VEGF transcription and activity (171). Although MSC demonstrate the capacity to act as a mural support cell type, previous work has shown that delayed exposure of MSC to endothelial cultures improves microvessel formation and develops better vasculature (172). Stromal cell support during neovascularization and vessel maturation identified *in vitro* is also recapitulated *in vivo*, suggesting that paracrine interactions that mediate endothelial behavior and sprouting angiogenesis coax MSC differentiation into mural support cells, and support the engraftment of cellular constructs and host integration at the wound site (172–176).

Although EC/MSC cocultures support these phenomena, the degree and efficiency of neovascularization is highly dependent on the tissue source of MSC derivation (177,178). However, discrepancies between tissue specific MSC induction of vessel initiation and maturation

exists; therefore, information regarding MSCs derived from one source cannot be extrapolated to MSCs derived from an alternative source. Work by Kachgal et al. has shown that tissue-specific MSCs promote angiogenesis through distinct paracrine mechanisms (179–181). Although tissue specific MSCs contribute to variations in pro-angiogenic potential, EC derivation may serve a less important role in mediating comparable degrees of neovascularization. MSC cocultured with ECs derived from umbilical cord, peripheral blood, and neonatal cord blood, demonstrated comparable differentiation potential, αSMA expression via ERK activation, cell-cell communication, and MSC colocalization to endothelial tubules (182). Thus, concerns regarding the origin of ECs used for wound healing therapies may be more focused on utilizing minimally invasive isolation procedures that guarantee high EC yield and expansion, whereas derivation of autologous MSCs from distinct tissue sources may require deeper consideration to meet the specific needs for individualized treatment.

ENVIRONMENTAL CONSIDERATIONS FOR VASCULAR CONSTRUCTS USING EBB

Biofabricated tissues must acquire the appropriate biological and mechanical properties of distinct native tissue to be successful upon transplantation. Growth factor supplementation and matrix protein selection are insufficient for coaxing stem cells down lineage-specific paths and developing mechanically robust, pre-vascularized constructs capable of long-term survival and tissue-specific functionality. Acute microenvironmental stress, including ischemia and inflammation, are occurrences that take place during healthy wound healing to support angiogenesis in areas of microvascular inadequacy. In addition to these biological phenomena, substrate mechanics and local perfusion are also important in mediating vascularization of newly developed tissues. Therefore, exploitation of these environmental pro-angiogenic stimuli can

supplement current tissue engineering strategies to initiate and maintain stable, vascularized biomaterials for adequate wound recovery.

Hypoxia

The oxygenation of ischemic tissues via endothelial tubule formation is a critical step in the initiation and progression of wound healing. Under hypoxic conditions, perivascular stromal cells maintain their stemness, multipotency, and stability, while promoting pro-angiogenic factor secretion and limiting apoptotic behavior (183–186). Secretion of pro-angiogenic factors (VEGFA/B, EGF-1, HIF-1a, TGF-β1, BMP Ang-1, and FGF-2) accelerates vascular sprout formation and stabilization via paracrine signaling between ASCs and MVECs (168,187–189). Work by Li et al. revealed that microvessel and capillary formation are mediated by R-Ras/Akt activity promotes endothelial cytoskeletal stabilization *in vitro* and the reperfusion of ischemic tissue *in vivo* (190). Further investigation of oxygen levels on endothelial behavior confirmed that hypoxia regulates EC migration, whereas normoxia modulates cell adhesion, with comparable effects on EC proliferation (185). As acute wound healing mechanisms progresses, local hypoxic regions at the injured site are also crucial to the promotion of sufficient skin regeneration and lesion closure. Tang et al. demonstrated that oxygen tense conditions activate epidermal stem cells (EpSCs), pushing these cells from a quiescent state to a proliferative state, via HIF-1α signaling *in vitro*, and that this activation diminishes healing time through accelerating EpSC proliferation and epidermis regeneration *in vivo* (191). Although oxygen tense microenvironments support MSC stemness and local angiogenesis, chronic hypoxia can have deleterious effects on the maintenance of pericyte phenotype and recruitment to the vascular endothelium of established blood vessels. Silenced expression of HypERlnc, a hypoxia-induced long noncoding RNA, perturbs pericyte

viability, proliferation, and behavior via Cas9-based transcriptional activation, reversing its differentiated state and increasing endothelium permeability in MVEC/pericyte Matrigel cocultures (192).

Inflammation

The inflammatory response is also a key regulator in the formation of neovessels during wound repair. Butoi et al. demonstrated that crosstalk between M1 macrophages and SMCs mediates matrix protein deposition, ECM maintenance, and neoangiogenesis. When M1 macrophages were cocultured with SMCs, the deposition of ECM structural ligands, collagen and elastin, was diminished while the expression and activity of MMP and VEGF were enhanced (193). This study also confirmed the pro-angiogenic potential of inflammatory macrophages by examining endothelial sprout formation of EC-monocultures in pre-conditioned medium extracted from SMC/M1 cocultures, whereby robust secretion of VEGF into the conditioned medium augmented EC tubulogenesis. In another study, Womba et al. sought to examine the proteomic and metabolic changes in MSCs upon acute injury and chronic disease under oxygen-tense and pro-inflammatory conditions. MSC 2D-cultures subjected to ischemia adapted to local environmental conditions, secreting proteins associated with autophagy, anaerobic metabolism, angiogenesis, and cell migration. However, inflammatory stimulation via interferon-gamma (INF-γ) of MSCs prompted injury containment through the active reduction of inflection, inflammation, and tissue fibrosis (194). Overall, these studies indicate that both ischemia and inflammation enhance the angiogenic behavior of endothelial cells under highly regulated events; however, pathological conditions that prolong these phenomena can have deleterious effects on microvascular maintenance and functionality.

Hemodynamics and Cyclic Strain

Fluid shear stress induced by blood flow is crucial for endothelial phenotype regulation, microvessel lumen formation, vascular network remodeling and homeostasis. Laminar shear stress applied to a lawn of ECs on a collagenous hydrogel, promoted cell invasion deep into the underlying matrix, increasing angiogenic sprout length, repeated bifurcations and endpoints, and tubular structure formation in relation to static controls (195,196). This phenomenon is partially attributed to sphingosine-1-phosphate (S1P) activity, whereby wall shear stress stimulates S1P-induced EC sprouting, invasion, and vascular maintenance via PI3K/Akt signaling and MMP-2 activation (196–198). Additionally, mature microvessel equivalents of gelatin seeded with HUVEC and ASC exhibited enhanced cell viability, capillary density, and mural cell recruitment at the lumen wall of constructs subjected to pulsatile perfusion in comparison to rotating culture, which had shorter and interrupted capillary network (199). Blood-flow induced shear stress induced at the vascular endothelium is also important for mediating the behavior of perivascular smooth muscle cells. Previous work confirms that the co-presence of smooth muscle and endothelial cells stimulates SMC migratory potential and EPC activation. However, the application of physiological shear stress to the vascular endothelium diminishes this phenomenon through reduced MMP-2 and Akt activity, indicating a protective feature of the vessel wall against vascular pathogenesis (200–202).

Computational analysis on vascular fluid dynamics has also contributed to the growing understanding of hemodynamic flow on angiogenic sprouting behavior. Using a multiscale modeling approach, Bazamara et al. investigated the tissue, cellular, and intracellular phenomena

responsible for the initiation and maturation of capillary networks as it pertains to closed-loop blood flow. Upon sprout anastomosis, blood flow is initiated, and endothelial phenotype transitions from a quiescent state to an active state, stimulating the expression of proliferative and migratory signals and subsequent loop elongation (203). Further investigation revealed that shear-induced endothelial activation is necessary for loop maintenance and endothelium barrier function, and that perturbations in hemodynamic intracellular signaling paths inhibits pro-angiogenic factor expression, impeding angiogenesis and disrupting vascular integrity (203–207).

Hemodynamic flow patterns not only address the influence of local shear stress presented at the vascular endothelium, but also describe the effects of vortical flow, pressure differences, and cyclic tension on pro-angiogenic gene expression and regional vascular morphogenesis. Ghaffari et al. developed a fluid dynamics computational model to analyze the hemodynamic microenvironment during avian embryonic development and to predict the local regions of sprout formation from a perfused vascular network. Their work revealed that endothelial sprouts originate from regions of low pressure and elongate towards vessels of higher pressure, regardless of the overall magnitude of pressure difference. Additionally, it was demonstrated that sprout formation generally occurs in areas of low shear stress in the arterial plexus but not at the regions where channels converge, establishing local vorticity. This phenomenon was attributed to the changes in angular velocity experienced at the bifurcation site, rather than the recirculation of fluid. With this model, the location of sprout formation could be successfully predicted to occur at regions with low and positive pressure differentials with minimal shear stress and nonzero vortical flow (208). Additional work by Gebala et al. describes pressure-driven endothelial blebbing, whereby flow-induced lumen expansion increases external vessel pressure, inducing spherical deformation of the

apical endothelium and initiating sprout formation in developing tissues (209). Altogether, these studies reveal the importance of various hemodynamic flow parameters, such as shear stress, vorticity, pressure, and strain, on regulating vascular morphogenesis and maintenance.

Table 1.1 Characteristic Traits and Therapies for 4 Chronic Wound Types

Type	Anatomic Locations	Characteristics	Etiology and Factors	Therapies
Pressure Ulcers[1]	• Pressure points • Bony protuberances • Hip, lower back, buttock, foot heel, ankle, back of head, shoulder, elbow, inner knee	• Discolored and tender wound bed • Blistered and swollen skin • Ruptured skin, subcutis exposure, lymphatic drainage	• Sustained pressure, friction, or shear stress applied to local tissue regions • Susceptibility increased due to cardiometabolic and perivascular diseases, immobility, and old age	• Negative pressure wound therapy • Hyperbaric oxygen therapy • Electrotherapy
Diabetic Foot Ulcers[2]	• Lower extremities • Big toe • Bottom of the foot	• Redness, swelling, and irritation • Subcutis exposure • Foul odor and foot drainage • Eschar formation • Gangrene • Numbness • Callus formation	• Sensory neuropathy • Compromised microvasculature • Poor circulation • Irregular gait mechanics • Hyperglycemia • Diabetes and obesity	• Hyperbaric oxygen therapy • Maggot therapy • Autologous platelet-rich plasma therapy
Venous Ulcers[3]	• Medial or lateral ankle • Lateral bony prominences of the leg	• Rash or dry skin • Itchy and burning sensation • Discoloration • Foul odor • Redness and swelling • Edema • Exposed subcutis	• Varicose veins • Cardiometabolic syndromes • Smoking • Venous hypertension • Previous leg injuries • Poor blood circulation	• Vascular surgery • Compression therapy
Arterial Insufficient Ulcers[4]	• Lower extremities with poor circulation • Lateral side of the lower leg	• Thin, dry, taut skin • Claudication • Blocked arteries • Painful, demarcated wounds • Necrotic tissue and slough • Minimal exudate	• Peripheral vascular disease • Cardiometabolic syndromes Compromised microvascular flow • Chronic ischemia	• Hyperbaric oxygen therapy • Angioplasty

[1] Bluestein and Javaheri, 2008; Ontario Health Technology Advisory Committee in October 2008; National Institute for Health and Care Excellence 2013; Boyko et al., 2018; Prevention and management, 2014
[2] Waniczek et al. 2013 Alexiadou et al. 2019; Armstrong et al. 2017; Wu et al., 2007; Bus et al., 2016; Monteriro-Soares et al., 2012
[3] Grey et al., 2006; Collins and Seraj, 2010 Werchek, 2010; Lim et al., 2018; Alavi et al. 2016
[4] Hedayati et al., 2015; Grey et al., 2016; Bhutani and Vishwanath, 2012

- Delayed capillary refill
- Exposed subcutis

Table 1.2 Donor-site Characteristics and Flap Considerations for Soft Tissue Reconstruction (L: local flaps; R: regional flaps; D: distal flaps)

Injury Site	Defect Causes	Considerations for Tissue Reconstruction	Donor-Site Characteristics	Typical Flaps	Key Donor-Site Regions
Facial (Cheek)[5]	• Traumatic injury • Congenital anomaly • Tumor resection • Lymph node dissection	• Tissue pigment, character, and texture matching • Minimal scarring	• Pliable skin for external coverage and cheek lining • Low subcutaneous fat content • Re-establish mandible lining	**L**: advancement, rotational, transposition flaps **R**: myocutaneous major flap D: microvascular free flap	**L**: lateral facial planes R: lateral facial planes, upper chest **D**: radial forearm, anterolateral thigh, scapular, lateral arm
Breast[6]	• Tumor resection • Radiation therapy	• Re-establish breast contour, texture, and lift • Nipple reconstruction • Minimal scarring	• Sufficient subcutaneous fat volume • Adequate muscle tissue and strength • Pliable skin • Well-defined vascularity	**R**: TRAM and latissimus dorsi (LD) pedicle **D**: DIEP and SIEA free flap	**R**: lower abdomen, lateral side of the middle back **D**: buttock region, Inner thigh
Lower Back (Sacrum)[7]	• Pressure ulcers (bed sores)	• Soft tissue defect coverage • Weight-bearing support in supine position	• Pliable skin with sufficient tensile properties circulation	**L**: Limberg bilateral and unilateral rotation and advancement flaps, myocutaneous or fascio- cutaneous transverse flap	**L**: gluteus maximus, lower back axial to the defect site
Knee and Elbow[8]	• Venous ulcers, arterial insufficient ulcers, severe burns, tumor excision	• Soft tissue defect coverage subcutis	• Thin pliable coverage with hairless skin (elbow) • Low subcutaneous adipose content	**L**: advancement, island, transposition flaps **R**: pedicles, posterior interosseous artery flap **D**: microvascular and SIEA free flaps	**L & R**: lateral arm, radial forearm, LD **D**: radial forearm, groin, scapula, lateral arm, anterolateral thigh

[5] Heller et al., 2008; Pilsl et al., 2012
[6] Lee and Sheckter, 2018; Dayan and Allen, 2017; Pinel-Giroux et al., 2013
[7] Oksman et al.,2018; Chasmar, 2007; Bamba et al., 2017; Borman and Maral, 2002; Hill et al., 1978; George et al., 2018
[8] Griffin et al., 2014 Wu et al., 2015 Kamath et al., 2012, Shiwei et al., 2007

			• Withstand flexion and extension about the elbow		
Hand, Foot, Ankle[9]	• Diabetic foot ulcers, pressure ulcers, arterial insufficient ulcers, tumor resection	• Soft tissue defect coverage • Fat pad re-establishment for weight-bearing regions of skeletal stability • Sensation preservation	• Adequate skin thickness, nerve endings, and fat supply for weight-bearing regions • Pliable skin with thin subcutaneous fat layer for non-weight bearing regions	**L:** myocutaneous VY flaps, fasciocutaneous sural artery (SA) flaps, transposition flap, propeller flap, perforator flap **D**: myocutaneous or fasciocutaneous free flap, pedicle, fascia flap, contralateral leg free flaps, SA free flap	**L**: gastrocnemius muscle, radial forearm, ulnar nerve D: abdominus rectus, latissimus, anterolateral thigh, parascapular, radial forearm, groin, scapula, gastrocnemius

[9] Sato et al., 2017; Ring et al., 2016; Friedrich et al., 2009

Table 1.3 Attributing Factors of Vessel Anastomosis

Attributing Factors	Major Findings	Limitations
Inflammation[10]	• Non-inflammatory myeloid cells (e.g, macrophages, neutrophils, and monocytes) enhance graft-host anastomosis, host vasculature integration, and graft perfusion in the absence of thrombosis	• Inadequate blood supply to the center of the graft will induce tissue necrosis • Loss of endogenous vessels in the pre-vascularized construct may result in graft failure
Cellular and Biomolecular Components[11]	• Fibroblast cocultured with ECs and bFGF supplementation accelerate vascular graft integration and graft-host anastomosis, typically in regions of low VEGFR1 expression in the vascular endothelium	• Mechanistic studies, involving niche-specific biomolecular, cellular, and biophysical components, are required to fully elucidate the precise mechanisms that contribute to graft-host anastomosis
Hemodynamics[12]	• In comparison to normal flow, pulsatile vorticity at anastomotic ends of graft and host macrovasculature enhances end-to-end joining, with negligent effects on platelet activation, decreasing monocyte adhesion and the potential for thrombus formation	• Additional hemodynamic flow properties have not been considered, including cyclic strain, wall shear stress, and interstitial pressure
Prepatterned Vascular Hierarchy (Top-down approach)[13]	• Prepatterned vasculature with defined geometry enhances graft integration and rescues ischemic tissue perfusion in comparison to un-patterned endothelium	• Spatial resolution of current 3D-bioprinting modalities is not precise enough to recapitulate the microarchitectural complexity of the capillary plexus
Preestablished Microvasculature (Bottom-up approach)[14]	• Bioengineered constructs equipped with stable, complex, and elongated vasculature accelerate graft-host microvessel anastomosis, via wrapping-and-tapping, in comparison to non-vascularized or poorly vascularized implants	• *De novo* formation of vasculature within bioengineered constructs is less regulated, potentially leading to tortuous vessel network formation, tumor-like vessel density, and lack of directionality • Occluded microvessels and improper graft perfusion may invoke necrotic tissue formation at the center of the graft

[10] Fantin et al., 2010; Gerri et al., 2017; Lin et al., 2017
[11] Chen et al., 2010; Sekine et al., 2013; Nesmith et al., 2017
[12] Zhan et al., 2010; Chen et al., 2012; Ha et al., 2015; Zhang et al., 2016
[13] Baranski et al., 2013; Chaturvedi et al., 2015; Mirabella et al. 2017; Stevens et al., 2017
[14] Cheng et al., 2011; Koffler et al., 2011; Samuel et al., 2013; Franco et al., 2015; Heller et al., 2016; Asano et al., 2017; Sugden et al., 2017; Ben-Shaul et al., 2019

Table 1.4 Vascular Biofabrication Using EBB

Author	Methodology	Major Findings	Limitations
Miller et al. 2012	• EBB was used to fabricate rigid, filamentous networks of fugitive carbohydrate glass entombed in cellularized PEG- or agarose-based bulk material	• The viability and activity of bulk material resident cells can be maintained if adequate nutrient and oxygen diffusion is permissible by a leaky macrovasculature, which is a function of endothelialized lumen saturation	• Cells in the innermost region of the bulk mass did not remain viable after 3 days due to their limited accessibility to nutrients
Kolesky et al. 2014	• Bifurcated, acellular lumens were fabricated in GelMA bulk hydrogels using a fugitive ink, Pluronic®	• Hollow lumens withstood perfusion of animal blood, and supported the attachment, survival, and proliferation HUVEC, HNDF, and 10T1/2 MSCs	• No information is provided on the effects of macrovessel permeability on nutrient diffusion and cell viability in bulk resident cell populations
Lee et al. 2014	• GFP-HUVEC-laden fibrin matrix was printed and positioned between two parallel, gelatin-based channels, lined with RFP-HUVEC, and perfused to invoke de novo microvessel formation and matrix-channel anastomosis	• Biofabricated system facilitates sprout anastomosis between lumen HUVEC and bulk HUVEC, permitting perfusion of 10kDa dextran throughout the spontaneously formed capillary networks within the fibrin bulk	• These studies do not address whether or not nutrient diffusion through de novo capillary networks supports cell viability of non-vascular cells within the bulk material • Fibrin is thrombogenic and not mechanically robust enough to withstand implantation and perfusion *in vivo*
Jia et al. 2016	• A multilayered coaxial system was used to print hollow, cellularized macro-lumens of biomimetic PEGTA and sodium alginate, with varying diameters and wall thickness	• Fabricated macrovessel supported HUVEC and MSC viability and proliferation, and matrix degradation over a 21-day period at the lumen	• Implantation of a highly organized, patent lumen into a defect site requires bulk material for long-term stability

Table 1.5 Skin Biofabrication Using EBB

Author	Methodology	Major Findings	Limitations
Skardal et al. 2012	• Cell-laden composite bioinks (fibrin and collagen), encapsulating amniotic-fluid stem cells (AFSCs) and BM-MSCs, were bioprinted, implanted over a murine mid-dorsal skin defect model, and assessed based on wound closure rate at 0-, 7-, and 14-days post-surgery	• Wound closure, contraction, and re-epithelialization of the defect site was accelerated in implanted cellular constructs when compared to acellular constructs • Robust microvessel integration into the implanted construct was enhanced, primarily due to AFSC cytokine secretion	• Lack of cell integration from the implant to the wound bed indicates that tissue-engineered implants possess limited engraftment potential, compromising their long-term stability
Lee et al. 2014	• Fibroblast-laden collagen constructs were 3D-bioprinted and keratinized to recapitulate the native structure of the epidermal-dermal junction • Bioengineered constructs were cultured with the fabricated dermis submerged in media and the epidermal layer at the air-liquid interface	• Bioengineered constructs resembled the morphological appearance and biological structure of native skin tissue in vitro	• Methods do not fully recapitulate the architectural complexity of skin, which requires the presence of hair follicles, pigment cells, sweat glands, blood vessels, and sensory neurons
Pourchet et al. 2017	• Fibroblasts-laden composite bioinks (alginate, gelatin, and fibrinogen) were printed and cured onto a cooling plate to emulate dermal tissue, keratinized to mimic epidermal tissue, and conditioned to D26	• Bioengineered constructs exhibited comparable morphological and biological features as native skin tissue, with defined epidermal stratification and dermal tissue maturation within 3 weeks	• Vascularization of bioprinted skin flaps are required to maintain stable and functional tissue • Studies lack information on the integrative potential (both vasculature and dermal tissue) of bioprinted skin in an *in vivo* defect model
Kim et al. 2018	• Native skin scaffolds were EBB-printed to fabricate the dermis (fibroblast-laden S-dECM) and inkjet-printed to fabricate the epidermis • Constructs were cultured until stratification and keratinization • EPC/ASC-laden S-dECM were printed and pre-vascularized prior to implantation in wound healing murine model	• S-dECM maintained its endogenous biophysical and biomolecular features, and can serve as a bioink • Printed pre-vascularized S-dECM can promote wound healing *in vivo* • EPCs and ASCs in S-dECM bioink enhance wound closure, re-epithelialization, and neovascularization of a full-thickness wound	• Biofabrication of functional skin for full-thickness defects will require the presence of tissue-engineered subcutaneous fat to replenish the hypodermis

Table 1.6 Fat Biofabrication Using EBB

Author	Methodology	Major Findings	Limitations
Colle et al. 2022	• 3D-bioprinted GelMA scaffolds containing ASC spheroids for fat tissue engineering and breast reconstruction • Optimal size and shape of ASC spheroids were selected using a high-throughput non-adhesive agarose microwell system. • ASC spheroids underwent adipogenic differentiation to observe viability, maturation, and gene expression after 2 weeks	• Bioprinted ASC spheroids remained viable and maintained an adipogenic phenotype for up to 14 days differentiation Microtissues were able to self-assemble randomly to form a macro-tissue and are a useful tool for soft tissue engineering	• No animal studies were performed to verify the efficacy of methodology in vivo
Zhou et al., 2019	• Designed polyurethane scaffolds (N5S4, N9S8, N7S6, N4S6) with varying mechanical properties by altering its crystal lattice microstructures to establish a clinical option for breast tissue engineering • Bioprinted scaffolds were injected with fat and implanted in nude rats	• Lattice structure for each scaffolding type achieved comparable porosity but varying compressive moduli • Soft scaffolds displayed higher adipose survival, increased vascularization, and milder fibrosis	• Did not demonstrate the capacity to print cell-laden polymers, which is an important need for bioprinting tissues • Only considered the elastic (or stiffness) feature of tissue mechanics and not the viscoelastic nature of materials or tissues
Xue et al. 2022	• Engineered a 3D-bioprinted white adipose tissue model (eWAT) with vasculature (veWAT) to study the pathophysiology of fat loss in cancer-associated cachexia (CAC)	• Conditioned medium displayed inflammatory markers, increasing eWAT lipolysis and ECM accumulation • Conditioned veWAT improved angiogenesis, decreased glycerol release, and increased UCP1 expression in comparison to eWAT • eWAT is a robust model for studying cachectic fat loss, adipose tissue remodeling, CAC physiologies and potential therapies	• No testing was performed to determine if CAC-associated phenomena were reduced with a therapeutic supplement

Schmitt et al. 2021	• Innovated a fat processing system (MiniTCTM) that produces microfat clusters with native ASCs and ECs from lipoaspirates • Bioprinted microfat-laden clusters in collagen to improve graft retention for chronic wound treatment	• MiniTCTM retained cell survival from lipoaspirate • Bioprinted micro-fat clusters remained viable and metabolically active, as well as promoted a wound healing environment after 10 days in vitro	• No animal studies were performed to verify the efficacy of bioprinted microfat-laden collagen as a treatment option in vivo
Kesavan et al. 2021	• Utilized 3D-bioprinted MA-ECM made from autologous adipose tissue to treat chronic foot ulcers	• Patients treated with 3D-bioprinted MA-ECM showed complete wound closure and re-epithelialization after 4 weeks • Patients with standard wound care treatment had delayed wound healing	• Only used one type of standard wound care treatment for the control group and did not consider other options

Table 1.7 Muscle and Fascia Biofabrication Using EBB

Author	Methodology	Major Findings	Limitations
Merceron et al. 2012	• Integrated tissue-organ printing (ITOP) was used to fabricate a linear MTU construct, containing alternating layers thermoplastic polymeric scaffolds and cellular-based bioinks • On one end, a polyurethane scaffold and myoblast-laden composite bioink of fibrinogen, gelatin, and hyaluronan were concurrently deposited to support muscle development • On the opposite end, a poly(caprolactone) (PCL) scaffold and fibroblast-laden composite bioinks for tendon development were co-printed	• After a week of in vitro culture, the MTU construct exhibited more elastic and rigid properties on the designated muscle and tendon sides, respectively, whereas the muscle-tendon interface region of the MTU attained intermediate mechanical properties of both tissues after a week in culture	• Biofabrication of avascular muscle tissue must be equipped with its own hierarchical vascular supply to support the longevity of implanted tissue, graft-host anastomosis, and host vascular integration
Kang et al. 2016	• ITOP was used to print myoblast-laden composite bioinks (fibrinogen, gelatin, hyaluronan, and glycerol) supported by PCL pillars, which induce compaction by invoking cell directionality • Cellular constructs were matured for 7 days in myogenic culture conditions upon subcutaneous implantation in a murine gastrocnemius defect model	• Constructs underwent contraction as myoblast began to extend along the length of the fabricated myofiber-like structure in vitro • Implantation of mature, biofabricated muscle (7d maturation period) displayed sufficient muscle fiber organization, neuronal innervation, vascularization, and increased myogenic receptor expression after 2 weeks in vivo • Myofiber-like structures attained partial muscle function, invoking measurable action potentials upon electrical stimulation	• Pre-vascularized bioengineered constructs may enhance the engraftment of implants and graft-host anastomosis • Tendon repair may be required to fully restore musculocutaneous wounds

Kim et al. 2018	• ITOP was used to print spatially organized, densely packed, and aligned myofiber-like filaments of human muscle progenitor cell (hMPC)-laden composite (fibrinogen, gelatin, hyaluronan, and glycerol) bioinks supported by a PCL polymeric base • Bioengineered muscle was myogenically induced for 9 days for in vitro studies • Pre-conditioned bioengineered muscle was implanted in a rodent anterior tibialis defect model for 8 weeks	• Bioprinted pre-myofiber demonstrated enhanced myogenic marker expression and structural alignment upon mechanical stimulation in comparison to non-printed constructs • 8-week explants revealed successful vascularization and innervation by host, and nearly full functional recovery of the deranged muscle	• Avascular tissue-engineered muscle is unsuitable for long-term in vivo functionality if blood supply is inadequate • Tendon repair may be required to fully restore musculocutaneous wounds

Table 1.8 Bone Biofabrication Using EBB

Author	Methodology	Major Findings	Limitations
Cui et al. 2016	• ITOP combined with CAD modeling was used to recreate precise vascular and bone tissue complex architecture fabricated with a soft, EC-laden, VEGF-incorporated GelMA hydrogel surrounded by a mechanically rigid PLA scaffold with immobilized BMP-2 ligands	• The viability and activity of bulk material resident cells can be maintained if adequate nutrient and oxygen diffusion is permissible by a leaky macrovasculature, which is a function of endothelialized lumen saturation	• Requires various 3D-bioprinting modalities to generate a biomimetic scaffold with the precise, anatomical bone structure and hierarchical vascular architecture
Kang et al. 2016	• An arbitrary mandibular fragment, derived from a traumatic craniofacial injury, was printed using a hAFSC-laden composite (fibrinogen, gelatin, hyaluronan, and glycerol) bioink and exposed to osteogenic conditions for 28 days • Circular implants of hAFSC-laden composite bioinks were printed and preconditioned in defined osteogenic media for 10 days, and subsequently implanted into a murine calvarial defect model for assessment after 5 months	• In the mandibular bone model, matrix calcification was observed upon 28 days of osteogenic differentiation in vitro • In the calvarial bone model, 5-month explants demonstrated host vascularization, mature bone and osteoid formation, and no necrotic tissue formation	• Tissue-engineered bone architecture that recapitulates the native mandible is important but was not assessed • Constructs must be able to support host vascular integration for long-term survival, but this was not assessed in this study • Proper tissue mechanics that are physiologically relevant to the mandible would be necessary to assess the functionality of bioengineered bone
Ahlfeld et al. 2017	• hMSC-encapsulated alginate and methylcellulose bioinks were combined with a nano-silicate clay, Laponite, to print rigid, geometrically complex architectures	• Addition of Laponite to bioink improved printability of hMSC-laden scaffolds with high shape fidelity • Cell-laden composite bioinks functionalized with the VEGF and BSA promoted optimal hMSC functionality, decreased scaffold stiffness indicative of matrix modification, and increased release of morphogens over 21 days	• Constructs must be equipped with preexisting vasculature to support stable and functional bone tissue replacement for long-term stability

Byambaa et al. 2017	• Print cylindrical filaments of low-efficient GelMA with EBB, encapsulating pericytes and HUVEC in highly synthesized GelMA, functionalized with pro-osteoblastic silicate nanoparticles and increasing concentrations of VEGF	• Printed highly organized and perfusable bone-like structures that support cell migration, proliferation, osteoblastic differentiation of MSCs, matrix mineralization, colocalization of the HUVEC and pericytes on the lumen wall, and angiogenic sprout lengthening and branching	• Rapid degradation rate of perfused GelMA constructs limits its use for long-term studies, indicating that composite bioinks that maintain their mechanical robustness over an extended period of time will be required for tissue stability and functionality

Table 1.9 General Structure, Composition, Function, and Mechanics, of Tissue-Specific Organs in Full-Thickness Tissue Flaps

Tissue	Structure and Composition	Function	Relative Stiffness and Tissue Mechanics
Cortical Bone[15]	• Dense, compact, osseous shell of concentric lamellae in parallel along the longitudinal axis (anisotropic) • Innervated tissue • Vascularized Haversian (parallel) and Volkmann's (perpendicular) canals • Encased by periosteum (outer) and endosteum (inner)	• Outer protective shell of bone • Contributes the most to overall mechanical properties of the bone • Withstand bending moments (combined shear, tension, and compression) generated by connected muscle	• Bone toughness (due to collagen content) and strength (due to mineral content) depend on the bone thickness, location, and classification • More brittle and vulnerable to fracture
Cancellous Bone[16]	• Spongy, porous network of lamellae • Less dense, homogenous, and oriented than cortical bone (anisotropic) • Bone marrow and fat • Vascularized and innervated • High water content	• Transfers mechanic load from cortical bone and serves as a shock absorber • Bear bulk of load in highly trabeculated tissue (e.g., vertebrae) • Withstand repetitive compressive axial loads	• High surface-to-volume ratio allows tissue to support greater compressive loads and strain • Varies depending on bone type and location
Muscle[17]	• Cylindrical myofibers of serial sarcomeres encapsulated by collagenous sheaths and packaged in fascicles in parallel alignment • Vascularized and innervated	• Sarcomere contractile elements facilitate muscle contraction to induce or restrict movement • Under voluntary and involuntary control • Tensile forces support muscle stiffening • Inertial forces support muscle bending and twisting • Hydrostatic forces support muscle lengthening and shorting	• Tensile strength is greater in the orientation parallel to the longitudinal axis • Collagen density of muscle is less than tendon, contributing to its weaker stiffness

[15] Ott., 2018; Osterhoff et al., 2017; Bankoff, 2012; Augat and Schorlemmer, 2006
[16] Oftadeh et al., 2015; Ott. 2018; Osterhoff et al., 2017; Bankoff., 2012
[17] Ting and Chiel, 2017; Korthius 2011; Broek et al., 2010

Tendon[18]	• Cylindrical collagen molecules arranged in a hierarchical, parallel alignment • Vascularized and innervated	• Transmit forces generated by muscle to bone • Long tendons (e.g., hand flexors) for finer movement • Short tendons (e.g., Achilles) for power and endurance • Withstand large loads with little deformation	• Acquires a greater tensile strength than muscle • Stiffness varies based on tendon diameter, length, and collagen orientation • Tensile strength is greater in the axial direction
Ligaments[19]	• Cylindrical collagen molecules arranged in a hierarchical, parallel alignment • Less collagen content than tendons • Vascularized and innervated	• Promote motion and stability of the musculoskeletal system • Secure joints between bone • Transmit tensile forces along the longitudinal axis of the tissue • Resist bone torsion	• Less dense collagenous fascicles result in a toughness that is inferior to tendon • Increase in the cross-sectional area diameter increases tissue strength • Tensile strength is greater in the axial direction
WAT[20]	• Lipid-containing adipocytes in WAT exhibiting a round morphology within a collagenous matrix • Highly vascularized loose connective tissue covering skeletal muscle	• Lipid storage and metabolism • Thermal insulation and mechanical protection • Supports load transfer to the underlying bone • Metabolic regulation through endocrine functions	• Stiffness of adipose tissue depends on the anatomical location and the fatty acid composition of resident adipocytes
Skin[21]	• Avascular epidermis with nerve endings present • Vascularized dermis innervated by PNS sensory neurons • Dermis also contains hair follicles and varies in thickness depending on its location • Heterogeneous and anisotropic material	• Barrier protection from external environment • Thermal regulation, prevent water loss, and UV protection	• Tissue mechanics depend on the anatomical location • Dermal collagen contributes to the bulk of skin's elastic properties • Intact skin is under a constant state of tension • Viscous properties require tissue fibers to align before tissue can withstands tensile deformation (hysteresis)

[18] Bordoni and Varacallo, 2018; Thorpe and Screen, 2016
[19] Massel,1999; Amis, 2004
[20] Trayhurn and Beattie, 2001; Alkhouli et al., 2013; Mariman and Wang, 2010; Shoham and Gefen, 2016
[21] Joodaki and Panzer, 2018; Rognoni and Watt, 2018

Table 1.10 Cortical-to-Cancellous Ratio Composition of Distinct Bone Types

Bone Type	Structure and Composition	Function	Physiological Leads	Examples	Cortical-Cancellous Ratio
Long Bone[22]	• Cylindrical and long • Longer in length than width • Cancellous bone surrounded by a cortical outer shell	• Locomotion with muscle contraction • Provide levers for movement	• Tension • Compression • Torsion • Bending • Shear	• Femur, tibia, fibula, humerus, radius, ulna, metacarpals, metatarsals, phalanges	• Proximal/Distal (50:50) • Central (95:5)
Short Bone[23]	• Cube-shaped with equal length, width, and thickness • Cancellous bone surrounded by a cortical outer shell	• Provides stability and support • Limited motion	• Tension • Compression	• Wrist carpals, ankle tarsals	• (40:60)
Flat Bone[24]	• Thin and curved • Cancellous bone sandwiched between thin cortical bone	• Protect internal vital organs • Serves as base for muscle	• Tension	• Cranium, sternum, scapulae, pelvis, ilium, ribs	• (45:55)
Irregular Bone[25]	• Non-uniform bone of irregular shapes • Primarily cancellous bone encased by a thin cortical bone layer	• Anchor points for nervous tissue • Provides stability and support	• Tension • Compression • Torsion	• Vertebrae, sacrum, mandible	• (25:75)

[22]Bankoff, 2012; Clarke, 2008
[23] Clarke, 2008
[24] Clarke, 2008; Graeber and Nazim, 2007
[25] Clarke, 2008; Cramer, 2014

Sesamoid Bone[26]	• Small and round bone embedded within tendon	• Protects tendons from severe compressive forces	• Tension • Compression	• Patellae	• (40:60)

[26] Clarke, 2008; Toumi et al., 2006; Townsend et al., 1976

Table 1.11 Resident Cell Populations in Tissue-Specific Niches

Tissue	Cell Composition	ECM Composition
Bone[27]	• Osteoblast, osteoclasts, osteocytes, osteoprogenitors, MSCs, hematopoietic stem cells (BM), bone lining cells	• Inorganic salts (calcium, phosphate, hydroxyapatite) • Organic structural ligands (collagen, osteonectin, osteopontin, fibronectin)
Muscle[28]	• Myocytes, myoblasts, muscle-derived stem cells, satellite cells, mesenchymal stem cells	• Collagen Type 1, proteoglycans, glycosaminoglycans, glycoproteins
Tendon[29]	• Tenocytes and tenoblasts (tendon fibroblasts)	• Collagen type 1, proteoglycans, glycoprotein, glycosaminoglycans
Ligaments[30]	• Fibrocytes and fibroblast	• Collagen type 1, elastin, glycoproteins, glycolipids
Adipose[31]	• Adipocyte, pre-adipocytes, mesenchymal stem cells, fibroblasts	• Collagen type IV, laminin, fibronectin
Skin[32]	• Keratinocytes, fibroblasts, melanocytes, Langerhans, Merkel's cells, epithelial stem cells, hair follicle stem cells	• Collagen type I and III, elastin, hyaluronan

[27] Ott, 2018; Osterhoff et al., 2017; Bankoff, 2012; Augat and Schorlemmer, 2006; Florencio-Silva et al., 2015
[28] Ting and Chiel, 2017; Korthuis, 2011; Broek et al., 2010; Gillies and Lieber, 2012
[29] Bordoni and Varacallo, 2018; Thorpe and Screen, 2016
[30] Massel, 1999
[31] Alkhouli et al., 2013; Mariman and Wang, 2010
[32] Rognoni and Watt, 2018

CHAPTER 2. ESTABLISHING A MECHANICALLY TUNABLE MATRIX TO STUDY ADIPOGENESIS AND VASCULOGENESIS

This chapter was adapted and expanded on from the following publication:

Stephens CJ, Kobayashi R, Berry DC, Butcher JB. The role of matrix stiffness and viscosity on lipid phenotype and fat lineage potential. Tissue Eng. Part A. 2024 (In Review)

INTRODUCTION

Reconstruction of soft tissues defects caused by trauma, surgery, burns, congenital anomalies, and disease are prevalent, with over 6.5 million procedures performed annually in the United States. (210,211) These types of wounds typically require the replenishment of hierarchical vasculature and subcutaneous fat. (212,213) A current strategy for treating soft tissue injuries include autologous grafts, where healthy tissue is harvested from a healthy, donor region of the patient and transferred to the deranged site. (214) However, these strategies often lead to subpar clinical outcomes due to inadequate vascularization during wound repair. (215) Tissue engineering offers an alternative approach to replace defective and pathological tissues with viable and functional tissues. (216) Yet, while the biological factors that govern cell behavior and tissue formation have been well studied, the mechanical features of the matrix, which also play a significant role in regulating these phenomena, require further elucidation. Therefore, there is a need to better understand how matrix mechanics governs fat and vascular formation in order to biofabricate large, vascularized soft tissues for chronic wound repair.

Tunable polymers, such as gelatin methacryloyl (GelMA), serve as ideal biomaterials for studying the role of mechanobiological cues that govern cell fate. Previous work has demonstrated that

variations in the weight percentage and degree of methacrylation (DoM) of GelMA can alter its matrix properties to achieve tissue-specific mechanics and regulate the behavior of human adipose-derived mesenchymal stem cells (HAdMSCs). (9,217,218) Further work by Kim et al. uncovered that alterations to local GelMA stiffness can invoke differences in hAdMSCs behavior and push them down a distinct maturation pathway *in vitro*. More specifically, hAdMSCs encapsulated in softer matrices exhibited attenuated cell spreading with increased adipose gene expression, whereas ASCs embedded in stiffer matrices enhanced cell spreading, invoking a muscle-like genotype. (219) While this work revealed the importance of stiffness in adipogenic cell differentiation, additional *in vivo* studies by Quan et al. paradoxically showed that beige adipose tissue organoids (BAO) cultivated in stiffer GelMA-based matrices improved liver function, metabolism, and thermogenic activity in obese and type 2 diabetic mice in comparison to softer matrices. (220) The contradictory findings of these studies indicate that there may be additional biomechanical parameters at play which determine cell fate and function during adipogenesis.

The use of GelMA has also shown great promise in supporting robust microvascular formation *in vitro*, as well as superior applicability *in vivo* in comparison to traditional biomaterials such as fibrin. (221,222) Further work by Kim et al. demonstrated that mechanical alterations to dual hydrogel matrices containing GelMA impact microvascular tube formation and maturation differently, with softer matrices supporting the production of more but leaky microvessels in comparison to stiffer matrices. (14) In addition to these findings, recent work by Cheng et al. revealed that 3D-bioprinted GelMA hydrogels with adipose stem cells (ASC) and human umbilical vein endothelial cells (HUVEC) serve as a promising biomaterial for large tissue engineering

applications. When ASC and HUVEC cocultures were encapsulated in GelMA, an increase in tubular structure formation *in vitro* and blood vessel density *in vivo* was observed. (223) While these adipose and vascular studies demonstrate the mechanical range of GelMA and its valuable use in regenerative medicine, there is limited information on the full scope of GelMA mechanics on cell fate. For instance, much of the work that emphasizes the effects of matrix stiffness on cell behavior prioritizes the study of matrix stiffness over matrix viscosity. However, soft tissues, such as fat and vasculature, are viscoelastic, which means that they not only have an instantaneous elastic response to deformation but also a time-dependent response. Therefore, approaches to engineer tissues should incorporate both stiffness and viscosity when examining how matrix mechanics affect cell maturation.

The aim of this present work was to fabricate a polymer with tunable stiffness and viscosity, and to assess how variations in these properties govern cell behavior during adipogenesis and vasculogenesis. **We hypothesized that GelMA with low DoM can elicit significant variations in matrix stiffness and viscosity that create a testable matrix for fat and vascular formation**. GelMA was synthesized with varying DoM to produce polymers with a range in mechanical properties. In our fat studies, hAdMSCs were then encapsulated in GelMA polymers to assess the influences of matrix mechanics on adipogenesis. Additionally, in our vascular studies, HUVEC were co-cultured with hAdMSCs in GelMA hydrogels to uncover the role of biomechanics on vasculogenesis. Overall, the major findings of this study reveal that matrix stiffness, viscosity, and crosslinking efficiency have unique influences on general cell behavior, such as cell viability, circularity, and hydrogel compaction. Furthermore, these studies offer insight on the effects of

matrix stiffness and viscosity on adipogenesis and vasculogenesis for large soft tissue engineering applications.

MATERIALS & METHODS

GelMA Synthesis

GelMA polymers, with a 40% and 100% degree of methacrylation (DoM), were prepared using the sequential and one-pot facile methods, respectively, as described by Shirahama et al. 2016.

Sequential Method

GelMA polymers with 40% DoM (GelMA40, G40) were synthesized by preparing a 10% (w/v) gelatin solution (from porcine, ~300 Bloom, Type A, Sigma-Aldrich®, MA, USA) in 0.1M carbonate-bicarbonate buffer (CBB, ThermoFisher Scientific®, MA, USA) at 60°C. The gelatin solution was then transferred to a round-bottom flask and titrated to a pH of 9 using 0.1M sodium hydroxide. A small volume of methacrylic anhydride (MAA, Sigma-Aldrich®, MA, USA) was then added to the reaction mixture every hour and titrated back to a pH of 9 each time for a total of 5 hours (**Table 2.1**). After the fifth hour, the reaction mixture was left overnight at 60°C and terminated the following day by titrating the GelMA solution to a pH of 7.4 using 5N acetic acid (**Fig. 2.1A**). After synthesis, GelMA40 was dialyzed against deionized water at 50°C using a 1kDa MWCO porous membrane (SpectraPor®, NC, USA) for 3 days, lyophilized for 5 days, and stored at -20°C until usage. *(See **Appendix A** for more details)*

One-Pot Facile Method

GelMA polymers with 100% DoM (GelMA100, G100) were synthesized by preparing a 10% gelatin solution in 0.1M CBB at 60◦C. The gelatin solution was then transferred to a round-bottom flask and excess MAA was added to the reaction mixture (**Fig. 2.1B**). After 2 hours, GelMA100 was dialyzed against deionized water at 50◦C using a 1kDa MWCO porous membrane for 3 days, lyophilized for 5 days, and stored at -20◦C until usage.

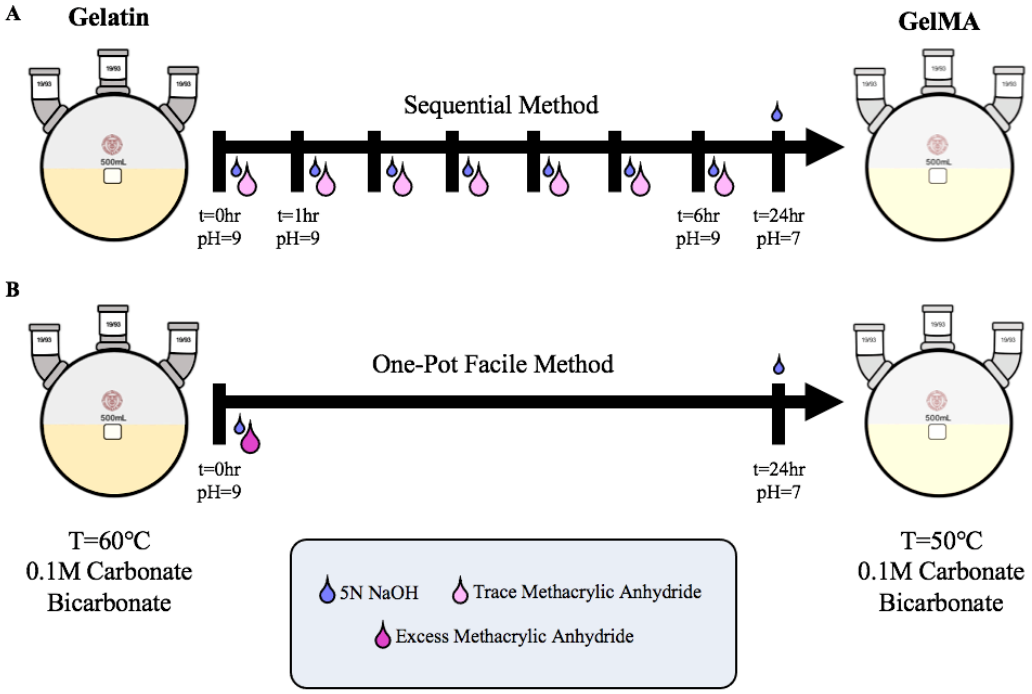

Figure 2.1 GelMA Synthesis. Schematic of the sequential method (A) and one-pot facile method (B) used to synthesize GelMA40 and GelMA100 polymers, respectively. The protocol was established by Shirahama et al. In the sequential method, GelMA polymers with 40% DoM were synthesized by preparing a 10% (w/v) gelatin solution in 0.1M Carbonate-bicarbonate buffer at 60◦C. The gelatin solution was then transferred to a round-bottom flask and titrated to a pH of 9 using 0.1M sodium hydroxide. A small volume of methacrylic anhydride was then added to the reaction mixture every hour and titrated back to a pH of 9 each time for 5 hours. After the fifth hour, the reaction mixture was left overnight at 60◦C and terminated the following day by titrating the GelMA solution to a pH of 7.4 with 5N acetic acid. After synthesis, GelMA40 was dialyzed against deionized water at 50◦C using a 1kDa MWCO porous membrane for 3 days, lyophilized for 5 days, and stored at -20◦C until usage. In the one-pot facile method, GelMA polymers with 100% DoM (GelMA100, G100) were synthesized by preparing a 10% gelatin solution in 0.1M CBB at 60◦C. The gelatin solution was then transferred to a round-bottom flask and excess MAA was added to the reaction mixture (Fig. S1B). After 2 hours, GelMA100 was dialyzed, lyophilized, and stored at -20◦C as stated earlier.

Table 2.1 Customization of GelMA Polymers with Varying Degrees of Methacrylation

Polymer	DoM (%)	MAA (µL) per 1g Gelatin	Synthesis Protocol	MAA (µL) per 200mL
GelMA-35	35%	25 ± 2.8	Sequential	500µL
GelMA-50	50%	36 ± 4.1	Sequential	720µL
GelMA-60	60%	43 ± 4.9	Sequential	840µL
GelMA-65	65%	47 ± 5.3	Sequential	940µL
GelMA-75	75%	54 ± 6.4	Sequential	1080µL
GelMA-100	100%	1000 (excess)	One-Pot	20mL

Proton nuclear magnetic resonance (^1H NMR) Analysis

A Bruker AV400 spectrometer (Bruker, Billerica, MA, USA) was used to acquire the ^{1}H NMR spectra of 1% (w/v) GelMA40, GelMA100, and gelatin dissolved in D_2O. The final DoM of GelMA40 and GelMA100 was confirmed by integrating the methacrylate proton signals from δ= 5.3-5.8 ppm ($GelMA_{5.3\text{-}5.8}$) and normalizing it against the lack of signal in gelatin within that range ($Gel_{5.3\text{-}5.8}$) and the decrease in lysine proton signal at δ= 2.9-3.1 ppm ($Lys_{2.9\text{-}3.1}$). The following equation was used to quantify GelMA DoM:

$$DoM\ (\%) = \frac{(\int GelMA_{5.3-5.8} - \int Gel_{5.3-5.8})}{\int Lys_{2.9-3.1} + (\int GelMA_{5.3-5.8} - \int Gel_{5.3-5.8})} * 100\%$$

Uniaxial Compression

GelMA40 and GelMA100 polymers were UV polymerized at 5% and 10% (w/v) concentrations each in cylindrical silicone molds (6mm diameter, 4-5mm thickness) for 7 minutes. After photopolymerization, GelMA hydrogels were incubated in 1X Phosphate Buffered Solution (PBS, ThermoFisher Scientific®, MA, USA) overnight at 4°C and underwent uniaxial compression at the ramp rate 0.1N/min with a DMA Q800 Dynamic Mechanical Thermal Analysis (TA

Instruments). The stress-strain curve for each sample was plotted up to 20% strain or failure, and the Young's modulus for each sample was calculated as the slope of the linear region between 0-10% strain.

Oscillatory Frequency Sweep

GelMA40 and GelMA100 polymers were UV polymerized at 5% and 10% (w/v) concentrations each in 35mm petri dishes (Sigma-Aldrich®, MO, USA) for 7 minutes and incubated in PBS overnight at 4◦C. The following day, samples were extracted from their dishes and biopsied into a cylindrical shape (20mm diameter, 2-3mm thickness) before performing rheological tests. Using a Discovery HR3 Hybrid Rheometer (TA Instrument) and Peltier plate geometry (20mm plate diameter, 3mm gap), the linear viscoelastic region was determined with an oscillatory strain sweep (0.1-100% strain and 1 Hz frequency at room temperature). Storage moduli were measured using an oscillatory frequency sweep (0.01-100Hz frequency and 1% strain at room temperature). The shear viscosity of each sample was then calculated as the change in storage moduli recorded between a frequency of 100-1000Hz.

Fat-Induced Cell Culture in 3D GelMA Hydrogel

Human adipose-derived mesenchymal stem cells (hAdMSCs, RoosterBio®, MD, USA) were expanded with complete RoosterBasal^{TM}-MSC medium (RoosterBio®, MD, USA) and conditioned for 4 days in 2D culture with adipogenic medium, which consisted of Dulbecco's Modified Eagle Medium: Nutrient Mixture F-12 (D-MEM/F-12, Gibco® Life Technologies Pty Ltd., Australia) supplemented with 1% fetal bovine serum (FBS, CORNING® Life Sciences, NY, USA), 1% antibiotic antimycotic (AA, CORNING® Life Sciences, NY, USA), 1% insulin-

transferrin-selenium (ITS, CORNING® Life Sciences, NY, USA), 0.25mM 3-isobutyl-1-methylxanthine (IBMX, ThermoFisher Scientific®, MA, USA), and 0.1µM dexamethasone (DEX, MP Biomedicals, LLC, CA, USA). On the fifth day, hAdMSCs were resuspended in GelMA polymer solutions (5%G40, 5%G100, 10%G40, 10%G100) at 5 million cells/mL and UV polymerized (λ=365nm) for 7 minutes with 0.1% Irgacure 2959 photoinitiator (IRG, Advanced BioMatrix®, CA, USA) to form cellularized hydrogels. hAdMSC-laden hydrogels were then cultured in adipogenic medium for up to 21 days and medium was changed every other day in both 2D and 3D culture. Data collected from each experimental condition was analyzed at D0, D7, D14, and D21 timepoints. **(Fig. 2.2)**

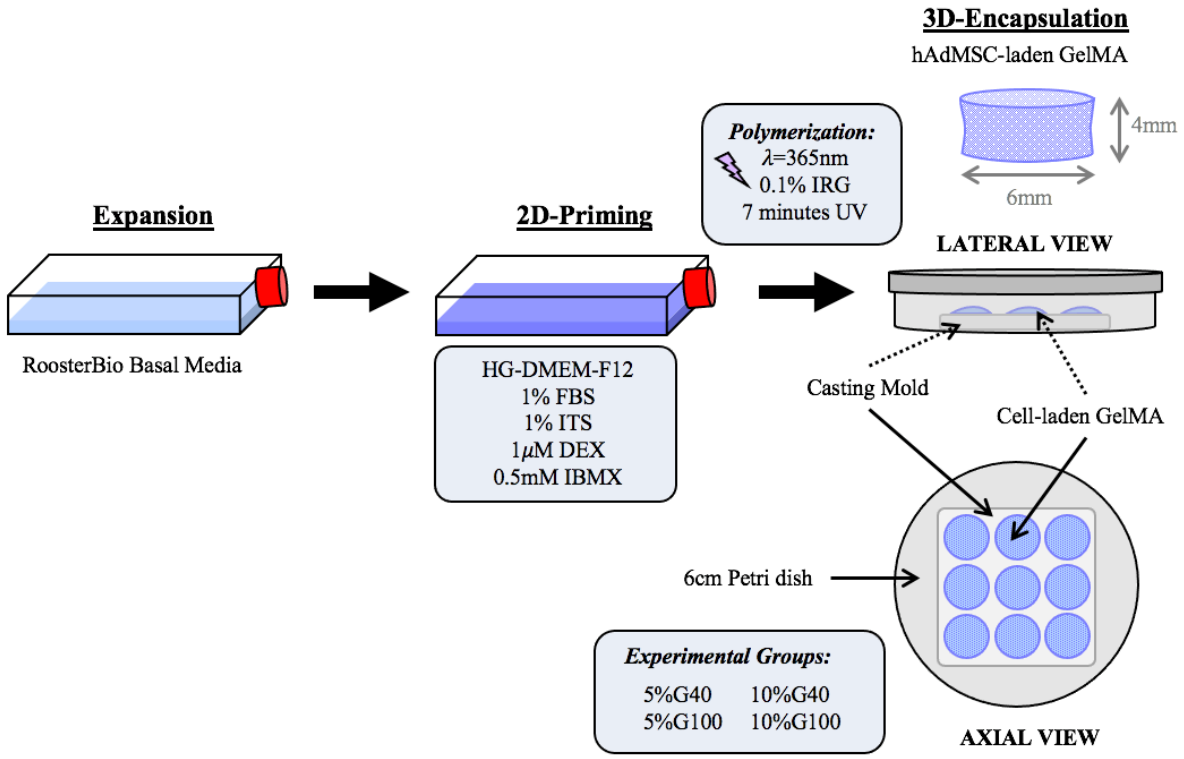

Figure 2.2. Adipogenic Cell Culture Workflow. Schematic of the experimental workflow for expanding, priming, and inducing hAdMSCs embedded in 5%G40, 5%G100, 10%G40, and 10%G100 hydrogels. hAdMSCs were encapsulated in GelMA polymers at 5e6 cells/mL, cultured in adipogenic medium, and taken down for analysis at D0, D7, D14, and D21 timepoints.

Vascular-Induced Cell Culture in 3D GelMA Hydrogel

Human umbilical cord endothelial cells (HUVEC, PromoCell, Heidelberg, Germany) were expanded with complete Endothelial Growth Medium-2 (EGM2, PromoCell, Heidelberg, Germany) and co-suspended with hAdMSCs in GelMA polymer solutions (5%G40, 5%G100, 10%G40, 10%G100) at 4.5 million cells/mL and 0.5 million cells/mL, respectively. Cell-laden hydrogel solutions were then UV polymerized (λ=365nm) for 7 minutes with 0.1% IRG to form 3D co-culture hydrogels. Cell-laden hydrogels were then cultured in vasculogenic medium, which consisted of EGM2 supplemented with 2% fetal calf serum (FCS, PromoCell, Heidelberg, Germany), 100ng/µL vascular endothelial growth factor-165 ($VEGF_{165}$, PeproTech, NJ, USA), 100ng/µL angiopoietin 1 (Ang1, PeproTech, NJ, USA), and 22µg/mL heparin (STEMCELL Technologies, Vancouver, Canada). Hydrogel conditions were cultured up to 10 days and medium was changed every other day. Data collected from each experimental condition was analyzed at D0, D5, and D10 timepoints. **(Fig. 2.3)**

Cell Viability and Circularity

After each timepoint, live hAdMSC-laden GelMA hydrogels were washed in 1X PBS and stained with the calcien acetoxymethyl ester (calcien AM, ThermoFisher Scientific®, MA, USA) and ethidium homodimer-1 (EthD-1, ThermoFisher Scientific®, MA, USA) for 30 minutes at room temperature. Images were acquired using a Zeiss LSM 710 Confocal Microscope (Leica Geosystems, GA, USA) and cell viability and cell circularity were analyzed using FIJI software.

GelMA Compaction

After each timepoint, GelMA hydrogels were washed in 1X PBS, fixed with 4% paraformaldehyde (PFA) and stored at 4°C overnight. Images were acquired using QCapture Pro 7 software with a Zeiss Discovery V.20 Microscope (Leica Geosystems, GA, USA) and the surface area of each hydrogel was quantified using FIJI software.

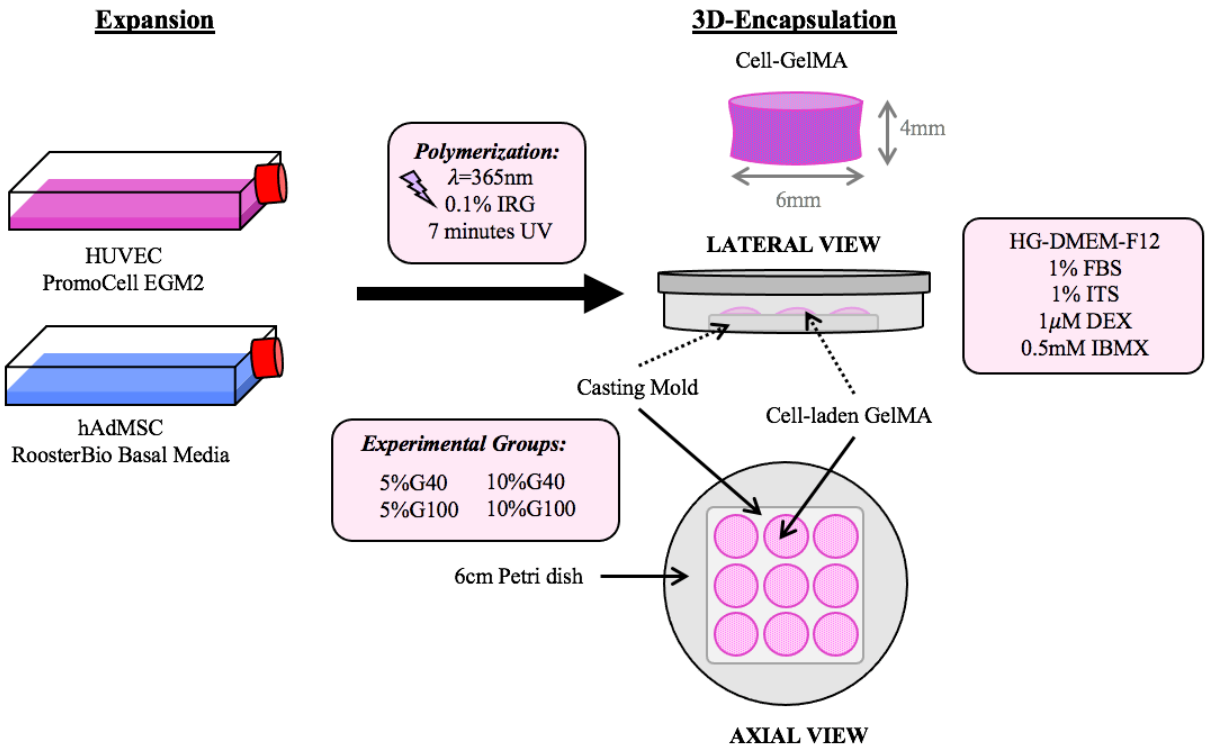

Figure 2.3. Vasculogenic Cell Culture Workflow. Schematic of the experimental workflow for expanding HUVEC and hAdMSCs and embedding co-cultures in 5%G40, 5%G100, 10%G40, and 10%G100 hydrogels. HUVEC and hAdMSCs were co-encapsulated in GelMA polymers at a 10:1 (HUVEC: hAdMSC) ratio at 5e6 cells/mL, cultured in adipogenic medium, and taken down for analysis at D0, D5, and D10 timepoints.

Statistics

Quantitative analyses were performed in quintuplicates for cell viability, circularity, and mechanical testing. A one-way ANOVA was performed followed by a post-hoc Tukey HSD test

and a two-tailed t-test with unequal variance to evaluate any significant difference between experimental groups. All quantitative data was reported as the mean ± standard deviation with a significant difference defined when $p<0.05$. The data are shown as * ($p<0.05$), # ($p<0.01$), **ζ** ($p<0.001$).

RESULTS

Matrix Chemical and Mechanical Characterization

GelMA with varying mechanical properties were synthesized at 40% and 100% DoM and confirmed using H^1-NMR spectroscopy **(Fig. 2.4)**. After synthesis, GelMA40 and GelMA100 hydrogels were polymerized at 5% and 10% (w/v) concentrations **(Fig. 2.5A)** and subjected to uniaxial compression **(Fig. 2.5B)** and an oscillatory frequency sweep test **(Fig. 2.5C)** to measure the stiffness and viscosity of each hydrogel composition, respectively. These tests revealed that the stiffness of GelMA hydrogels increased with both increasing DoM and increasing weight composition (**Fig. 2.5D**). However, the viscosity of GelMA hydrogels only increased with decreasing weight composition but not DoM (**Fig. 2.5E**). Additionally, it was shown that 5%G100 and 10%G40 hydrogels exhibited a comparable stiffness (7.4 ± 3.0 kPa and 6.0 ± 1.0 kPa respectively) despite having distinct viscosities (383 ± 133 Pa•s and 234 ± 70 Pa•s respectively), while 5%G40 and 5%G100 hydrogels displayed a similar viscosity (401 ± 73 Pa•s and 383 ± 133 Pa•s respectively) but different stiffnesses (1.74 ± 0.3 kPa and 7.4 ± 3.0 kPa respectively). Similarly, 10%G40 and 10%G100 hydrogels also presented analogous viscosity values (234 ± 71 Pa•s and 228 ± 83 Pa•s respectively) but dissimilar stiffness values (6.0 ± 1.0 kPa and 24.7 ± 6.5 kPa respectively) (**Fig. 2.5F**). Overall, these results reveal that GelMA stiffness is dependent on both the DoM and polymer weight percentage, while the viscosity is determined by the latter. Due

to these findings, the influence of GelMA stiffness and viscosity on adipogenesis can be investigated independently in the remainder of this study.

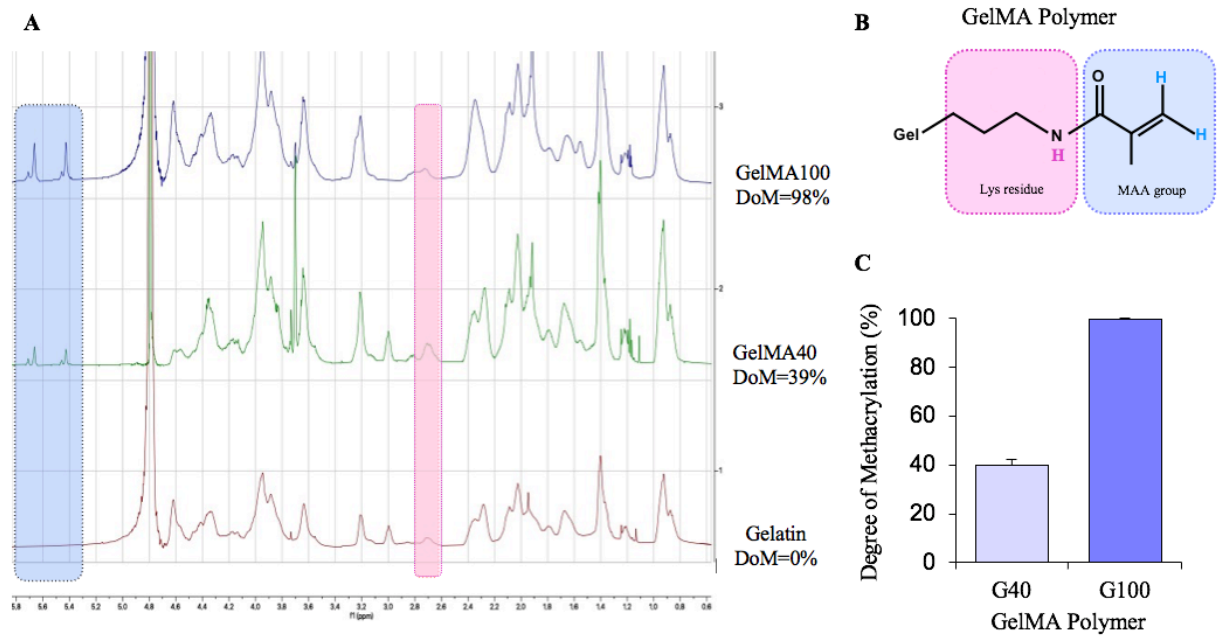

Figure 2.4. Chemical Characterization of GelMA. (A) 1H NMR spectra of GelMA and gelatin polymers with methacrylate and lysine groups highlighted in blue and pink, respectively. (B) Schematic of GelMA polymer with gelatin (Gel) backbone and lysine (Lys) residues substituted with methacrylate groups. Protons from methacrylate groups and lysine residues are highlighted in blue and pink, respectively. (C) Quantitative analysis of GelMA at 40% and 100% DoM.

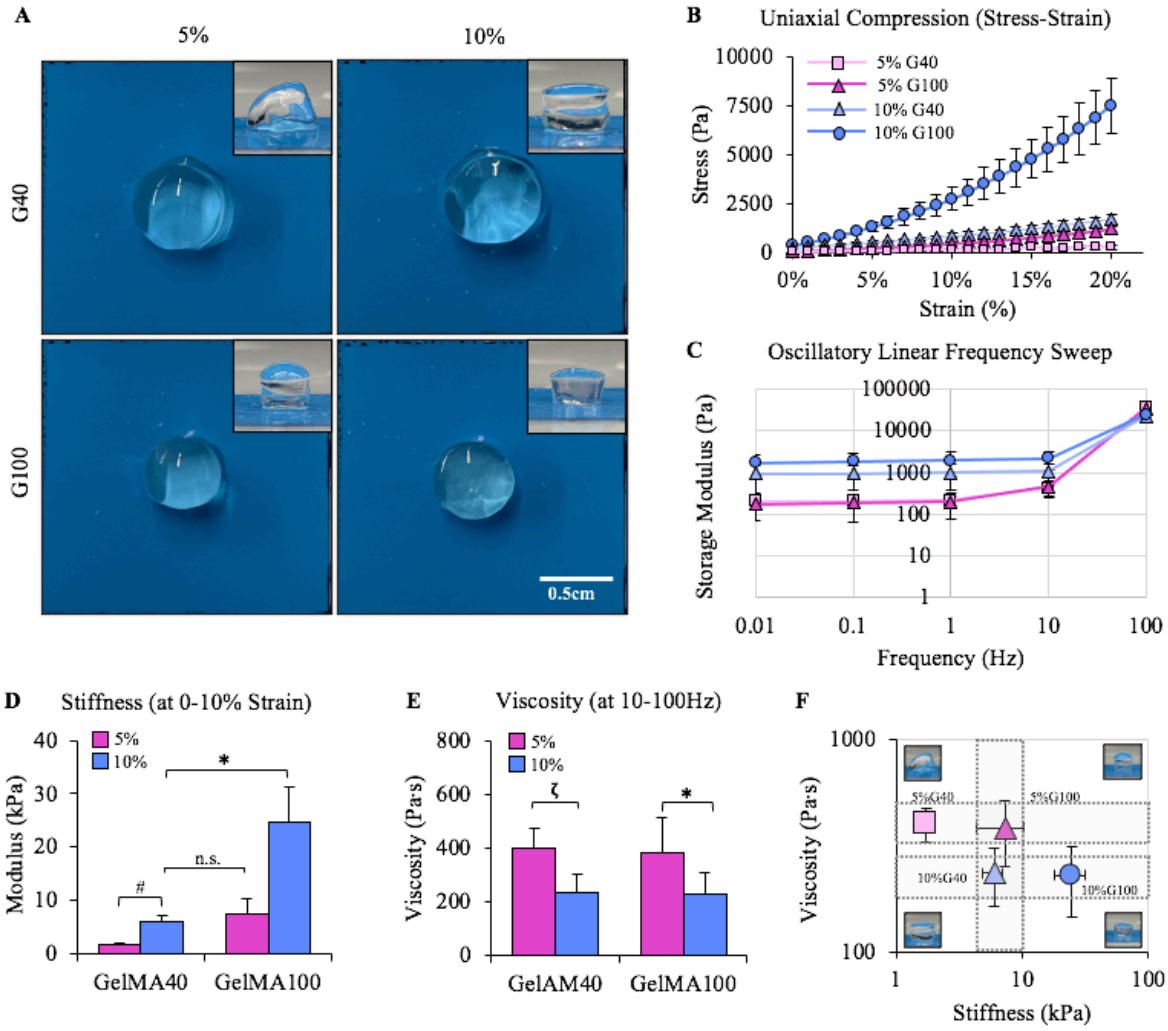

Figure 2.5. Mechanical Characterization of GelMA. (A) Optical images of GelMA40 and GelMA100 hydrogels at 5%(w/v) and 10%(w/v) composition. Stress-strain curves (B) and Young's moduli (D) for 5%G40, 5%G100, 10%G40, and 10%G100 hydrogels subjected to uniaxial compression. Frequency sweep curves (C) and viscosity (E) for 5%G40, 5%G100, 10%G40, and 10%G100 hydrogels subjected to an oscillatory linear frequency sweep. (F) Comparative analysis of the relationship between hydrogel stiffness and viscosity for each GelMA composition. Data are presented as the mean ± SD, n = 4-7. *, $p < 0.05$; #, $p < 0.01$ and **ζ**, $p < 0.001$.

Matrix Mechanics on hAdMSC Viability and Morphology

The viability of hAdMSCs embedded in GelMA was assessed to examine the effects of stiffness and viscosity on cell survival **(Fig. 2.6A)**. hAdMSC-laden GelMA demonstrated high cell viability

in each condition, without surpassing more than 33% cell death **(Fig. 2.6B).** Each condition experienced a significant decrease in cell viability during 3 weeks of adipogenesis except for hAdMSCs encapsulated in 5%G100 hydrogels. It should also be noted that moderately stiff hydrogels with a high viscosity (5%G100) and a low viscosity (10%G40) exhibited the greatest and least cell survival, respectively, over time. Altogether, these results suggest that GelMA viscosity, in comparison to stiffness, is a significant player in regulating cell survival.

The circularity of hAdMSCs embedded in GelMA were also analyzed to determine the effects of stiffness and viscosity on cell morphology. In general, adipocytes exhibit a spherical morphology due to the presence of either a single or multiple lipid droplets (224). In this study, a significant change in cell circularity was seen over time across each condition **(Fig. 2.6C)**. However, hAdMSCs encapsulated in GelMA hydrogels with high and low viscosities demonstrated similar changes in morphology over time. hAdMSCs present in high viscous hydrogels (5% groups) transitioned from a circular to an elongated and back to a circular morphology again. Conversely, cells present in low viscous hydrogels (10% groups) showed decreasing cell circularity over time, with 10%G40 hydrogels invoking the most significant change in cell elongation by the end of the culture period. It should also be noted that while a trend between cell circularity and stiffness could not be defined **(Fig. 2.6D)**, cell circularity appeared to increase with increasing GelMA viscosity **(Fig. 2.6E).** Overall, these results indicate that GelMA viscosity also plays a more prominent role in invoking cell morphological changes in comparison to hydrogel stiffness.

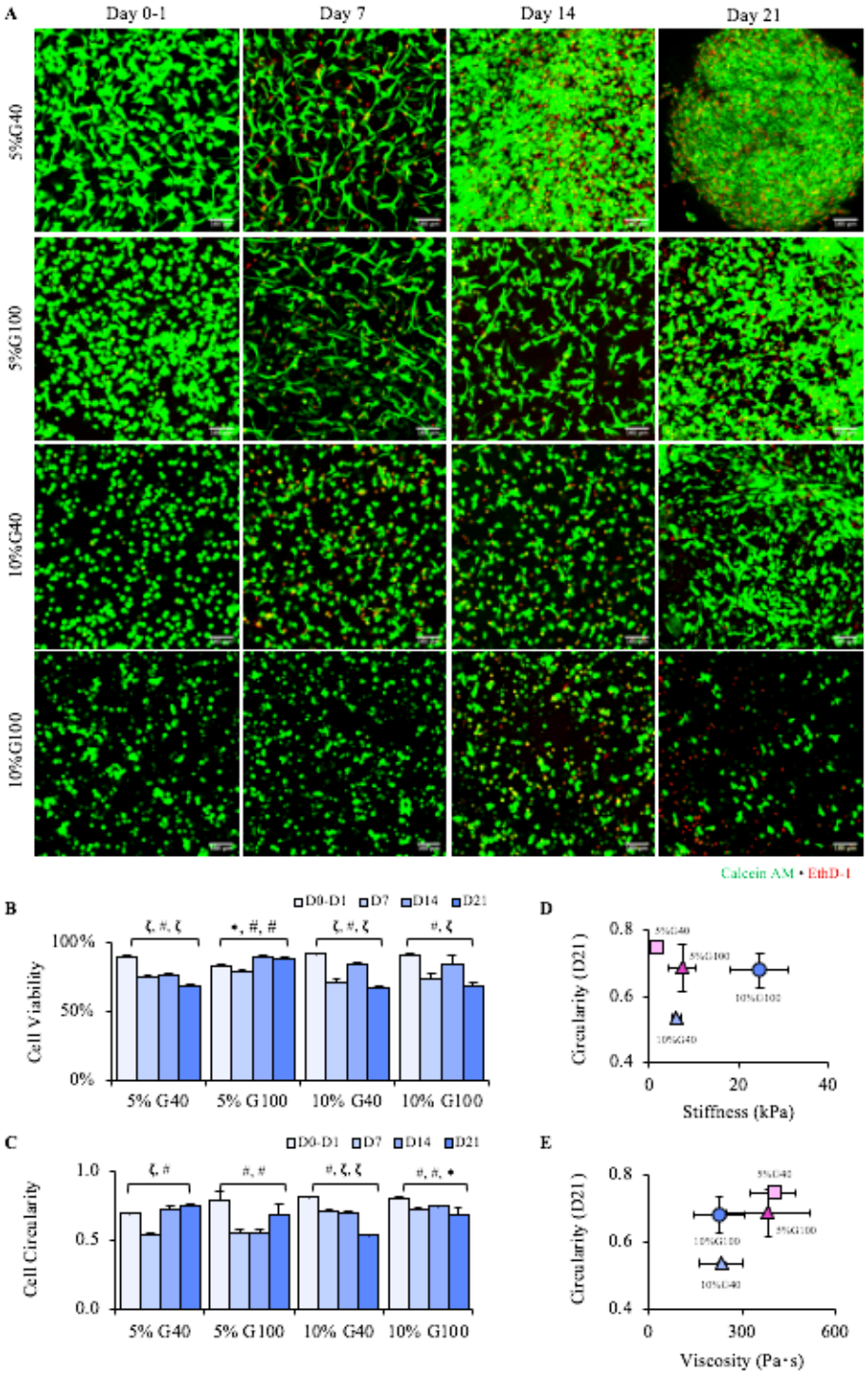

Figure 2.6. hAdMSC Viability and Morphology in GelMA. (A) Live/dead analyses of hAdMSCs encapsulated in 5%G40, 5%G100, 10%G40, and 10%G100 hydrogel conditions after 0, 7, 14, and 21 days of adipogenic differentiation. Live cells were represented by Calcien AM (green) and dead cells were represented by EthD-1 (red). Quantification of the cell viability (B) and cell circularity (C) of hAdMSCs encapsulated in hydrogel conditions at days 0, 7, 14, and 21. Quantitative analysis of the relationship of hydrogel stiffness (D) and viscosity (E) on cell circularity at day 21 only. Data are presented as the mean ± SD, n = 4-7. *, $p < 0.05$; #, $p < 0.01$ and **ζ**, $p < 0.001$.

Matrix Mechanics on HUVEC and hAdMSC Viability and Circularity

The viability of HUVEC and hAdMSCs co-embedded in GelMA was also examined to determine the effects of stiffness and viscosity on cell survival **(Fig. 2.7A).** Cell laden GelMA hydrogels demonstrated high and comparable levels of cell viability throughout the culture period, with each group exhibiting an initial increase in cell viability mid-culture followed by a decrease in cell viability after 10 days **(Fig. 2.7B).** However, the 5%G100 group was the only condition to support a continuous increase in cell viability overtime, indicating that these matrix properties may promote cell proliferation during vasculogenesis. Additionally, while each hydrogel condition experienced minimal cell death during the culture period, it should be noted that matrices with high viscosity (5% groups) contributed to the least cell death in comparison to matrices with low viscosity (10% groups). Altogether, these results suggest that GelMA viscosity, in comparison to stiffness, is also a significant player in regulating cell survival of HUVEC and hAdMSC co-cultures.

The circularity of co-cultured cells was also analyzed to determine the effects of stiffness and viscosity on cell morphology. During vasculogenesis, endothelial cells form cobblestone-like aggregates that invoke the sprouting and spindle-shape morphology of cells, which eventually form tubes. (225) In this study, a significant change in cell circularity was observed over time across all groups **(Fig. 2.7C)**. When cells were initially encapsulated in each matrix condition, they exhibited a round morphology. However, upon vasculogenic induction, cells began to elongate throughout the matrix, exhibiting vessel-like structure especially in matrices with low to moderate stiffness. Cells encapsulated in matrices with the highest stiffness (10%G100) demonstrated the least potential for cell elongation, while matrices with a low to moderate stiffness supported the

greatest capacity for this cell behavior. Specifically, co-encapsulation of HUVEC and hAdMSCs in GelMA hydrogels with moderate matrix stiffness values (5%G100 and 10%G40) demonstrated comparable changes in cell morphology after 10 days. Additionally, co-cultures present in the softest matrices (5%G40) displayed the greatest capacity for cell elongation, indicating that this cell behavior is stiffness dependent. When matrix stiffness was measured against cell morphology at D10, cell elongation increased with decreasing stiffness **(Fig. 2.7D).** However, when cell morphology was compared to matrix viscosity a trend could not be determined (Fig. 2.7E). Lastly, it should be noted that cell circularity appears to decline at a more uniform, stepwise rate in matrices that have low DoM (G40 groups) in comparison to hydrogels with high DoM (G100 groups). Overall, these results indicate that GelMA stiffness, rather than viscosity, plays a more prominent role in invoking cell morphological changes.

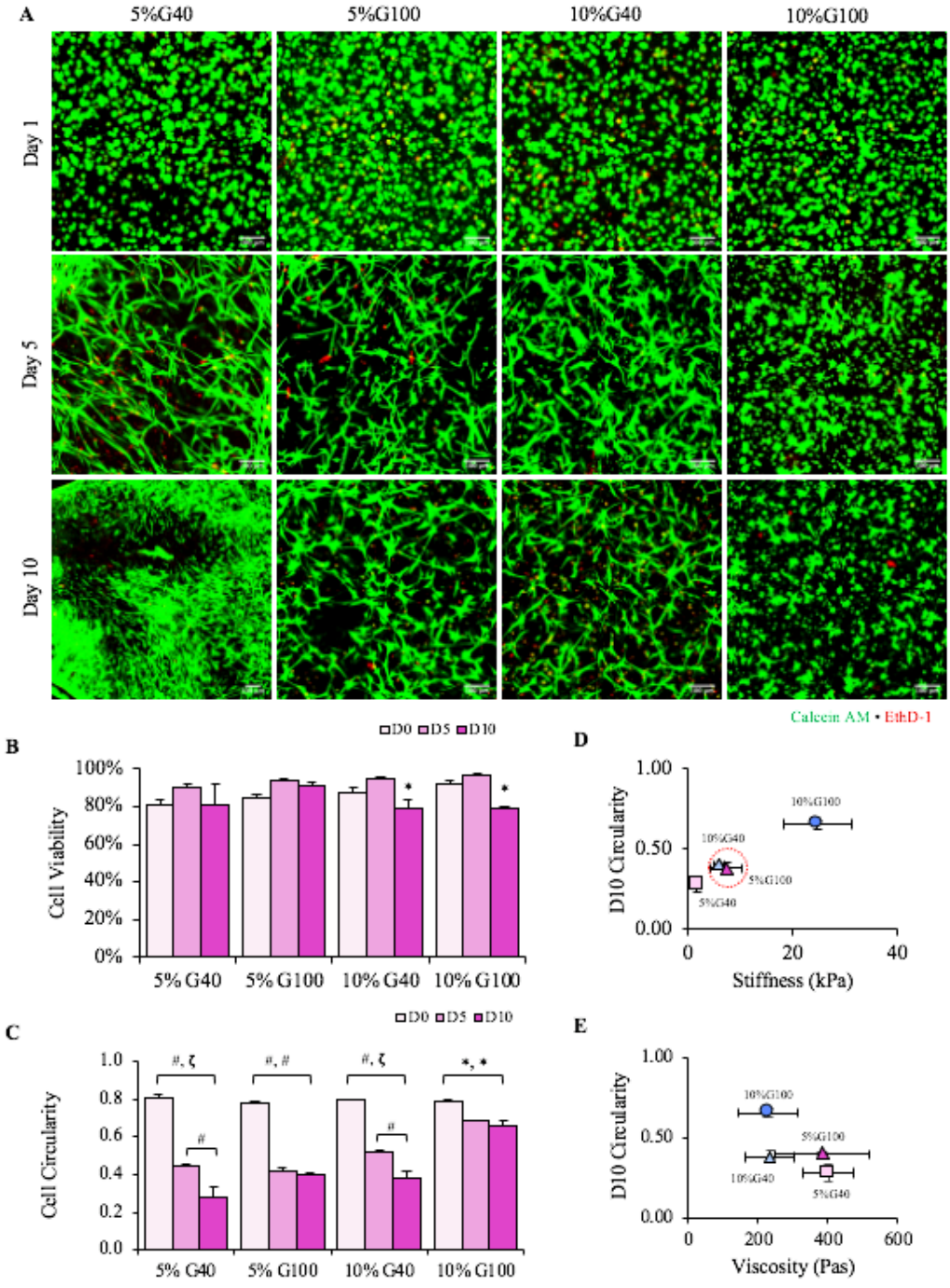

Figure 2.7. HUVEC and hAdMSC Viability and Morphology in GelMA. (A) Live/dead analyses of HUVEC-hAdMSCs co-encapsulated in 5%G40, 5%G100, 10%G40, and 10%G100 hydrogel conditions after 0, 7, 14, and 21 days of adipogenic differentiation. Live cells were represented by Calcien AM (green) and dead cells were represented by EthD-1 (red). Quantification of the cell viability (B) and cell circularity (C) of HUVEC and hAdMSCs co-cultures in hydrogel conditions at days 0, 7, 14, and 21. Quantitative analysis of the relationship of hydrogel stiffness (D) and viscosity (E) on cell circularity at day 10 only. Data are presented as the mean ± SD, n = 4-7. *, $p < 0.05$; #, $p < 0.01$ and **ζ**, $p < 0.001$.

Matrix Modification During Adipogenesis and Vasculogenesis

In addition to quantifying the viability and circularity of cells embedded in a mechanically tunable matrix, GelMA compaction, or the change in surface area, during adipogenesis **(Fig. 2.8A)** and vasculogenesis **(Fig. 2.9A)** was measured. It is well understood that cells encapsulated in 3D systems eventually home and modify their matrices, which leads to hydrogel compaction.(226) With regard to adipogenesis, matrix compaction and swelling were both detected in this study. The surface area of GelMA polymers with lower DoM (5%G40 and 5%G100) significantly decreased by 4X during the culture period, demonstrating hydrogel compaction. Alternatively, GelMA polymers with high DoM (5%G100 and 10%G100) displayed a slight increase in surface area overtime, displaying hydrogel swelling. **(Fig. 2.8B-C)** When the change in hydrogel surface area (% compaction) for each condition was analyzed against matrix DoM **(Fig. 2.8D),** stiffness **(Fig. 2.8E**), and viscosity **(Fig. 2.8F),** it was revealed that % compaction was neither stiffness- nor viscous-dependent, but rather DoM-dependent.

With regard to vasculogenesis, minimal matrix compaction was observed overtime for each condition. **(Fig. 2.9B)**. 5%G40 experienced the most significant change in hydrogel surface area, followed by matrices with a moderate stiffness (5%G100 and 10%G40) and high stiffness (10%G100). It should also be noted that when matrices with moderate stiffness exhibited comparable changes in hydrogel surface area. (**Fig. 2.9C**) When the % compaction for each condition was analyzed against matrix DoM **(Fig. 2.9D),** stiffness **(Fig. 2.9E),** and viscosity (**Fig. 2.9F**), it was revealed that % compaction was neither DoM- nor viscous-dependent, but rather stiffness-dependent. Overall, these results indicate that changes in hydrogel surface area is DoM-dependent for adipogenesis and stiffness-dependent for vasculogenesis.

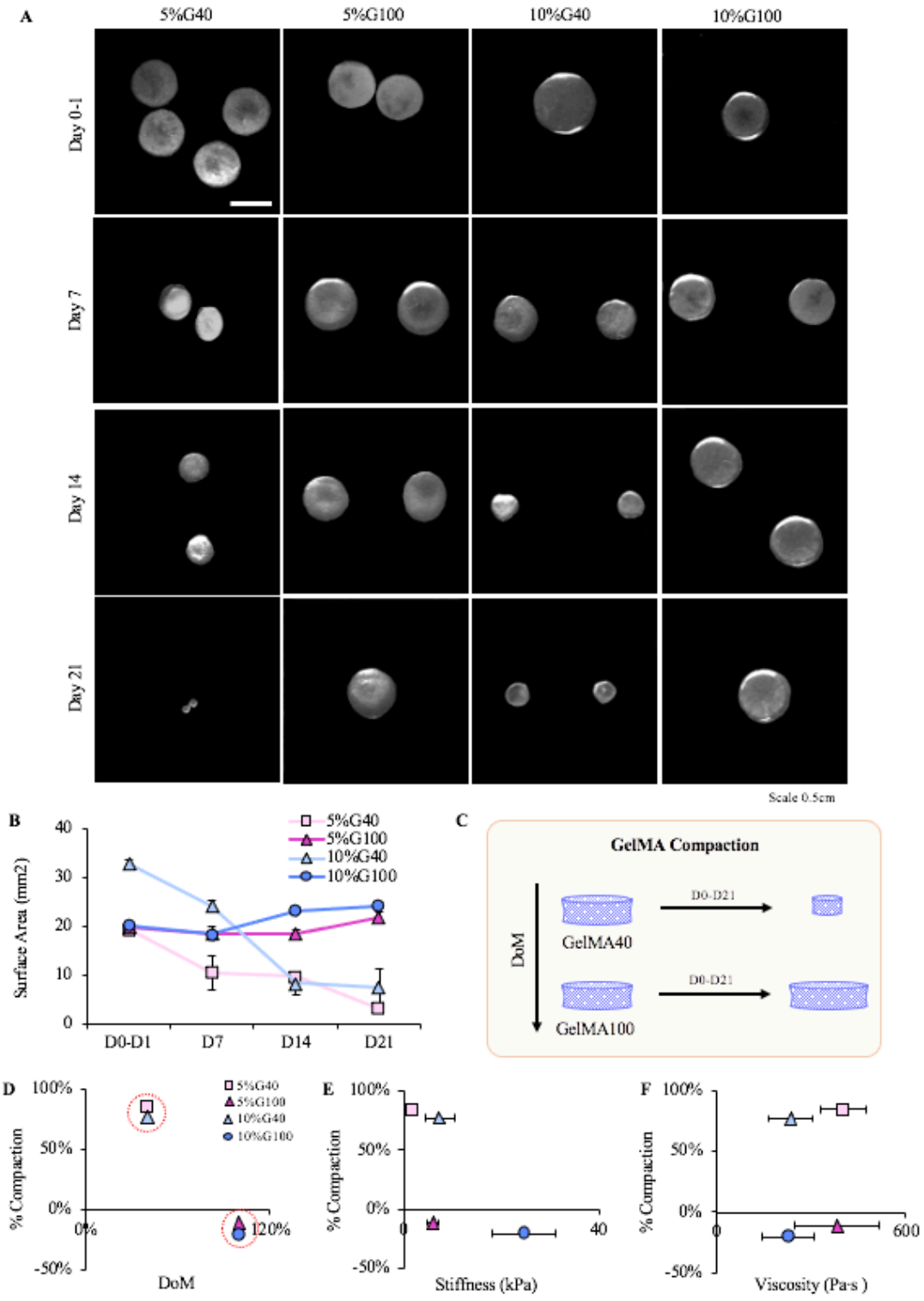

Figure 2.8. GelMA Compaction During Adipogenesis. (A) Brightfield images of 5%G40, 5%G100, 10%G40, and 10%G100 constructs at D0, D7, D14, and D21. (B) Changes in GelMA hydrogel surface area at D0, D7, D14, and D21. (C) Schematic of the relationship between hydrogel compaction and DoM. Quantitative analysis of the relationship of hydrogel compaction percentage and DoM (D), stiffness (E), and viscosity (F).

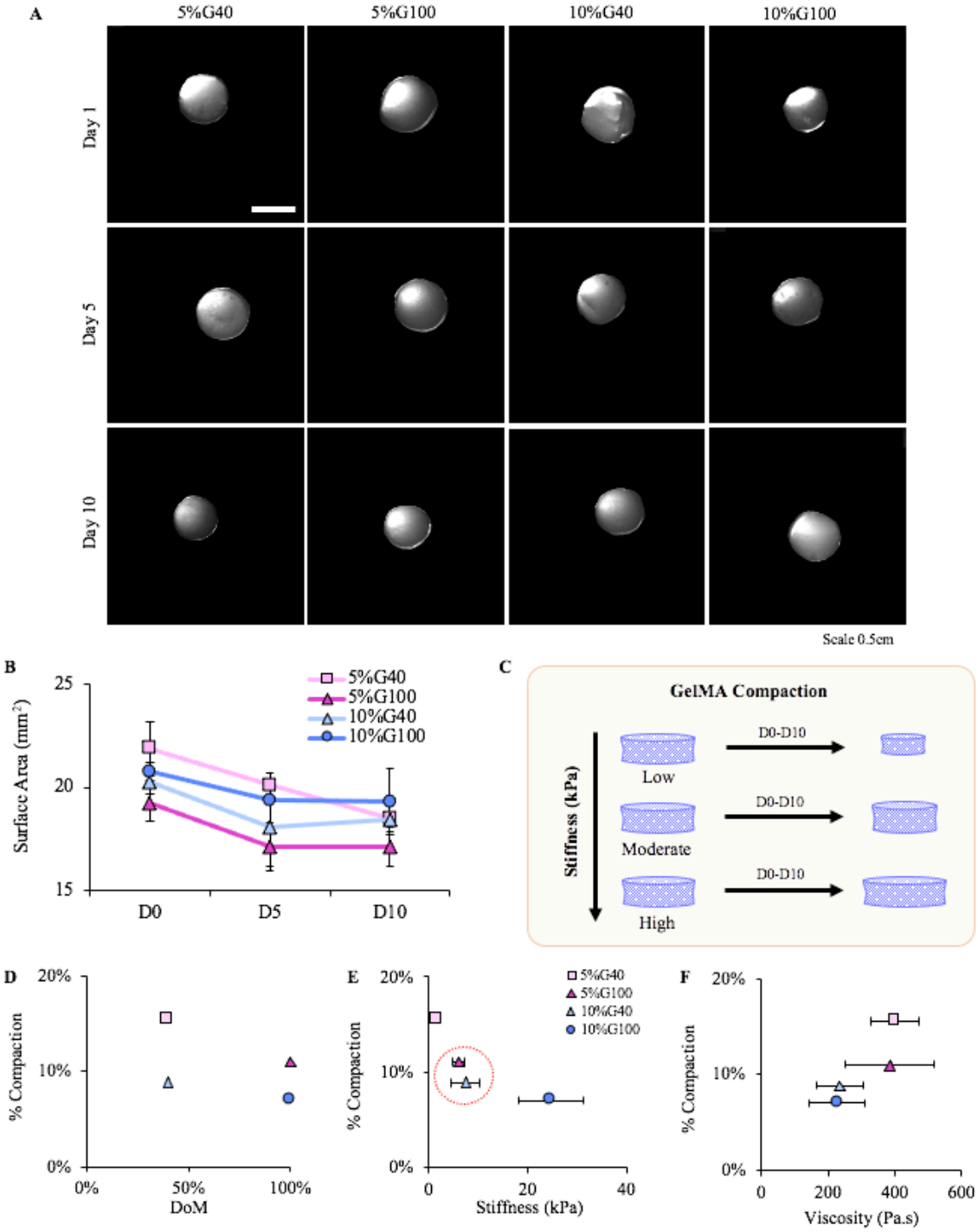

Figure 2.9. GelMA Compaction During Adipogenesis. (A) Brightfield images of 5%G40, 5%G100, 10%G40, and 10%G100 constructs at D0, D5, and D10. (B) Changes in GelMA hydrogel surface area at D0, D7, and D10 (C) Schematic of the relationship between hydrogel compaction and stiffness. Quantitative analysis of the relationship of hydrogel compaction percentage and DoM (D), stiffness (E), and viscosity (F).

DISCUSSION

In this study, we established a mechanically tunable system to elucidate the role of matrix stiffness and viscosity on cell behavior during adipogenesis and vasculogenesis. While there is a deep understanding of the effect of matrix stiffness on these phenomena, tissues bare viscoelastic properties, and there is less information on the impact of matrix viscosity on fat and vascular formation. (227) The novelty of this work addresses this limitation by fabricating GelMA polymers with variable stiffness and viscous values. We hypothesized that GelMA with low DoM can elicit significant variations in stiffness and viscosity that create a testable matrix to study adipogenesis and vasculogenesis. After synthesizing GelMA polymers with varying DoM, we uncovered that GelMA stiffness was dependent on both the DoM and polymer weight composition, while the viscosity was solely dependent on the latter. We not only fabricated GelMA polymers with tunable stiffness and viscosity, but also achieved this a regime that is physiologically relevant to the stiffness of fat and vascular tissues. Previous work by Hoch et al. is one of few studies to actually reveal that alterations to GelMA DoM and polymer weight composition can impact its viscous properties. However, significant differences in matrix viscosity were only achieved in a stiffness regime (20kPa+) that is incompatible to fat and vasculature, in comparison to a more relevant stiffness regime (1-10kPa), which did not exhibit a significant difference in viscosity. (228) One rationale for these findings could be due to the fabrication of GelMA polymers with a DoM that elicit comparable mechanical properties. For instance, the GelMA polymers used in this study were fabricated at 67%, 80%, and 100% DoM. Preliminary work in our lab suggested that GelMA polymers with a DoM of 75% or greater performed the same mechanically at both 5% and 10% (w/v) (data not shown). However, GelMA with a DoM that is less than 50% demonstrated significant differences in mechanical behavior. In our studies, we successfully methacrylated

GelMA at a low enough DoM (GelMA40) to where we can achieve alterations in matrix viscosity in a stiffness regime that is applicable to fat and vascular tissue engineering.

Next, we investigated how variations in hydrogel mechanics regulate hAdMSC viability and morphology during adipogenesis. Our results indicated that matrix viscosity, rather than stiffness, played a more prominent role in invoking cell circularity throughout the culture period. hAdMSCs encapsulated in high viscous GelMA polymers (5%G40 and 5%G100) exhibited a rounder morphology in comparison to hAdMSC embedded in low viscous matrices (10%G40 and 10%G100). However, it should be noted that while 10%G100 has a low viscosity, cell roundness was not only significantly greater than that in 10%G40 but also more comparable to the morphology presented in 5%G40 and 5%G100 conditions. A potential explanation for this occurrence is that the high crosslinking efficiency of the 10%G100 matrix is too rigid to permit cells to spread throughout the hydrogel, as seen in the other conditions, forcing the hAdMSCs to remain in their spherical structure. (229) Additionally, it should be noted that previous studies by Lee et al. report contradictory evidence on the impact of matrix viscosity on adipogenesis. MSCs encapsulated in high viscous GelMA-gelatin composite scaffolds exhibited inferior adipogenic gene expression and lipid accumulation in comparison to low and moderate viscous scaffolds. (230) However, our work suggests the opposite, where hAdMSCs embedded in high viscous GelMA conditions are more spherical in shape, a key characteristic of mature adipocytes, in comparison to cells within low viscous matrices. (231) These contrasting findings may be due to the amorphous state at which the polymer was used in each study. In our work, we utilized viscoelastic GelMA polymers that were completely crosslinked. Alternatively, Lee et al. performed their studies with cell-laden viscous solutions of gelatin incorporated in a fully

crosslinked GelMA hydrogel. Currently, there is no apparent information that ascertains how the distinct properties of viscous solutions versus viscoelastic materials regulate similar cellular phenomenon. However, additional evidence on the gene expression and lipid accumulation of hAdMSC incorporated in our GelMA matrices is necessary to truly uncover role of matrix stiffness and viscosity on adipogenic phenotype.

In addition to examining cell survival and morphology during adipogenesis, we also explored the role of matrix mechanics on cell behavior during vasculogenesis. Our results revealed that GelMA stiffness, rather than viscosity, played a more significant role in invoking cell elongation throughout the culture period, which was the opposite effect observed during adipogenesis. A hallmark feature of microvessels include an organized network of endothelial tube formation. (232) In our work, softer matrices (5%G40) exhibited the greatest cell spreading, while conditions with moderate stiffness (5%G100 and 10%G40) demonstrated reduced but comparable changes in spreading followed by high stiffness matrices (10%G100), which completely prohibited cell spreading. These findings are similar to what has been revealed in previous studies by Chen et al., who also reported that softer matrices (1-2kPa) improved vascular network formation of EC/MSC co-cultures incorporated in GelMA polymers in comparison to stiffer matrices (5kPa). (233) Although this work confirmed the effect of stiffness on vasculogenesis, there is still a lack of information on the impact of matrix viscosity on this phenomenon. Our work addresses this limitation by also incorporating the influence of matrix viscosity in our studies. However, further analyses are required to distinguish the cell types undergoing elongation and morphological changes, as well as measure vascular gene expression and colocalization between HUVEC and hAdMSCs throughout the culture period.

We also inspected the changes in hydrogel size throughout the culture period in both adipogenesis and vasculogenesis. Our results showed that while matrix compaction was DoM-dependent and significantly different between groups during adipogenesis, it was stiffness-dependent and less distinct between groups during vasculogenesis. Specifically, in our vascular studies, changes to hydrogel surface area were low and insignificant across all conditions. A possible explanation for this occurrence is likely due to the low ratio of hAdMSC to HUVEC, where the concentration of HUVEC (4.5M cells/mL) significantly outweighed the concentration of hAdMSC (0.5M cells/mL) by 10 to 1. Unlike ECs, MSCs are highly contractile and metabolic, which would allow them to drastically remodel their matrix. (234,235) In fact, this phenomenon was present in our adipose studies, where the elevated concentration of MSCs incorporated in GelMA significantly altered the size of each hydrogel, particularly in GelMA with low DoM. A rationale for this incidence may be due to the low crosslinking efficiency of the G40 polymer, regardless of its weight composition. GelMA materials with low DoM allow for greater exposure to MMP binding sites, causing the hydrogel to compact. In particular, MMP2 and MMP9 are two gelatinases that are produced and secreted by MSCs to trigger adipogenesis and could help shed light on the factors that contribute to the robust matrix compaction observed in these studies. (236,237)

Lastly, it should also be noted that substrate stiffness played a minor role in hydrogel compaction. Although 5%G40 and 10%G40 exhibited a comparable reduction in hydrogel surface area, 5%G40 experienced the greatest decrease in size followed by 10%G40. This phenomenon was also true for 5%G100 and 10%G100 polymers, where the stiffer matrix underwent less compaction. Nevertheless, hydrogel compaction was primarily dependent on low DoM and less dependent on

matrix stiffness. Overall, while we were able to successfully fabricate GelMA polymers with tunable stiffness and viscosity, further analyses are crucial to adequately elucidate the impact of these mechanical features on adipogenic and vasculogenic phenotype.

CHAPTER 3. THE ROLE OF MATRIX STIFFNESS AND VISCOSITY ON ADIPOGENESIS

This chapter was adapted and expanded on from the following publication:

Stephens CJ, Kobayashi R, Berry DC, Butcher JB. The role of matrix stiffness and viscosity on lipid phenotype and fat lineage potential. Tissue Eng. Part A. 2024 (In Review)

INTRODUCTION

Autologous fat transfer for soft tissue reconstruction is necessary for restoring deep, chronic wounds.(4,238,239) In particular, these soft tissue defects can arise from burns, trauma, tumor resection or infection and require large volumes of autologous fat to be harvested and donated to the defect site for full recovery. (4,240,241) Ideal donor sites of sourcing autologous fat for these applications include the abdomen, thigh, inner knee, and buttock region. (242) However, these surgeries are complicated by low donor-site volume, high donor-site morbidity, lack of anatomic specificity, and susceptibility to necrosis. (243–246) Therefore, fat tissue engineering strategies must be established to serve as a clinical option for the rejuvenation of large soft tissue defects.

Tissue engineering approaches to regenerate fat require 3D matrices, such as gelatin methacryloyl (GelMA), that are both biocompatible and mechanically tunable. (8,217,229,247–249) In regard to biocompatibility, previous studies have shown that GelMA supports the viability, proliferation, and differentiation of adipose-derived stem cells (ASCs) in 2D and 3D cultures. (250–252) Additionally, it has been shown that GelMA containing ASCs and mature adipocytes can be successfully coaxed to form adipose-like microtissues. (99,253) In regard to the matrix biomechanics, it has been widely accepted in tissue engineering that softer 2D matrices support fat formation in comparison to stiffer matrices, which are more suitable for robust tissues like bone.

Paradoxically, recent work by Major et al. uncovered confounding results where stiff and soft GelMA matrices enhanced ASC adipogenesis and osteogenesis, respectively. (257) Additionally, it has been shown that as preadipocytes undergo differentiation, they become stiffer yet exhibit decreased cell spreading and exert lower traction forces, which are phenomena typically associated with softer matrices. (258) Altogether, these inconsistent findings suggest that additional mechanics, aside from stiffness, could also critically impact adipogenesis.

Since fat and other soft tissues are viscoelastic, its development and function are governed by its instantaneous elastic response and time-dependent viscous response to deformation. (259–261) Previous work has shown that high- and low-viscosity gelatin solutions induce osteogenesis and adipogenesis, respectively. (230,262,263) However, while these studies shed more light on the influence of viscosity on adipogenesis, the combined effects of stiffness and viscosity on adipogenic differentiation require further elucidation. Additionally, it should be noted that there are variations in fat phenotype, namely metabolic (or white) and thermogenic (or brown and beige) fat, which are not only characterized by distinct phenotypic features, but also responsible for different bodily functions. (264) Although the biological drivers of metabolic and thermogenic fat are well known, there is still a lack of information on how tissue mechanics vary during adipogenesis and how these drivers influence fat lineage potential.

The aim of this present work was to elucidate the effects of matrix stiffness and viscosity on adipogenesis and to uncover the biomechanical shifts that drive metabolic versus thermogenic fat potential. **We hypothesized that soft matrices with low viscosity (10%G40) will enhance adipogenic phenotype (large lipid size and few lipid droplets)**. GelMA was synthesized with

varying degrees of methacrylation (DoM) to produce polymers with a range in mechanical properties. Human adipose-derived stem cells (hAdMSCs) were then encapsulated in GelMA polymers to assess the influences of matrix mechanics on adipogenic differentiation. Overall, the major findings of this study reveal that matrix viscosity played a more superior role in driving lipid phenotype and fat lineage potential. Furthermore, these studies shed light on the role of stiffness and viscosity on adipogenesis and offer promising methods for engineering fat for large soft tissue defects.

MATERIALS & METHODS

Fat-Induced Cell Culture in 3D GelMA Hydrogel

HAdMSC were expanded, encapsulated in GelMA polymer solutions (5%G40, 5%G100, 10%G40, 10%G100), and induced using adipogenic media as previously described in chapter 2. Data collected from each experimental condition was analyzed at D0, D7, D14, and D21 timepoints.

RNA Isolation, Reverse Transcription, and qRT-PCR

After each timepoint, samples were washed with PBS twice, flash frozen in liquid nitrogen, resuspended in TRIzol® reagent (ThermoFisher Scientific®, MA, USA) and homogenized using pellet pestles (Sigma-Aldrich®, MO, USA). Chloroform was then added to extract the RNA from each sample through phase separation. RNA was precipitated with isopropanol and 70% ethanol and reconstituted in nuclease-free water (ThermoFisher Scientific®, MA, USA). The concentration of each RNA sample was quantified and tested for purity using the NanoDrop™ 2000 Spectrophotometer (ThermoFisher Scientific®, MA, USA). RNA was then converted to

cDNA using a qScript™ cDNA Synthesis Kit (Quantabio®, MA, USA) and a 5331 MasterCycler Gradient Thermal Cycler (Eppendorf®, Hamburg, Germany). After reverse transcription, cDNA was amplified using iTaq™ Universal SYBR® Green Supermix (Bio-Rad Laboratories®, CA, USA) and the Applied Biosystems real-time PCR instrument (Bio-Rad Laboratories®, CA, USA). The relative expression of adipogenic genes were measured against the endogenous control gene (or housekeeping gene) 18S using the $2^{-\Delta\Delta Ct}$ method. The adipogenic genes measured in this study include peroxisome proliferator-activated receptor gamma (PPAR-γ), fatty acid binding protein 4 (FABP4), uncoupling protein 1 (UCP-1). The primer and probe sequences for each target gene are presented in **Table 3.1**.

Table 3.1 PCR Primers and Function

Marker	Function	Forward Primer Sequence	Reverse Primer Sequence	Reference
PPARg	Nuclear receptor master regulator of adipogenesis	TTACGAAGACATTCCA TTCACAAG	TATCTCCACAGACACGA CATTC	Toosi et al., 2019
AP2	Fatty acid transporter protein	ACTGGGCCAGGAATTT GACG	CTCGTGGAAGTGACGCC TT	Fang et al., 2019
UCP1	Mitochondrial membrane protein for thermogenesis	GTGTGCCCAACTGTGC AATG	CCAGGATCCAAGTCGCA AGA	Pisani et al., 2011
18S	Housekeeping gene	CTTAGAGGGACAAGTG GCG	ACGCTGAGCCAGTCAGTG TA	Farmer et al., 2013

Immunofluorescence

After each timepoint, live hAdMSC-laden GelMA hydrogels were washed in 1X PBS and prepped for staining. Each sample was stained with MitoTracker™ Red CMXRos dye (ThermoFisher Scientific®, MA, USA) for 30 minutes at room temperature. After initial staining, samples were immediately fixed in 4% PFA 4°C and washed in 1X PBS 3 times the following day. Fixed samples

were then permeabilized with 0.1% saponin (Sigma-Aldrich®, MO, USA) for 1 hour at room temperature, washed with 1X PBS 3 times, and co-stained with HCS LipidTOX™ Green Neutral (ThermoFisher Scientific®, MA, USA) and 4′,6-diamidino-2-phenylindole (DAPI, ThermoFisher Scientific®, MA, USA) overnight at 4°C. Images were acquired using a Zeiss LSM 710 Confocal Microscope and lipid accumulation and mitochondrial abundance were quantified using FIJI software.

Uniaxial Compression

After each timepoint, the stiffness of fat-induced HAdMSC-laden hydrogels was determined by uniaxial compression as previously described in chapter 2.

Stress Relaxation

After each timepoint, live hAdMSC-laden GelMA hydrogels (5%G40, 5%G100, 10%G40, 10%G100) immediately underwent stress relaxation with 10% strain (ε_0) using a DMA Q800 Dynamic Mechanical Thermal Analysis (TA Instruments, DE, USA). The stress relaxation plot that was generated reported changes in stress (σ) over a 10-minute time interval (t). The time constant (τ) was then calculated using the standard linear viscoelastic (SLV) model and used to characterize the viscosity (η) of GelMA hydrogels. The spring constants of the equilibrium arm and Maxwell arm of the SLV model were represented by k_E and k_M, respectively, and the following equations were used to quantify the viscosity of cell laden GelMA:

$$\sigma(t) = \varepsilon_0(k_E + k_M e^{\left(-\frac{t}{\tau}\right)})$$

$$\tau = \frac{\eta}{k_1}$$

Statistics

Quantitative analyses were performed in triplicates for qRT-PCR and quintuplicates for immunofluorescence and mechanical testing. A one-way ANOVA was performed followed by a post-hoc Tukey HSD test and a two-tailed t-test with unequal variance to evaluate any significant difference between experimental groups. All quantitative data was reported as the mean ± standard deviation with a significant difference defined when $p<0.05$. The data are shown as * ($p<0.05$), # ($p<0.01$), ζ ($p<0.001$). The trendline and correlation coefficient (R^2) for each relationship were presented as highly correlated ($R2>0.8$).

RESULTS

Matrix Mechanics on Lipid Phenotype and Gene Expression

In order to determine the effects of stiffness and viscosity on adipogenesis, hAdMSC-laden GelMA hydrogels were induced in adipogenic medium and analyzed for lipid quantity, size, density, and fat gene expression. In general, immunofluorescent images demonstrate that each condition facilitated an increase in lipid quantity and diameter overtime **(Fig. 3.1A).** At the beginning of the culture period, each group exhibited a significantly higher number of small lipid droplets (<0.5μm in diameter), followed by medium (0.5-2μm), large (2-8μm), and extra-large (8< μm) lipid droplets **(Fig. 3.1B).** However, by the end of the culture period, medium and large lipid droplets significantly outnumbered small lipids in high-viscous and low-viscous conditions, respectively **(Fig. 3.1C).** In addition to these findings, the average size **(Fig. 3.1D)** and density **(Fig. 3.1E)** of lipids appear to increase with decreasing stiffness rather than viscosity. Hydrogels with low stiffness (5% G40) supported the greatest size and density of lipids, followed by conditions with moderate (5%G100 and 10%G40) and high (10%G100) stiffnesses. While these

phenomena were present throughout the culture period, the stiffness-dependent property of GelMA on lipid size and density were more significant on day 21 **(Fig. 3.1F-G).** Despite this outcome, the production of extra-large lipids, a characteristic of white adipocytes, appears to be governed by viscosity rather than stiffness. hAdMSCs embedded in low-viscous or high-viscous hydrogels produced fewer or more extra-large lipids, respectively **(Fig. 3.1H).** These results show that GelMA stiffness and viscosity affect different markers of adipogenesis. While matrix stiffness regulates the quantity, size, and density lipid droplets, GelMA viscosity supports the production of extra-large lipid droplets.

After observing the relationship between matrix mechanics and lipid formation, the influence of GelMA stiffness and viscosity on white and thermogenic fat gene expression was examined. While all conditions demonstrated comparable decreasing expression levels of PPAR-γ **(Fig. 3.2A),** the expression of aP2 **(Fig. 3.2B),** either significantly increased or decreased overtime in matrices with high or low viscosity, respectively. In terms of thermogenic fat genes, each condition demonstrated a 10-fold increase in the expression of UCP1 despite having comparable levels of PPAR-γ **(Fig. 3.2C).** UCP1 displayed viscous-dependent behavior similar to aP2, where high viscous GelMA supported a significant increase in UCP1 in comparison to low viscous GelMA. However, it should be noted that matrix conditions with low stiffness and high viscosity (5%G40) exhibited the most significant increase in aP2 and UCP1 expression. Additionally, while 5%G40 hydrogels supported the greatest production of extra-large lipids, a feature of white fat, it also supported the highest expression levels of UCP1, a feature of thermogenic fat.

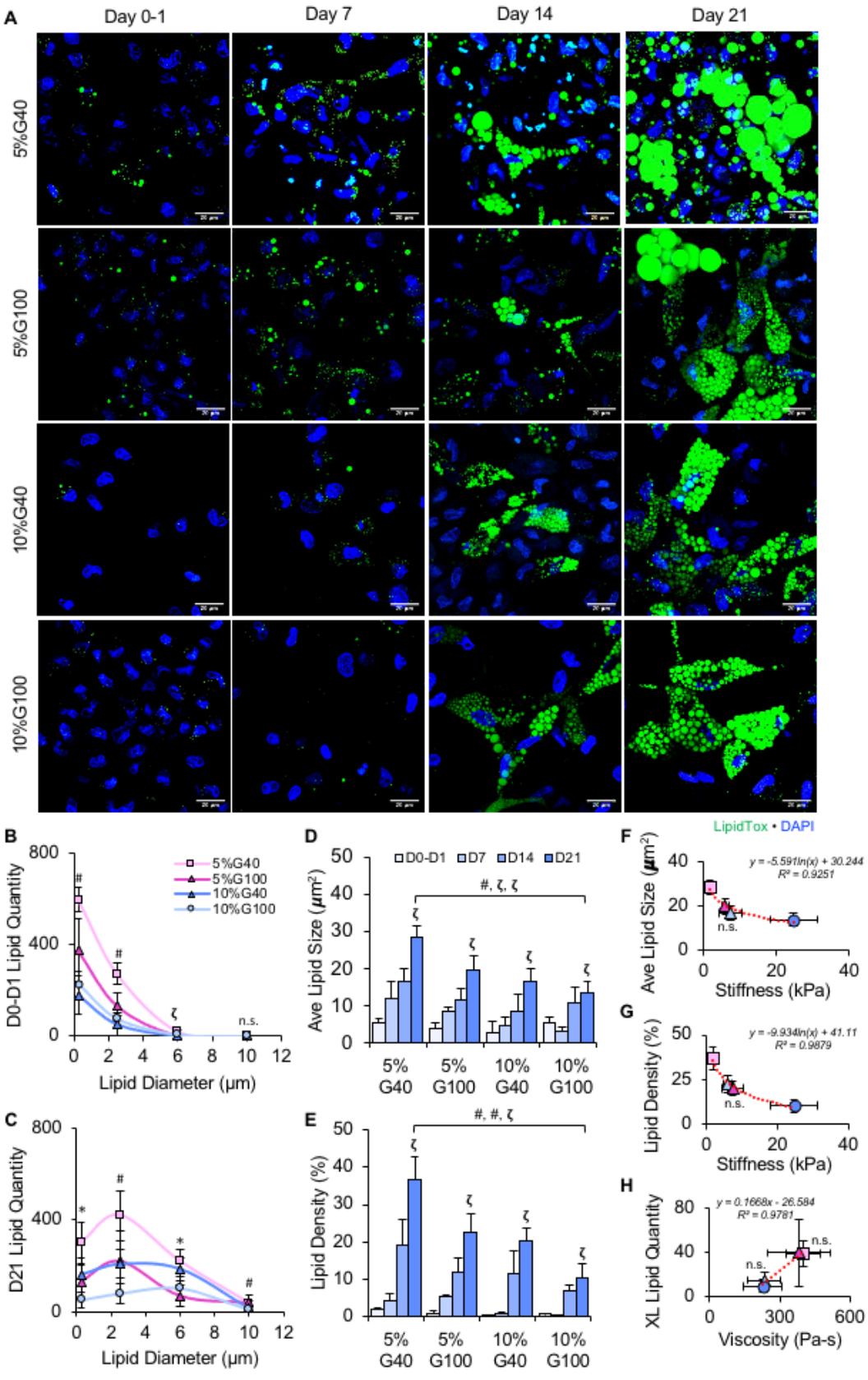
A
Day 0-1
Day 7
Day 14
Day 21
5%G40
5%G100
10%G40
10%G100
LipidTox • DAPI
B
D0-D1 Lipid Quantity
Lipid Diameter (μm)
5%G40
5%G100
10%G40
10%G100
C
D21 Lipid Quantity
Lipid Diameter (μm)
D
Ave Lipid Size (μm²)
D0-D1
D7
D14
D21
#, ζ, ζ
5% G40
5% G100
10% G40
10% G100
E
Lipid Density (%)
#, #, ζ
F
Ave Lipid Size (μm²)
y = -5.591ln(x) + 30.244
R² = 0.9251
Stiffness (kPa)
G
Lipid Density (%)
y = -9.934ln(x) + 41.11
R² = 0.9879
Stiffness (kPa)
H
XL Lipid Quantity
y = 0.1668x - 26.584
R² = 0.9781
Viscosity (Pa-s)
n.s.

Figure 3.1. Lipid Accumulation in hAdMSC-laden GelMA Hydrogels During Adipogenesis. (A) Confocal images of hAdMSCs encapsulated in 5%G40, 5%G100, 10%G40, and 10%G100 conditions after 0, 7, 14, and 21 days of adipogenic differentiation. Lipids and nuclei were co-stained with LipidTox (green) and DAPI (blue), respectively. Distribution of lipid droplets based on size (reported as the lipid diameter) at D0 (B) and D21 (C). Lipids were categorized as small (0.5<D<2μm), medium (2<D<4μm), large (4<D<8μm), and extra-large (D>8μm) in size. Quantitative analysis of the average lipid size (reported as lipid surface area) (D) and lipid density per nuclei (E) for each condition overtime. Quantitative analysis of the relationship of initial hydrogel stiffness on average lipid size (F) and density (G) at D21. (H) Quantitative analysis of the relationship of XL lipid quantity and initial hydrogel viscosity. Data are presented as the mean ± SD, n = 5. *, $p < 0.05$; #, $p < 0.01$ and **ζ**, $p < 0.001$. The trendline (red dashed line) and correlation coefficient (R^2) for each relationship were presented as highly correlated (R^2>0.8).

White and thermogenic fat gene expression were also related to changes in lipid diameter and density, where the fold change in PPAR-γ diminished slightly with increasing lipid diameter and density **(Fig. 3.2D-E).** Additionally, higher levels of AP2 and UCP1 gene expression correlated with increased lipid diameter and density **(Fig. 3.2F-I).** However, this phenomenon was only present in high-viscous matrices and had the opposite effect in low-viscous matrices, with 10%G40 exhibiting the most inferior levels of gene expression for all adipogenic markers. High viscous GelMA supported increased UCP1 and AP2 expression, lipid density and diameter. Alternatively, low viscous GelMA displayed a decrease in UCP1 and aP2 expression, lipid density and diameter. Altogether, these results show that despite the insignificant differences in PPAR-γ expression across all conditions, AP2 and UCP1 exhibited viscous-dependent behavior that correlated with lipid density and diameter.

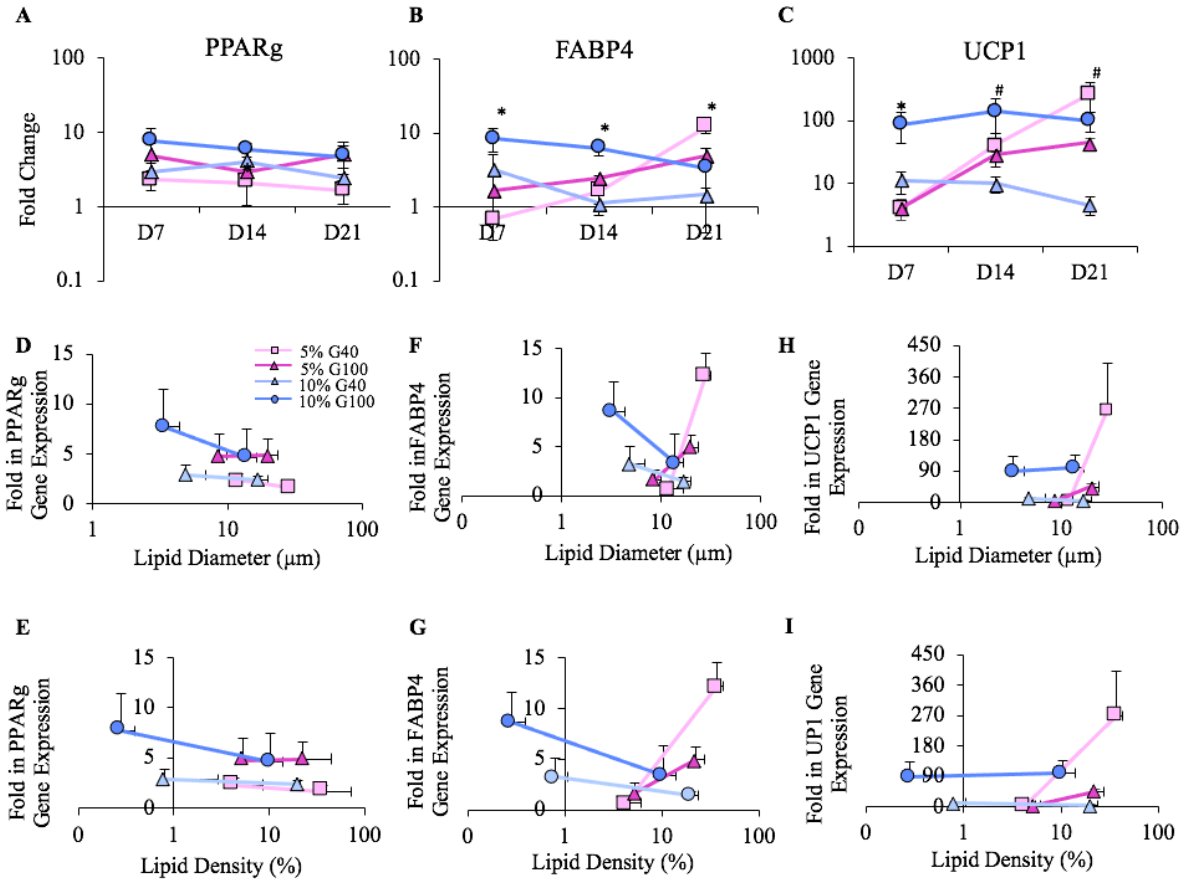

Figure 3.2. Gene Expression of hAdMSC-laden GelMA Hydrogels During Adipogenesis. Gene expression of (A) PPARg, (B) AP2, and (C) UCP1 activity after 7, 14, and 21 days of adipogenesis. Data were normalized by 18S housekeeping gene for each condition and the gene expression levels of D0 hAdMSC-laden GelMA control samples. Quantitative analysis of the relationship of lipid diameter and density and PPARg (D-E), AP2 (F-G), and UCP1 (H-I) expression. Data are presented as the mean ± SD, n = 3 (3 hydrogels per sample). *, $p < 0.05$; #, $p < 0.01$ and **ζ**, $p < 0.001$.

Alterations in Matrix Mechanics During Adipogenesis

Although it is common to design polymers that mimic the biomechanical properties of native tissues, it is well understood that these properties evolve as cells home and modify their matrices (226). In this study, significant changes in GelMA compaction and mechanics were observed and correlated with lipid phenotype throughout adipogenesis. 5%G40 and 10%G40 exhibited a 4X decrease in surface area, while 5%G100 and 10%G100 demonstrated a slight increase in surface

area overtime **(Fig. 3.3A-B).** These results suggest that hydrogel compaction due to adipose induction is neither viscous- nor stiffness dependent. Instead, this phenomenon appears to be dependent on GelMA polymer crosslinking efficiency, where polymers with low DoM are more susceptible to hydrogel compaction.

In addition to examining hydrogel compaction, variations in GelMA stiffness and viscosity during adipogenesis were also quantified. This work showed a general decrease in stiffness **(Fig. 3.3C)** and viscosity **(Fig. 3.3D)** for each condition overtime. In regard to stiffness, 10%G100 obtained the stiffest modulus, while 5%G100 and 10%G40 achieved lower and comparable moduli despite their opposing compaction behavior. In regard to viscosity, GelMA hydrogels initially displayed an increase in viscous values with increasing DoM and weight composition. However, by the end of the culture, 5%G100 and 10%G40 achieved low and comparable viscosity, while 10%G100 maintained a significantly higher viscosity that exceeded all other conditions 100-fold. Lastly, while the compaction of 5%G40 was quantified, the bulk stiffness and viscosity of this condition could not be analyzed due to its drastic reduction in hydrogel size. Overall, this work shows that matrix stiffness and viscosity decreased during adipogenesis.

The contribution of matrix mechanics on lipid phenotype was then assessed by evaluating alterations in lipid density, size, and quantity in relation to changes in stiffness and viscosity during adipogenesis. In general, hydrogel stiffness decreased as viscosity decreased across each condition **(Fig. 3.3E).** This phenomenon also correlated with increasing lipid quantity and lipid size, where conditions with high viscous and stiffness (Position 1 and 2) display fewer lipid droplets that are smaller in size, while conditions with low viscosity and stiffness (Position 3 and 4) give rise to

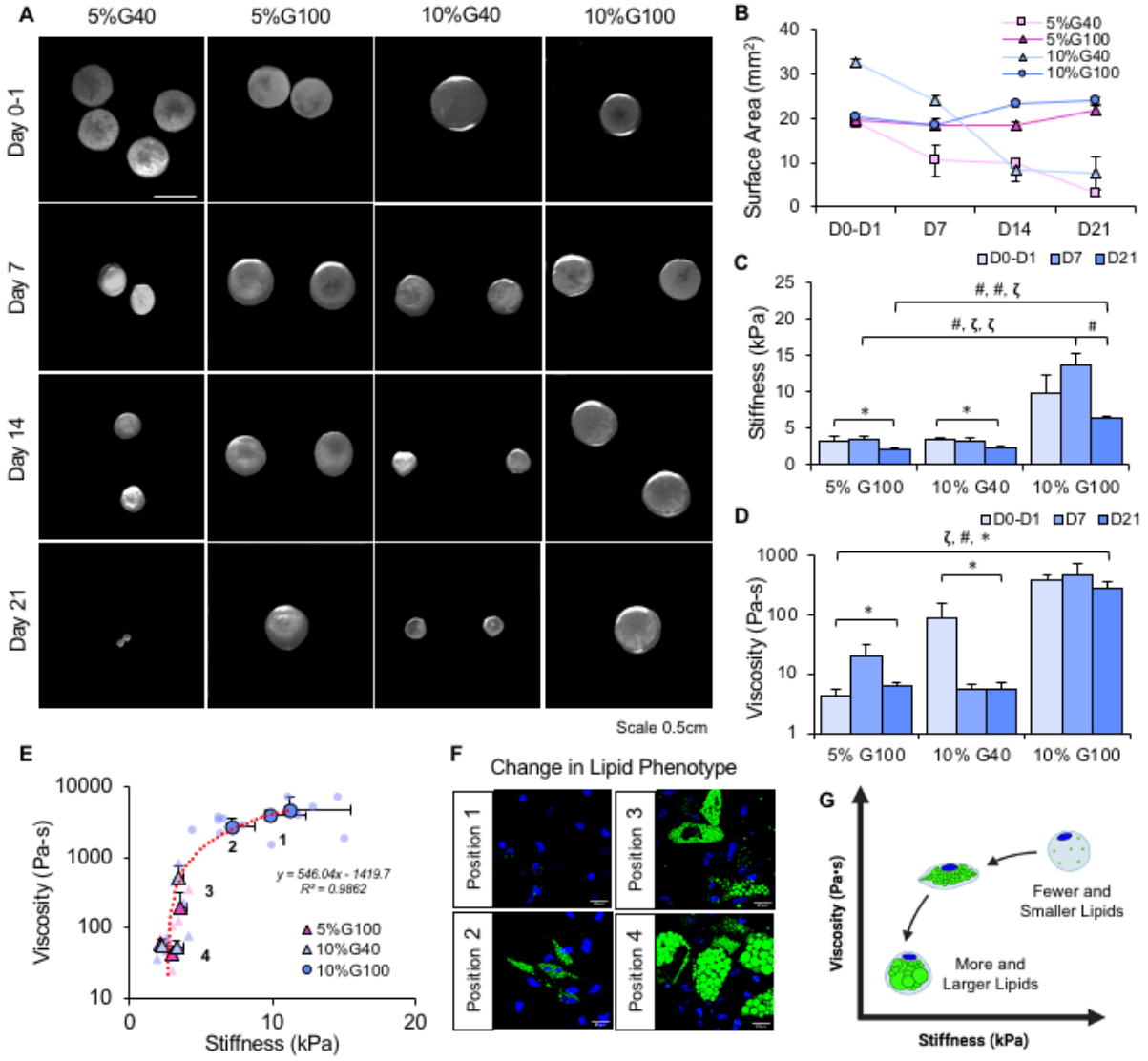

Figure 3.3. Alterations in GelMA Stiffness and Viscosity During Adipogenesis. (A) Brightfield images of 5%G40, 5%G100, 10%G40, and 10%G100 constructs at D0, D7, D14, and D21. Changes in GelMA hydrogel surface area (B), stiffness (C), and viscosity (D) were observed for each measurable condition at D0, D7, and D21. Mechanical testing for the 5%G40 condition could not be performed due its significant compaction during adipogenesis. (E) Quantitative analysis of the relationship of hydrogel stiffness and viscosity overtime. (F) Representative confocal images of lipid phenotype at varying stiffness and viscosity regimes. (G) Schematic of lipid size and quantity variations with decreasing stiffness and viscosity. Data are presented as the mean ± SD, n = 4-7. *, $p < 0.05$; #, $p < 0.01$ and **ζ**, $p < 0.001$. The trendline (red dashed line) and correlation coefficient (R^2) for each relationship were presented as highly correlated (R^2>0.8).

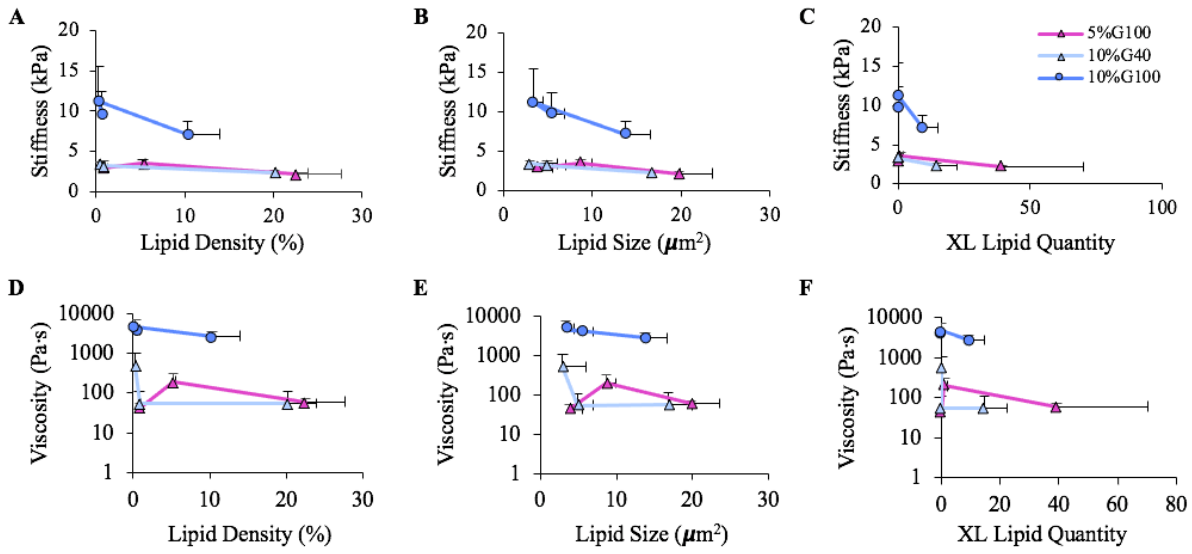

Figure 3.4. Comparative Analysis Between Matrix Mechanics and Lipid Phenotype. Quantitative analysis of the relationship of stiffness (A-C) and viscosity (D-F) on lipid density, size, and XL lipid quantity.

Matrix Mechanics on Mitochondrial Density and Lipid Phenotype

Mitochondrial density was quantified to evaluate the effects of matrix mechanics on white and thermogenic fat potential. Thermogenic fat, such as brown or beige fat, is characterized by multi-locular lipids and high mitochondrial density, while white fat is defined by unilocular lipids and low mitochondrial density **(Fig. 3.5A).** In this study, all groups demonstrated high levels of mitochondrial abundance that increased overtime **(Fig. 3.6A-B).** At the beginning of adipogenesis, high viscous matrices exhibited comparable but lower mitochondrial abundance, in comparison to low viscous matrices, which displayed similar but a greater concentration of mitochondria **(Fig. 3.6C)**. Alternatively, matrices with increasing stiffness showed increasing levels of mitochondria by the end of the culture period **(Fig. 3.6D)**. At this time, there was also a general decrease in mitochondria as the number and size of lipids increased **(Fig. 3.6E-G).** Specifically, cells containing more XL lipid droplets had a tendency to produce fewer mitochondria, with 5%G40

exhibiting the most notable drop in mitochondria overtime. Lastly, it should be noted that when mitochondrial abundance was analyzed against changes in matrix stiffness and viscosity over time, there was no significant correlation observed **(Fig. 3.5B-C).** This work suggests that mitochondrial density is inversely related to lipid quantity and size. Cells that generate larger and more abundant lipids also produce less mitochondria, regardless of matrix mechanics. These results also suggest that mitochondrial abundance may be regulated by distinct mechanical parameters of the matrix, where viscosity and stiffness appear to drive mitochondria production during the early and later stages of adipogenesis, respectively.

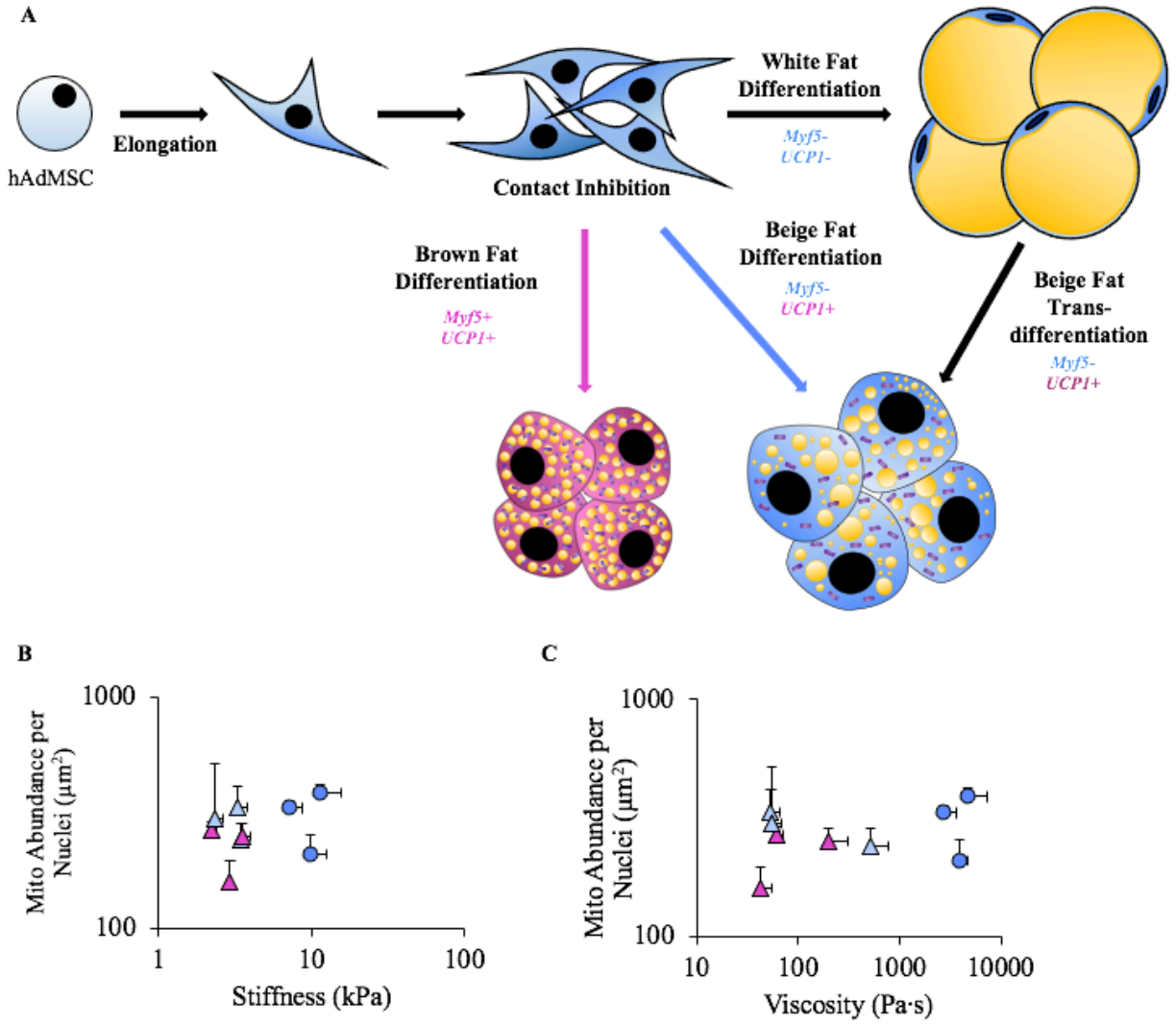

Figure 3.5. Metabolic Versus Thermogenic Adipogenesis. (A) Schematic of hAdMSC undergoing brown, beige, and white fat differentiation. Quantitative analysis on the relationship of mitochondrial abundance, stiffness (B) and viscosity (C).

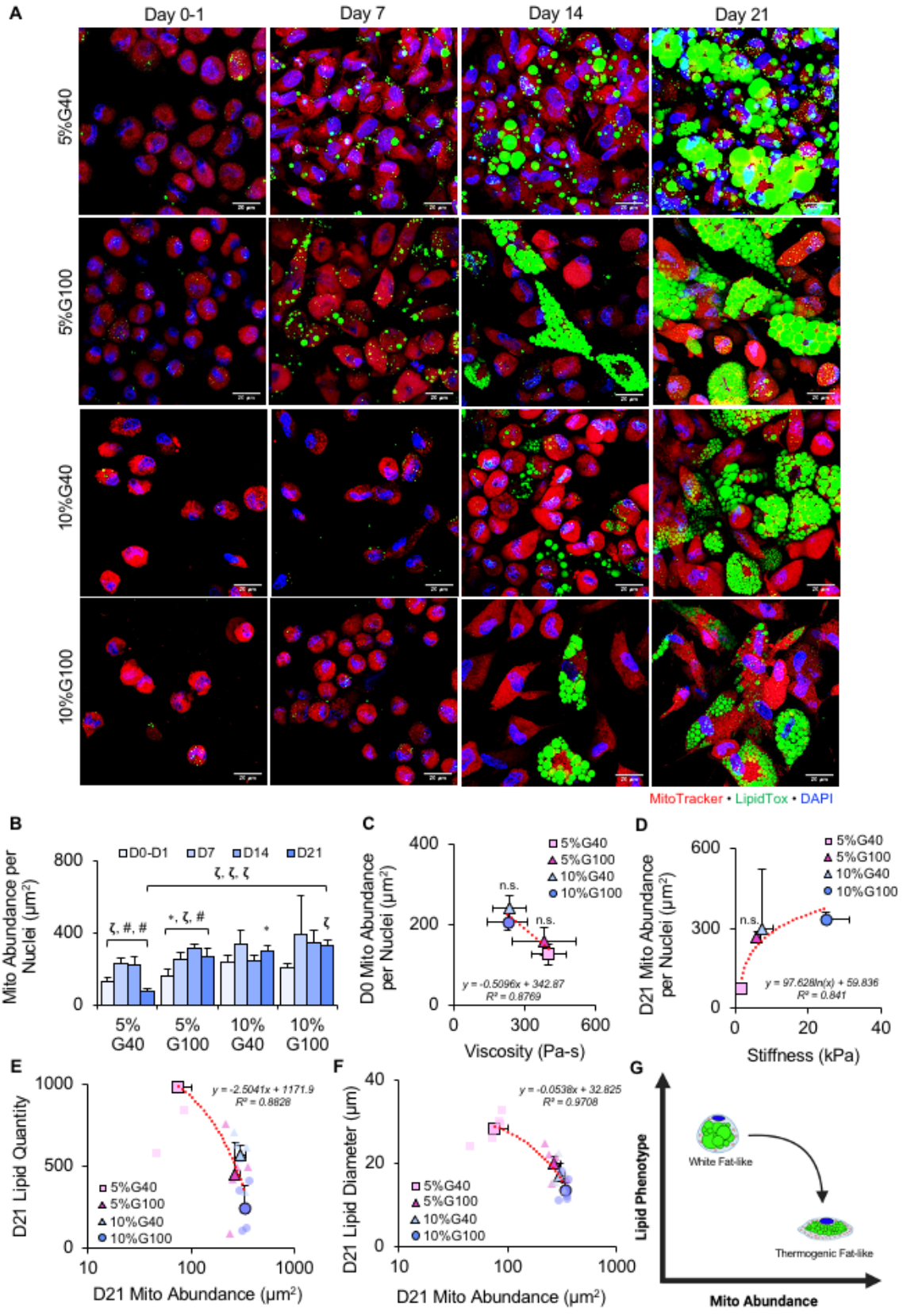
A
Day 0-1
Day 7
Day 14
Day 21
5%G40
5%G100
10%G40
10%G100
MitoTracker • LipidTox • DAPI
B
Mito Abundance per Nuclei (μm²)
D0-D1
D7
D14
D21
ζ, ζ, ζ
ζ, #, #
*, ζ, #
*
ζ
5% G40
5% G100
10% G40
10% G100
C
D0 Mito Abundance per Nuclei (μm²)
5%G40
5%G100
10%G40
10%G100
n.s.
n.s.
y = -0.5096x + 342.87
R² = 0.8769
Viscosity (Pa-s)
D
D21 Mito Abundance per Nuclei (μm²)
n.s.
y = 97.628ln(x) + 59.836
R² = 0.841
Stiffness (kPa)
E
D21 Lipid Quantity
y = -2.5041x + 1171.9
R² = 0.8828
D21 Mito Abundance (μm²)
F
D21 Lipid Diameter (μm)
y = -0.0538x + 32.825
R² = 0.9708
D21 Mito Abundance (μm²)
G
Lipid Phenotype
White Fat-like
Thermogenic Fat-like
Mito Abundance

Figure 3.6. Mitochondrial Abundance of hAdMSC-laden GelMA Hydrogels During Adipogenesis. (A) Confocal images of hAdMSCs encapsulated in 5%G40, 5%G100, 10%G40, and 10%G100 conditions after 0, 7, 14, and 21 days of adipogenic differentiation. Mitochondria, lipids, and nuclei were co-stained with MitoTracker (red), LipidTox (green) and DAPI (blue), respectively. (B) Changes in mitochondrial abundance for hAdMSC-laden 5%G40, 5%G100, 10%G40, and 10%G100 hydrogels at D0, D7, D14, and D21. (C) Quantitative analysis of the relationship of mitochondrial abundance and the initial hydrogel stiffness at D0. (D) Quantitative analysis of the relationship of mitochondrial abundance and the initial hydrogel viscosity at D21. Quantitative analysis of the relationship of mitochondrial abundance, lipid quantity (E), and lipid diameter (F) at D21. (G) Schematic of the relationship of lipid phenotype and mitochondrial abundance. Data are presented as the mean ± SD, n = 5. *, $p < 0.05$; #, $p < 0.01$ and **ζ**, $p < 0.001$. The trendline (red dashed line) and correlation coefficient (R^2) for each relationship were presented as highly correlated (R^2>0.8).

DISCUSSION

In this study, we examined the influence matrix stiffness and viscosity on lipid phenotype and fat lineage potential by producing GelMA polymers with varying mechanical properties. The use of GelMA in this study is particularly important because this polymer is a bioink that is commonly used in 3D-bioprinting applications. 3D-bioprinting has become increasingly popular in regenerative medicine due to its ability to fabricate thick, heterogenous tissues that address patient-specific needs. (4,265–267). Our results showed that GelMA40 and GelMA100 polymers could be fabricated using the sequential and one-pot facile methods, respectively, from the protocol established by Shirahama et. al. (217) A uniaxial compression and oscillatory frequency sweep test confirmed that GelMA stiffness was dependent on its DoM and weight composition, while viscosity was only dependent on the latter. Although *in vivo* and *in vitro* studies have demonstrated that alterations in matrix mechanics regulate adipogenesis, much of this work focuses more on matrix stiffness but not viscosity. (268,269) The lack of studies that investigate matrix viscosity has limited the field's ability to ascertain how mechanobiological cues impact adipogenesis, as well as the formation of other tissue types. In our work, we were able to synthesize GelMA polymers with tunable stiffness and viscosity, which further allowed us to investigate how both of these biomechanical contributions influence fat lineage potential. In general, these methods for

modifying matrices can be implemented to alter the biomechanical properties of other polymers that are relevant to different tissue types. For instance, Ali et al. demonstrated the ability to fabricate a photo-crosslinkable and mechanically tunable kidney ECM-derived bioink suitable for renal tissue bioprinting. (270)

After fabricating and characterizing mechanically tunable GelMA, the effects of stiffness and viscosity on adipogenesis were examined. We hypothesized that soft matrices with low viscosity (10%G40) will enhance adipogenic phenotype (large lipid size and few lipid droplets). In this work, GelMA viscosity played a greater role in driving lipid phenotype and differentiating between metabolic versus thermogenic fat potential in comparison to matrix stiffness. Our system demonstrated a continuum that drives hAdMSCs down distinct fat lineage pathways, where high- or low-viscous matrix conditions supported either a metabolic or thermogenic fat phenotype, respectively. Cell viability, morphology and lipid size were predominantly driven by viscosity, while stiffness impacted lipid quantity and mitochondrial abundance. This work also revealed that the adipogenic markers, FABP4 and UCP1, demonstrated viscous-dependent behavior despite comparable expression levels of PPAR-γ. PPAR-γ is the master regulator of adipogenesis and required for both metabolic and thermogenic fat tissues. In our study, FABP4 and UCP1 expression levels significantly increased over time, specifically in matrices with a high initial viscosity. In particular, 5%G40 not only supported the greatest expression of UCP1, a marker for non-shivering thermogenesis in brown adipocytes, but also produced lipid droplets with the largest diameter, a marker of white adipocytes. A possible explanation for this these confounding results could be that the differentiated hAdMSCs in this condition take on a phenotype that is more comparable to beige fat as opposed to white or brown fat. Beige fat is a type of thermogenic fat

that is located in white fat but characterized by lower UCP1 expression, moderate mitochondrial density, and multilocular lipid droplets that range in size, which were all present in our 5%G40 condition. (278)

Another likely explanation for these results could be that the matrix conditions of 5%G40 support a low-thermogenic, rather than high-thermogenic, brown adipocyte phenotype. Previous work by Song et al. revealed a subpopulation of low-thermogenic brown adipocytes within murine adipose tissue that also exhibited significantly lower UCP1 expression, larger lipid droplets, and lower mitochondrial content. (279) This possibility is important as the incorporation of brown fat in other bioengineered tissues types could serve as a therapeutic element in cancer- or diabetic-related procedures. Nevertheless, in order to adequately identify the mechanical properties that push hAdMSCs toward white, brown, or beige fat, further investigation on metabolic- or thermogenic-specific fat markers and mitochondrial activity is necessary.

Additionally, based on the trends presented in this study, matrices that are more viscous and less stiff should support the induction of metabolic fat, while stiffer matrices that are less viscous should invoke thermogenic fat formation. However, it should also be noted that metabolic and thermogenic fat are only 2 major types of adipose tissue. Articular fat pads (AFPs), or mechanical fat, are another category of adipose tissue that retain structural features similar to subcutaneous, or metabolic fat, but instead are located within synovial joints and play major role in joint biomechanics and mechanical support. (280) While the structure of mechanical fat is comparable to metabolic fat, AFPs tend to have greater vascularity, innervation, fibrosis, and immuno-infiltration in comparison to subcutaneous tissues. It also believed that while AFPs maintain their

volume and structure regardless of extreme subcutaneous conditions, such as obesity or cachexia, they may be regulated by distinct metabolic pathways that are independent from subcutaneous tissue. (280,281) Lastly, since AFPs are constantly subjected to a mechanical load, it is important to recapitulate these native biomechanics *in vitro* for the proper development of AFPs in hand, foot, facial, and joint reconstruction. Overall, while there is a lack of knowledge on the differentiating factors of mechanical versus metabolic fat, the introduction of biomechanical stimuli, such as compression, should be included in AFP tissue engineering.

The field of fat tissue engineering has highlighted matrix mechanics as a key target for regulating adipogenesis. Biological polymers, such as GelMA, can be tuned to study how variations in mechanical properties govern the adipogenic potential of hAdMSCs. Specifically, identifying the unique role of matrix viscosity and stiffness on adipogenesis can provide an important target for understanding how various matrix properties influence cell fate. The findings from this work demonstrated that lipid phenotype and hAdMSC fat potential are greatly impacted by matrix viscosity in comparison to stiffness. However, despite the predominant role of matrix viscosity in adipogenesis, there are some aspects of our system that exhibit stiffness-dependent behavior, such mitochondrial abundance. Altogether, high viscous GelMA not only produced larger lipids, a feature of metabolic fat, but also a greater quantity of lipids and mitochondria, a feature of thermogenic fat. Ultimately, this differentiating factor in fat production will be important knowledge for engineering specific adipose tissue types relevant to distinct soft tissue defects.

CHAPTER 4. THE ROLE OF MATRIX STIFFNESS AND VISCOSITY ON VASCULOGENESIS

INTRODUCTION

Deep tissue wounds are a prevalent clinical concern that impacts millions of individuals in the U.S. annually and requires invasive surgical intervention for full rejuvenation. (282) Autologous flap transfer is a common reconstructive treatment option for replacing deranged tissues. (283) In brief, this procedure involves the resection and transferal of autologous soft tissues, equipped with hierarchical vasculature, from a healthy donor region to the defective recipient site. (4,244) However, this procedure demands highly skilled surgical training and is complicated by donor-site morbidity, tissue availability, and post-operative debilitation. (4,284) While tissue engineering strategies offer a promising solution to overcome these limitations, a major issue that remains in regenerative medicine is the ability to engineer the appropriate vascular networks that are necessary for adequate cell survival, tissue function, and anastomosis to host vasculature.

In vascular tissue engineering, there are several biological and environmental factors that drive and maintain vascular network formation, including biochemical signaling, hemodynamics, cyclic strain, matrix composition and mechanics. (285–288) In terms of matrix mechanics, the effects of stiffness on vasculogenesis have been well-studied. Previous work has demonstrated that while stiffer substrates enhanced vascular EC proliferation and adhesion, softer matrices actually promoted the pro-angiogenic activity and phenotype these cells. (100,289,290) Complementary studies reveal that stiff substrates not only perturb the release of nitric oxide and formation of capillary structures, but also cannot recover these features even in the presence of the pro-

angiogenic factor, VEGF. (289) Ferrari et al. further displayed that softer 3D matrices increased microvessel diameter and number of sprouts in comparison to stiffer matrices in both the presence and absence of VEGF. (291) Additionally, it should be noted that matrix stiffness influences the behavior of other cell types within the vascular niche aside from ECs, including pericytes. Work by Yu et al. revealed that when microvascular ECs and pericytes were co-cultured on stiff matrices (120kPa), pericytes differentiated into myofibroblasts even in the presence of a TGFβ inhibitor. However, when each cell type was cocultured on soft matrices (6kPa), microvascular formation enhanced, pericytes maintained a stable phenotype, and fibrosis was inhibited *in vivo* after using a bone graft skull transplantation model. (292) While there is great insight on the impact of matrix stiffness on vascular formation, living tissues behave like viscoelastic materials. Yet, the influence of matrix viscosity on vasculogenesis and other tissue formation is understudied. (293) Therefore, there is a need to develop a tunable platform that not only modulates matrix stiffness and viscosity but also uses these features to gain a deeper understanding of how matrix mechanics regulates this vascular formation.

GelMA is an ideal polymer for developing this platform due to its biocompatible and mechanical characteristics. In terms of biocompatibility, many studies have confirmed that GelMA can support the formation of vasculature and other soft tissue types *in vitro*. (16,233,253,294) Specifically, work by Chen et al. not only demonstrated the capacity to culture microvessels in GelMA hydrogels, but also confirmed that softer GelMA matrices (1-2kPa) are more suitable for driving *de novo* vasculogenesis in comparison to stiffer matrices (4-5kPa). (233) In terms of mechanics, GelMA properties can be altered by carefully manipulating is crosslinking density, namely through changes in DoM or weight composition. Previous studies have revealed that increasing GelMA

DoM and weight composition results in stiffer hydrogels, decreased porosity, and increased cell spreading in 2D cultures. (9,217,229,233,295,296) Additionally, Hoch et al. is one of few who investigated the change in GelMA viscosity due to varying DoM and weight composition. In this work, it was revealed that GelMA polymers with a decreasing DoM (100%, 80%, and 67%) only exhibited greater matrix viscosity in higher GelMA concentrations (20-30% w/v) in comparison to lower GelMA concentrations (10-15% w/v). (228) More recently, work by Liu et al. demonstrated that the viscous parameter (or loss modulus) of GelMA can be elevated by incorporating increasing concentrations of phenylboronic acid-modified gelatin, despite having a comparable matrix elasticity (or storage modulus). (262) While these findings reveal the impact of GelMA DoM and weight composition on matrix mechanics, much of this work primarily focuses on changes in GelMA stiffness and not viscosity. Additionally, in the few studies that actually examine the tunability of GelMA viscosity, distinct viscosity values were only achieved through either the incorporation of hydrogel additives or in stiffness regimes that are not physiologically relevant to vascular formation. Therefore, there is a need to fabricate standalone GelMA polymers within a stiffness regime that are suitable for developing vasculature.

The aim of this present work was to study the effects of matrix stiffness and viscosity on vasculogenesis using our tunable GelMA matrix. **We hypothesized that soft matrices with high viscosity (5%G100) will enhance vasculogenic phenotype (microvessel formation and structure).** GelMA was fabricated with 40% and 100% DoM to achieve variations in crosslinking density and polymerized at 5% and 10% (w/v) to achieve differences in matrix stiffness and viscosity. Co-cultures of GFP-tagged HUVEC and hAdMSCs were encapsulated in tunable GelMA hydrogels and underwent vasculogenic induction for 10 days. Overall, the major findings

of this study revealed that moderately stiff matrices with low viscosity and crosslinking density enhance vasculogenic phenotype (microvessel density, structure, and thickness). Furthermore, this work provides a deeper understanding on the role of matrix stiffness, viscosity, and crosslinking efficiency on vasculogenesis for autologous flap tissue engineering.

MATERIALS & METHODS

Vascular-Induced Cell Culture in 3D GelMA Hydrogel

GFP-tagged human umbilical cord endothelial cells (GFP-HUVEC, Angio-Proteomie, MA, USA) were expanded with complete Endothelial Growth Medium (EGM, Angio-Proteomie, MA, USA), co-suspended with hAdMSCs in GelMA polymer solutions, photo-polymerized, and cultured in vasculogenic medium for up to 10 days as previously described in chapter 2. Data collected from each experimental condition was analyzed at D0, D5, and D10 timepoints. **(Fig. 2.3)**

Immunofluorescence

After each timepoint, live cell laden GelMA hydrogels were washed in 1X PBS and prepped for staining. Each sample was immediately fixed in 4% PFA and washed in 1X PBS 3 times the following day. Fixed samples were then permeabilized with 0.1% saponin for 1 hour at room temperature, washed with 1X PBS 3 times, and blocked overnight. After blocking, each sample was washed with 1X PBS 3 times and co-stained with Cy3^{TM}-conjugated alpha-smooth muscle actin primary antibody (αSMA, Sigma-Aldrich®, MA, USA) and DAPI overnight at 4°C. Images were acquired using a Zeiss LSM 710 Confocal Microscope and αSMA expression, microvessel density, junctions, branches, and thickness were quantified using FIJI software.

Uniaxial Compression

After each timepoint, the stiffness of vascular-induced cell-laden hydrogels was determined by a uniaxial compression test as previously described in chapter 2.

Stress Relaxation

After each timepoint, the viscosity of vascular-induced cell-laden hydrogels was determined by a stress relaxation test as previously described in chapter 3.

Statistics

Quantitative analyses were performed in quintuplicates for immunofluorescence and mechanical testing. A one-way ANOVA was performed followed by a post-hoc Tukey HSD test and a two-tailed t-test with unequal variance to evaluate any significant difference between experimental groups. All quantitative data was reported as the mean ± standard deviation with a significant difference defined when $p<0.05$. The data are shown as ***** ($p<0.05$), **#** ($p<0.01$), **ζ** ($p<0.001$). The trendline and correlation coefficient (R^2) for each relationship was presented as either greater or less than moderately correlated ($R^2>0.5$).

RESULTS

Matrix Mechanics on Microvessel Formation

In order to determine the effect of stiffness and viscosity on vasculogenesis, GFP-tagged HUVEC and hAdMSCs were co-cultured in tunable GelMA hydrogels, induced in vasculogenic medium for 10 days, and analyzed for microvessel density and αSMA expression. In general,

immunofluorescent images demonstrated that each condition invoked some microvascular structures overtime (**Fig. 4.1A**) However, moderately stiff matrices with low viscosity (10%G40) was the only condition that supported an increase in microvascular formation throughout the duration of the culture period. All other conditions experienced a peak in microvessel density at D5 and a slight decrease by D10, with 5%G40 and 10%G100 exhibiting the greatest and least amount of microvessel density, respectively (**Fig. 4.1B**). When microvessel density was normalized by the number of nuclei per field view, high viscous matrices (5% groups) displayed a comparable microvessel density as the unnormalized data, while low viscous matrices (10% groups) displayed contrasting results (**Fig. 4.1C**). More specifically, 10%G40 revealed a slight dip in microvessel density after normalization, suggesting that significant cell proliferation may have occurred in this condition. Conversely, 10%G100 revealed a slight uptick in microvessel density after normalization, suggesting that cell death may have occurred in this condition. αSMA expression, a marker for smooth muscle cells, was also quantified and normalized by the number of nuclei per field view to distinguish between HUVEC and hAdMSC cell types within each matrix condition. These findings revealed that αSMA expression generally increased with increasing stiffness (**Fig. 4.1D**). Soft matrices (5%G40) displayed the least amount of a αSMA expression, followed by moderately stiff (5%G100 and 10%G40) and stiff (10%G100) matrices. Similar to the changes in microvessel density observed, αSMA expression also peaked at D5 and slightly declined by D10 in all conditions except 10%G100. When microvessel density and αSMA expression were analyzed against matrix properties, these phenomena demonstrated DoM- and stiffness dependent behavior, respectively (**Fig. 4.1E-H**), while matrix viscosity did not have an apparent impact (**Fig. 4.1I-J**). Microvessel density was then analyzed against αSMA expression and exposed an inverse relationship between these two parameters, where αSMA decreased with

increasing microvessel density (**Fig.4.1K-L**). These results ultimately show that matrices with an initial moderate stiffness, low viscosity, and low DoM enhance microvessel formation and diminish αSMA expression.

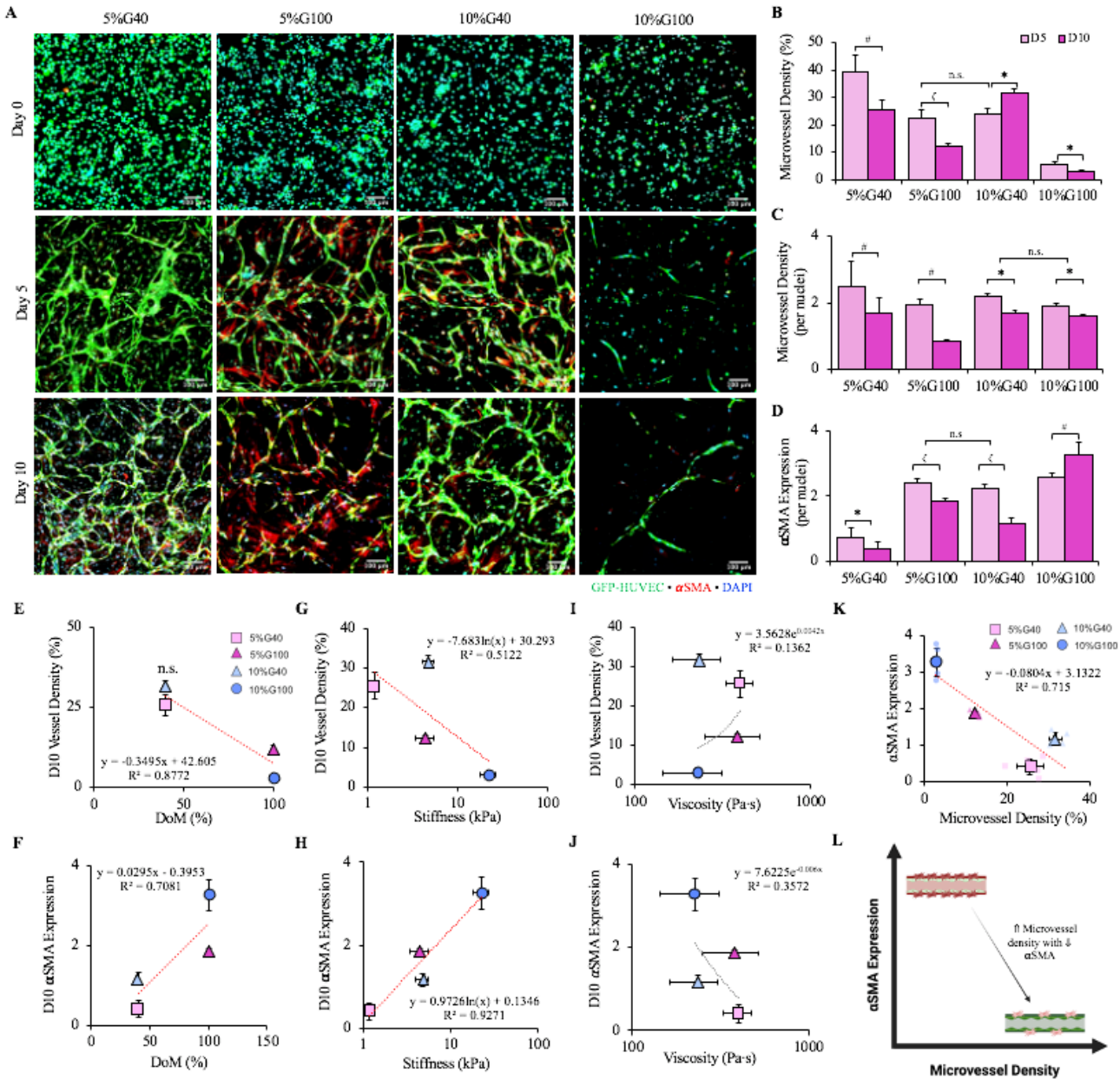

Figure 4.1. Microvessel Formation Co-laden GelMA Hydrogels During Vasculogenesis. (A) Confocal images of HUVEC and hAdMSCs co-encapsulated in 5%G40, 5%G100, 10%G40, and 10%G100 conditions after 0, 5, and 10 days of vasculogenic differentiation. HUVEC were pre-tagged with GFP, while αSMA and nuclei were co-stained with anti-actin αSMA-Cy3 (red) and DAPI (blue), respectively. Microvessel density was quantified (B) and normalized by cell count per field view (C) at D5 and D10. (D) The expression of αSMA was also quantified and normalized by cell count per field view at D5 and D10. Quantitative analysis of the relationship between microvessel density or αSMA expression and DoM (E-F), stiffness (G-H), and viscosity (I-J) were quantified at D10 of vasculogenesis (K) Comparative analysis between the relationship of microvessel density and αSMA expression in relation to initial matrix stiffness and viscosity. (L) Schematic of variations in microvessel density and αSMA expression during vasculogenesis. Data are presented as the mean ± SD, n = 5. *, $p < 0.05$; #, $p < 0.01$ and **ζ**, $p < 0.001$. The trendline and correlation coefficient for each relationship is indicated as either greater than (red; $R^2>0.5$) or less than (gray; $R^2<0.5$) moderately correlated.

After examining the relationship between matrix mechanics, microvessel density, and αSMA expression, the influence of matrix stiffness and viscosity on microvascular junctions, branches, and thickness were also investigated. In general, immunofluorescent images demonstrated more established networks by D10 in matrices with low DoM or crosslinking efficiency (**Fig. 4.2A**). This is further shown in quantitative analyses, where matrices with low DoM (G40) exhibited thicker vessels and more junctions and branches in comparison to high DoM matrices (G100), regardless of weight composition (**Fig. 4.2B-D**). In fact, it should be noted that the number of junctions, branches, and vessel thickness in G100 conditions were either consistent or slightly decreased throughout the culture period. When the number of junctions, branches, and vessel thickness were analyzed against matrix properties, these phenomena were generally influenced by matrix stiffness with a DoM-dependent feature. Specifically, the number of junctions and branches each displayed decreasing quantity with increasing stiffness (**Fig. 4.3A-F**). However, matrices with low DoM exhibited the greatest number of junctions and branches in both high (5%) and low (10%) groups. In terms of microvessel thickness, there was no apparent relationship with either stiffness or viscosity, but rather crosslinking efficiency (**Fig.4.3G-I**). G40 matrices supported the formation of thicker vessels in comparison to G100 matrices. Overall, these results reveal that the

number of junctions and branches decreased with increasing stiffness and DoM, while microvessel thickness only diminished in stiffer matrices.

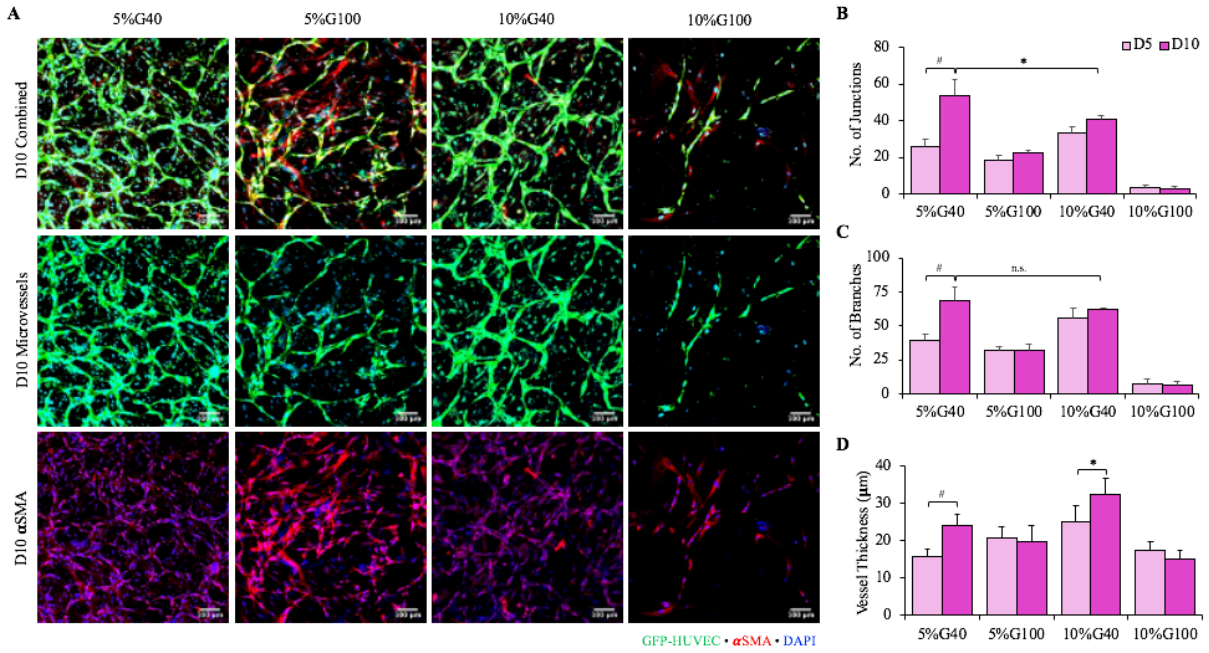

Figure 4.2. Microvessel Characterization of Co-laden GelMA During Vasculogenesis. (A) Confocal images of HUVEC and hAdMSCs co-encapsulated in 5%G40, 5%G100, 10%G40, and 10%G100 conditions at 10 days of differentiation. HUVEC were pre-tagged with GFP, while αSMA and nuclei were co-stained with anti-actin αSMA-Cy3 (red) and DAPI (blue), respectively. Microvessel junctions (B), branches (C), and thickness (D) were quantified at D5 and D10 of vasculogenesis. Data are presented as the mean ± SD, n = 5. *, $p < 0.05$; #, $p < 0.01$ and **ζ**, $p < 0.001$.

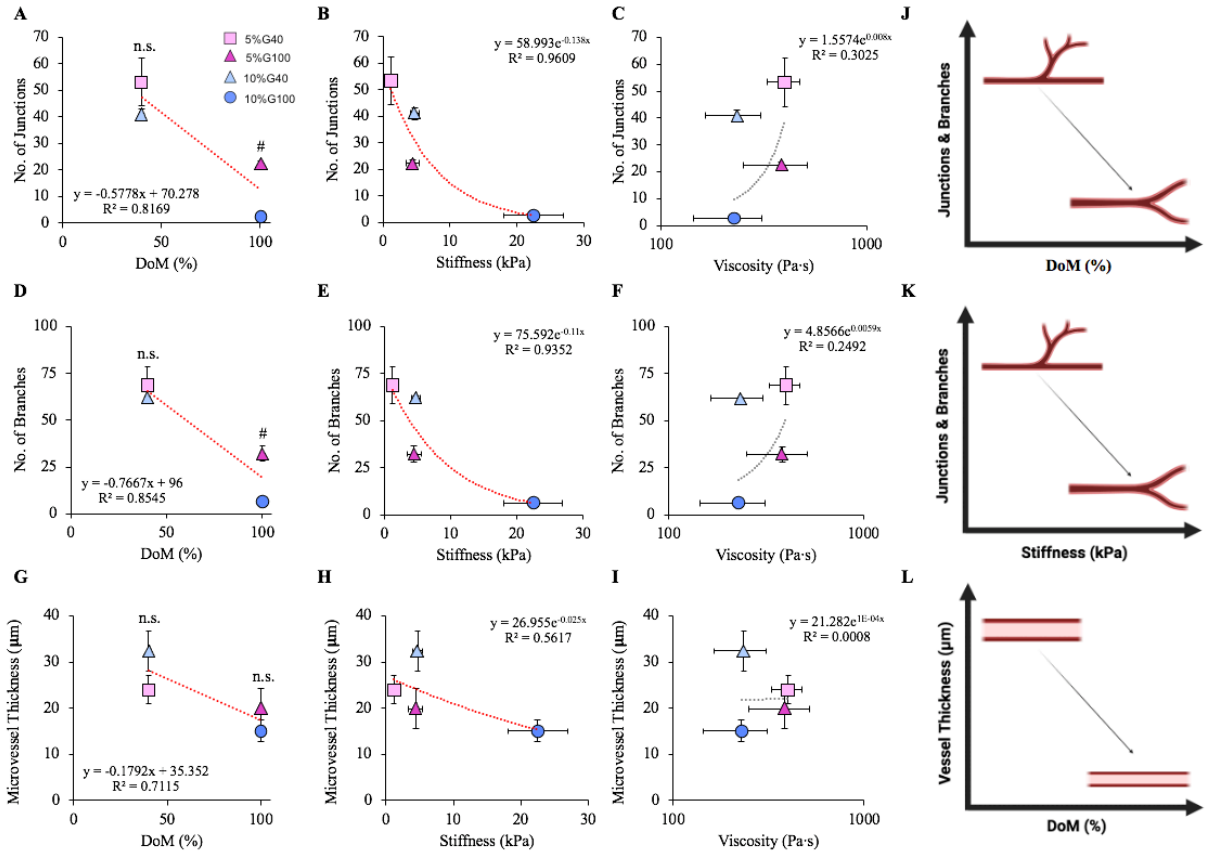

Figure 4.3. Influence of Matrix Stiffness and Viscosity on Microvessel Phenotype. Quantitative analysis of the relationship between DoM, stiffness, or viscosity and microvessel junctions (A-C), branches (D-F), and thickness (G-I), respectively. Schematic of the relationship between microvessel junctions and branches and DoM (J) and stiffness (K). The trendline and correlation coefficient for each relationship is indicated as either greater than (red; R^2>0.5) or less than (gray; R^2<0.5) moderately correlated.

Alterations in Matrix Mechanics During Vasculogenesis

It is well understood that cells within a matrix tend to modify their surroundings as they undergo proliferation and differentiation, which ultimately alters the mechanics of the original microenvironment. Therefore, the changes in matrix stiffness and viscosity were quantified in this study to capture a more complete understanding of how matrix mechanics were impacted by cell maturation during vasculogenesis. At first glance, there is very little change in hydrogel size over the 10-day culture period, as described in greater detail in chapter 2 (**Fig. 4.4A**). This work showed

a general increase in both stiffness (**Fig. 4.4B**) and viscosity (**Fig. 4.4C**) overtime for only 5% groups. Although 10%G100 obtained the stiffest modulus in comparison to other groups, there were no significant changes in stiffness throughout the culture period. Alternatively, both 5% groups exhibited comparable increases in matrix stiffness overtime. It should also be noted that 10%G40, the condition that supported the most robust microvessel network formation, was the only matrix that decreased in stiffness during vasculogenesis. Overall, soft and moderately stiff matrices (5%G40, 5%G100, and 10%G40) were able to undergo significant changes in stiffness by the end of the culture period, while stiff matrices (10%G100) did not undergo any modifications.

In terms of matrix viscosity, while 5% groups had an initial viscosity that was lower than 10% groups, 5%G40 and 5%G100 both achieved a final viscosity that was greater than 10%G40 and 10%G100. Additionally, 5% groups experienced comparable increases in viscosity overtime, while 10% groups demonstrated either no change or decreases in viscosity. Although 10%G40 maintained its viscosity throughout the culture period, it exhibited a final viscosity that was similar to 5%G100. It should also be noted that 10%G100 was the only group to experience a decrease matrix viscosity. When changes in matrix stiffness were analyzed against viscosity overtime, the matrix viscosity appeared to increase as stiffness decreased (**Fig. 4.4D**). Further comparative analyses between microvessel phenotype and matrix mechanics revealed that microvessel density and αSMA increased with decreasing stiffness and viscosity (**Fig. 4.4E-F**), respectively, and the number of microvessel junction and branches increased with increasing viscosity (**Fig. 4.4G-H**). Altogether, our results reveal that cells incorporated in matrices with a high native viscosity are more capable of modifying their matrix to a greater degree than matrices with a low native

viscosity. Albeit native matrices that are moderately stiff with low viscosity and DoM (10%G40) appear to have the most desirable mechanics for vascular network formation, as this is the only condition that not only experiences the least amount of matrix alterations during vasculogenesis, but also exhibits the most superior microvessel phenotype in terms of high microvessel density, low αSMA expression, numerous junctions and branches, and thick vessels.

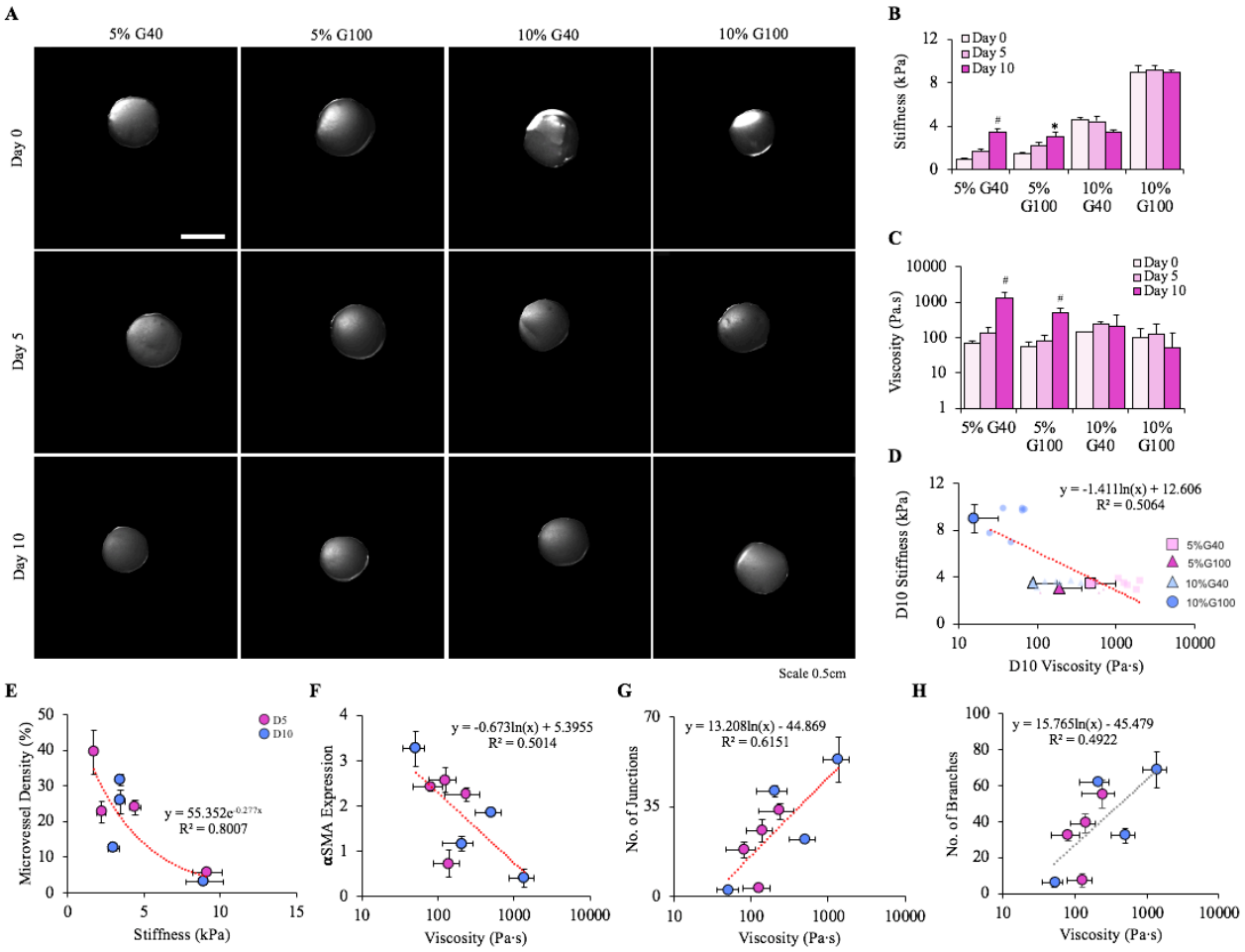

Figure 4.4. Alterations in Matrix Stiffness and Viscosity During Vasculogenesis. (A) Brightfield images of 5%G40, 5%G100, 10%G40, and 10%G100 hydrogel constructs at D0, D5, and D10. Changes in GelMA stiffness (B) and viscosity (C) were observed for each measurable condition at D0, D5, and D10. (D) Quantitative analysis of the relationship of hydrogel stiffness and viscosity at D10 of vasculogenesis. Quantitative analysis of the relationship between stiffness and microvessel density (E) and viscosity and αSMA expression (F), microvessel junctions (G) and branches (H) at D5 and D10 of vasculogenesis. Data are presented as the mean ± SD, n = 6. *, $p < 0.05$; #, $p < 0.01$ and **ζ**, $p < 0.001$. The trendline and correlation coefficient for each relationship is indicated as either greater than (red; $R^2>0.5$) or less than (gray; $R^2<0.5$) moderately correlated.

DISCUSSION

In this study, we used our mechanically tunable GelMA platform to examine the role of matrix stiffness and viscosity on vasculogenesis. While there is a plethora of knowledge regarding the impact of stiffness on endothelial cell behavior, fewer studies have investigated the influence of matrix viscosity. (227) The novelty of this work addresses this limitation by fabricating GelMA polymers with variable viscosities that lie within a stiffness regime relevant to vasculature. We hypothesized that soft matrices with high viscosity (5%G100) will enhance microvessel phenotype. After synthesizing GelMA polymers with either 40% or 100% DoM, HUVEC and hAdMSCs were co-encapsulated in 5% and 10% (w/v) conditions and induced with vasculogenic media for 10 days. Our work actually revealed that moderately stiff matrices with low viscosity and DoM (10%G40) enhanced microvessel formation and attenuated αSMA expression. Particularly, 10%G40 was the only condition to support a consistent increase in microvessel density, whereas all other conditions experienced a peak in microvessel density at D5 and a slight decrease by D10. A potential reason for the decline in microvessel phenotype is likely due to the absence of shear stress. Although matrix stiffness is an important factor in the development of vasculature and other tissue types, shear stress is also a crucial player. It is well understood that shear stress is not only beneficial to invoking angiogenic sprouts but also necessary for maintaining stable microvascular networks. (14,297–299) In fact, work by Kohn et al. investigated the cooperative effects of matrix stiffness and shear stress on EC behavior. The findings from this study exposed that ECs cultured on compliant matrices and subjected to laminar fluid shear stress displayed a superior microvessel phenotype, namely through increased elongation, cell-cell junctions, eNOS secretion, and decreased RhoA activity. (300) It should also be noted that vascular pruning, or the regression of selected microvessels, must occur to form functional and mature

vasculature. (301,302) Thus, another potential explanation for the decrease in vascular networks by D10 could be due to the occurrence of vascular pruning. However, additional analyses that capture features of vascular pruning must be acquired in order to explain these phenomena.

In addition to analyzing microvessel density, we also quantified αSMA expression throughout the culture period. Similar to these changes, αSMA also peaked at D5 and slightly declined by D10 in all conditions except matrices with high stiffness, low viscosity, and high DoM (10%G100). A possible explanation for this observation is that MSCs tend to differentiate into myofibroblast, a cell type implicated in scarring in vivo, fibrosis, and contractility, when embedded in stiff matrices. (303–307) It is widely known that myofibroblast are not only tightly connected to pathology but also exhibit high expression levels of αSMA. (308) Previous work by Yu et al. revealed that stiff matrices push pericytes down a myofibroblastic pathway even after TGFβ inhibition. (292) It has also been proven that TGFβ is a transcription factor linked to the differentiation of myofibroblast, an intermediate phenotype between healthy fibroblasts and SMCs. (309) Additionally, it should be noted that moderately stiff matrices with high viscosity and DoM (5%G100), also exhibited the greatest αSMA expression in comparison to all other groups, indicating that crosslinking efficiency, rather than stiffness and viscosity, may be the culprit of this increased pathological feature. While significant work has been done to uncover how ECM crosslinking can influence its structure, disrupt matrix accumulation and degradation homeostasis, and subsequently, drive fibrosis, additional work in our study is required to pinpoint crosslinking efficiency as a main driver of pathological αSMA expression. (310)

Another phenomenon observed in our work displayed that moderately stiff matrices with low viscosity and DoM (10%G40) gave rise to robust microvessels but diminished αSMA expression overtime. It is well accepted that mural support cells, which express αSMA, are necessary for the formation and stabilization of mature vasculature. Work by Jang et al. exposed that HUVEC spheroids co-cultured with rising vascular MSCs densities increasingly improved angiogenic sprouting in comparison to isolated endothelial spheroids. (311) However, as previously described, high αSMA expression is also linked to vascular pathology byway of myofibroblast differentiation. This conundrum emphasizes the importance of understanding the mechanisms that drive αSMA expression among healthy mural support cells and pathological myofibroblasts. Additional studies by Gan et al. uncovered that SMC and myofibroblast use distinct transcriptional mechanisms, such as transcriptional enhancer factor-2 (TEF-1) and related TEF-1 (RTEF-1), respectively, to drive αSMA expression. (312) Therefore, further analyses on SMC-, pericyte- and myofibroblast-specific markers is necessary to properly distinguish between the potential phenotype of the differentiated hAdMSCs in our system.

We also examined alterations in matrix mechanics during vasculogenesis and found that compliant matrices (5%G40, 5%G100, 10%G40) underwent the most significant changes in stiffness, while stiff matrices did not undergo any modifications. Specifically, compliant matrices, which exhibited defined microvascular networks, achieved final stiffness values comparable to each other despite having dissimilar stiffnesses at the beginning of the culture period. Prior to vasculogenic induction, 5% groups and 10%G40 presented a stiffness at 1-2kPa and 4-5kPa, respectively. However, all compliant matrices achieved a final stiffness of 3kPa. A plausible explanation for this could be that specific stiffness conditions must be achieved in order to invoke the establishment of adequate

vasculature. Although it appears that a modulus of 3kPa is the most ideal for vascular network formation, the literature reports that a wider range of values (1-10kPa) have the capacity to drive the proper function and behavior of ECs and other relevant vascular cell types. (313,314) It should also be addressed that the rigidity of 10%G100 and subsequent lack of microvessel formation may be attributed to its limited ability to modify its matrix. As reported earlier, deregulated matrix accumulation and degradation can perturb vasculogenesis and give rise to vascular pathologies. However, while this was the case for matrix stiffness, a similar phenomenon was not observed with respect to matrix viscosity.

Lastly, our work uncovered that the compliant matrices with low viscosity and DoM (10%G40) create the most desirable mechanics for vascular network formation. With respect to all complaint matrices, 10%G40 not only experienced the least modifications in mechanics but also exhibited the most superior microvessel phenotype in terms of high microvascular density and thickness, low αSMA expression, and numerous junctions and branches. These findings suggest that there is an optimal matrix stiffness, viscosity, and crosslinking efficiency that supports robust vasculogenesis. It also appears that when vascular cells are incorporated in compliant matrices that deviate from the native properties of 10%G40, they remodel their matrix to achieve comparable mechanics, particularly a similar stiffness value, to 10%G40. However, more robust and fine-tuned studies are required to properly investigate this hypothesis. A potential approach to addressing this question is to create a modifiable GelMA system that can be mechanically controlled during cell culture. For instance, Mora-Boza et al. reported that GelMA can undergo dual crosslinking when combined with chitosan to alter its crosslinking density and mechanical properties. When GelMA/chitosan composites were photo-polymerized via UV stimulation and subsequently

crosslinked via ionic polymerization, using glycerylphytate (G1Phy), GelMA exhibited enhanced shape fidelity, swelling, and long-term stability. (315,316) Thus, the incorporation of chitosan in our system can be used to regulate GelMA mechanics, where addition of the ionic crosslinker, G1Phy, can occur at distinct timepoints to adjust GelMA's material properties, regardless of how the encapsulated cells modify the matrix. Ultimately, by enforcing greater control over these shifts in matrix mechanics during vasculogenesis, we can better ascertain the optimal material properties for favorable microvascular formation and soft tissue regeneration.

CHAPTER 5. FABRICATION OF A MACRO-PERFUSION BIOREACTOR TO INVESTIGATE HEMODYNAMIC SHEAR STRESS AND VORTICITY ON LOCAL ANGIOGENESIS

INTRODUCTION

Large, gaping wounds are characterized by chronic defects to the skin and underlying soft tissues including fascia, fat, vasculature, muscle, and even bone. (210) Conditions such as diabetes, severe burns, cancer resection, and congenital defects are the main causes of soft tissue injuries, contributing to over 6.5 million reconstructive cases in the U.S. annually. (211) Full restorative treatment options not only prioritize the reconstruction of deranged tissues but also the maintenance of healthy tissue functionality, stability, and durability, as well as its capacity to interact with the surrounding host tissue at the recipient site. (210) In order to achieve this, large volumes of healthy and autologous donor tissue are required for its transplantation and anastomosis to host vasculature. (4,317) However, these procedures are highly invasive and limited by extended post-operative debilitation, donor-site morbidity, and donor tissue supply. (4,284) While tissue engineering strategies provide an excellent alternative to current reconstructive methods for chronic wound repair, the inability to fabricate hierarchical vasculature within bioengineered tissues has not fully been elucidated.

Microvascular networks, or capillary beds, are important for nutrient and oxygen diffusion, as well waste removal from tissues, and is crucial to the survival, maintenance, and function of all cell types in the body. In general, microvessels develop through a highly coordinated series of steps that involve: (1) vasculogenesis, the de novo formation of blood vessels; (2) angiogenesis, the

sprouting of vasculature from pre-existing vessels; and (3) vascular pruning, the select regression of preestablished vessels. (318) It is well understood that microvascular formation is not only driven by chemical signaling but also by matrix structure, composition, mechanics, and hemodynamics. (285–288,305,319,320) With regard to the latter, fluid shear stress (FSS) is one of the primary physical forces exerted on an endothelium in the presence of hemodynamic flow. (288,321,322) Previous work has shown that the application of physiological FSS to an engineered endothelium supports matrix remodeling and subsequently, enhances EC alignment, capillary-like tube formation, angiogenic sprouting, and pro-angiogenic gene expression in comparison to ECs subjected to pathological flow or static conditions. (299,323–328) In fact, work by Chen et al. revealed that the arterial specification of capillary networks is predominantly regulated by FSS, and that the presence of VEGF actually reverses this phenomenon, underlining the significant impact of FSS in capillary specification and maintenance. (329) However, while shear stress is a dominant factor in driving angiogenic sprouting and maturation, additional hemodynamic forces, such as vorticity, are also crucial to proper EC behavior and microvessel formation.

Hemodynamic vorticity is defined as the angular velocity of fluid, which is primarily present at vascular bifurcations, and has been shown to have a substantial influence on microvessel development, remodeling, and maintenance. (330) Computer simulations of quail embryo vascular development by Ghaffari et al. revealed that high vortical flow is achieved at regions of stream convergence, which are the least desirable sites for angiogenic sprouting. (331) *In vitro* work by Sedlak et al. further displayed that recirculating flow and low shear stress attenuates endothelial elongation, alignment, and NO production, and enhances proliferation, permeability, and monocyte adhesion in comparison to ECs subjected to laminar shear stress. (332) While there is

some knowledge on the influence of vorticity on angiogenic sprouting, these systems are limited in their approach to uncovering the combined effects of shear stress and vorticity on angiogenesis. In particular, microfluidics and organ-on-a-chip devices are heavily relied on to ascertain the role of hemodynamic forces on angiogenesis. (288,291,333–335) However, these systems are low-throughput and can only generate either bidirectional or non-pulsatile flow, which is not physiologically relevant to biomechanics of native vasculature. Additionally, while *in vivo* models present an opportunity to look closure at the influence of hemodynamic vorticity on endothelial behavior, these methodologies are limited by its complexity and inability to simulate pathological conditions, a feat that is more feasible *in vitro*. Thus, there is a need to fabricate a macro-perfusion system capable of generating variable hemodynamic regimes under unidirectional and pulsatile (UNP) flow to study the combined effect of shear stress and vorticity on vascular formation, maturation, and maintenance.

The aim of our work was to engineer a macro-perfusion bioreactor (MPB) that supports UNP flow across high-throughput lumen geometry with varying shear stress and vorticity regimes. In addition to this goal, the secondary aim of our study was to examine the combinatorial effects of hemodynamic shear stress and vorticity on angiogenesis. High-throughput channel geometry, also known as the *Squiggle*, was first designed to generate varying shear stress and vorticity profiles and confirmed using ANSYS software. Next, MPBs were manufactured to house voluminous GelMA hydrogels with patent *Squiggle* channels that can withstand long-term perfusion. In order to minimize the use of functional GelMA for this system, a new polymer, GelMA60 (G60), was synthesized and confirmed using ^{1}H NMR analysis. Our results indicated that 6% GelMA60 exhibited comparable native mechanics as 10%G40 but invoked similar vasculogenic behavior as

5%G100, as highlighted in chapter 4. Once our MPBs were optimized and tested for long-term perfusion, the non-steady state diffusion of 20kD FITC-dextran through cellular and acellular *Squiggle* channels was examined using UNP flow. These studies revealed that acellular regions of low shear stress and vorticity experienced the greatest diffusion in comparison to hemodynamic sites of low shear stress and vorticity. However, after endothelialization, particle displacement was perturbed at the locations that initially supported robust diffusion. Lastly, when MPB *Squiggle* channels were endothelialized and perfused with UNP flow for 7 days, evidence of lumen maturation and closure throughout the channel was observed, regardless of the hemodynamic shear stress and vorticity profile. While cellular studies in our MPB system require further optimization, our work sets the foundation for fabricating voluminous hydrogels with complex patent channel geometry to study the vascularization of bioengineered soft tissues.

MATERIALS & METHODS

GelMA60 Synthesis

GelMA with 60% DoM was prepared using the Shirahama et al. sequential method as previously described in chapter 2. (Table 2.1)

^{1}H NMR Characterization of GelMA60

The degree of methacrylation for GelMA60 was confirmed using ^{1}H NMR analysis as previously described in chapter 2.

Oscillatory Frequency Sweep

The native viscosity of polymerized GelMA60 was determined by an oscillatory frequency sweep test as previously described in chapter

Uniaxial Compression

After each timepoint, the stiffness of vascular-induced co-laden hydrogels was determined by a uniaxial compression test as previously described in chapter 2.

GelMA Compaction

After each timepoint, the change in surface area of GelMA60 was quantified as previously described in chapter 2.

Stress Relaxation

After each timepoint, the viscosity of vascular-induced co-laden hydrogels was determined by a stress relaxation test as previously described in chapter 3.

Vascular-Induced Cell Culture in 6% GelMA60

GFP-HUVEC and hAdMSCs were co-cultured in GelMA60 and induced in vasculogenic media for 10 days as previously described in chapter 4.

Immunofluorescence

After each timepoint, cell laden GelMA60 constructs were prepared and co-stained with Cy3™ conjugated αSMA and DAPI for confocal imaging as previously described in chapter 4.

ANSYS Simulation of Hemodynamic Flow Through "Squiggle" Channel

ANSYS FLUENT was used to produce 3D geometric simulations of shear stress, vorticity, and flow lines along our *Squiggle* channel design (L= 44.3mm and D=1mm), which was created using Siemens NX software. A computational mesh with 63,152 elements and 302,178 nodes was then generated prior to simulations. Cell culture media was approximated as a Newtonian fluid with a viscosity of 9.5e-3 Pa·s and density of 1000 kg/m3. The wall shear stress of the channel was measured along its 3D length and selected to achieve a physiological shear stress of 1-2Pa along the straight paths of the channel. Boundary conditions were set at the wall along distinct positions of the channel, including the elbow, plenum, and arch, while a velocity of 4.2e-2 m/s was applied at the inlet to achieve a flow rate of 2.5mL/min. Flow within the Squiggle channel geometry was then simulated in 3D and under pressure-driven and steady-state laminar flow.

Fabrication of "Squiggle" Channel

Dehydrated Squiggle channels were prepared by casting a sterile 20% gelatin solution in PDMS Squiggle (-) Molds and storing them at 4°C for at least a week. After dehydration, Squiggle channels were extracted and stored back at 4°C until further use. It should be noted that Squiggle (+) Molds were designed using Siemens NX software and 3D-printed to generate the Squiggle (-) Molds. *(See **Appendix B** for more details)*

Preparation of GelMA with Patent "Squiggle" Geometry in MPB System

Our MPB system was carefully designed to support the fabrication of a voluminous GelMA construct containing our Squiggle channel geometry. In order to assemble the MPB system, a Silicone Mold and two syringe catheters were first inserted into the MPB Case Bottom. The Silicone Mold was placed in the cavity of the MPB Case Bottom, while the syringe catheters were incorporated on each side of the MPB Case Bottom, through the Silicone Mold, and secured by Catheter Seals. Next, a dehydrated Squiggle channel was lodged into each Catheter, in the proper orientation, and secured with 20% gelatin plugs that were injected throughout the entire length of each Catheter and allowed to solidify at room temperature for 5 minutes. After casting gelatin plugs, approximately 3-3.5mL of 6%GelMA60 containing 0.5% Lithium phenyl-2,4,6-trimethylbenzoylphosphinate (LAP) was casted around the Squiggle channel in the cavity of the Silicone Insert and UV polymerized (λ=365nm) for 4 minutes. Once polymerization was complete, 1X PBS was added to the surface of the hydrogel, to maintain hydration, in the MPB system. Finally, the MPB Case Bottom, containing the polymerized GelMA construct with an embedded Squiggle channel, was secured with a MPB Case Cover and Clamp Assembly and prepped for clearing (**Fig. 5.1**). *(See **Appendices C and D** for more details)*

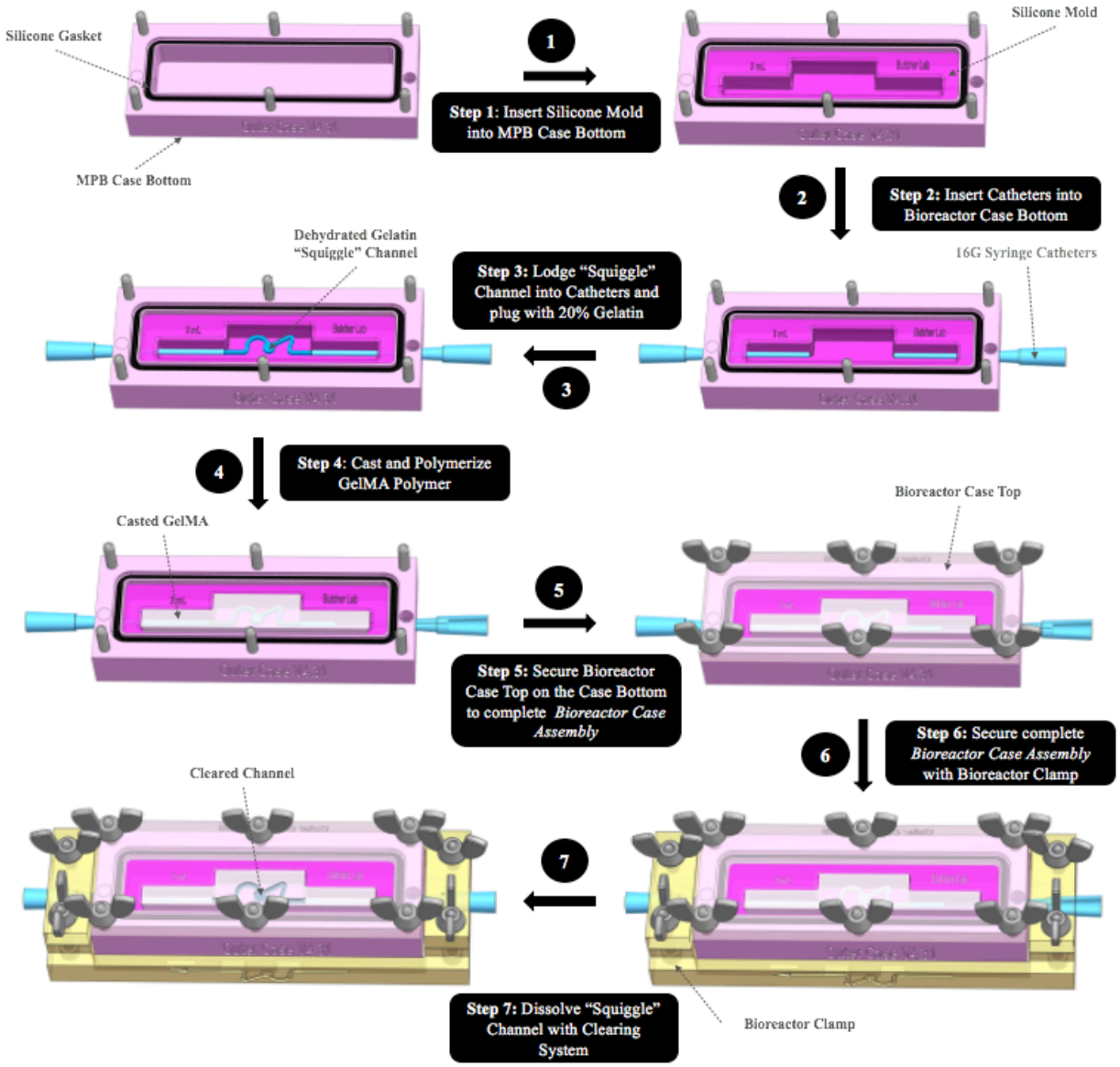

Figure 5.1 Schematic of Bioreactor Design and Assembly. A silicone mold and two catheters were inserted into the bioreactor case bottom. A dehydrated *Squiggle* channel made from 20% Gelatin was lodged into the catheters and secured with gelatin plugs on each side. GelMA hydrogel solution was then casted and polymerized around the channel in the open cavity of the silicone mold. The bioreactor case bottom was closed and secured with a bioreactor case top to form the complete bioreactor case assembly. The bioreactor case assembly was then secured with the bioreactor clamp and connected to a clearing system to dissolve the gelatin channel and establish a patent GelMA hydrogel construct.

The process of clearing was designed to carefully flush out the gelatin residue from Squiggle channels embedded in the GelMA matrix. In order to prepare the Clearing system, the inlet and outlet Clearing Reservoirs were filled with 50mL and 20mL of 1X PBS, respectively, and stored at 37°C until for at least 24 hours to eliminate the formation of microbubbles. The inlet and outlet of the MPB system was then connected to the inlet and outlet Clearing Reservoirs, respectively. Once the Clearing system was connected to the MPB device and fully assembled, it was stored at 37°C for an hour to allow the dehydrated gelatin Squiggle to dissolve and the inlet Clearing Reservoir to passively pass through the channel to the outlet Clearing Reservoir until the system equilibrated (**Fig. 5.2A-B**). After the channel cleared, the MPB system was ready for endothelization and perfusion (**Fig. 5.2C-D**). It should be noted that all engineered parts were designed using Siemens NX software and fabricated either through milling, 3D-printing, or casting and curing, as specified in **Table 5.1**. Additionally, the supplemental parts needed to carry out this procedure were purchased from various manufacturers, as specified in **Table 5.2**. *(See **Appendices C and D** for more details)*

Table 5.1 Engineered Parts for the Macro-Perfusion Bioreactors and Clearing Systems

Engineered Part	Material	Fabrication Method	Comments
Case Bottom	Polycarbonate	Milled	90x34x13mm (L x W x D)
Case Cover	Polycarbonate	Milled	90x34x5mm
Catheter Clamp Assembly	High-Temperature Resin v.2	Resin 3D-Printed	O: 116x42x19mm I: 90x34x13mm Includes: *Hex Aligner*, *Clamp Bottom*, and *Clamp Tops*
Silicone Insert	PDMS	Casted and Cured	O: 74.3x17.4x8mm I: Holds ~3mL of volume

Catheter Seal	PDMS	Casted and Cured	Used to secure catheters in MPB
Tube Holders	Polyethylene terephthalate glycol (PETG)	Extrusion 3D-Printed	PLA and other filament materials may be used to meet specific criteria
Dampener	Biomedical Resin v.1	Resin 3D-Printed	Biomed Clear and Amber resins were used
Reservoir Caps	Biomedical Resin v.1	Resin 3D-Printed	Biomed Clear and Amber resins were used, and *Reservoir Caps* were modeled based on the dimensions of Falcon™ 50mL conical caps
MPB Reservoir	Polypropylene	Falcon™ 50mL Conical Tubes	No adaptations were made
Clearing Reservoir	Polypropylene	Falcon™ 50mL Conical Tubes	Modified to include a conduit from the *Clearing Reservoir* to the MPB
Squiggle (-) Mold	PDMS	Casted and Cured	Prepared from *Squiggle (+) Mold*
PDMS Molds	High-Temperature Resin v.2	Resin 3D-Printed	Used to cast MPB *Silicone Inserts, Catheter Seals* and *Squiggle (+) Mold*

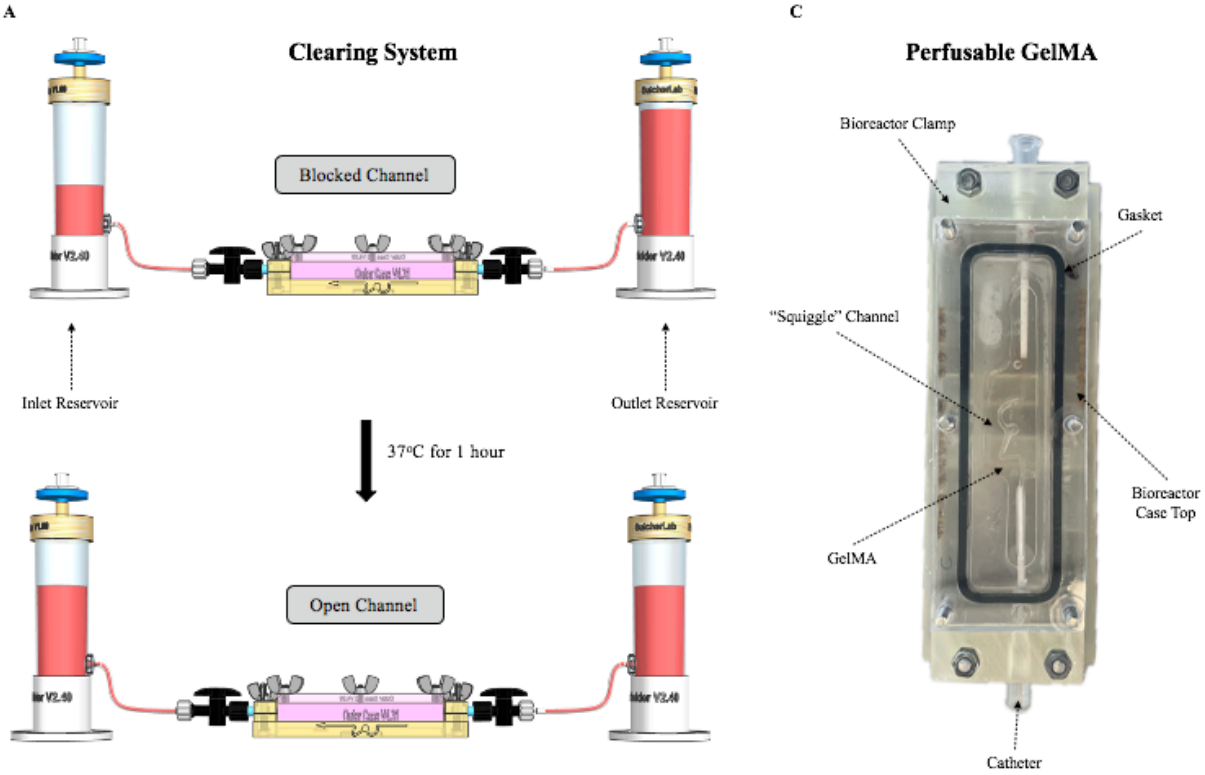

Figure 5.2 Design and Assembly of Bioreactor Clearing System. (A) Schematic of the bioreactor clearing system used to dissolve the gelatin channel embedded in GelMA. (B) Optical image of bioreactor clearing system connected to the complete bioreactor case assembly and clamp. (C) Optical image of perfusable GelMA containing high throughput *Squiggle* geometry within the complete bioreactor case assembly and clamp. (D) Optical image of patent GelMA perfused with Trypan blue to illustrate intact *Squiggle* geometry.

Table 5.2 Purchased Parts for the Macro-Perfusion Bioreactors and Clearing Systems

Purchased Part	Manufacturer	Reference No.
Wing Nuts	McMaster-Carr	94543A320_316
Hex Nuts	McMaster-Carr	90591A250
Socket Head Screws	McMaster-Carr	91274A-107
Rubber O-Ring Gasket (2mm x 59mm)	McMaster-Carr	9262K698
Masterflex® Precision Pump Tubing	Cole-Parmer Instrument Co.	06508-14
Masterflex® Tygon® Tubing (Size 14)	Cole-Parmer Instrument Co.	6409-14
Polycarbonate	McMaster-Carr	Discontinued
BioMed Amber, Clear, and High-Temperature Resin	Formlabs	Amber: RS-F2-BMAM-01 Clear: RS-F2-BMCL-01 High-Temp: RS-F2-HTAM-02
PETG Filament	Atomic Filament	230-245C
Masterflex® Luer Hose Barb to Luer Lock	Cole-Parmer Instrument Co.	MFLX30800-16
Masterflex® Female to Female Luer Lock Connector	Cole-Parmer Instrument Co.	MFLX45501-01
Masterflex® Female to Male Luer Lock Valves	Cole-Parmer Instrument Co.	MFLX31200-91
Masterflex® L/S Peristaltic Pump	Cole-Parmer Instrument Co.	Model: 7519-06
Masterflex® Luer Lock Plug	Cole-Parmer Instrument Co.	MFLX40319-00
VWR® 50mL Conical Tubes	Avantor	525-1075
SURFLO® Syringe Catheters (16Gx1¼'')	Terumo Corporation	SR-0X1632CA
Acrodisc® 32mm Syringe Filters (0.2µm)	Pall Corporation	4652

Endothelialization of the Squiggle Channel in the MPB System

In order to endothelialize a cleared Squiggle channel within our MPB system, a suspension of 8-10 million cells/mL was prepared with GFP-HUVEC and about 500µL of suspension was gently

injected from the inlet catheter through the Squiggle channel to the outlet catheter until flow was visible. After seeding the endothelium on one side, the MPB system was reconnected to the Clearing system, oriented right-side up, and stored at 37°C overnight to allow cells to adhere to the bottom of the Squiggle channel. The next day, another suspension of 8-10 million cells/mL was prepared with GFP-HUVEC and 500µL of volume was gently injected from the outlet catheter through the Squiggle channel to the inlet catheter until flow was visible. After the second round of seeding, the MPB system was reconnected to the Clearing system again, oriented upside down, and stored at 37°C overnight to allow cells to adhere to the top of the Squiggle channel. Once the endothelium was seeded on both sides of the channel, the endothelialized MPB system was ready for perfusion (**Fig. 5.3**).

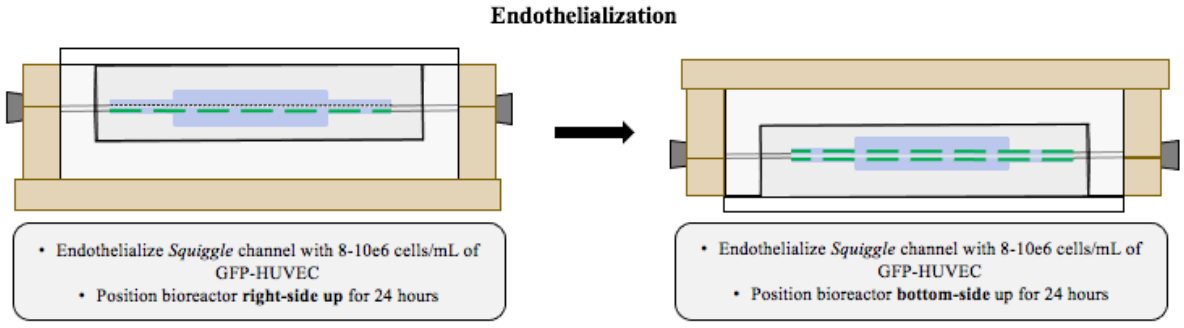

Figure 5.3 Endothelialization of Perfusable GelMA with *Squiggle* Channel Geometry. (A) Schematic of the workflow involved with lining a patent *Squiggle* channel with GFP-HUVEC over a 48-hr period. (B) Light sheet 3D image of the high throughput and patent *Squiggle* geometry embedded GelMA, lined with GFP-HUVEC, and perfused for 7 days.

MPB Perfusion

Our perfusion set up was designed as a single flow loop, which included a reservoir, dampener, MPB device, and peristaltic pump. In order to perfuse our MPB devices, media was pulled from

the reservoir and through a dampener prior to flowing through the inlet of our device. Once the flow reached the outlet of the MPB, it was returned back to the reservoir, creating a single flow loop (**Fig. 5.4**).

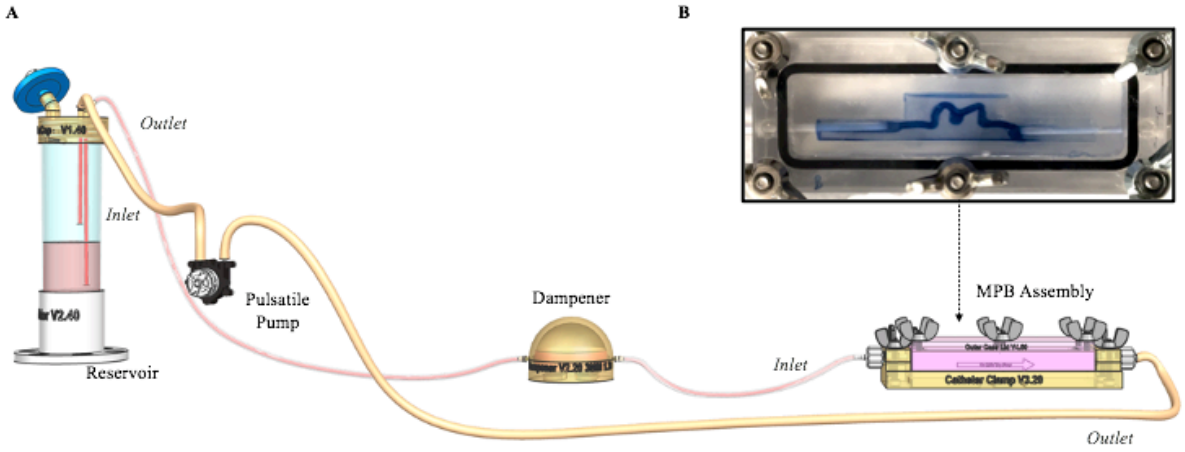

Figure 5.4 Bioreactor Perfusion System with Unidirectional and Pulsatile Flow. (A) Schematic of the bioreactor case assembly undergoing perfusion with a pulsatile pump. Media is pulled from the reservoir and through the dampener before flowing into the lumen within the bioreactor case assembly. Media is continuously pulled through the lumen and back into the reservoir, where it is recycled. (B) Optical image of the MPB assembly perfused with Trypan blue to highlight high throughput *Squiggle* channel geometry

In order to determine if our MPB systems could withstand long-term perfusion, each MPB device was assembled as described above, and immediately subjected to 24 hours of UNP flow at a rate of 2.5mL/min with a 0.1% Trypan blue solution. The diffusion of Trypan blue throughout the construct was only observed and not quantified for these studies. After verifying that long-term perfusion was achievable in acellular MPB devices, the effects of hemodynamic shear stress and vorticity on endothelium development was examined. For these studies, MPB devices were endothelialized and subjected to UNP flow at a rate of 2.5mL/ min for 7 days with vasculogenic

media as described in chapter 2. After perfusion, samples were fixed in 4% PFA overnight and prepped for imaging using light sheet fluorescence microscopy (LaVision BioTech, Bielefeld, Germany).

20kD FITC-Dextran Diffusion

In order to determine the effects of shear stress and vorticity on diffusion throughout the bulk, complete MPB devices, with either a cellular or acellular Squiggle lumen, were perfused with 20kD FITC-dextran (Sigma-Aldrich®, MO, USA) for 2 hours. In acellular studies, MPB devices were prepared and immediately subjected to 2.5mL/min of UNP flow with a 0.25% 20kD FITC-dextran solution. Alternatively, in cellular studies, MPB devices were endothelialized and subjected to 2.5mL/min of UNP flow with vasculogenic media for 48 hours, prior to performing diffusion analysis. Images of particle diffusion throughout GelMA were acquired using Image-Pro software. Additionally, particle displacement and concentration along the Squiggle channel were measured from the lumen into the bulk using FIJI and MATLAB software, respectively.

Statistics

Quantitative analyses were performed in quintuplicates for immunofluorescence, mechanical testing, and compaction, and triplicates for diffusion analysis. A one-way ANOVA was performed followed by a post-hoc Tukey HSD test and a two-tailed t-test with unequal variance to evaluate any significant difference between experimental groups. All quantitative data was reported as the mean ± standard deviation with a significant difference defined when $p<0.05$. The data are shown as * ($p<0.05$), # ($p<0.01$), **ζ** ($p<0.001$). The trendline and correlation coefficient (R^2) for each relationship was presented as either greater or less than moderately correlated ($R^2>0.5$).

RESULTS

Simulated Profiles of WSS and Vorticity Throughout "Squiggle" Channel Geometry

A simulation of the shear stress and vorticity profiles along our Squiggle channel geometry was generated using ANSYS software. In general, the shear stress and vorticity appeared to be homogenous along the length of the channel except at five distinct points defined as the inlet, elbow, plenum, arch, and outlet. On the interior side of the Squiggle channel, shear stress is the lowest at the plenum (0.7Pa), followed by the bends present at inlet and outlet (1.5Pa), which recapitulate a physiological environment. However, the shear stress at the interior elbow is the highest (7Pa), representing the most severe pathological flow, while the shear stress along the remainder of the channel is only slightly pathological (3-4Pa). Alternatively, on the exterior side of the Squiggle channel, the elbow and the arch exhibit similar shear stress values that exist within the physiological regime of hemodynamic flow (1-2Pa), whereas all other point along the channel are also comparable and slightly pathological (**Fig. 5.5A).**

In addition to examining shear stress, the vorticity profile along our Squiggle channel was also generated, which displayed distinct vorticities at the same regions of variable shear stress (**Fig. 5.5B**). With regard to the interior channel, vorticity was greatest at the elbow (850s-1) and the least at the plenum (2.8s-1). Additionally, the bends at the inlet and outlet also exhibited lower values in vorticity, while all other location points showed moderate vorticities (300-500s-1). Similarly, on the exterior side, the elbow and plenum also achieved low vorticity values (10-70s-1) as seen in the shear stress profile. Overall, these results show that variations in hemodynamic flow can be achieved at unique locations along the Squiggle channel, creating a high throughput design, and

that our geometry is suitable for investigating the effects of shear stress and vorticity on diffusion, lumen maturation, and angiogenesis.

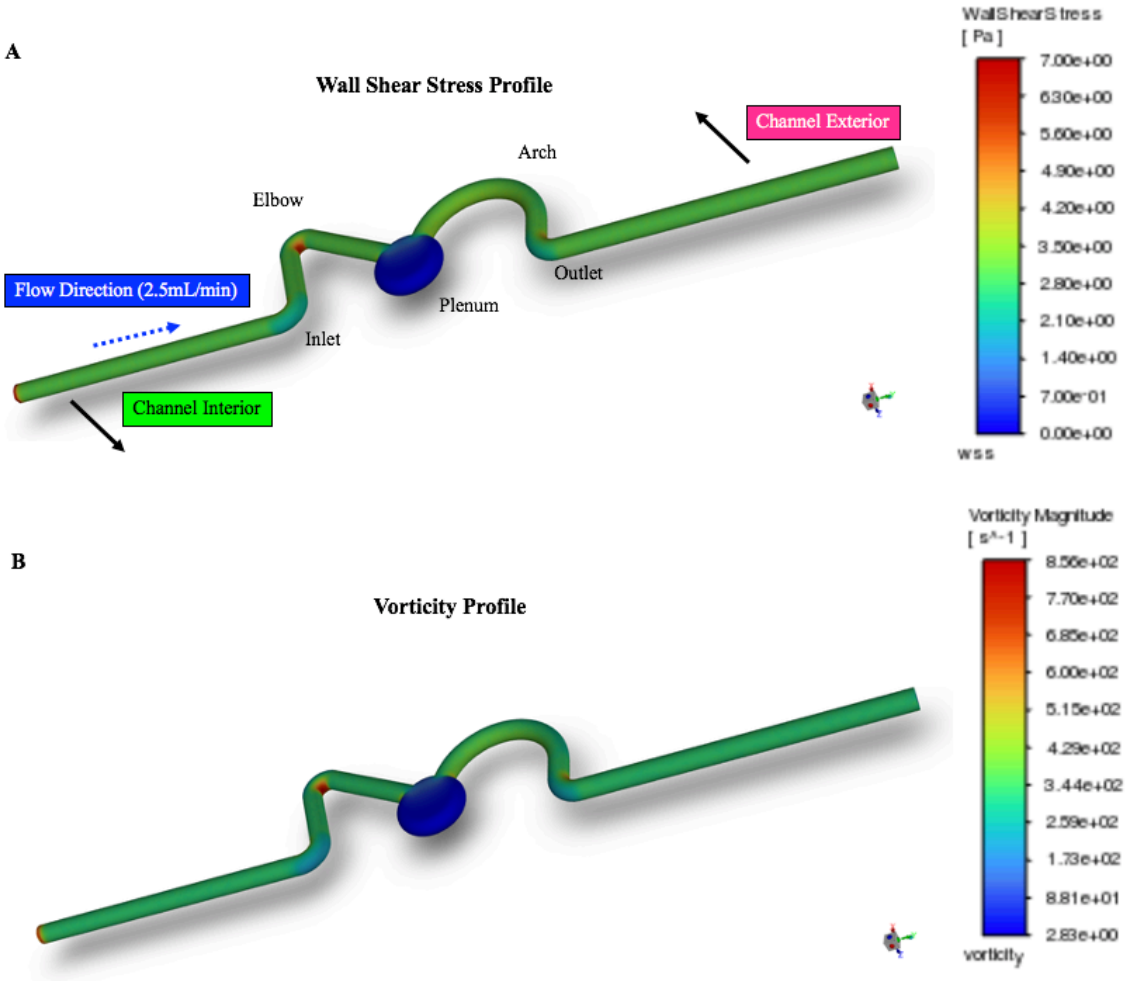

Figure 5.5 ANSYS Simulations of Wall Shear Stress and Vorticity Along the *Squiggle* Channel. Hemodynamic profiles of wall shear stress (A) and vorticity (B) along the high-throughput *Squiggle* channel geometry. Five regions of interest were defined as the inlet, elbow, plenum, arch, and outlet. A volumetric flow rate of 2.5mL/min was simulated in the direction from the inlet to the outlet (blue). The interior (green) and exterior (pink) sides of the channel were also identified in relation to the plenum.

GelMA60 Mechanics on Microvessel Formation

In order to fabricate our MPB devices with high throughput Squiggle geometry, the rate of GelMA polymerization and Squiggle hydration had to be optimized during hydrogel casting. In previous chapters, we used 0.1% IRD as our photo-crosslinker to create solid GelMA hydrogels approximately 100μL in volume. However, crosslinking larger volumes of 5%G40 and 5%G100 (3-3.5mL) with Irgacure could not be achieved within a reasonable timeframe. Extended exposure of our dehydrated Squiggle channels in aqueous GelMA caused them to rehydrate and dissolve prior to polymerization was complete (**Table 5.3**). Specifically, large volumes of 5%G40 could not be polymerized with IRG and resulted in a poorly crosslinked polymer with the texture and consistency of snot (**Fig. 5.6A**). Alternatively, 5%G100 could be polymerized with IRG but the material was too soft to support gentle perfusion (**Fig. 5.6B**). Although 10%G40 and 10%G100 could have been used to overcome these challenges, they were ruled out since these conditions either required excessive amounts of material or were not physiologically relevant to fat and vascular formation. Despite these findings, a new polymer, GelMA60, was successfully polymerized with 0.5% LAP instead of 0.1% IRG and used at a 6% (w/v) composition to construct a complete MPB device with Squiggle channel geometry (**Fig. 5.6C**). Polymerization of 6%GelMA60 with 0.5%LAP only took 4 minutes as opposed to 7-10 minutes and did not require excessive amounts of material (data not shown).

Table 5.3 GelMA Optimization for Macro-Perfusion Bioreactor

Fabrication Step	5%G40	5%G100	6%G60
Casting	Successful	Successful	Successful
Polymerization	Successful	Successful	Successful
Maintenance	Failed *(hydrogel became runny and snot-like)*	Successful	Successful
Clearing	-	Successful	Successful
Perfusion	-	Failed *(channel ruptured)*	Successful

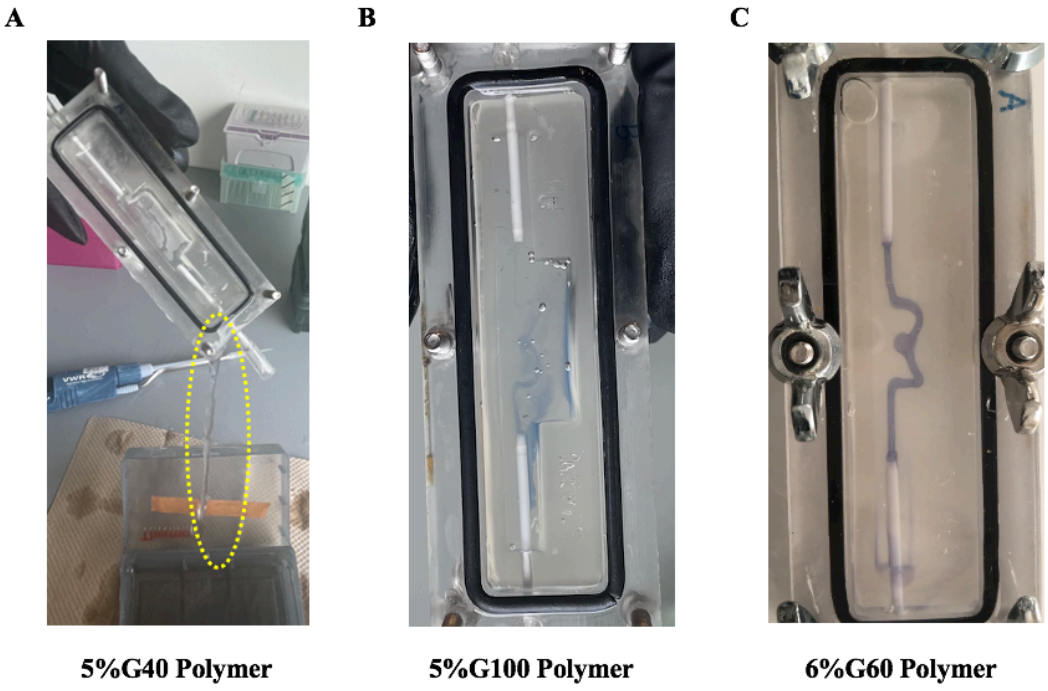

Figure 5.6. Optimization of GelMA for Macro-Perfusion Bioreactors with *Squiggle* Geometry. Optical images of 5%G40 (A), 5%G100 (B), and 6%G60 (C) used to develop the MPB system. GelMA materials were photo-polymerized and perfused to determine the optimal polymer composition and conditions for long-term perfusion studies. 5%G40 and 5%G100 experienced failure, while 6%G60 was successfully fabricated and perfused.

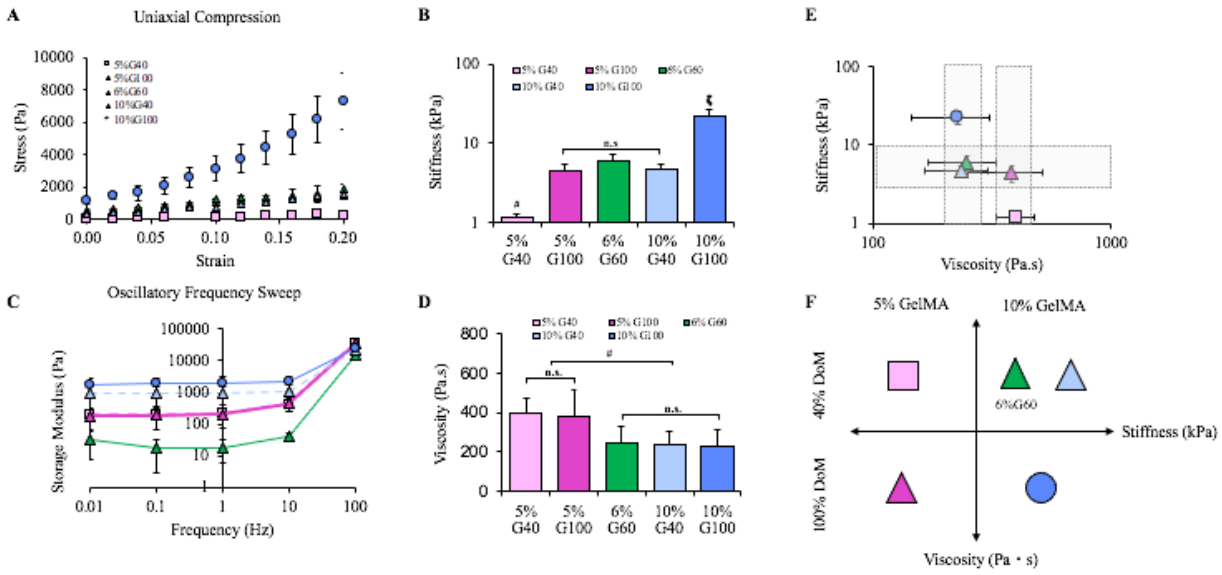

Figure 5.7 Mechanical Characterization of 6%G60. Stress-strain curves (A) and Young's moduli (B) for 5%G40, 5%G100, 6%G60, 10%G40, and 10%G100 hydrogels subjected to uniaxial compression. Frequency sweep curves (C) and viscosity (D) for 5%G40, 5%G100, 6%G60, 10%G40, and 10%G100 hydrogels subjected to an oscillatory linear frequency sweep. (E) Comparative analysis of the relationship between hydrogel stiffness and viscosity for each GelMA composition. (F) Schematic of segmented GelMA hydrogel conditions based on initial stiffness and viscous values. Data are presented as the mean ± SD, n = 4-7. *, $p < 0.05$; #, $p < 0.01$ and **ζ**, $p < 0.001$.

Since a new polymer was necessary for our MPB devices, we measured the native mechanics of 6%G60 against previously studied GelMA compositions. First, a uniaxial compression test was performed to quantify the stiffness of GelMA60. This work revealed that the stiffness of 6%G60 (6.02±1.4kPa) was intermediate to the two extreme regimes, 5%G40 and 10%G100, and comparable to the other moderately compliant matrices, 5%G100 and 10%G40 (**Fig 5.7A-B**). Next, 6%G60 was subjected to an oscillatory frequency sweep test to measure the native viscosity of this material. We found that 6%G60 exhibited a viscosity of 287.7±30.1 Pa·s, which was in alignment with the other low viscous conditions, 10%G40 and 10%G100 (**Fig. 5.7C-D**). These findings revealed that the matrix mechanics of 6%G60 perform similarly to that of 10%G40.

After characterizing the native mechanics of 6%G60, we investigated how its distinct matrix properties influenced microvessel formation. In general, 6%G60 invoked similar increases in microvessel density as 5%G100 and 10%G40 throughout the culture period (**Fig. 5.8A**). Further investigation displayed that 6%G60 elicited a microvessel phenotype that was more comparable to 5%G100 as opposed to 10%G40. 5%G100 and 6%G60 matrix conditions both supported sufficient microvessel density by D5, which eventually decreased by half on D10. Whereas microvessel density in 10%G40 consistently increased throughout the culture period (**Fig 5.8B**). Despite these outcomes, microvessel density per nuclei was similar across all conditions (**Fig. 5.8C**), while the expression of $\boldsymbol{\alpha}$SMA in 6%G60 was more analogous to 5%G100 rather than 10%G40 (**Fig. 5.8D**). When the number of microvascular junctions, branches, and thickness was quantified, 6%G60 produced vasculature with fewer junctions and branches in comparison to 5%G100 and 10%G40 (**Fig. 5.8E-**F) but a vessel thickness that was intermediate to 5%G100 and 10%G40 (**Fig. 5.8G**).

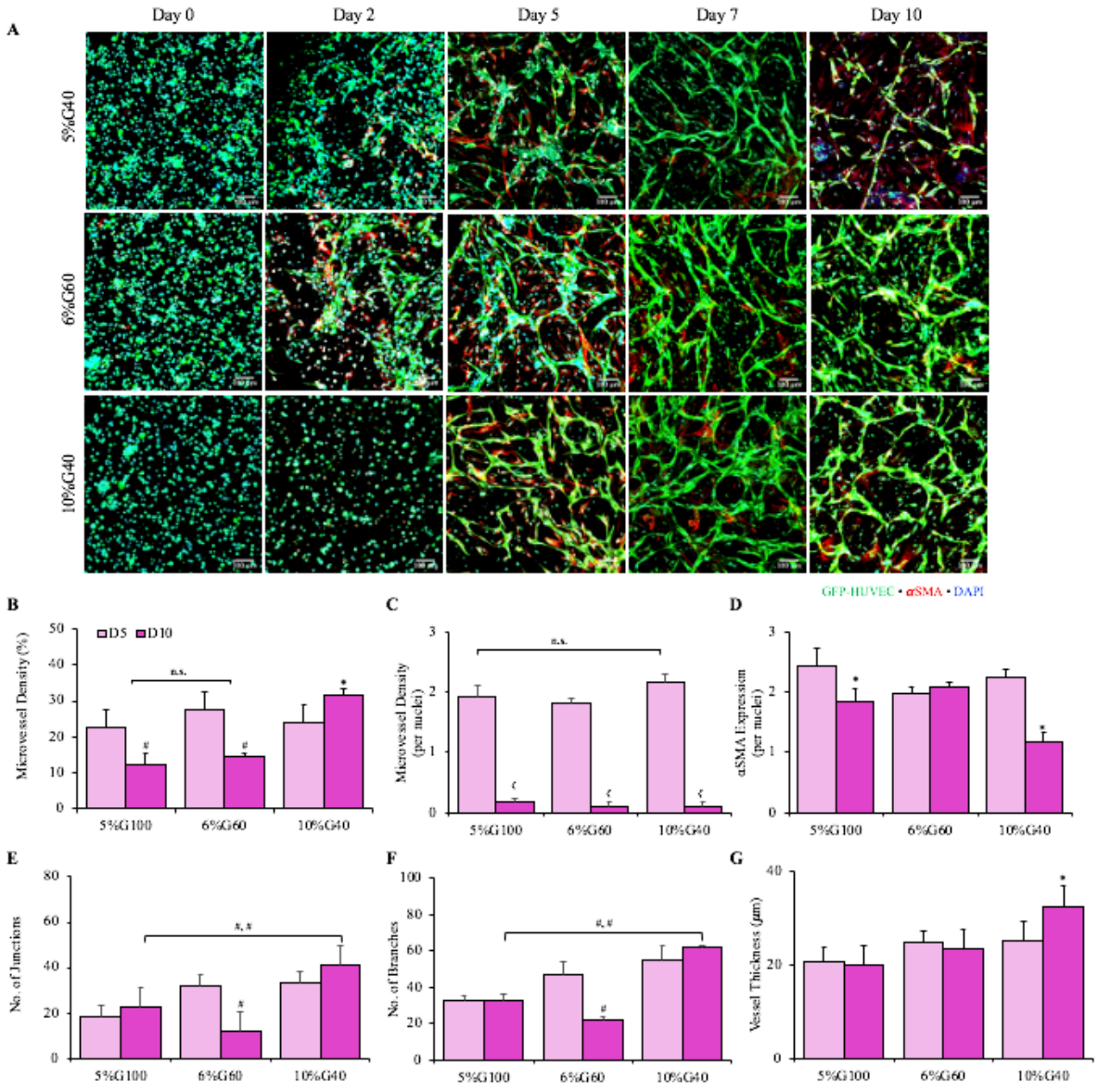

Figure 5.8 Microvessel Characterization of Co-laden 6%G60 During Vasculogenesis. (A) Confocal images of HUVEC and hAdMSCs co-encapsulated in 5%G100, 6%G60, and 10%G40 conditions after 0, 5, and 10 days of vasculogenic differentiation. HUVEC were pre-tagged with GFP, while ***α***SMA and nuclei were co-stained with anti-actin ***α***SMA-Cy3 (red) and DAPI (blue), respectively. Microvessel density was quantified (B) and normalized by cell count per field view (C) at D5 and D10. (D) The expression of ***α***SMA was also quantified and normalized by cell count per field view at D5 and D10. Microvessel junctions (E), branches (F), and thickness (G) were quantified at D5 and D10 of vasculogenesis. Data are presented as the mean ± SD, n = 5. *, $p < 0.05$; #, $p < 0.01$ and **ζ**, $p < 0.001$.

Lastly, in order to determine the relationship between the initial matrix properties of 6%G60 and microvessel formation, we conducted a comparative analysis between select microvascular phenotypic features and GelMA DoM, stiffness, and viscosity. In general, 6%G60 invoked an intermediate microvascular phenotype in comparison to other conditions as expected. Specifically, microvessel density, the number of junctions and branches looked to be DoM- and stiffness-dependent, decreasing with increasing DoM and stiffness (**Fig. 5.9A-C** and **Fig. 5.9 G-L**). Alternatively, $\boldsymbol{\alpha}$SMA expression was primarily dependent on stiffness (**Fig. 5.9D-F**), while microvessel thickness was dependent on DoM (**Fig. 5.9M-O**). Moderately compliant matrices (5%G100, 6%G60, 10%G40) all achieved comparable levels of $\boldsymbol{\alpha}$SMA expression and microvessel thickness appeared to decrease with increasing DoM. Although the initial matrix stiffness and DoM had the most influence on microvessel phenotype, matrix viscosity did not seem to have any influence on these phenomena. Notwithstanding, these results confirm that 6%G60 is a viable polymer composition to study fat and vascular formation within our MPB devices

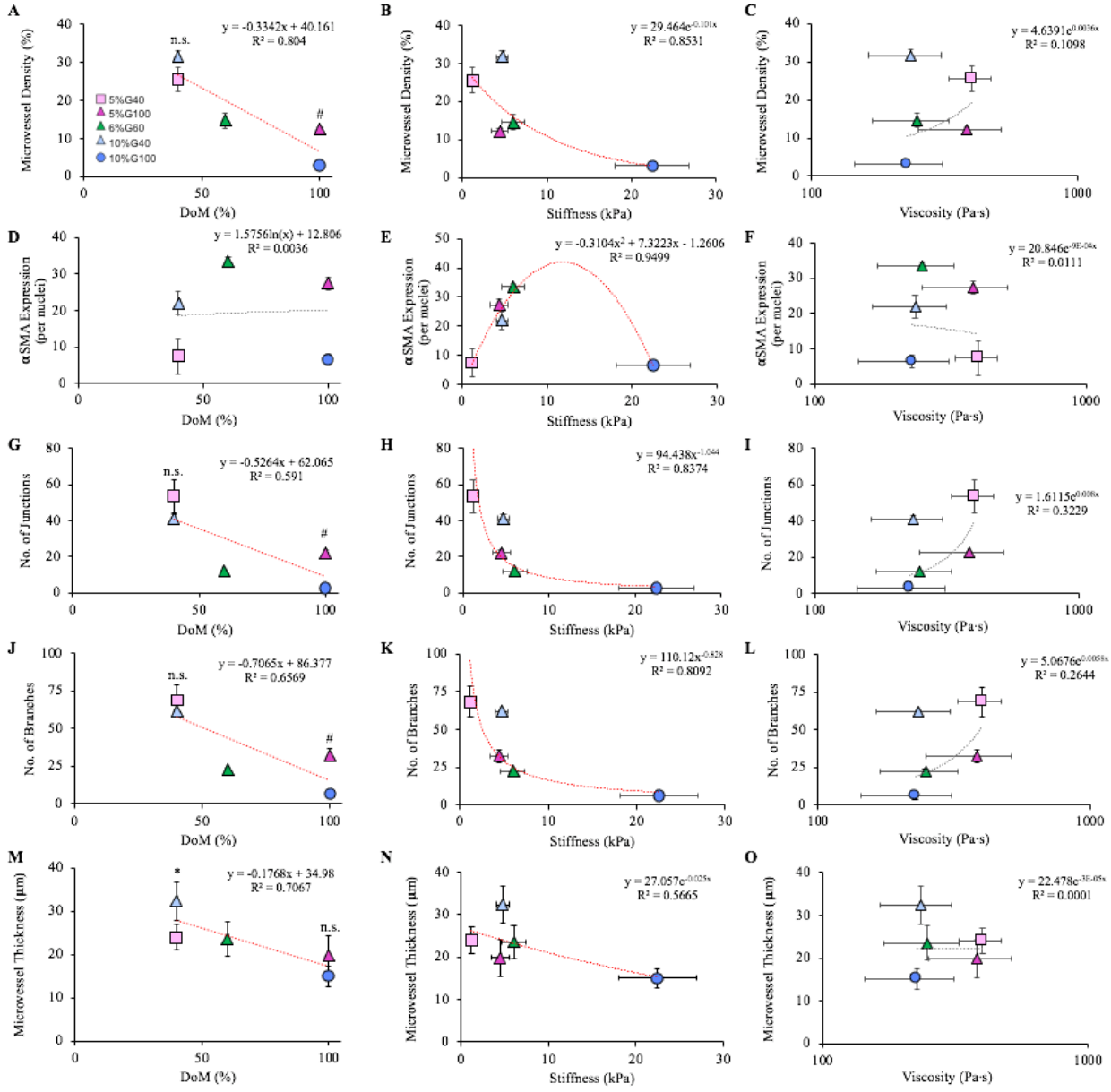

Figure 5.9 Influence of 6%G60 Properties on Microvessel Phenotype. Quantitative analysis of the relationship between DoM, stiffness, or viscosity and microvessel density (A-C), ***α***SMA expression (D-F), junctions (G-I), branches (J-L), and thickness (M-O), respectively. Data are presented as the mean ± SD, n = 5. *, $p < 0.05$; #, $p < 0.01$ and **ζ**, $p < 0.001$. The trendline and correlation coefficient for each relationship is indicated as either greater than (red; $R^2>0.5$) or less than (gray; $R^2<0.5$) moderately correlated.

Alterations in GelMA60 Mechanics During Vasculogenesis

In order to verify that the alterations in matrix mechanics of 6%G60 we comparable across all moderately compliant matrices, compression and stress relaxation tests were performed at D0, D5, and D10 of the culture period. In general, the size of the constructs did not change significantly overtime across all groups (**Fig 5.10A-B**). When a uniaxial compression test was performed, 6%G60 exhibited a comparable increase in stiffness (**Fig 5.10C**) as 5%G100 throughout the culture period. Similarly, stress relaxation tests performed at distinct time points of vasculogenesis revealed that the viscosities of 6%G60 and 5%G100 both increased in an equivalent manner (Fig 5.10D). When the final stiffness and viscosity of each matrix composition was compared against each other, it was found that stiffness generally decreased with increasing viscosity (**Fig 5.10E**). Additionally, when select features of microvessel phenotype were measured against matrix mechanics at D10, 6%G60 materials fell within the trend established by 5%G100 and 10%G40 conditions. Specifically, the number of microvessel junctions increased (**Fig 5.10F**) and **α**SMA expression decreased (**Fig 5.10G**) with increasing stiffness, while microvessel thickness decreased with increasing viscosity (**Fig 5.10H**) Overall, these findings reveal that the alterations in 6%G60 mechanics during vasculogenesis aligned with that of other moderately compliant matrices (5%G100 and 10%G40) and is a reasonable polymer composition to use for cellular studies in MPB devices. However, it should be noted that while the native mechanics of 6%G60 are analogous to 10%G40, the cellular behavior within 6%G60 during vasculogenesis is more comparable to that seen in 5%G100.

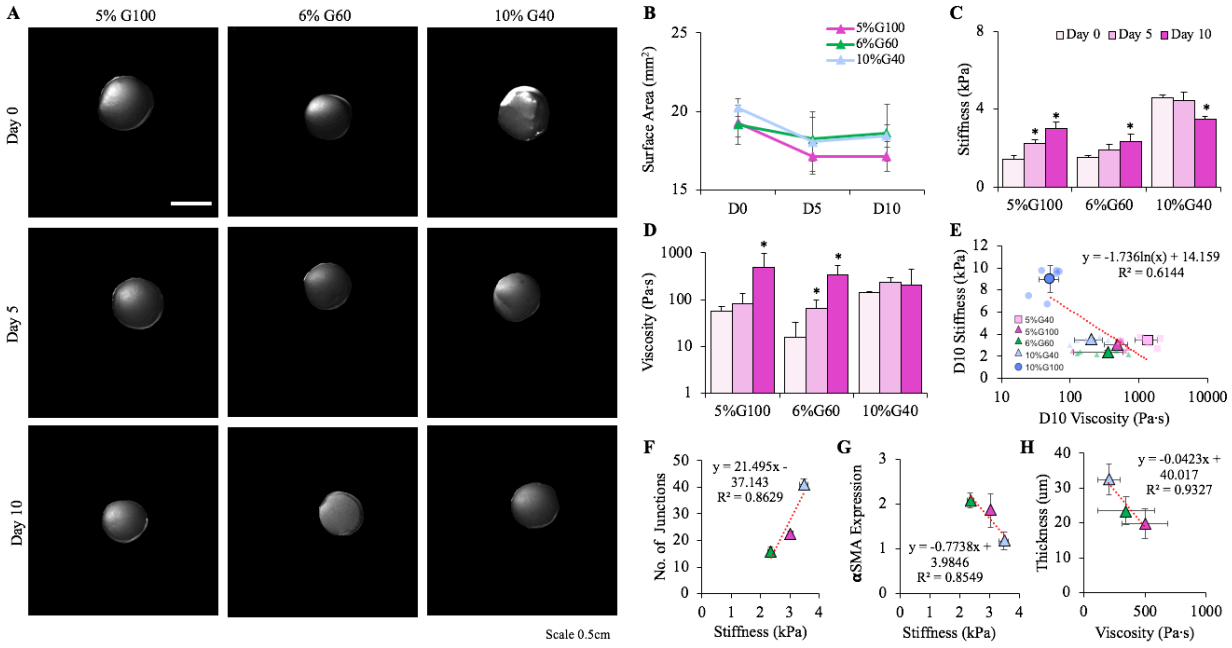

Figure 5.10 Alterations in 6%G60 Mechanics During Vasculogenesis. (A) Brightfield images of 5%G100, 6%G60, and 10%G40 hydrogel constructs at D0, D5, and D10. Changes in GelMA compaction (B), stiffness (C), and viscosity (D) were observed for each measurable condition at D0, D5, and D10. (E) Quantitative analysis of the relationship of hydrogel stiffness and viscosity at D10 of vasculogenesis. Quantitative analysis of the relationship between stiffness and microvessel junctions (E) and ***α***SMA expression at D10 of vasculogenesis (F). Quantitative analysis of the relationship of hydrogel viscosity and microvessel thickness at D10 of vasculogenesis. Data are presented as the mean ± SD, n = 6. *, $p < 0.05$; #, $p < 0.01$ and **ζ**, $p < 0.001$. The trendline and correlation coefficient for each relationship is indicated as either greater than (red; $R^2>0.5$) or less than (gray; $R^2<0.5$) moderately correlated.

Shear Stress and Vorticity on Particle Diffusion in Acellular MPBs

After confirming the mechanical properties and vasculogenic response of HUVEC-hAdMSC cocultures in 6%G60, this polymer composition was used in all future experiments with cellular and acellular MPB devices. We found that 6%G60 not only supported the effective clearing of our *Squiggle* channel consistently (**Fig. 5.11A**), but also facilitated particle diffusion from the channel to the bulk under UNP perfusion for 24 hours (**Fig. 5.11B**).

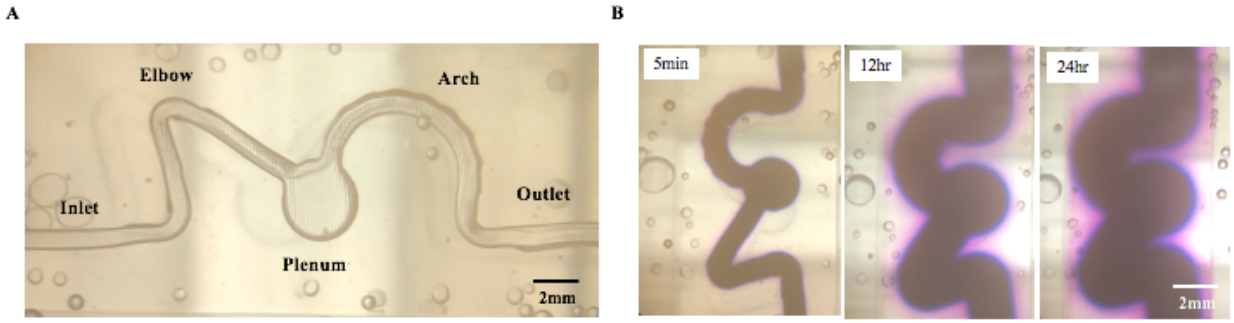

Figure 5.11 Bioreactor Perfusion System with Unidirectional and Pulsatile Flow. (A) Optical image of high throughput *Squiggle* channel geometry incorporated in GelMA. Key areas of interest include the inlet, outlet, plenum, elbow, and arch. (B) Optical images of patent GelMA, containing high throughput *Squiggle* channel geometry, subjected to 24 hours of pulsatile flow at 2.5mL/min.

In order to examine the influence of shear stress and vorticity on diffusion, 20kD FITC-dextran was perfused through an acellular *Squiggle* channel for 2 hours (**Fig. 5.12A-B**). First, we observed multiple vortices that developed in the plenum (**Fig. 5.12C**), which was confirmed by a simulation of flow lines generated at that region (**Fig. 5.12D**). The flow lines present at the edge of the plenum moved the slowest (2s) which predictively corresponded to the low shear stress seen at that region. Alternatively, flow moved much faster at the center of the plenum, spending less than 0.2s at any point within that region. Once the flow profile through the *Squiggle* channel was confirmed with simulations, we mapped particle displacement from the lumen into the bulk material at 15 minutes (**Fig. 5.12G**) and 120 minutes (**Fig. 5.12F**) of perfusion. These findings revealed that 10 distinct locations along the *Squiggle* channel exhibited stark differences in particle displacement, which increased over time. Specifically, after 15 minutes of perfusion, the interior side of the *Squiggle* channel presented more locations of high particle diffusion (E_3, P_1, P_2, A_3) in comparison to the

exterior side (A_1, A_2). However, after 120 minutes, additional regions on the exterior side (E_1, E_2, A_4) of the *Squiggle* channel developed and showed significant increases in particle displacement.

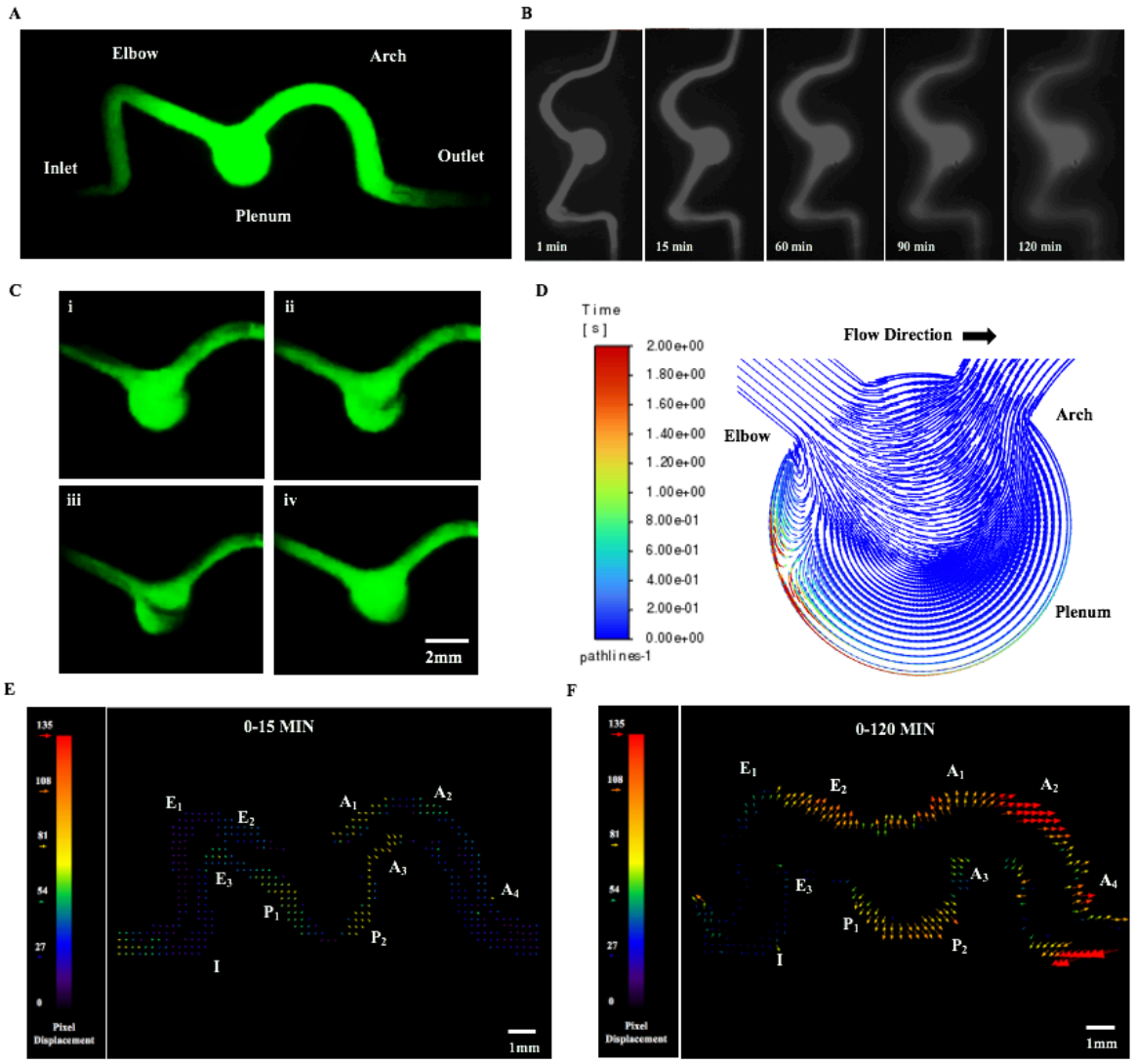

Figure 5.12 Flow and Diffusion Characterization Through Acellular *Squiggle* Channel Geometry. (A) Confocal image of an MPB device, acellular "Squiggle" lumen, perfused with FITC-dextran at 2.5mL/min of UNP flow for 1 minutes. (B) Representative time-lapse images of a MPB device under UNP perfusion at 1, 15, 60, 90, and 120 minutes. (C) Representative confocal images of flow traveling through the plenum display the 2 major vortices that form within the plenum. (D) ANSYS simulation of flow lines moving through the plenum of the Squiggle channel and the time it takes particles to travel along distinct regions of the plenum. Particles flowed quickly (red) along the edges of the plenum, while particles flowed slowly (blue) within the inner regions of the plenum. Displacement of particles from the lumen to the bulk along the dimensions of the "Squiggle" channel at 15 minutes (E) and 120 minutes (F). Regions of interest were identified by significant changes observed at 10 distinct locations of the "Squiggle" inlet (I), elbow (E1, E2, E3), plenum (P1, P2), and arch (A1, A2, A3, A4).

While many of the distinct regions along the *Squiggle* channel showed a general increase in particle diffusion over time, this phenomenon was not present at every location. Particularly, location E_3 displayed a decrease in particle displacement despite generating the greatest shear stress and vorticity. Whereas hemodynamic regions of intermediate shear stress and vorticity (E_2, A_2) exhibited the most significant increase in particle displacement, followed by sites of low shear stress and vorticity (E_1, P_1, P_2, A_1, A_4). Additionally, while the flow profile at the interior site A_3 also generated intermediate shear stress and vorticity, a slight decrease in particle displacement was observed at this location. Although this information provided us with some insight on the general trend of particle displacement from the channel into the bulk, further quantification of the diffusion profile and changes in concentration throughout the matrix is necessary.

A diffusion map of a perfused acellular *Squiggle* channel was generated to quantify the change in concentration presented at the channel boundary (**Fig. 5.13A**). In general, it appeared that particle diffusion from the channel to the bulk increased from the inlet to the outlet (**Fig 5.13B**). Hemodynamic sites at the inlet and elbow of the channel experienced far less diffusion that the regions towards the plenum and arch of the channel. While this was the trend, 2 distinct sites along the *Squiggle* channel experienced the most significant change in concentration. In the region of high shear stress and vorticity at the elbow (E_1), diffusion was perturbed. However, the middle of the channel arch (A_3), a region of intermediate shear stress and vorticity, facilitated more particle diffusion into the bulk. This data was further confirmed by the diffusion profiles generated at all distinct regions for t= 1, 15, 60, 90, and 120 minutes of perfusion. In comparison to the diffusion profiles at the inlet (**Fig. 5.13C**), the diffusion profile at E_1 (**Fig. 5.13D**) was much tighter overtime, demonstrating a low change in concentration. With regard to the middle of the channel, the

diffusion profiles between the elbow and the beginning of the arch (E_2, E_3, P_2, A_1, A_2) were comparable and slightly broader than at the inlet, with the exception of P_1 (**Fig. 5.13E-J**). The diffusion profile at the middle of the arch (A_3) was also broader over time, demonstrating a high change in concentration (**Fig. 5.13K**). However, this phenomenon was not exhibited at the end of the arch (A_4) (**Fig. 5.13L**). Although these findings ultimately showed that the change in concentration from the channel into the bulk was greater at the outlet, the calculated diffusion coefficient was contradictorily greater at the inlet ($D \approx 1.7E\text{-}09 \pm 1.5E\text{-}10$ m^2/s) in regions with low to moderate shear stress and vorticity, in comparison to the outlet ($D \approx 4.0E\text{-}10 \pm 2.1E\text{-}11$ m^2/s), in regions with moderate to high shear stress and vorticity (**Table 5.4, Appendix G**). Overall, these results suggest that hemodynamic regions of high shear stress and vorticity attenuate diffusion, while sites of low or intermediate shear stress and vorticity enhance diffusion. This information is vital for future cellular experiments, as it will provide us with insight on how nutrients will be distributed throughout the matrix, and how bulk cells may behave at distinct locations within the matrix.

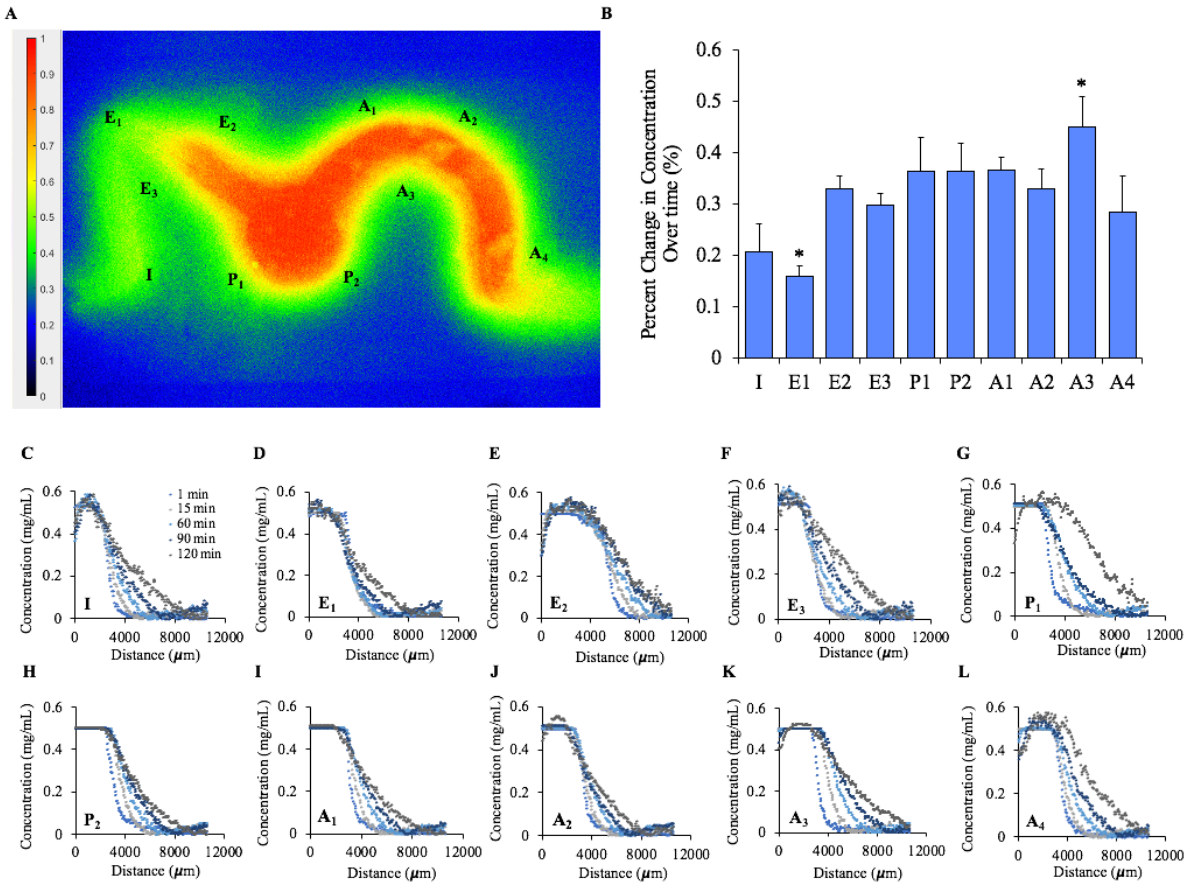

Figure 5.13 Diffusion Profile of 20kD FITC-Dextran Through an Acellular *Squiggle* Lumen. Diffusion map of FITC-dextran perfused through an acellular MPB device with "Squiggle" channel geometry (A) and the corresponding measurements (B) and profiles (C-L) of the changes in concentration exhibited at regions of interest along the length of the channel.

Table 5.4 Diffusion Coefficient of 20kD FITC-Dextran Through 6%G60 at Distinct *Squiggle* Regions

Location	Shear Stress	Vorticity	Diffusion Coefficient (m^2/s)
I	low	low	**1.9E-09 ± 1.3E-10**
E1	low	low	**1.7E-09 ± 1.5E-10**
E2	moderate	moderate	**1.5E-09 ± 9.2E-10**
E3	high	high	4.1E-10 ± 2.7E-11
P1	low	low	3.3E-10 ± 3.6E-11
P2	low	low	3.9E-10 ± 2.1E-11
A1	moderate	moderate	3.8E-10 ± 1.4E-11
A2	moderate	moderate	3.5E-10 ± 2.7E-11
A3	moderate	moderate	5.9E-10 ± 4.6E-11
A4	high	high	5.2E-10 ± 5.4E-11

Shear Stress and Vorticity on Particle Diffusion and Endothelium Development

In order to examine diffusion changes along the *Squiggle* channel in the presence of an endothelium, MPB devices were endothelialized with GFP-HUVEC, subjected to UNP flow at 2.5mL/min for 48 hours, and perfused with FITC-dextran for 15 minutes (**Fig. 5.14A**). Brightfield images along the cell laden *Squiggle* channel revealed that EC adhesion was more visible and prevalent at distinct hemodynamic regimes of the inlet, elbow, plenum, and arch. Specifically, regions of low shear stress and vorticity were the least dense (**Fig. 5.14B**), followed by regions of intermediate shear stress and vorticity (**Fig. 5.14D-E)**. Alternatively, hemodynamic regions of high shear and vorticity did not appear to retain any cell density after 2 days of perfusion. It should be noted that EC retention at the inlet seems to be greater than that at the outlet. However, these phenomena may only be present due to poor seeding.

After 2 days of UNP perfusion, the diffusion of 20kD FITC-dextran from the endothelium into the bulk was observed. A particle displacement field after 15 minutes of UNP diffusion was generated and revealed that *Squiggle* regions with high cell density attenuated particle displacement in comparison to seemingly acellular regions. This was further confirmed by generating a diffusion map to measure the change in concentration presented at the cellularized channel border (**Fig. 5.14G**). Regions along the *Squiggle* channel where cell density is high, particle intensity is the greatest (i, ii, iii, iv), resulting in less diffusion throughout matrix. Alternatively, in regions where cell density is the low or absent, particle intensity is attenuated, contributing to more diffusion into the bulk. When the change in concentration was measured at these 4 local regions, cellularized *Squiggle* channels diminished particle diffusion in comparison to acellular *Squiggle* channels (**Fig. 5.14H**). These results indicate that the presence of an endothelium will perturb particle diffusion

into the matrix and this feature must be optimized to ensure that bulk cells are not cut off from their supply of nutrients distributed by the flow through the *Squiggle* channel.

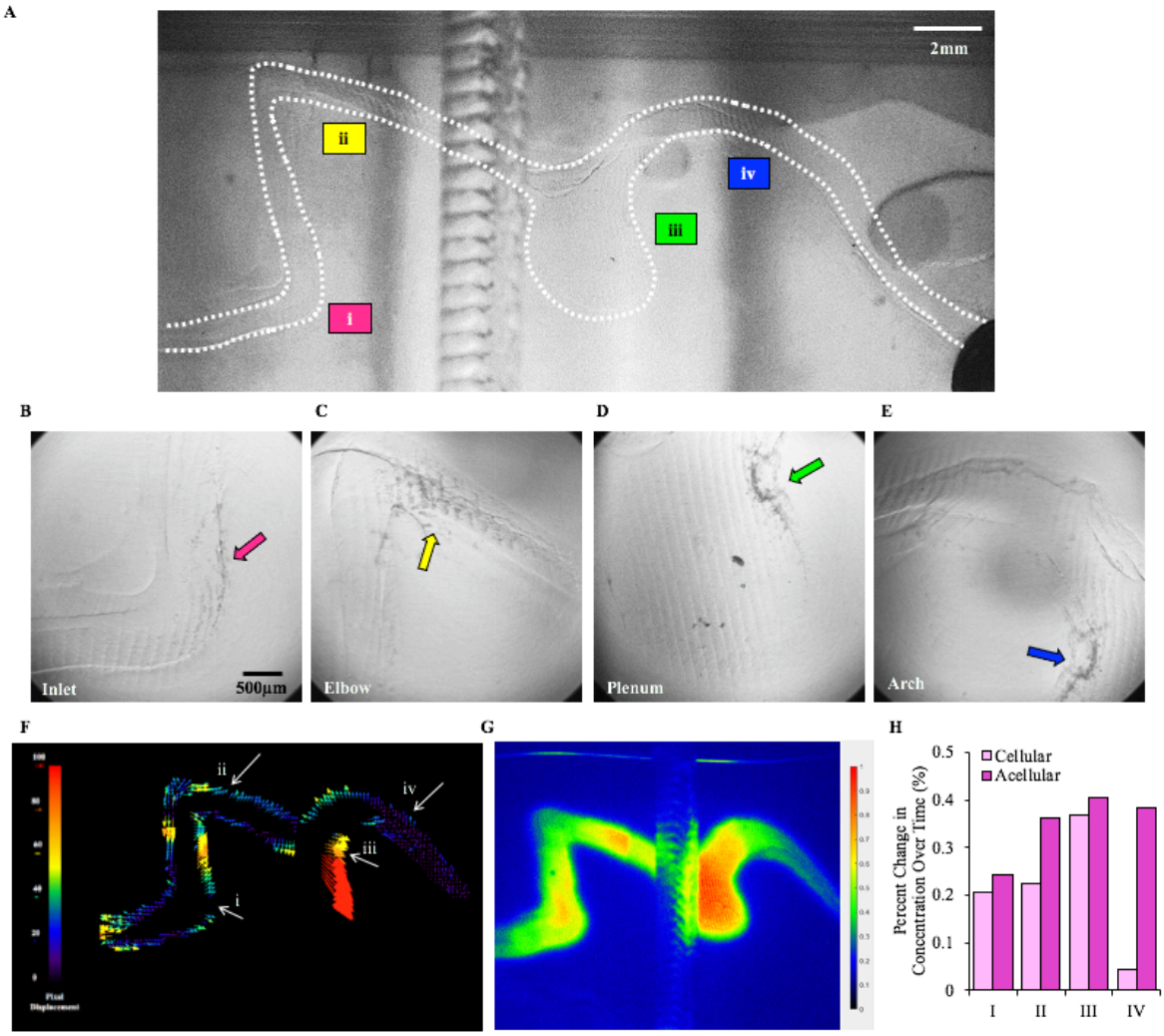

Figure 5.14 Diffusion Profile of 20kD FITC-Dextran through a Cellular *Squiggle* Lumen. Brightfield images of a cellularized *Squiggle* channel (A) and high cell density at distinct locations of the inlet (B), arch (C), plenum (D), and arch (E). (F) Displacement of particles from the lumen to the bulk along the dimensions of the "Squiggle" channel at 15 minutes. Diffusion map of FITC-dextran perfused through a cellularized MPB device with *Squiggle* channel geometry (G) and the corresponding measurements (H) of the changes in concentration exhibited at regions of interest along the length of the channel.

Lastly, cell laden MPB devices were perfused with UNP flow at 2.5mL/min for 7 days to assess endothelium maturation. These studies revealed that select regions of the *Squiggle* channel are more capable of retaining EC density than other regions over an extended period of time. Specifically, the hemodynamic flow profile presented at the inlet and elbow are more supportive of endothelium maintenance than at the plenum, arch, or outlet (**Fig. 5.15**). Locations of high shear stress and vorticity at the elbow and inlet (angled regions, red) appear to have the greatest density of endothelium retained in comparison to the location of moderate shear stress and vorticity (straight regions, blue). Despite these contradictory findings, additional cell laden MPB devices must be fabricated and subjected to UNP flow for 7 days in order to achieve statistical significance and validate the aforementioned claims. Analysis of the endothelium must also be captured at earlier timepoints to track the change in endothelium maturation over time, as opposed to simply documenting the endothelium present at the end. Additionally, optimization studies must be conducted to improve the overall yield of functional MPB devices and adequately study the effects of hemodynamic shear stress and vorticity on lumen maturation and angiogenesis. Overall, the presented work and findings of this study bring us significantly closer to establishing a MPB device capable of supporting the vascularization of bioengineered tissues.

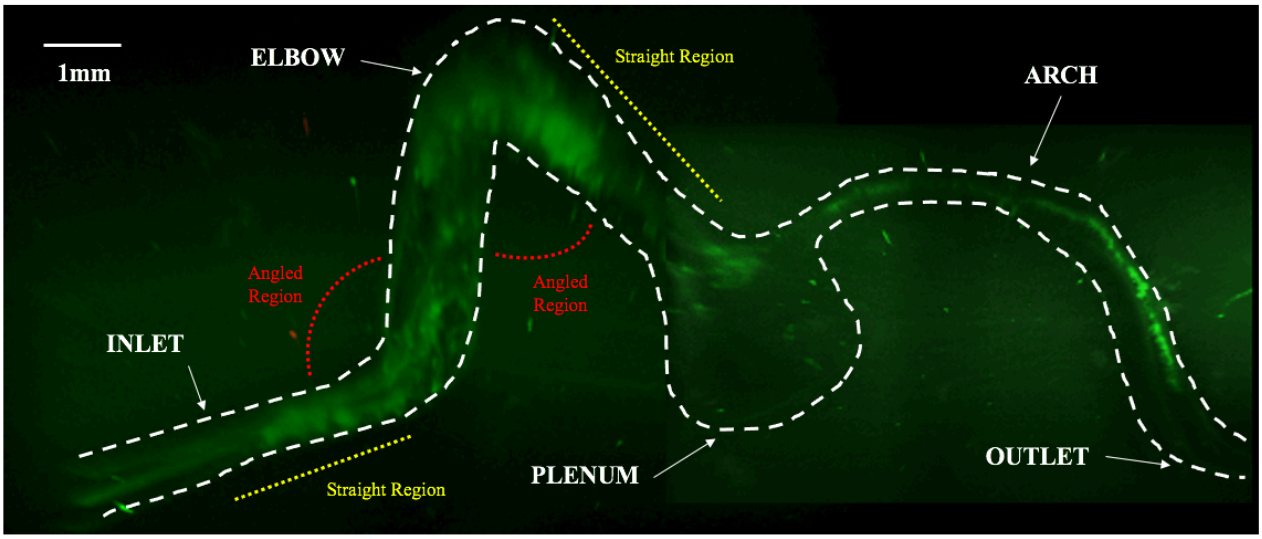

Figure 5.15 Endothelium Development Along *Squiggle* Channel After UNP Perfusion. Light sheet 3D image of the high throughput and patent Squiggle channel geometry embedded in GelMA, lined with GFP-HUVEC, and perfused for 7 days. The inlet, elbow, plenum, arch, and outlet were identified in white. The straight and angled regions along the channel were identified in yellow and red, respectively.

DISCUSSION AND FUTURE WORK

The objective of this work was to engineer a macro-perfusion bioreactor device capable of supporting patent, high-throughput channel geometry and the vascularization of bioengineered tissues. High throughput channel geometry, also known as the *Squiggle*, was successfully created to generate multiple shear stress and vorticity profiles along a singular lumen. In general, we found that the angled regions of the channel, situated at the elbow interior, inlet exterior, and outlet exterior, generated high shear stress and vorticity (7Pa and $850s^{-1}$), while curved features positioned at the arch, plenum, inlet interior, and outlet interior produced low shear stress and vorticity (0.7-2Pa and $2.8s^{-1}$). We also discovered that all other sites along the *Squiggle* channel, that were not mentioned, invoked a similar hemodynamic profile of intermediate shear stress and vorticity (3-4Pa and $300\text{-}500s^{-1}$). Altogether, ANSYS simulations revealed only 3 distinct regions

of varying shear stress and vorticity throughout the entire *Squiggle* channel with a flow rate of 2.5mL/min. Despite these findings, additional variations of these parameters can be included by redesigning the geometry of the *Squiggle* channel or introducing new features. For instance, decreasing the diameter of the plenum or radius of curvature in the arch, can establish a region of intermediate shear stress and higher vorticity or turbulence. (336) Additionally, increasing the lumen diameter along one region of the *Squiggle* channel can create low shear stress but enhance vorticity or turbulence at that location. (337) Ultimately, in order to establish a channel with produced more hemodynamic regions, alterations to the current lumen geometry must be considered.

Next, we aimed to develop a macro-perfusion bioreactor that can support the fabrication of voluminous GelMA with patent *Squiggle* channel geometry. One of the major limitations we faced in designing this system was optimizing the rate of *Squiggle* rehydration with GelMA polymerization. In brief, our complete MPB devices were fabricated by casting a GelMA solution around a suspended solid *Squiggle* channel made from dehydrated gelatin. In our previous work, 5% GelMA polymers crosslinked with 0.05% IRG for 7 minutes was sufficient for making hydrogels that were only 100uL in volume. However, larger GelMA constructs (3mL) made with this same IRG concentration required longer UV polymerization time, which interfered with retaining the shape of the *Squiggle* during channel rehydration. Although increasing the concentration of IRG could improve crosslinking time, this solution was ruled out as IRG has been found to be cytotoxic to cells. (338,339) Another possible solution explored for addressing this problem was to increase the weight composition of GelMA from 5%(w/v) to 10%(w/v). However, our previous work reports that 10%G100 was not ideal for invoking fat and vascular formation.

Additionally, the of 10%G40 in our MPB device would require extensive rounds of manufacturing and characterizing excessive amounts of G40 polymer. Therefore, in order to avoid these problems, a new polymer, G60, was fabricated and IRG was switched with LAP, an effective and non-cytotoxic crosslinker, for studies in our MPB devices. With these modifications, we were able to cast and polymerize 6%G6and 0 around a dehydrated *Squiggle* channel with 0.5% LAP in 4 minutes. These iterations were proven to be necessary for fabricating sizable GelMA hydrogels with perfusable *Squiggle* channel geometry.

Since our MPB device required a new polymer that had not been previously tested in vascular studies, we performed mechanical testing to quantify the native stiffness and viscosity of the material and induced vasculogenesis to elucidate how its matrix properties impact microvessel phenotype. We found that 6%G60 invoked similar microvessel structures as 5%G100 despite having comparable mechanics as 10%G40. Additionally, our work revealed that 5% and 10% G40 polymer compositions produced superior microvessel density in comparison to their G100 counterparts. Altogether, these results suggested that crosslinking density is also an important matrix feature that regulates endothelial behavior and organization. Specifically, our findings demonstrate that microvessel formation is more robust in matrices with low DoM and high RGD-binding potential, and slowly declines with increasing DoM and decreasing RGD-binding sites, regardless of matrix stiffness. Previous work has not only shown that the presence of RGD in polyethylene glycol (PEG) hydrogels significantly improves EC biocompatibility, but also confirmed that moderately high concentrations of RGD in PEG enhance endothelial tube formation in comparison to matrices with either low or extremely high concentrations of RGD. (340,341) While these studies do not report on the mechanics of their matrix, many studies have shown that

the presence of RGD in hydrogels does not significantly impact its mechanical properties. (342) Overall, these findings infer that matrix crosslinking density and RGD binding capacity influence cell behavior and function independent of its mechanics.

After validating the mechanical and pro-angiogenic properties of our new polymer composition, we characterized the diffusion profile at distinct hemodynamic regions along the *Squiggle* in our MPB device fabricated with 6%G60. We found that diffusion was attenuated at the inlet and elbow of the channel but enhanced at plenum and arch. While this phenomenon may be due to the distinct hemodynamic regions at the beginning of the *Squiggle* channel, the opposite result of decreased diffusion at the outlet rather than the inlet was actually expected. A possible explanation for this finding is that the increase in channel diameter experienced at the plenum forces fluid to remain in that region for a longer time period. Another potential explanation for this confounding result is that the UNP flow generated in the closed flow loop is being pulled from the outlet as opposed to pushed from the inlet. This feature may cause fluid to spend less time at the inlet than the outlet between each pulse. Ultimately, additional flow studies that introduce UNP flow from the inlet to the outlet are required to adequately elucidate this phenomenon.

In addition to mapping diffusion along the *Squiggle* channel, the change in concentration across the lumen into the bulk material was quantified. Our work revealed that only 2 distinct regions along the channel produced significantly different concentration changes. The hemodynamic profile at the elbow interior (E_1) facilitated the least diffusion, while the arch interior (A_3) invoked the greatest diffusion. All other regions between those two points (E_2, P_1, P_2, A_1, A_2) exhibited moderate changes in concentration except for at the plenum (P_1), where a broad range in diffusion

profiles was observed over 2 hours, indicating robust diffusion. However, only a moderate change in concentration was calculated at this region. In fact, the difference in diffusion profiles at t=1 and 120 minutes for P_1 was more in alignment with A_3 rather than the other middle range points. This inconsistency in data could be attributed to the limited sample size that was acquired from these experiments (n=3). We anticipated that the diffusion at P_1 would be high due to the hemodynamic profile at that region. Our ANSYS simulations revealed that three vortices actually form in the plenum, one of which is a small vortex that develops at the intersection between the elbow and plenum (or P_1). Not to mention, the small vortex that develops in the plenum spends more time circulating at that point and could therefore contribute more to diffusion. Previous work has shown that diminished flow at specific regions of capillary beds increased particle exposure time at the membrane and subsequently enhanced diffusion. (343) However, in order for us to properly ascertain this phenomenon additional sample must be prepared and analyzed for statistical significance.

Once we mapped diffusion through an acellular *Squiggle* channel, we performed the same analysis across a cellularized lumen. We found that cell density was only retained in regions of either low or intermediate shear stress and vorticity along the *Squiggle* channel after being subjected to a UNP flow rate of 2.5mL/min for 2 days. When a particle displacement field and a diffusion map were generated after 15 minutes of perfusion, diffusion was attenuated at the sites of high cell density and unperturbed at locations with low or no apparent cell density. Despite these findings, longer perfusion studies performed on MPB devices with a *Squiggle* endothelium revealed slightly confounding results. After 7 days of UNP flow, cell density was the greatest at the inlet, elbow, and arch exterior. More specifically, a sufficient endothelium was not only retained in regions of

low and intermediate shear stress and vorticity, but also at locations of high shear stress and vorticity (inlet interior, elbow exterior). This conundrum is likely due to improper seeding along the channel and low sample size. Therefore, optimization studies to improve EC seeding is required to clarify the impact of shear stress and vorticity on endothelium maturation and subsequently angiogenesis. A potential solution for address this would be to enhance cell adhesion along the *Squiggle* channel by pre-coating the lumen with a collagen solution. While much work has been done to demonstrate GelMA's biocompatibility for 3D cell culture systems, previous studies have shown that gelatin is far inferior in supporting EC adhesion and proliferation in 2D in comparison to collagen and other naturally derived ECM proteins. (344,345) It should also be noted that a low sample size was acquired from these studies. Thus, more experiments and samples must be performed and collected, respectively, to resolve these perplexing results.

Altogether, these studies confirm the possibility of engineering a model platform that is not only capable of examining the variable effects of hemodynamic forces on EC behavior, but also suitable for invoking hierarchical vasculature within voluminous bioengineered fat, muscle, skin, and bone. Despite these findings, additional studies are required to optimize the efficacy of our macro-perfusion bioreactor system. Future work would range from addressing optimization problems related to channel seeding and sample size to characterizing EC behavior along the channel and engineering soft tissues in the matrix. With regard to the latter, future studies would need to include EC phenotype characterization, specifically eNOS and VCAM-1 expression, at distinct hemodynamic regions of the *Squiggle* channel. For instance, eNOS is an anti-thrombotic and anti-atherosclerotic enzyme that is primarily expressed by ECs when subjected to laminar shear stress. (346,347) Therefore, hemodynamic regions with shear stress that deviate from physiological

conditions should demonstrate perturbations in endothelial eNOS expression. Similarly, vascular cell adhesion molecule-1 (VCAM-1) expression is also influenced by flow and increases with low but physiological shear stress. (348) Future studies could also investigate effect of hemodynamic shear stress and vorticity on lumen maturation over time. In our work, we only acquired data at the end of each experiment and could not document the EC behavior throughout the duration of perfusion studies. This was primarily due to the high failure rates that occurred at varying stages of the biofabrication process. Although this was the case, further optimization of our MPB device should improve efficacy. Lastly, once our MPB device is fully optimized and characterized, future work could include changing variable parts of the system to test alternative channel designs and engineer different tissue types. For example, our MPB can support varying channel shapes that produce hemodynamic profiles outside of those generated by our *Squiggle* design. We can also use different types of GelMA or other polymers as the bulk material in our system to achieve explicit matrix mechanics for distinct soft tissues, such as skin, fat, muscle, and bone.

OVERARCHING CONCLUSION

Tissue engineering strategies are increasingly becoming considered as an alternative to current reconstructive procedures for chronic wound therapy and soft tissue rejuvenation. Specifically, engineering adipose tissue is of great importance because it is one of the major tissue types required for reconstructive surgery. However, in order to fabricate healthy adipose tissue, a thorough understanding of the factors that drive tissue formation, maturation, and survival is necessary. In particular, tissue mechanics, such as stiffness and viscosity, play a significant role in governing cell behavior, differentiation, and function. While much work has been done to elucidate the role of matrix stiffness on adipogenesis, fewer studies have investigated matrix viscosity as a key player in tissue formation. Additionally, in order to develop large heterogenous tissues that can survive in vitro and be anastomosed in vivo, engineered tissues must be equipped with its own hierarchical vascular supply of macrovessels that branch into smaller microvessels and eventually capillary networks, a feat that cannot be achieved in the absence of hemodynamic flow. Therefore, the goal of this thesis was not only to develop a material with tunable stiffness and viscosity for fat and vascular formation, but also to engineer a macro-perfusion bioreactor that can invoke angiogenic sprouting in response to hemodynamic flow along high-throughput channel geometry.

The goal of this thesis was divided into three addressable aims. First, we aimed to establish a mechanically tunable material, with distinct stiffness and viscosity values, that could be used to study the effects of matrix mechanics on cell behavior during adipogenesis and vasculogenesis. We found that GelMA was a suitable material to achieve this because it bears lysine residues that can be methacrylated at varying efficiencies, which alter its native mechanical properties. When GelMA was synthesized with distinct degrees of methacrylation, it was found that matrix stiffness

was dependent on its DoM and weight composition, while viscosity was only dependent on the latter. Specifically, this was only accomplished by fabricating GelMA with low DoM, which allowed us to examine MSC and HUVEC behavior in a testable matrix that is physiologically relevant to the mechanics of native fat and vascular tissues.

Next, we set out to examine the influence of matrix stiffness and viscosity on fat and vascular phenotypes. Overall, it was determined that matrix stiffness and viscosity mediated unique features of adipogenesis and vasculogenesis and have the potential to either push fat down different lineage pathways (thermogenic vs. metabolic) or mediate distinct vascular phenotypes, respectively. Particularly in fat studies, we found that soft matrices with high viscosity enhanced overall adipogenic phenotype in terms of producing more lipids that were larger in size. While this phenotype was demonstrated under select conditions, it is important to recognize that there are multiple fat types with distinct structural and functional characteristics that are different from metabolic fat. Further analysis revealed that lipid phenotype was inversely related to mitochondrial abundance (a feature of thermogenic fat), which enhanced with decreasing viscosity and stiffness. Thus, our findings ultimately revealed that softer matrices supported an adipogenic phenotype that was more metabolic, with larger lipids and low mitochondria density, while stiffer matrices supported a thermogenic phenotype, with smaller lipids and high mitochondria density. In regard to our vascular studies, it was revealed that microvessel phenotype is not only dependent on matrix stiffness and viscosity, but also on crosslinking density. Compliant matrices with low viscosity and DoM supported the most robust vascular phenotype in terms of high microvessel density, structure, and low αSMA expression. Specifically, microvessel density and thickness were inversely related to αSMA expression and primarily regulated by stiffness with a DoM-dependent

feature, while microvessel structure, defined by junctions and branches, were dependent on matrix viscosity. These findings ultimately allowed us to pinpoint an optimal GelMA composition capable of fabricating fat and vascular tissues within a macro-perfusion bioreactor.

Lastly, our work aimed to engineer a macro-perfusion bioreactor capable of supporting unidirectional and pulsatile flow through high throughput channel geometry to elucidate the role of hemodynamic shear stress and vorticity on lumen maturation and angiogenesis. We ultimately found that our unique Squiggle geometry was able to elicit variations in shear stress and vorticity at distinct locations along the channel. In particular, hemodynamic regions of low shear stress and vorticity enhanced particle diffusion from the channel to the surrounding matrix, while areas of high shear stress and vorticity diminished diffusion. This work further showed that the presence of an endothelium attenuated diffusion from the channel, regardless of the local hemodynamic conditions. However, it should be noted that a new GelMA polymer, GelMA60, was synthesized in order to carry out these experiments. Previously made GelMA materials could not be used to fabricate voluminous constructs in our macro-perfusion bioreactors due to either poor crosslinking efficiency (in 5%G40 and 5%G100 conditions) or excessive use of material (in 10%G40 and 10%G100 conditions). Despite this conundrum, we found that 6%G60 achieved a stiffness and viscosity intermediate to 5%G100 and 10%40, making it a suitable polymer for microvessel formation. Albeit our system requires further optimization to adequately elucidate the effects of hemodynamic shear stress and vorticity on lumen maturation and angiogenesis. Altogether, these studies provide a model platform that can be adapted to engineer a variety of thick tissues equipped with hierarchical vasculature for regenerative medicine.

FUTURE OUTLOOK

Chronic wounds caused by trauma, cardiometabolic syndromes, tumor resection, and severe burns experience great difficulty in restoring healthy tissue within a timely manner. Advanced therapeutic strategies, in conjunction with standard wound care technique, have been implemented to address this clinical concern. Wound healing procedures utilized to restore partial- and full-thickness skin defects include stem cell therapy, growth factor supplementation, skin substitutes, and adjunctive treatments such as hyperbolic oxygen therapy or negative wound pressure therapy. These strategies are typically ideal for wounds that have a vascular wound bed suitable for the transplantation and revascularization of implanted tissue upon engraftment. However, in severe cases, chronic wound bed vasculature may be too deranged due to prolonged infection or ischemia at local regions of repetitive trauma or pathological loads. Thus, autologous flap transfer serves as a viable alternative to restore deranged tissue with compromised wound bed vasculature since it is equipped with its own hierarchical vascular supply.

The characteristics of tissue-specific defects including wound severity, location, size, composition, and vasculature must be taken into consideration when choosing donor-site tissue for transplantation to ensure the adequate tissue aesthetic and functional demands are met. Although autologous flap transfer is capable for restoring tissue with compromised wound bed vasculature, these invasive procedures can be complicated by the limited availability of donor tissue, increased donor-site morbidity, and extended post-operative recovery time. Thus, tissue engineering strategies can be utilized to engineer full-thickness vascularized flaps for chronic wound repair. Previous work has begun to exploit the use of 3D bioprinting technology to fabricate thick constructs with hierarchical vascular networks, which is crucial for adequate nutrient and oxygen

diffusion throughout the bulk of voluminous, cell-laden constructs. Tissue engineers have also examined the use of extrusion-based bioprinting to fabricate functional bone, muscle, tendon, and skin for chronic wound lesions. Despite these advances, successful tissue flap biofabrication will require printed constructs to recapitulate the various niches of each distinct tissue to restore subcutaneous, fasciocutaneous, musculocutaneous, or osteocutaneous defects. Proper selection of stem cell source, materials, conditioning, and bioprinting modalities will be crucial for the successful fabrication of full-thickness flaps for chronic wound lesions.

Cellularized bioinks, in particular, must attain the niche-specific structural ligands that not only acquire appropriate substrate mechanics and architecture to invoke stem cell differentiation into lineage-specific cell types, but also permit *de novo* vasculogenesis and angiogenic sprouting throughout the bulk material. Since matrix stiffness plays a key role in regulating stem cell differentiation, optimizing the compliance of bioprinted ECM will be more critical in engineering vascularized constructs of hard tissue (e.g., bone), as opposed to soft tissue (e.g., fat). Appropriate stem cell type and source is also important for bioprinting vascularized tissues. Under the appropriate conditions, MSCs are capable of differentiating to the various cell types present in the vasculature, including pericytes and smooth muscle cells, as well as the distinct tissues of full-thickness flaps, including adipocytes, myoblasts, fibroblasts, and osteoblasts. In addition to cell source and substrate mechanics, the rheological properties of bioinks for EBB must be sufficient in order to print 3D materials will anatomical precision. Inferior bioinks can be supplemented with rheological additives (e.g., alginate) to increase viscosity solely for extrusion purposes and sacrificed upon bioink polymerization to achieve structural integrity with high spatial resolution, while maintaining the appropriate microenvironmental stiffness. Optimal crosslinking methods for

bioprinted tissue must also be investigated to polymerize 3D biomaterials efficiently and with high shape fidelity, while maintaining high cell viability and appropriate matrix stiffness. Lastly, dynamic preconditioning of viable cell-laden constructs, is not only necessary for the establishment of multi-level neovascularization, but also for the development of distinct, functional tissues. Bioreactor designs that will simultaneously promote the maturation of bifurcated vascular networks, using hemodynamic flow, along with bone or muscle formation, using cyclic loading or tension, respectively, may augment the growth and development of specific bioprinted tissues harboring with their own vascular supply. Thus, a combination of different 3D-bioprinting modalities in tandem with the appropriate selection of cells types, biostructural polymers, bioink rheology and curing methods, and construct preconditioning may be necessary to achieve this multi-layered, tissue-engineered construct suitable for the adequate repair of full-thickness wounds.

REFERENCES

1. Eming SA, Martin P, Tomic-Canic M. Wound repair and regeneration: Mechanisms, signaling, and translation. Sci Transl Med. 2014 Dec 3;6(265):265sr6.

2. Han G, Ceilley R. Chronic Wound Healing: A Review of Current Management and Treatments. Adv Ther. 2017;34(3):599–610.

3. Horch RE, Weigand A, Wajant H, An R, Sun JM, Arkudas A. Towards the future of plastic surgery: from flaps to microsurgery and regenerative medicine and biofabrication? Plast Aesthetic Res. 2017 Oct 31;4(10):185.

4. Stephens CJ, Spector JA, Butcher JT. Biofabrication of thick vascularized neo-pedicle flaps for reconstructive surgery. Transl Res. 2019 Sep 1;211:84–122.

5. Do AV, Khorsand B, Geary SM, Salem AK. 3D Printing of Scaffolds for Tissue Regeneration Applications. Adv Healthc Mater. 2015 Aug;4(12):1742–62.

6. Richards D, Jia J, Yost M, Markwald R, Mei Y. 3D bioprinting for vascularized tissue fabrication. Ann Biomed Eng. 2017 Jan;45(1):132–47.

7. Radisic M, Malda J, Epping E, Geng W, Langer R, Vunjak-Novakovic G. Oxygen gradients correlate with cell density and cell viability in engineered cardiac tissue. Biotechnol Bioeng. 2006 Feb 5;93(2):332–43.

8. Yue K, Trujillo-de Santiago G, Alvarez MM, Tamayol A, Annabi N, Khademhosseini A. Synthesis, properties, and biomedical applications of gelatin methacryloyl (GelMA) hydrogels. Biomaterials. 2015 Dec;73:254–71.

9. Pepelanova I, Kruppa K, Scheper T, Lavrentieva A. Gelatin-Methacryloyl (GelMA) Hydrogels with Defined Degree of Functionalization as a Versatile Toolkit for 3D Cell Culture

and Extrusion Bioprinting. Bioengineering [Internet]. 2018 Jul 18 [cited 2020 Aug 5];5(3). Available from: https://www.ncbi.nlm.nih.gov/pmc/articles/PMC6165498/

10. Nichol JW, Koshy ST, Bae H, Hwang CM, Yamanlar S, Khademhosseini A. Cell-laden microengineered gelatin methacrylate hydrogels. Biomaterials. 2010 Jul;31(21):5536–44.

11. Zhu M, Wang Y, Ferracci G, Zheng J, Cho NJ, Lee BH. Gelatin methacryloyl and its hydrogels with an exceptional degree of controllability and batch-to-batch consistency. Sci Rep. 2019 May 3;9(1):6863.

12. Yin J, Yan M, Wang Y, Fu J, Suo H. 3D Bioprinting of Low-Concentration Cell-Laden Gelatin Methacrylate (GelMA) Bioinks with a Two-Step Cross-linking Strategy. ACS Appl Mater Interfaces. 2018 Feb 28;10(8):6849–57.

13. Kolesky DB, Truby RL, Gladman AS, Busbee TA, Homan KA, Lewis JA. 3D Bioprinting of Vascularized, Heterogeneous Cell-Laden Tissue Constructs. Adv Mater. 2014;26(19):3124–30.

14. Kim S, Pan CC, Yang YP. Development of a Dual Hydrogel Model System for Vascularization. Macromol Biosci. 2020;20(10):2000204.

15. Kessler L, Gehrke S, Winnefeld M, Huber B, Hoch E, Walter T, et al. Methacrylated gelatin/hyaluronan-based hydrogels for soft tissue engineering. J Tissue Eng [Internet]. 2017 Dec 21 [cited 2020 Aug 5];8. Available from: https://www.ncbi.nlm.nih.gov/pmc/articles/PMC5753891/

16. Costantini M, Testa S, Fornetti E, Barbetta A, Trombetta M, Cannata SM, et al. Engineering Muscle Networks in 3D Gelatin Methacryloyl Hydrogels: Influence of Mechanical Stiffness and Geometrical Confinement. Front Bioeng Biotechnol [Internet]. 2017 [cited 2020 Dec 9];5. Available from: https://www.frontiersin.org/articles/10.3389/fbioe.2017.00022/full

17. García-Lizarribar A, Fernández-Garibay X, Velasco-Mallorquí F, Castaño AG, Samitier J, Ramon-Azcon J. Composite Biomaterials as Long-Lasting Scaffolds for 3D Bioprinting of Highly Aligned Muscle Tissue. Macromol Biosci. 2018;18(10):e1800167.

18. Sen CK, Gordillo GM, Roy S, Kirsner R, Lambert L, Hunt TK, et al. Human Skin Wounds: A Major and Snowballing Threat to Public Health and the Economy. Wound Repair Regen Off Publ Wound Heal Soc Eur Tissue Repair Soc. 2009;17(6):763–71.

19. Ning L, Chen X. A brief review of extrusion-based tissue scaffold bio-printing. Biotechnol J. 2017 Aug;12(8).

20. Armulik A, Abramsson A, Betsholtz C. Endothelial/pericyte interactions. Circ Res. 2005 Sep 16;97(6):512–23.

21. Caplan AI, Dennis JE. Mesenchymal stem cells as trophic mediators. J Cell Biochem. 2006 Aug 1;98(5):1076–84.

22. Watt SM, Gullo F, van der Garde M, Markeson D, Camicia R, Khoo CP, et al. The angiogenic properties of mesenchymal stem/stromal cells and their therapeutic potential. Br Med Bull. 2013;108:25–53.

23. Bowers SLK, Meng CX, Davis MT, Davis GE. Investigating human vascular tube morphogenesis and maturation using endothelial cell-pericyte co-cultures and a doxycycline-inducible genetic system in 3D extracellular matrices. Methods Mol Biol Clifton NJ. 2015;1189:171–89.

24. Hsiai TK, Wu JC. Hemodynamic forces regulate embryonic stem cell commitment to vascular progenitors. Curr Cardiol Rev. 2008 Nov;4(4):269–74.

25. Logsdon EA, Finley SD, Popel AS, Mac Gabhann F. A systems biology view of blood vessel growth and remodelling. J Cell Mol Med. 2014 Aug;18(8):1491–508.

26. LaValley DJ, Reinhart-King CA. Matrix stiffening in the formation of blood vessels. Adv Regen Biol. 2014 Sep 25;1(1):25247.

27. Guo S, DiPietro LA. Factors Affecting Wound Healing. J Dent Res. 2010 Mar;89(3):219–29.

28. Bonar RA, Lippi G, Favaloro EJ. Overview of Hemostasis and Thrombosis and Contribution of Laboratory Testing to Diagnosis and Management of Hemostasis and Thrombosis Disorders. Methods Mol Biol Clifton NJ. 2017;1646:3–27.

29. Ellis S, Lin EJ, Tartar D. Immunology of Wound Healing. Curr Dermatol Rep. 2018;7(4):350–8.

30. Ramasastry SS. Acute wounds. Clin Plast Surg. 2005 Apr;32(2):195–208.

31. Brancato SK, Albina JE. Wound macrophages as key regulators of repair: origin, phenotype, and function. Am J Pathol. 2011 Jan;178(1):19–25.

32. Eming SA, Martin P, Tomic-Canic M. Wound repair and regeneration: mechanisms, signaling, and translation. Sci Transl Med. 2014 Dec 3;6(265):265sr6.

33. MacLeod AS, Mansbridge JN. The Innate Immune System in Acute and Chronic Wounds. Adv Wound Care. 2016 Feb;5(2):65–78.

34. Sorg H, Tilkorn DJ, Hager S, Hauser J, Mirastschijski U. Skin Wound Healing: An Update on the Current Knowledge and Concepts. Eur Surg Res Eur Chir Forsch Rech Chir Eur. 2017;58(1–2):81–94.

35. Ali N, Rosenblum MD. Regulatory T cells in skin. Immunology. 2017;152(3):372–81.

36. Boyko TV, Longaker MT, Yang GP. Review of the Current Management of Pressure Ulcers. Adv Wound Care. 2018 Feb 1;7(2):57–67.

37. Bluestein D, Javaheri A. Pressure Ulcers: Prevention, Evaluation, and Management. 2008;78(10):9.

38. Ontario, Ministry of Health and Long-Term Care, Medical Advisory Secretariat. Behavioural interventions for urinary incontinence in community-dwelling seniors: an evidence-based analysis. Toronto: Medical Advisory Secretariat; 2008.

39. Lyder CH, Ayello EA. Pressure Ulcers: A Patient Safety Issue. In: Hughes RG, editor. Patient Safety and Quality: An Evidence-Based Handbook for Nurses [Internet]. Rockville (MD): Agency for Healthcare Research and Quality (US); 2008 [cited 2019 Feb 12]. (Advances in Patient Safety). Available from: http://www.ncbi.nlm.nih.gov/books/NBK2650/

40. Alexiadou K, Doupis J. Management of Diabetic Foot Ulcers. Diabetes Ther [Internet]. 2012 Dec [cited 2019 Feb 12];3(1). Available from: https://www.ncbi.nlm.nih.gov/pmc/articles/PMC3508111/

41. Armstrong DG, Boulton AJM, Bus SA. Diabetic Foot Ulcers and Their Recurrence. N Engl J Med. 2017 Jun 15;376(24):2367–75.

42. S S. An Overview on Diabetic Foot Ulcer (DFU): Mini Review. Diabetes Case Rep [Internet]. 2018 [cited 2019 Feb 12];03(01). Available from: https://www.omicsonline.org/open-access/an-overview-on-diabetic-foot-ulcer-dfu-mini-review-2572-5629-1000134-100525.html

43. Wu SC, Driver VR, Wrobel JS, Armstrong DG. Foot ulcers in the diabetic patient, prevention and treatment. Vasc Health Risk Manag. 2007 Feb;3(1):65–76.

44. Monteiro-Soares M, Boyko EJ, Ribeiro J, Ribeiro I, Dinis-Ribeiro M. Predictive factors for diabetic foot ulceration: a systematic review. Diabetes Metab Res Rev. 2012;28(7):574–600.

45. Bus SA, van Deursen RW, Armstrong DG, Lewis JEA, Caravaggi CF, Cavanagh PR, et al. Footwear and offloading interventions to prevent and heal foot ulcers and reduce plantar pressure

in patients with diabetes: a systematic review. Diabetes Metab Res Rev. 2016 Jan;32 Suppl 1:99–118.

46. Grey JE, Harding KG, Enoch S. Venous and arterial leg ulcers. BMJ. 2006 Feb 9;332(7537):347–50.

47. O'Meara S, Cullum NA, Nelson EA. Compression for venous leg ulcers. Cochrane Database Syst Rev. 2009 Jan 21;(1):CD000265.

48. Collins LG, Seraj S. Diagnosis and Treatment of Venous Ulcers. Am Fam Physician. 2010 Apr 15;81(8):989–96.

49. Werchek S. Diagnosis and treatment of venous leg ulcers. Nurse Pract. 2010 Dec;35(12):46.

50. Lim CS, Baruah M, Bahia SS. Diagnosis and management of venous leg ulcers. BMJ. 2018 Aug 14;362:k3115.

51. Crawford JM, Lal BK, Durán WN, Pappas PJ. Pathophysiology of venous ulceration. J Vasc Surg Venous Lymphat Disord. 2017 Jul 1;5(4):596–605.

52. Hedayati N, Carson JG, Chi YW, Link D. Management of mixed arterial venous lower extremity ulceration: A review. Vasc Med Lond Engl. 2015 Oct;20(5):479–86.

53. Forster R, Pagnamenta F. Dressings and topical agents for arterial leg ulcers. Cochrane Database Syst Rev. 2015 Jun 29;(6):CD001836.

54. Nelson EA, Bradley MD. Dressings and topical agents for arterial leg ulcers. Cochrane Database Syst Rev. 2007 Jan 24;(1):CD001836.

55. Greer N, Foman NA, MacDonald R, Dorrian J, Fitzgerald P, Rutks I, et al. Advanced wound care therapies for nonhealing diabetic, venous, and arterial ulcers: a systematic review. Ann Intern Med. 2013 Oct 15;159(8):532–42.

56. Han SK. Growth Factor Therapy. In: Han SK, editor. Innovations and Advances in Wound Healing [Internet]. Berlin, Heidelberg: Springer Berlin Heidelberg; 2016 [cited 2019 Feb 12]. p. 201–13. Available from: https://doi.org/10.1007/978-3-662-46587-5_9

57. Piaggesi A, Låuchli S, Bassetto F, Biedermann T, Marques A, Najafi B, et al. Advanced therapies in wound management: cell and tissue based therapies, physical and bio-physical therapies smart and IT based technologies. J Wound Care. 2018 Jun 1;27(Sup6a):S1–137.

58. Park JW, Hwang SR, Yoon IS. Advanced Growth Factor Delivery Systems in Wound Management and Skin Regeneration. Mol Basel Switz. 2017 Jul 27;22(8).

59. Badiavas EV, Abedi M, Butmarc J, Falanga V, Quesenberry P. Participation of bone marrow derived cells in cutaneous wound healing. J Cell Physiol. 2003 Aug;196(2):245–50.

60. Badiavas EV, Ford D, Liu P, Kouttab N, Morgan J, Richards A, et al. Long-term bone marrow culture and its clinical potential in chronic wound healing. Wound Repair Regen Off Publ Wound Heal Soc Eur Tissue Repair Soc. 2007 Dec;15(6):856–65.

61. Rigotti G, Marchi A, Galiè M, Baroni G, Benati D, Krampera M, et al. Clinical treatment of radiotherapy tissue damage by lipoaspirate transplant: a healing process mediated by adipose-derived adult stem cells. Plast Reconstr Surg. 2007 Apr 15;119(5):1409–22; discussion 1423-1424.

62. Falanga V, Iwamoto S, Chartier M, Yufit T, Butmarc J, Kouttab N, et al. Autologous bone marrow-derived cultured mesenchymal stem cells delivered in a fibrin spray accelerate healing in murine and human cutaneous wounds. Tissue Eng. 2007 Jun;13(6):1299–312.

63. Garcia-Olmo D, Garcia-Arranz M, Herreros D. Expanded adipose-derived stem cells for the treatment of complex perianal fistula including Crohn's disease. Expert Opin Biol Ther. 2008 Sep;8(9):1417–23.

64. Dash NR, Dash SN, Routray P, Mohapatra S, Mohapatra PC. Targeting nonhealing ulcers of lower extremity in human through autologous bone marrow-derived mesenchymal stem cells. Rejuvenation Res. 2009 Oct;12(5):359–66.

65. Lee K, Silva EA, Mooney DJ. Growth factor delivery-based tissue engineering: general approaches and a review of recent developments. J R Soc Interface. 2011 Feb 6;8(55):153–70.

66. Duscher D, Neofytou E, Wong VW, Maan ZN, Rennert RC, Inayathullah M, et al. Transdermal deferoxamine prevents pressure-induced diabetic ulcers. Proc Natl Acad Sci U S A. 2015 Jan 6;112(1):94–9.

67. Duscher D, Barrera J, Wong VW, Maan ZN, Whittam AJ, Januszyk M, et al. Stem Cells in Wound Healing: The Future of Regenerative Medicine? A Mini-Review. Gerontology. 2016;62(2):216–25.

68. Mester A, Opincariu D, Benedek I, Benedek I. Stem Cell Therapy in Wound Healing. Vol. 2. 2017. 20 p.

69. Herskovitz I, Hughes OB, Macquhae F, Rakosi A, Kirsner R. Epidermal skin grafting: Epidermal skin grafting. Int Wound J. 2016 Sep;13(S3):52–6.

70. Nicholas MN, Yeung J. Current Status and Future of Skin Substitutes for Chronic Wound Healing. J Cutan Med Surg. 2017 Feb;21(1):23–30.

71. Simman R. Letter from the editor in chief. J Am Coll Certif Wound Spec. 2009 Dec;1(4):104.

72. Horch R, Weigand A, Wajant H, An R, Sun JM, Arkudas A. Towards the future of plastic surgery: from flaps to microsurgery and regenerative medicine and biofabrication? Vol. 4. 2017. 185 p.

73. Dunn R. Grafts and flaps. Surg Oxf. 2006 Jan 1;24(1):27–32.

74. Basu A. Classification of flaps and application of the concept of vascular territories. In 2016. p. 93–120.

75. Tschoi M, Hoy EA, Granick MS. Skin Flaps. Clin Plast Surg. 2005 Apr;32(2):261–73.

76. Geddes CR, Morris SF, Neligan PC. Perforator flaps: evolution, classification, and applications. Ann Plast Surg. 2003 Jan;50(1):90–9.

77. Kim JT. New nomenclature concept of perforator flap. Br J Plast Surg. 2005 Jun;58(4):431–40.

78. Saint-Cyr M, Schaverien MV, Rohrich RJ. Perforator flaps: history, controversies, physiology, anatomy, and use in reconstruction. Plast Reconstr Surg. 2009 Apr;123(4):132e–45e.

79. McGregor IA, Morgan G. Axial and random pattern flaps. Br J Plast Surg. 1973 Jul;26(3):202–13.

80. Fujioka M. Surgical Reconstruction of Radiation Injuries. Adv Wound Care. 2014 Jan 1;3(1):25–37.

81. Agrawal K. Cleft palate repair and variations. Indian J Plast Surg Off Publ Assoc Plast Surg India. 2009 Oct;42(Suppl):S102–9.

82. Healy C, Allen RJ. The Evolution of Perforator Flap Breast Reconstruction: Twenty Years after the First DIEP Flap. J Reconstr Microsurg. 2014 Feb;30(2):121–6.

83. Do AV, Khorsand B, Geary SM, Salem AK. 3D Printing of Scaffolds for Tissue Regeneration Applications. Adv Healthc Mater. 2015 Aug 26;4(12):1742–62.

84. Cui X, Boland T, D'Lima DD, Lotz MK. Thermal Inkjet Printing in Tissue Engineering and Regenerative Medicine. Recent Pat Drug Deliv Formul. 2012 Aug;6(2):149–55.

85. Pati F, Jang J, Lee JW, Cho DW. Chapter 7 - Extrusion Bioprinting. In: Atala A, Yoo JJ, editors. Essentials of 3D Biofabrication and Translation [Internet]. Boston: Academic Press; 2015

[cited 2019 Feb 12]. p. 123–52. Available from: http://www.sciencedirect.com/science/article/pii/B9780128009727000074

86. Derakhshanfar S, Mbeleck R, Xu K, Zhang X, Zhong W, Xing M. 3D bioprinting for biomedical devices and tissue engineering: A review of recent trends and advances. Bioact Mater. 2018 Jun 1;3(2):144–56.

87. van Kogelenberg S, Yue Z, Dinoro JN, Baker CS, Wallace GG. Three-Dimensional Printing and Cell Therapy for Wound Repair. Adv Wound Care. 2018 May 1;7(5):145–55.

88. Radisic M, Malda J, Epping E, Geng W, Langer R, Vunjak-Novakovic G. Oxygen gradients correlate with cell density and cell viability in engineered cardiac tissue. Biotechnol Bioeng. 2006 Feb 5;93(2):332–43.

89. Richards D, Jia J, Yost M, Markwald R, Mei Y. 3D Bioprinting for Vascularized Tissue Fabrication. Ann Biomed Eng. 2017;45(1):132–47.

90. Miri AK, Khalilpour A, Cecen B, Maharjan S, Shin SR, Khademhosseini A. Multiscale bioprinting of vascularized models. Biomaterials. 2018 Aug 3;

91. Datta P, Ayan B, Ozbolat IT. Bioprinting for vascular and vascularized tissue biofabrication. Acta Biomater. 2017 15;51:1–20.

92. Jia W, Gungor-Ozkerim PS, Zhang YS, Yue K, Zhu K, Liu W, et al. Direct 3D bioprinting of perfusable vascular constructs using a blend bioink. Biomaterials. 2016 Nov 1;106:58–68.

93. Kolesky DB, Truby RL, Gladman AS, Busbee TA, Homan KA, Lewis JA. 3D Bioprinting of Vascularized, Heterogeneous Cell-Laden Tissue Constructs. Adv Mater. 2014;26(19):3124–30.

94. Lee VK, Kim DY, Ngo H, Lee Y, Seo L, Yoo SS, et al. Creating perfused functional vascular channels using 3D bio-printing technology. Biomaterials. 2014 Sep;35(28):8092–102.

95. Miller JS, Stevens KR, Yang MT, Baker BM, Nguyen DHT, Cohen DM, et al. Rapid casting of patterned vascular networks for perfusable engineered three-dimensional tissues. Nat Mater. 2012 Sep;11(9):768–74.

96. Skardal A, Mack D, Kapetanovic E, Atala A, Jackson JD, Yoo J, et al. Bioprinted amniotic fluid-derived stem cells accelerate healing of large skin wounds. Stem Cells Transl Med. 2012 Nov;1(11):792–802.

97. Pourchet LJ, Thepot A, Albouy M, Courtial EJ, Boher A, Blum LJ, et al. Human Skin 3D Bioprinting Using Scaffold-Free Approach. Adv Healthc Mater. 2017 Feb;6(4).

98. Kim BS, Kwon YW, Kong JS, Park GT, Gao G, Han W, et al. 3D cell printing of in vitro stabilized skin model and in vivo pre-vascularized skin patch using tissue-specific extracellular matrix bioink: A step towards advanced skin tissue engineering. Biomaterials. 2018 Jun 1;168:38–53.

99. Colle J, Blondeel P, De Bruyne A, Bochar S, Tytgat L, Vercruysse C, et al. Bioprinting predifferentiated adipose-derived mesenchymal stem cell spheroids with methacrylated gelatin ink for adipose tissue engineering. J Mater Sci Mater Med. 2020 Mar 23;31(4):36.

100. Zhou M, Hou J, Zhang G, Luo C, Zeng Y, Mou S, et al. Tuning the mechanics of 3D-printed scaffolds by crystal lattice-like structural design for breast tissue engineering. Biofabrication. 2019 Dec 31;12(1):015023.

101. Xue W, Yu SY, Kuss M, Kong Y, Shi W, Chung S, et al. 3D bioprinted white adipose model forin vitrostudy of cancer-associated cachexia induced adipose tissue remodeling. Biofabrication. 2022 May 26;14(3).

102. Schmitt T, Katz N, Kishore V. A Feasibility Study on 3D Bioprinting of Microfat Constructs Towards Wound Healing Applications. Front Bioeng Biotechnol. 2021;9:707098.

103. Kesavan R, Sheela Sasikumar C, Narayanamurthy VB, Rajagopalan A, Kim J. Management of Diabetic Foot Ulcer with MA-ECM (Minimally Manipulated Autologous Extracellular Matrix) Using 3D Bioprinting Technology - An Innovative Approach. Int J Low Extrem Wounds. 2024 Mar;23(1):161–8.

104. Yoon HM, Song WJ. Using 3D Bioprinted Autologous Minimally Manipulated Homologous Adipose Tissue for Limb Salvage in Treating Diabetic Foot Ulcer. Arch Plast Surg. 2024 May;51(3):332–6.

105. Kang HW, Lee SJ, Ko IK, Kengla C, Yoo JJ, Atala A. A 3D bioprinting system to produce human-scale tissue constructs with structural integrity. Nat Biotechnol. 2016 Mar;34(3):312–9.

106. Merceron TK, Burt M, Seol YJ, Kang HW, Lee SJ, Yoo JJ, et al. A 3D bioprinted complex structure for engineering the muscle-tendon unit. Biofabrication. 2015 Jun 17;7(3):035003.

107. Kim JH, Seol YJ, Ko IK, Kang HW, Lee YK, Yoo JJ, et al. 3D Bioprinted Human Skeletal Muscle Constructs for Muscle Function Restoration. Sci Rep [Internet]. 2018 Dec [cited 2019 Feb 12];8(1). Available from: http://www.nature.com/articles/s41598-018-29968-5

108. Ahlfeld T, Cidonio G, Kilian D, Duin S, Akkineni AR, Dawson JI, et al. Development of a clay based bioink for 3D cell printing for skeletal application. Biofabrication. 2017 Jul 25;9(3):034103.

109. Byambaa B, Annabi N, Yue K, Trujillo-de Santiago G, Alvarez MM, Jia W, et al. Bioprinted Osteogenic and Vasculogenic Patterns for Engineering 3D Bone Tissue. Adv Healthc Mater. 2017 Aug;6(16).

110. Cui H, Zhu W, Nowicki M, Zhou X, Khademhosseini A, Zhang LG. Hierarchical Fabrication of Engineered Vascularized Bone Biphasic Constructs via Dual 3D Bioprinting:

Integrating Regional Bioactive Factors into Architectural Design. Adv Healthc Mater. 2016;5(17):2174–81.

111. Tucker WD, Mahajan K. Anatomy, Blood Vessels. In: StatPearls [Internet]. Treasure Island (FL): StatPearls Publishing; 2018 [cited 2019 Feb 13]. Available from: http://www.ncbi.nlm.nih.gov/books/NBK470401/

112. Ucuzian AA, Gassman AA, East AT, Greisler HP. Molecular mediators of angiogenesis. J Burn Care Res Off Publ Am Burn Assoc. 2010 Feb;31(1):158–75.

113. Davis GE, Stratman AN, Sacharidou A, Koh W. Molecular basis for endothelial lumen formation and tubulogenesis during vasculogenesis and angiogenic sprouting. Int Rev Cell Mol Biol. 2011;288:101–65.

114. Bichsel CA, Hall SRR, Schmid RA, Guenat OT, Geiser T. Primary Human Lung Pericytes Support and Stabilize In Vitro Perfusable Microvessels. Tissue Eng Part A. 2015 Aug;21(15–16):2166–76.

115. Davis S, Aldrich TH, Jones PF, Acheson A, Compton DL, Jain V, et al. Isolation of Angiopoietin-1, a Ligand for the TIE2 Receptor, by Secretion-Trap Expression Cloning. Cell. 1996 Dec;87(7):1161–9.

116. Suri C, Jones PF, Patan S, Bartunkova S, Maisonpierre PC, Davis S, et al. Requisite Role of Angiopoietin-1, a Ligand for the TIE2 Receptor, during Embryonic Angiogenesis. Cell. 1996 Dec 27;87(7):1171–80.

117. Bergers G, Song S. The role of pericytes in blood-vessel formation and maintenance. Neuro-Oncol. 2005 Oct;7(4):452–64.

118. Eilken HM, Diéguez-Hurtado R, Schmidt I, Nakayama M, Jeong HW, Arf H, et al. Pericytes regulate VEGF-induced endothelial sprouting through VEGFR1. Nat Commun. 2017 Nov 17;8(1):1574.

119. Lobov IB, Brooks PC, Lang RA. Angiopoietin-2 displays VEGF-dependent modulation of capillary structure and endothelial cell survival in vivo. Proc Natl Acad Sci U S A. 2002 Aug 20;99(17):11205–10.

120. Teichert M, Milde L, Holm A, Stanicek L, Gengenbacher N, Savant S, et al. Pericyte-expressed Tie2 controls angiogenesis and vessel maturation. Nat Commun. 2017 Jul 18;8:16106.

121. Kim J, Chung M, Kim S, Jo DH, Kim JH, Jeon NL. Engineering of a Biomimetic Pericyte-Covered 3D Microvascular Network. PloS One. 2015;10(7):e0133880.

122. Stratman AN, Malotte KM, Mahan RD, Davis MJ, Davis GE. Pericyte recruitment during vasculogenic tube assembly stimulates endothelial basement membrane matrix formation. Blood. 2009 Dec 3;114(24):5091–101.

123. Smith AO, Bowers SLK, Stratman AN, Davis GE. Hematopoietic Stem Cell Cytokines and Fibroblast Growth factor-2 Stimulate Human Endothelial Cell-Pericyte Tube Co-Assembly in 3D Fibrin Matrices under Serum-Free Defined Conditions. PLOS ONE. 2013 Dec 31;8(12):e85147.

124. Greenberg JI, Shields DJ, Barillas SG, Acevedo LM, Murphy E, Huang J, et al. A role for VEGF as a negative regulator of pericyte function and vessel maturation. Nature. 2008 Dec 11;456(7223):809–13.

125. Augustin HG, Koh GY, Thurston G, Alitalo K. Control of vascular morphogenesis and homeostasis through the angiopoietin-Tie system. Nat Rev Mol Cell Biol. 2009 Mar;10(3):165–77.

126. Simonavicius N, Ashenden M, van Weverwijk A, Lax S, Huso DL, Buckley CD, et al. Pericytes promote selective vessel regression to regulate vascular patterning. Blood. 2012 Aug 16;120(7):1516–27.

127. Orlidge A, D'Amore PA. Inhibition of capillary endothelial cell growth by pericytes and smooth muscle cells. J Cell Biol. 1987 Sep;105(3):1455–62.

128. Waters JP, Kluger MS, Graham M, Chang WG, Bradley JR, Pober JS. In vitro self-assembly of human pericyte-supported endothelial microvessels in three-dimensional coculture: a simple model for interrogating endothelial-pericyte interactions. J Vasc Res. 2013;50(4):324–31.

129. Darland DC, D'Amore PA. TGF beta is required for the formation of capillary-like structures in three-dimensional cocultures of 10T1/2 and endothelial cells. Angiogenesis. 2001;4(1):11–20.

130. Zonneville J, Safina A, Truskinovsky AM, Arteaga CL, Bakin AV. TGF-β signaling promotes tumor vasculature by enhancing the pericyte-endothelium association. BMC Cancer [Internet]. 2018 Jun 19 [cited 2019 Feb 13];18. Available from: https://www.ncbi.nlm.nih.gov/pmc/articles/PMC6008941/

131. Kerkar S, Williams M, Blocksom JM, Wilson RF, Tyburski JG, Steffes CP. TNF-α and IL-1β Increase Pericyte/Endothelial Cell Co-Culture Permeability. J Surg Res. 2006 May 1;132(1):40–5.

132. Tattersall IW, Du J, Cong Z, Cho BS, Klein AM, Dieck CL, et al. In vitro modeling of endothelial interaction with macrophages and pericytes demonstrates Notch signaling function in the vascular microenvironment. Angiogenesis. 2016 Apr;19(2):201–15.

133. Heydarkhan-Hagvall S, Helenius G, Johansson BR, Li JY, Mattsson E, Risberg B. Co-culture of endothelial cells and smooth muscle cells affects gene expression of angiogenic factors. J Cell Biochem. 2003 Aug 15;89(6):1250–9.

134. Kurzen H, Manns S, Dandekar G, Schmidt T, Prätzel S, Kräling BM. Tightening of endothelial cell contacts: a physiologic response to cocultures with smooth-muscle-like 10T1/2 cells. J Invest Dermatol. 2002 Jul;119(1):143–53.

135. Dietrich F, Lelkes PI. Fine-tuning of a three-dimensional microcarrier-based angiogenesis assay for the analysis of endothelial-mesenchymal cell co-cultures in fibrin and collagen gels. Angiogenesis. 2006;9(3):111–25.

136. Joo HJ, Seo HR, Jeong HE, Choi SC, Park JH, Yu CW, et al. Smooth muscle progenitor cells from peripheral blood promote the neovascularization of endothelial colony-forming cells. Biochem Biophys Res Commun. 2014 Jul 11;449(4):405–11.

137. Ucuzian AA, Bufalino DV, Pang Y, Greisler HP. Angiogenic endothelial cell invasion into fibrin is stimulated by proliferating smooth muscle cells. Microvasc Res. 2013 Nov;90:40–7.

138. Shudo Y, Cohen JE, Macarthur JW, Atluri P, Hsiao PF, Yang EC, et al. Spatially oriented, temporally sequential smooth muscle cell-endothelial progenitor cell bi-level cell sheet neovascularizes ischemic myocardium. Circulation. 2013 Sep 10;128(11 Suppl 1):S59-68.

139. Bak S, Ahmad T, Lee YB, Lee J yup, Kim EM, Shin H. Delivery of a Cell Patch of Cocultured Endothelial Cells and Smooth Muscle Cells Using Thermoresponsive Hydrogels for Enhanced Angiogenesis. Tissue Eng Part A. 2016 Jan;22(1–2):182–93.

140. Bargehr J, Low L, Cheung C, Bernard WG, Iyer D, Bennett MR, et al. Embryological Origin of Human Smooth Muscle Cells Influences Their Ability to Support Endothelial Network Formation. Stem Cells Transl Med. 2016 Jul;5(7):946–59.

141. Korff T, Kimmina S, Martiny-Baron G, Augustin HG. Blood vessel maturation in a 3-dimensional spheroidal coculture model: direct contact with smooth muscle cells regulates endothelial cell quiescence and abrogates VEGF responsiveness. FASEB J Off Publ Fed Am Soc Exp Biol. 2001 Feb;15(2):447–57.

142. Molnar N, Siemann DW. Inhibition of endothelial/smooth muscle cell contact loss by the investigational angiopoietin-2 antibody MEDI3617. Microvasc Res. 2012 May;83(3):290–7.

143. Harvey KA, Welch Z, Sliva D, Siddiqui RA. Role of Rho kinase in sphingosine 1-phosphate-mediated endothelial and smooth muscle cell migration and differentiation. Mol Cell Biochem. 2010 Sep;342(1–2):7–19.

144. Jin F, Hagemann N, Sun L, Wu J, Doeppner TR, Dai Y, et al. High-density lipoprotein (HDL) promotes angiogenesis via S1P3-dependent VEGFR2 activation. Angiogenesis. 2018 May;21(2):381–94.

145. Wang H, Huang H, Ding SF. Sphingosine-1-phosphate promotes the proliferation and attenuates apoptosis of Endothelial progenitor cells via S1PR1/S1PR3/PI3K/Akt pathway. Cell Biol Int. 2018 Nov;42(11):1492–502.

146. Williams PA, Campbell KT, Silva EA. Alginate hydrogels of varied molecular weight distribution enable sustained release of sphingosine-1-phosphate and promote angiogenesis. J Biomed Mater Res A. 2018 Jan;106(1):138–46.

147. Liu H, Kennard S, Lilly B. NOTCH3 expression is induced in mural cells through an autoregulatory loop that requires endothelial-expressed JAGGED1. Circ Res. 2009 Feb 27;104(4):466–75.

148. Bhattacharyya A, Lin S, Sandig M, Mequanint K. Regulation of vascular smooth muscle cell phenotype in three-dimensional coculture system by Jagged1-selective Notch3 signaling. Tissue Eng Part A. 2014 Apr;20(7–8):1175–87.

149. Velazquez OC, Snyder R, Liu ZJ, Fairman RM, Herlyn M. Fibroblast-dependent differentiation of human microvascular endothelial cells into capillary-like 3-dimensional networks. FASEB J Off Publ Fed Am Soc Exp Biol. 2002 Aug;16(10):1316–8.

150. Twardowski RL, Black LD. Cardiac fibroblasts support endothelial cell proliferation and sprout formation but not the development of multicellular sprouts in a fibrin gel co-culture model. Ann Biomed Eng. 2014 May;42(5):1074–84.

151. Xu Y, Peng J, Dong X, Xu Y, Li H, Chang J. Combined chemical and structural signals of biomaterials synergistically activate cell-cell communications for improving tissue regeneration. Acta Biomater. 2017;55:249–61.

152. Lilly B, Kennard S. Differential gene expression in a coculture model of angiogenesis reveals modulation of select pathways and a role for Notch signaling. Physiol Genomics. 2009 Jan 8;36(2):69–78.

153. Costa-Almeida R, Gomez-Lazaro M, Ramalho C, Granja PL, Soares R, Guerreiro SG. Fibroblast-Endothelial Partners for Vascularization Strategies in Tissue Engineering. Tissue Eng Part A. 2015 Mar 1;21(5–6):1055–65.

154. Eckermann CW, Lehle K, Schmid SA, Wheatley DN, Kunz-Schughart LA. Characterization and modulation of fibroblast/endothelial cell co-cultures for the in vitro preformation of three-dimensional tubular networks. Cell Biol Int. 2011;35(11):1097–110.

155. Huber B, Volz AC, Kluger PJ. Understanding the effects of mature adipocytes and endothelial cells on fatty acid metabolism and vascular tone in physiological fatty tissue for vascularized adipose tissue engineering. Cell Tissue Res. 2015 Nov;362(2):269–79.

156. Volz AC, Huber B, Kluger PJ. Adipose-derived stem cell differentiation as a basic tool for vascularized adipose tissue engineering. Differ Res Biol Divers. 2016 Aug;92(1–2):52–64.

157. Chaurasiya V, Nidhina Haridas PA, Olkkonen VM. Adipocyte-endothelial cell interplay in adipose tissue physiology. Biochem Pharmacol. 2024 Apr 1;222:116081.

158. Sarkanen JR, Kaila V, Mannerström B, Räty S, Kuokkanen H, Miettinen S, et al. Human adipose tissue extract induces angiogenesis and adipogenesis in vitro. Tissue Eng Part A. 2012 Jan;18(1–2):17–25.

159. Volz AC, Hack L, Atzinger FB, Kluger PJ. Completely defined co-culture of adipogenic differentiated ASCs and microvascular endothelial cells. ALTEX. 2018;35(4):464–76.

160. Chaurasiya V, Pham DD, Harju J, Juuti A, Penttilä A, Emmagouni SKG, et al. Human visceral adipose tissue microvascular endothelial cell isolation and establishment of co-culture with white adipocytes to analyze cell-cell communication. Exp Cell Res. 2023 Dec 15;433(2):113819.

161. Yadav NVS, Barcikowski A, Uehana Y, Jacobs AT, Connelly L. Breast Adipocyte Co-culture Increases the Expression of Pro-angiogenic Factors in Macrophages. Front Oncol. 2020;10:454.

162. Watanabe H, Goto S, Kato R, Komiyama S, Nagaoka Y, Kazama T, et al. The neovascularization effect of dedifferentiated fat cells. Sci Rep. 2020 Jun 8;10:9211.

163. Jia X, Chai Y, Zhu J, Zhang X, Jiang C, Yin N, et al. Enhancing Fat Graft Survival via Upregulating Autophagy of Adipocytes. Aesthetic Plast Surg. 2024 May;48(9):1807–16.

164. Yu J, Hsu YC, Lee JK, Cheng NC. Enhanced angiogenic potential of adipose-derived stem cell sheets by integration with cell spheroids of the same source. Stem Cell Res Ther. 2022 Jun 28;13:276.

165. Muller S, Ader I, Creff J, Leménager H, Achard P, Casteilla L, et al. Human adipose stromal-vascular fraction self-organizes to form vascularized adipose tissue in 3D cultures. Sci Rep. 2019 May 10;9(1):7250.

166. Huttala O, Palmroth M, Hemminki P, Toimela T, Heinonen T, Ylikomi T, et al. Development of Versatile Human In Vitro Vascularized Adipose Tissue Model with Serum-Free Angiogenesis and Natural Adipogenesis Induction. Basic Clin Pharmacol Toxicol. 2018 Sep;123 Suppl 5:62–71.

167. Xue Y, Xing Z, Bolstad AI, Van Dyke TE, Mustafa K. Co-culture of human bone marrow stromal cells with endothelial cells alters gene expression profiles. Int J Artif Organs. 2013 Oct 3;36(9):650–62.

168. Zhang Y, Xia X, Yan J, Yan L, Lu C, Zhu X, et al. Mesenchymal stem cell-derived angiogenin promotes primodial follicle survival and angiogenesis in transplanted human ovarian tissue. Reprod Biol Endocrinol RBE. 2017 Mar 9;15(1):18.

169. Jeon JS, Bersini S, Whisler JA, Chen MB, Dubini G, Charest JL, et al. Generation of 3D functional microvascular networks with mural cell-differentiated human mesenchymal stem cells in microfluidic vasculogenesis systems. Integr Biol Quant Biosci Nano Macro. 2014 May;6(5):555–63.

170. Zhao D, Xue C, Lin S, Shi S, Li Q, Liu M, et al. Notch Signaling Pathway Regulates Angiogenesis via Endothelial Cell in 3D Co-Culture Model. J Cell Physiol. 2017 Jun;232(6):1548–58.

171. Boyd NL, Nunes SS, Krishnan L, Jokinen JD, Ramakrishnan VM, Bugg AR, et al. Dissecting the role of human embryonic stem cell-derived mesenchymal cells in human umbilical vein endothelial cell network stabilization in three-dimensional environments. Tissue Eng Part A. 2013 Jan;19(1–2):211–23.

172. McFadden TM, Duffy GP, Allen AB, Stevens HY, Schwarzmaier SM, Plesnila N, et al. The delayed addition of human mesenchymal stem cells to pre-formed endothelial cell networks results in functional vascularization of a collagen–glycosaminoglycan scaffold in vivo. Acta Biomater. 2013 Dec 1;9(12):9303–16.

173. Ma J, Yang F, Both SK, Prins HJ, Helder MN, Pan J, et al. In vitro and in vivo angiogenic capacity of BM-MSCs/HUVECs and AT-MSCs/HUVECs cocultures. Biofabrication. 2014 Mar;6(1):015005.

174. Pedersen TO, Blois AL, Xue Y, Xing Z, Sun Y, Finne-Wistrand A, et al. Mesenchymal stem cells induce endothelial cell quiescence and promote capillary formation. Stem Cell Res Ther. 2014 Feb 17;5(1):23.

175. Sueyama Y, Kaneko T, Ito T, Kaneko R, Okiji T. Implantation of Endothelial Cells with Mesenchymal Stem Cells Accelerates Dental Pulp Tissue Regeneration/Healing in Pulpotomized Rat Molars. J Endod. 2017 Jun;43(6):943–8.

176. Chen L, Xing Q, Zhai Q, Tahtinen M, Zhou F, Chen L, et al. Pre-vascularization Enhances Therapeutic Effects of Human Mesenchymal Stem Cell Sheets in Full Thickness Skin Wound Repair. Theranostics. 2017 Jan 1;7(1):117–31.

177. Verschueren JHM, Post MWM, de Groot S, van der Woude LHV, van Asbeck FWA, Rol M. Occurrence and predictors of pressure ulcers during primary in-patient spinal cord injury rehabilitation. Spinal Cord. 2011 Jan;49(1):106–12.

178. Esteves CL, Sheldrake TA, Dawson L, Menghini T, Rink BE, Amilon K, et al. Equine Mesenchymal Stromal Cells Retain a Pericyte-Like Phenotype. Stem Cells Dev. 2017 01;26(13):964–72.

179. Kachgal S, Putnam AJ. Mesenchymal stem cells from adipose and bone marrow promote angiogenesis via distinct cytokine and protease expression mechanisms. Angiogenesis. 2011 Mar;14(1):47–59.

180. Morris AD, Dalal S, Li H, Brewster LP. Human diabetic mesenchymal stem cells from peripheral arterial disease patients promote angiogenesis through unique secretome signatures. Surgery. 2018;163(4):870–6.

181. König J, Weiss G, Rossi D, Wankhammer K, Reinisch A, Kinzer M, et al. Placental mesenchymal stromal cells derived from blood vessels or avascular tissues: what is the better choice to support endothelial cell function? Stem Cells Dev. 2015 Jan 1;24(1):115–31.

182. Goerke SM, Plaha J, Hager S, Strassburg S, Torio-Padron N, Stark GB, et al. Human Endothelial Progenitor Cells Induce Extracellular Signal-Regulated Kinase-Dependent Differentiation of Mesenchymal Stem Cells into Smooth Muscle Cells upon Cocultivation. Tissue Eng Part A. 2012 Jun 26;18(23–24):2395–405.

183. Tsai CC, Chen YJ, Yew TL, Chen LL, Wang JY, Chiu CH, et al. Hypoxia inhibits senescence and maintains mesenchymal stem cell properties through down-regulation of E2A-p21 by HIF-TWIST. Blood. 2011 Jan 13;117(2):459–69.

184. Basciano L, Nemos C, Foliguet B, de Isla N, de Carvalho M, Tran N, et al. Long term culture of mesenchymal stem cells in hypoxia promotes a genetic program maintaining their undifferentiated and multipotent status. BMC Cell Biol. 2011 Mar 30;12:12.

185. Burlacu A, Grigorescu G, Rosca AM, Preda MB, Simionescu M. Factors secreted by mesenchymal stem cells and endothelial progenitor cells have complementary effects on angiogenesis in vitro. Stem Cells Dev. 2013 Feb 15;22(4):643–53.

186. Ahmed NEMB, Murakami M, Kaneko S, Nakashima M. The effects of hypoxia on the stemness properties of human dental pulp stem cells (DPSCs). Sci Rep. 2016 14;6:35476.

187. Xie Q, Xie J, Zhong J, Cun X, Lin S, Lin Y, et al. Hypoxia enhances angiogenesis in an adipose-derived stromal cell/endothelial cell co-culture 3D gel model. Cell Prolif. 2016 Apr;49(2):236–45.

188. Zhang L, Xing Q, Qian Z, Tahtinen M, Zhang Z, Shearier E, et al. Hypoxia Created Human Mesenchymal Stem Cell Sheet for Prevascularized 3D Tissue Construction. Adv Healthc Mater. 2016 Feb 4;5(3):342–52.

189. Oberringer M, Bubel M, Jennewein M, Guthörl S, Morsch T, Bachmann S, et al. The role of adipose-derived stem cells in a self-organizing 3D model with regard to human soft tissue healing. Mol Cell Biochem. 2018 Aug;445(1–2):195–210.

190. Liu X, Wan X, Kan H, Wang Y, Yu F, Feng L, et al. Hypoxia-induced upregulation of Orai1 drives colon cancer invasiveness and angiogenesis. Eur J Pharmacol. 2018 Aug 5;832:1–10.

191. Tang D, Zhang J, Yan T, Wei J, Jiang X, Zhang D, et al. FG-4592 Accelerates Cutaneous Wound Healing by Epidermal Stem Cell Activation via HIF-1α Stabilization. Cell Physiol Biochem Int J Exp Cell Physiol Biochem Pharmacol. 2018;46(6):2460–70.

192. Bischoff FC, Werner A, John D, Boeckel JN, Melissari MT, Grote P, et al. Identification and Functional Characterization of Hypoxia-Induced Endoplasmic Reticulum Stress Regulating lncRNA (HypERlnc) in Pericytes. Circ Res. 2017 Aug 4;121(4):368–75.

193. Butoi E, Gan AM, Tucureanu MM, Stan D, Macarie RD, Constantinescu C, et al. Cross-talk between macrophages and smooth muscle cells impairs collagen and metalloprotease synthesis and promotes angiogenesis. Biochim Biophys Acta. 2016 Jul;1863(7 Pt A):1568–78.

194. Wobma HM, Tamargo MA, Goeta S, Brown LM, Duran-Struuck R, Vunjak-Novakovic G. The influence of hypoxia and IFN-γ on the proteome and metabolome of therapeutic mesenchymal stem cells. Biomaterials. 2018;167:226–34.

195. Ueda A, Koga M, Ikeda M, Kudo S, Tanishita K. Effect of shear stress on microvessel network formation of endothelial cells with in vitro three-dimensional model. Am J Physiol-Heart Circ Physiol. 2004 Sep 1;287(3):H994–1002.

196. Kang H, Bayless KJ, Kaunas R. Fluid shear stress modulates endothelial cell invasion into three-dimensional collagen matrices. Am J Physiol-Heart Circ Physiol. 2008 Nov 1;295(5):H2087–97.

197. Jung B, Obinata H, Galvani S, Mendelson K, Ding B sen, Skoura A, et al. Flow-regulated endothelial S1P receptor-1 signaling sustains vascular development. Dev Cell. 2012 Sep 11;23(3):600–10.

198. Duran CL, Kaunas R, Bayless KJ. S1P Synergizes with Wall Shear Stress and Other Angiogenic Factors to Induce Endothelial Cell Sprouting Responses. Methods Mol Biol Clifton NJ. 2018;1697:99–115.

199. Frerich B, Zückmantel K, Winter K, Müller-Dürwald S, Hemprich A. Maturation of capillary-like structures in a tube-like construct in perfusion and rotation culture. Int J Oral Maxillofac Surg. 2008 May;37(5):459–66.

200. Sakamoto N, Ohashi T, Sato M. Effect of fluid shear stress on migration of vascular smooth muscle cells in cocultured model. Ann Biomed Eng. 2006 Mar;34(3):408–15.

201. Wang H, Huang L, Qu MJ, Yan ZQ, Liu B, Shen BR, et al. Shear stress protects against endothelial regulation of vascular smooth muscle cell migration in a coculture system. Endothel J Endothel Cell Res. 2006;13(3):171–80.

202. Ye C, Bai L, Yan ZQ, Wang YH, Jiang ZL. Shear stress and vascular smooth muscle cells promote endothelial differentiation of endothelial progenitor cells via activation of Akt. Clin Biomech Bristol Avon. 2008;23 Suppl 1:S118-124.

203. Bazmara H, Soltani M, Sefidgar M, Bazargan M, Mousavi Naeenian M, Rahmim A. The Vital Role of Blood Flow-Induced Proliferation and Migration in Capillary Network Formation in a Multiscale Model of Angiogenesis. PloS One. 2015;10(6):e0128878.

204. Ogunrinade O, Kameya GT, Truskey GA. Effect of fluid shear stress on the permeability of the arterial endothelium. Ann Biomed Eng. 2002 Apr;30(4):430–46.

205. Reneman RS, Arts T, Hoeks APG. Wall shear stress--an important determinant of endothelial cell function and structure--in the arterial system in vivo. Discrepancies with theory. J Vasc Res. 2006;43(3):251–69.

206. Bussmann J, Wolfe SA, Siekmann AF. Arterial-venous network formation during brain vascularization involves hemodynamic regulation of chemokine signaling. Dev Camb Engl. 2011 May;138(9):1717–26.

207. Bazmara H, Soltani M, Sefidgar M, Bazargan M, Mousavi Naeenian M, Rahmim A. Blood flow and endothelial cell phenotype regulation during sprouting angiogenesis. Med Biol Eng Comput. 2016 Mar;54(2–3):547–58.

208. Ghaffari S, Leask RL, Jones EAV. Flow dynamics control the location of sprouting and direct elongation during developmental angiogenesis. Development. 2015 Dec 1;142(23):4151–7.

209. Gebala V, Collins R, Geudens I, Phng LK, Gerhardt H. Blood flow drives lumen formation by inverse membrane blebbing during angiogenesis *in vivo*. Nat Cell Biol. 2016 Apr;18(4):443–50.

210. Peirsman A, Nguyen HT, Waeyenberge MV, Ceballos C, Bolivar J, Kawakita S, et al. Vascularized adipose tissue engineering: moving towards soft tissue reconstruction. Biofabrication. 2023 Jun;15(3):032003.

211. Gutowski KS, Chwa ES, Weissman JP, Garg SP, Simmons CJ, Brandt KE, et al. Practice Profile of Practicing Plastic Surgeons: A 20-year Review of Plastic Surgery Statistics. Plast Reconstr Surg Glob Open. 2023 Dec 22;11(12):e5486.

212. Rodrigues M, Kosaric N, Bonham CA, Gurtner GC. Wound Healing: A Cellular Perspective. Physiol Rev. 2019 Jan 1;99(1):665–706.

213. Singer AJ. Healing Mechanisms in Cutaneous Wounds: Tipping the Balance. Tissue Eng Part B Rev. 2022 Oct 1;28(5):1151–67.

214. Major GS, Simcock JW, Woodfield TBF, Lim KS. Overcoming functional challenges in autologous and engineered fat grafting trends. Trends Biotechnol. 2022 Jan;40(1):77–92.

215. Masson-Meyers DS, Tayebi L. Vascularization strategies in tissue engineering approaches for soft tissue repair. J Tissue Eng Regen Med. 2021 Sep;15(9):747–62.

216. Olson JL, Atala A, Yoo JJ. Tissue Engineering: Current Strategies and Future Directions. Chonnam Med J. 2011 Apr;47(1):1–13.

217. Shirahama H, Lee BH, Tan LP, Cho NJ. Precise Tuning of Facile One-Pot Gelatin Methacryloyl (GelMA) Synthesis. Sci Rep. 2016 Aug 9;6(1):31036.

218. Žigon-Branc S, Markovic M, Van Hoorick J, Van Vlierberghe S, Dubruel P, Zerobin E, et al. Impact of Hydrogel Stiffness on Differentiation of Human Adipose-Derived Stem Cell Microspheroids. Tissue Eng Part A. 2019 Oct;25(19–20):1369–80.

219. Kim C, Young JL, Holle AW, Jeong K, Major LG, Jeong JH, et al. Stem Cell Mechanosensation on Gelatin Methacryloyl (GelMA) Stiffness Gradient Hydrogels. Ann Biomed Eng. 2020 Feb;48(2):893–902.

220. Quan Y, Li J, Cai J, Liao Y, Zhang Y, Lu F. Transplantation of beige adipose organoids fabricated using adipose acellular matrix hydrogel improves metabolic dysfunction in high-fat diet-induced obesity and type 2 diabetes mice. J Cell Physiol. 2024;239(4):e31191.

221. Vaghela R, Arkudas A, Gage D, Körner C, von Hörsten S, Salehi S, et al. Microvascular development in the rat arteriovenous loop model in vivo-A step by step intravital microscopy analysis. J Biomed Mater Res A. 2022 Sep;110(9):1551–63.

222. Liang X, Xie L, Zhang Q, Wang G, Zhang S, Jiang M, et al. Gelatin methacryloyl-alginate core-shell microcapsules as efficient delivery platforms for prevascularized microtissues in endodontic regeneration. Acta Biomater. 2022 May 1;144:242–57.

223. Cheng MH, Chang CW, Wang J, Bupphathong S, Huang W, Lin CH. 3D-Bioprinted GelMA Scaffold with ASCs and HUVECs for Engineering Vascularized Adipose Tissue. ACS Appl Bio Mater. 2024 Jan 15;7(1):406–15.

224. Ojha S, Budge H, Symonds ME. Adipocytes in Normal Tissue Biology. In: McManus LM, Mitchell RN, editors. Pathobiology of Human Disease [Internet]. San Diego: Academic Press; 2014 [cited 2023 Jun 3]. p. 2003–13. Available from: https://www.sciencedirect.com/science/article/pii/B9780123864567044087

225. Wang X, Ackermann M, Neufurth M, Wang S, Li Q, Feng Q, et al. Restoration of Impaired Metabolic Energy Balance (ATP Pool) and Tube Formation Potential of Endothelial Cells under “high glucose”, Diabetic Conditions by the Bioinorganic Polymer Polyphosphate. Polymers. 2017 Nov 4;9(11):575.

226. Assunção M, Dehghan-Baniani D, Yiu CHK, Später T, Beyer S, Blocki A. Cell-Derived Extracellular Matrix for Tissue Engineering and Regenerative Medicine. Front Bioeng Biotechnol [Internet]. 2020 Dec 3 [cited 2024 Mar 28];8. Available from: https://www.frontiersin.org/articles/10.3389/fbioe.2020.602009

227. Huang D, Huang Y, Xiao Y, Yang X, Lin H, Feng G, et al. Viscoelasticity in natural tissues and engineered scaffolds for tissue reconstruction. Acta Biomater. 2019 Oct 1;97:74–92.

228. Hoch E, Schuh C, Hirth T, Tovar GEM, Borchers K. Stiff gelatin hydrogels can be photo-chemically synthesized from low viscous gelatin solutions using molecularly functionalized gelatin with a high degree of methacrylation. J Mater Sci Mater Med. 2012 Nov 1;23(11):2607–17.

229. Sun Y, Deng R, Ren X, Zhang K, Li J. 2D Gelatin Methacrylate Hydrogels with Tunable Stiffness for Investigating Cell Behaviors. ACS Appl Bio Mater. 2019 Jan 22;2(1):570–6.

230. Lee K, Chen Y, Yoshitomi T, Kawazoe N, Yang Y, Chen G. Osteogenic and Adipogenic Differentiation of Mesenchymal Stem Cells in Gelatin Solutions of Different Viscosities. Adv Healthc Mater. 2020;9(23):2000617.

231. Richard AJ, White U, Elks CM, Stephens JM. Adipose Tissue: Physiology to Metabolic Dysfunction. In: Feingold KR, Anawalt B, Blackman MR, Boyce A, Chrousos G, Corpas E, et al., editors. Endotext [Internet]. South Dartmouth (MA): MDText.com, Inc.; 2000 [cited 2024 Jul 15]. Available from: http://www.ncbi.nlm.nih.gov/books/NBK555602/

232. Krishnan L, Chang CC, Nunes SS, Williams SK, Weiss JA, Hoying JB. Manipulating the Microvasculature and Its Microenvironment. Crit Rev Biomed Eng. 2013;41(2):91–123.

233. Chen YC, Lin RZ, Qi H, Yang Y, Bae H, Melero-Martin JM, et al. Functional Human Vascular Network Generated in Photocrosslinkable Gelatin Methacrylate Hydrogels. Adv Funct Mater. 2012 May 23;22(10):2027–39.

234. Salazar-Noratto GE, Luo G, Denoeud C, Padrona M, Moya A, Bensidhoum M, et al. Understanding and leveraging cell metabolism to enhance mesenchymal stem cell transplantation survival in tissue engineering and regenerative medicine applications. STEM CELLS. 2020;38(1):22–33.

235. MacQueen L, Sun Y, Simmons CA. Mesenchymal stem cell mechanobiology and emerging experimental platforms. J R Soc Interface. 2013 Jul 6;10(84):20130179.

236. Almalki SG, Agrawal DK. Effects of matrix metalloproteinases on the fate of mesenchymal stem cells. Stem Cell Res Ther. 2016 Sep 9;7(1):129.

237. Mannello F, Tonti GAM, Bagnara GP, Papa S. Role and Function of Matrix Metalloproteinases in the Differentiation and Biological Characterization of Mesenchymal Stem Cells. Stem Cells. 2006 Mar 1;24(3):475–81.

238. Barnes CH, Maas CS. Autologous Fat Harvest and Preparation for Optimal Predictable Outcomes. Facial Plast Surg Clin N Am. 2019 Aug 1;27(3):419–23.

239. Luck J, Smith OJ, Malik D, Mosahebi A. Protocol for a systematic review of autologous fat grafting for wound healing. Syst Rev. 2018 Jul 18;7(1):99.

240. Malik D, Luck J, Smith OJ, Mosahebi A. A Systematic Review of Autologous Fat Grafting in the Treatment of Acute and Chronic Cutaneous Wounds. Plast Reconstr Surg Glob Open. 2020 May;8(5):e2835.

241. Turner A, Abu-Ghname A, Davis MJ, Winocour SJ, Hanson SE, Chu CK. Fat Grafting in Breast Reconstruction. Semin Plast Surg. 2020 Feb;34(1):17–23.

242. Clauser L. Autologous Facial Fat Transfer: Soft Tissue Augmentation and Regnenerative Therapy. J Craniofac Surg. 2020 Oct;31(7):1879.

243. Kaoutzanis C, Xin M, Ballard TNS, Welch KB, Momoh AO, Kozlow JH, et al. Autologous Fat Grafting After Breast Reconstruction in Postmastectomy Patients: Complications, Biopsy Rates, and Locoregional Cancer Recurrence Rates. Ann Plast Surg. 2016 Mar;76(3):270–5.

244. Upadhyaya SN, Bernard SL, Grobmyer SR, Yanda C, Tu C, Valente SA. Outcomes of Autologous Fat Grafting in Mastectomy Patients Following Breast Reconstruction. Ann Surg Oncol. 2018 Oct;25(10):3052–6.

245. Wederfoort JLM, Hebels SA, Heuts EM, van der Hulst RRWJ, Piatkowski AA. Donor site complications and satisfaction in autologous fat grafting for breast reconstruction: A systematic review. J Plast Reconstr Aesthet Surg. 2022 Apr 1;75(4):1316–27.

246. Yoshimura K, Coleman S. Complications of Fat Grafting. Clin Plast Surg. 2015 May 16;42.

247. Janmaleki M, Liu J, Kamkar M, Azarmanesh M, Sundararaj U, Nezhad AS. Role of temperature on bio-printability of gelatin methacryloyl bioink in two-step cross-linking strategy for tissue engineering applications. Biomed Mater Bristol Engl. 2020 Dec 16;16(1):015021.

248. Leu Alexa R, Iovu H, Ghitman J, Serafim A, Stavarache C, Marin MM, et al. 3D-Printed Gelatin Methacryloyl-Based Scaffolds with Potential Application in Tissue Engineering. Polymers. 2021 Feb 27;13(5):727.

249. Xie M, Yu K, Sun Y, Shao L, Nie J, Gao Q, et al. Protocols of 3D Bioprinting of Gelatin Methacryloyl Hydrogel Based Bioinks. J Vis Exp JoVE. 2019 Dec 21;(154).

250. Arguchinskaya NV, Isaeva EV, Kisel AA, Beketov EE, Lagoda TS, Baranovskii DS, et al. Properties and Printability of the Synthesized Hydrogel Based on GelMA. Int J Mol Sci. 2023 Jan 20;24(3):2121.

251. Choi BY, Chalisserry EP, Kim MH, Kang HW, Choi IW, Nam SY. The Influence of Astaxanthin on the Proliferation of Adipose-derived Mesenchymal Stem Cells in Gelatin-Methacryloyl (GelMA) Hydrogels. Mater Basel Switz. 2019 Jul 29;12(15):2416.

252. Tytgat L, Van Damme L, Ortega Arevalo MDP, Declercq H, Thienpont H, Otteveare H, et al. Extrusion-based 3D printing of photo-crosslinkable gelatin and κ-carrageenan hydrogel blends for adipose tissue regeneration. Int J Biol Macromol. 2019 Nov 1;140:929–38.

253. Albrecht FB, Schmidt FF, Volz AC, Kluger PJ. Bioprinting of 3D Adipose Tissue Models Using a GelMA-Bioink with Human Mature Adipocytes or Human Adipose-Derived Stem Cells. Gels Basel Switz. 2022 Sep 25;8(10):611.

254. Benayahu D, Wiesenfeld Y, Sapir-Koren R. How is mechanobiology involved in mesenchymal stem cell differentiation toward the osteoblastic or adipogenic fate? J Cell Physiol. 2019 Aug;234(8):12133–41.

255. Khan AU, Qu R, Fan T, Ouyang J, Dai J. A glance on the role of actin in osteogenic and adipogenic differentiation of mesenchymal stem cells. Stem Cell Res Ther. 2020 Jul 16;11(1):283.

256. Su T, Xu M, Lu F, Chang Q. Adipogenesis or osteogenesis: destiny decision made by mechanical properties of biomaterials. RSC Adv. 2022 Aug 30;12(38):24501–10.

257. Major LG, Holle AW, Young JL, Hepburn MS, Jeong K, Chin IL, et al. Volume Adaptation Controls Stem Cell Mechanotransduction. ACS Appl Mater Interfaces. 2019 Dec 11;11(49):45520–30.

258. Bouzid T, Esfahani AM, Safa BT, Kim E, Saraswathi V, Kim JK, et al. Rho/ROCK mechanosensor in adipocyte stiffness and traction force generation. Biochem Biophys Res Commun. 2022 May 28;606:42–8.

259. Calvo-Gallego JL, Domínguez J, Gómez Cía T, Gómez Ciriza G, Martínez-Reina J. Comparison of different constitutive models to characterize the viscoelastic properties of human abdominal adipose tissue. A pilot study. J Mech Behav Biomed Mater. 2018 Apr;80:293–302.

260. Sommer G, Eder M, Kovacs L, Pathak H, Bonitz L, Mueller C, et al. Multiaxial mechanical properties and constitutive modeling of human adipose tissue: a basis for preoperative simulations in plastic and reconstructive surgery. Acta Biomater. 2013 Nov;9(11):9036–48.

261. Sun Z, Gepner BD, Cottler PS, Lee SH, Kerrigan JR. In Vitro Mechanical Characterization and Modeling of Subcutaneous Adipose Tissue: A Comprehensive Review. J Biomech Eng. 2021 Jul 1;143(7):070803.

262. Liu C, Yu Q, Yuan Z, Guo Q, Liao X, Han F, et al. Engineering the viscoelasticity of gelatin methacryloyl (GelMA) hydrogels via small “dynamic bridges” to regulate BMSC behaviors for osteochondral regeneration. Bioact Mater. 2022 Aug 6;25:445–59.

263. Zheng J, Wang Y, Kawazoe N, Yang Y, Chen G. Influences of viscosity on the osteogenic and adipogenic differentiation of mesenchymal stem cells with controlled morphology. J Mater Chem B. 2022 Jun 1;10(21):3989–4001.

264. Yin X, Chen Y, Ruze R, Xu R, Song J, Wang C, et al. The evolving view of thermogenic fat and its implications in cancer and metabolic diseases. Signal Transduct Target Ther. 2022 Sep 16;7(1):1–21.

265. Dey M, Ozbolat IT. 3D bioprinting of cells, tissues and organs. Sci Rep. 2020 Aug 18;10(1):14023.

266. Matai I, Kaur G, Seyedsalehi A, McClinton A, Laurencin CT. Progress in 3D bioprinting technology for tissue/organ regenerative engineering. Biomaterials. 2020 Jan;226:119536.

267. Mughal M, Sindali K, Man J, Roblin P. “Fat chance”: a review of adipose tissue engineering and its role in plastic and reconstructive surgery. Ann R Coll Surg Engl. 2021 Apr;103(4):245–9.

268. Takata K, Goto T, Kuroda M, Kimura Y, Harada I, Ueda K, et al. Stiffness of the extracellular matrix regulates differentiation into beige adipocytes. Biochem Biophys Res Commun. 2020 Nov 5;532(2):205–10.

269. Li Y, Bi X, Wu M, Chen X, Zhan W, Dong Z, et al. Adjusting the stiffness of a cell-free hydrogel system based on tissue-specific extracellular matrix to optimize adipose tissue regeneration. Burns Trauma. 2023;11:tkad002.

270. Ali M, PR AK, Yoo JJ, Zahran F, Atala A, Lee SJ. A Photo-crosslinkable Kidney ECM-derived Bioink Accelerates Renal Tissue Formation. Adv Healthc Mater. 2019 Apr;8(7):e1800992.

271. Sabaté-Pérez A, Romero M, Sànchez-Fernàndez-de-Landa P, Carobbio S, Mouratidis M, Sala D, et al. Autophagy-mediated NCOR1 degradation is required for brown fat maturation and thermogenesis. Autophagy. 2023 Mar;19(3):904–25.

272. Angueira AR, Sakers AP, Holman CD, Cheng L, Arbocco MN, Shamsi F, et al. Defining the lineage of thermogenic perivascular adipose tissue. Nat Metab. 2021 Apr;3(4):469–84.

273. Samuelson I, Vidal-Puig A. Studying Brown Adipose Tissue in a Human in vitro Context. Front Endocrinol. 2020;11:629.

274. Cereijo R, Giralt M, Villarroya F. Thermogenic brown and beige/brite adipogenesis in humans. Ann Med. 2015 Mar;47(2):169–77.

275. Park A, Kim WK, Bae KH. Distinction of white, beige and brown adipocytes derived from mesenchymal stem cells. World J Stem Cells. 2014 Jan 26;6(1):33–42.

276. Giralt M, Villarroya F. White, brown, beige/brite: different adipose cells for different functions? Endocrinology. 2013 Sep;154(9):2992–3000.

277. Shao X, Wang M, Wei X, Deng S, Fu N, Peng Q, et al. Peroxisome Proliferator-Activated Receptor-γ: Master Regulator of Adipogenesis and Obesity. Curr Stem Cell Res Ther. 2016;11(3):282–9.

278. Rabiee A. Beige Fat Maintenance; Toward a Sustained Metabolic Health. Front Endocrinol. 2020 Sep 4;11:634.

279. Song A, Dai W, Jang MJ, Medrano L, Li Z, Zhao H, et al. Low- and high-thermogenic brown adipocyte subpopulations coexist in murine adipose tissue. J Clin Invest. 130(1):247–57.

280. Sun Y, Chen S, Pei M. Comparative advantages of infrapatellar fat pad: an emerging stem cell source for regenerative medicine. Rheumatology. 2018 Dec 1;57(12):2072–86.

281. Labusca L, Zugun-Eloae F. The Unexplored Role of Intra-articular Adipose Tissue in the Homeostasis and Pathology of Articular Joints. Front Vet Sci. 2018 Mar 5;5:35.

282. Mondragon N, Zito PM. Pressure Injury. In: StatPearls [Internet]. Treasure Island (FL): StatPearls Publishing; 2024 [cited 2024 Jul 17]. Available from: http://www.ncbi.nlm.nih.gov/books/NBK557868/

283. Bruce JC, Batchinsky M, Van Spronsen NR, Sinha I, Bharadia D. Analysis of online materials regarding DIEP and TRAM flap autologous breast reconstruction. J Plast Reconstr Aesthetic Surg JPRAS. 2023 Jul;82:81–91.

284. Knoedler S, Hoch CC, Huelsboemer L, Knoedler L, Stögner VA, Pomahac B, et al. Postoperative free flap monitoring in reconstructive surgery-man or machine? Front Surg. 2023;10:1130566.

285. Noh KM, Park SJ, Moon SH, Jung SY. Extracellular matrix cues regulate the differentiation of pluripotent stem cell-derived endothelial cells. Front Cardiovasc Med. 2023 Jun 26;10:1169331.

286. Chen Q, Wang W, Yuan C, Wang P. [Research progress of matrix stiffness in regulating endothelial cell sprouting]. Zhongguo Xiu Fu Chong Jian Wai Ke Za Zhi Zhongguo Xiufu Chongjian Waike Zazhi Chin J Reparative Reconstr Surg. 2023 Feb 15;37(2):202–7.

287. Gordon E, Schimmel L, Frye M. The Importance of Mechanical Forces for in vitro Endothelial Cell Biology. Front Physiol. 2020;11:684.

288. Costa L, Reis RL, Silva-Correia J, Oliveira JM. Microfluidics for Angiogenesis Research. Adv Exp Med Biol. 2020;1230:97–119.

289. Jannatbabaei A, Tafazzoli-Shadpour M, Seyedjafari E. Effects of substrate mechanics on angiogenic capacity and nitric oxide release in human endothelial cells. Ann N Y Acad Sci. 2020;1470(1):31–43.

290. Hanjaya-Putra D, Yee J, Ceci D, Truitt R, Yee D, Gerecht S. Vascular endothelial growth factor and substrate mechanics regulate in vitro tubulogenesis of endothelial progenitor cells. J Cell Mol Med. 2010 Oct;14(10):2436–47.

291. Ferrari D, Sengupta A, Heo L, Pethö L, Michler J, Geiser T, et al. Effects of biomechanical and biochemical stimuli on angio- and vasculogenesis in a complex microvasculature-on-chip. iScience. 2023 Feb 13;26(3):106198.

292. Yu Y, Leng Y, Song X, Mu J, Ma L, Yin L, et al. Extracellular Matrix Stiffness Regulates Microvascular Stability by Controlling Endothelial Paracrine Signaling to Determine Pericyte Fate. Arterioscler Thromb Vasc Biol. 2023 Oct;43(10):1887–99.

293. Elosegui-Artola A. The extracellular matrix viscoelasticity as a regulator of cell and tissue dynamics. Curr Opin Cell Biol. 2021 Oct 1;72:10–8.

294. Xu L, Zhang Z, Jorgensen AM, Yang Y, Jin Q, Zhang G, et al. Bioprinting a skin patch with dual-crosslinked gelatin (GelMA) and silk fibroin (SilMA): An approach to accelerating cutaneous wound healing. Mater Today Bio. 2023 Jan 14;18:100550.

295. Jung J, Oh J. Swelling characterization of photo-cross-linked gelatin methacrylate spherical microgels for bioencapsulation. E-Polym. 2014 May 1;14(3):161–8.

296. Lavrentieva A, Fleischhammer T, Enders A, Pirmahboub H, Bahnemann J, Pepelanova I. Fabrication of Stiffness Gradients of GelMA Hydrogels Using a 3D Printed Micromixer. Macromol Biosci. 2020;20(7):2000107.

297. Roux E, Bougaran P, Dufourcq P, Couffinhal T. Fluid Shear Stress Sensing by the Endothelial Layer. Front Physiol [Internet]. 2020 Jul 24 [cited 2024 Jul 19];11. Available from: https://www.frontiersin.org/journals/physiology/articles/10.3389/fphys.2020.00861/full

298. He M, Martin M, Marin T, Chen Z, Gongol B. Endothelial mechanobiology. APL Bioeng. 2020 Feb 20;4(1):010904.

299. Galie PA, Nguyen DHT, Choi CK, Cohen DM, Janmey PA, Chen CS. Fluid shear stress threshold regulates angiogenic sprouting. Proc Natl Acad Sci U S A. 2014 Jun 3;111(22):7968–73.

300. Kohn JC, Zhou DW, Bordeleau F, Zhou AL, Mason BN, Mitchell MJ, et al. Cooperative effects of matrix stiffness and fluid shear stress on endothelial cell behavior. Biophys J. 2015 Feb 3;108(3):471–8.

301. Korn C, Augustin HG. Mechanisms of Vessel Pruning and Regression. Dev Cell. 2015 Jul 6;34(1):5–17.

302. Santamaría R, González-Álvarez M, Delgado R, Esteban S, Arroyo AG. Remodeling of the Microvasculature: May the Blood Flow Be With You. Front Physiol. 2020 Oct 15;11:586852.

303. Shinde AV, Humeres C, Frangogiannis NG. The role of α-smooth muscle actin in fibroblast-mediated matrix contraction and remodeling. Biochim Biophys Acta BBA - Mol Basis Dis. 2017 Jan 1;1863(1):298–309.

304. Hinz B, Celetta G, Tomasek JJ, Gabbiani G, Chaponnier C. Alpha-Smooth Muscle Actin Expression Upregulates Fibroblast Contractile Activity. Mol Biol Cell. 2001 Sep;12(9):2730–41.

305. Shinde AV, Kelsh R, Peters JH, Sekiguchi K, Van De Water L, McKeown-Longo PJ. THE α4β1 INTEGRIN AND THE EDA DOMAIN OF FIBRONECTIN REGULATE A PROFIBROTIC PHENOTYPE IN DERMAL FIBROBLASTS. Matrix Biol J Int Soc Matrix Biol. 2015 Jan;41:26–35.

306. Willems IE, Havenith MG, De Mey JG, Daemen MJ. The alpha-smooth muscle actin-positive cells in healing human myocardial scars. Am J Pathol. 1994 Oct;145(4):868–75.

307. Grigorieva O, Basalova N, Vigovskiy M, Arbatskiy M, Dyachkova U, Kulebyakina M, et al. Novel Potential Markers of Myofibroblast Differentiation Revealed by Single-Cell RNA Sequencing Analysis of Mesenchymal Stromal Cells in Profibrotic and Adipogenic Conditions. Biomedicines. 2023 Mar 10;11(3):840.

308. Yuan SM. α-Smooth Muscle Actin and ACTA2 Gene Expressions in Vasculopathies. Braz J Cardiovasc Surg. 2015;30(6):644–9.

309. Hu B, Wu Z, Phan SH. Smad3 Mediates Transforming Growth Factor-β–Induced α-Smooth Muscle Actin Expression. Am J Respir Cell Mol Biol. 2003 Sep;29(3):397–404.

310. Lloyd SM, He Y. Exploring Extracellular Matrix Crosslinking as a Therapeutic Approach to Fibrosis. Cells. 2024 Jan;13(5):438.

311. Jang HH, Son Y, Park G, Park KS. Bone Marrow-Derived Vasculogenic Mesenchymal Stem Cells Enhance In Vitro Angiogenic Sprouting of Human Umbilical Vein Endothelial Cells. Int J Mol Sci. 2022 Dec 27;24(1):413.

312. Gan Q, Yoshida T, Li J, Owens GK. Smooth muscle cells and myofibroblasts use distinct transcriptional mechanisms for smooth muscle alpha-actin expression. Circ Res. 2007 Oct 26;101(9):883–92.

313. Cheng L, Yue H, Zhang H, Liu Q, Du L, Liu X, et al. The influence of microenvironment stiffness on endothelial cell fate: Implication for occurrence and progression of atherosclerosis. Life Sci. 2023 Dec 1;334:122233.

314. Butcher DT, Alliston T, Weaver VM. A tense situation: forcing tumour progression. Nat Rev Cancer. 2009 Feb;9(2):108–22.

315. Guo A, Zhang S, Yang R, Sui C. Enhancing the mechanical strength of 3D printed GelMA for soft tissue engineering applications. Mater Today Bio. 2023 Dec 30;24:100939.

316. Mora-Boza A, Włodarczyk-Biegun MK, Campo A del, Vázquez-Lasa B, Román JS. Glycerylphytate as an ionic crosslinker for 3D printing of multi-layered scaffolds with improved shape fidelity and biological features. Biomater Sci. 2019 Dec 17;8(1):506–16.

317. Myers PL, Nelson JA, Allen RJ. Alternative flaps in autologous breast reconstruction. Gland Surg. 2021 Jan;10(1):444–59.

318. Han C, Barakat M, DiPietro LA. Angiogenesis in Wound Repair: Too Much of a Good Thing? Cold Spring Harb Perspect Biol. 2022 Oct 1;14(10):a041225.

319. Katoh K. Effects of Mechanical Stress on Endothelial Cells In Situ and In Vitro. Int J Mol Sci. 2023 Nov 20;24(22):16518.

320. Gregorovicova M, Lashkarinia SS, Yap CH, Tomek V, Sedmera D. Hemodynamics During Development and Postnatal Life. In: Rickert-Sperling S, Kelly RG, Haas N, editors. Congenital Heart Diseases: The Broken Heart: Clinical Features, Human Genetics and Molecular Pathways [Internet]. Cham: Springer International Publishing; 2024 [cited 2024 Jul 25]. p. 201–26. Available from: https://doi.org/10.1007/978-3-031-44087-8_11

321. Ando J, Yamamoto K. Hemodynamic Forces, Endothelial Mechanotransduction, and Vascular Diseases. Magn Reson Med Sci MRMS Off J Jpn Soc Magn Reson Med. 2022 Mar 1;21(2):258–66.

322. Tanaka K, Joshi D, Timalsina S, Schwartz MA. Early events in endothelial flow sensing. Cytoskeleton. 2021;78(6):217–31.

323. Russo TA, Banuth AMM, Nader HB, Dreyfuss JL. Altered shear stress on endothelial cells leads to remodeling of extracellular matrix and induction of angiogenesis. PloS One. 2020;15(11):e0241040.

324. Hattori K, Munehira Y, Kobayashi H, Satoh T, Sugiura S, Kanamori T. Microfluidic perfusion culture chip providing different strengths of shear stress for analysis of vascular endothelial function. J Biosci Bioeng. 2014 Sep 1;118(3):327–32.

325. Sugiura S, Shin K, Kanamori T. Perfusion culture of endothelial cells under shear stress on microporous membrane in a pressure-driven microphysiological system. J Biosci Bioeng. 2023 Jan;135(1):79–85.

326. Satoh T, Narazaki G, Sugita R, Kobayashi H, Sugiura S, Kanamori T. A pneumatic pressure-driven multi-throughput microfluidic circulation culture system. Lab Chip. 2016 Jun 7;16(12):2339–48.

327. Li Y, Qin Z, Zhou L, Shahzad KA, Xia D. Collective influence of substrate chemistry with physiological fluid shear stress on human umbilical vein endothelial cells. Cell Biol Int. 2021 Sep;45(9):1926–34.

328. Avari H, Savory E, Rogers KA. An In Vitro Hemodynamic Flow System to Study the Effects of Quantified Shear Stresses on Endothelial Cells. Cardiovasc Eng Technol. 2016 Mar 1;7(1):44–57.

329. Chen D, Rukhlenko OS, Coon BG, Joshi D, Chakraborty R, Martin KA, et al. VEGF counteracts shear stress-determined arterial fate specification during capillary remodeling. BioRxiv Prepr Serv Biol. 2024 Jan 25;2024.01.23.576920.

330. Ghaffari S, Leask RL, Jones EAV. Simultaneous imaging of blood flow dynamics and vascular remodelling during development. Development. 2015 Dec 1;142(23):4158–67.

331. Ghaffari S, Leask RL, Jones EAV. Flow dynamics control the location of sprouting and direct elongation during developmental angiogenesis. Development. 2015 Dec 1;142(23):4151–7.

332. Sedlak JM, Clyne AM. A Modified Parallel Plate Flow Chamber to Study Local Endothelial Response to Recirculating Disturbed Flow. J Biomech Eng. 2020 Apr 1;142(4):0410031–04100312.

333. Shirure VS, Hughes CCW, George SC. Engineering Vascularized Organoid-on-a-Chip Models. Annu Rev Biomed Eng. 2021 Jul 13;23:141–67.

334. Yu T, Yang Q, Peng B, Gu Z, Zhu D. Vascularized organoid-on-a-chip: design, imaging, and analysis. Angiogenesis. 2024 May;27(2):147–72.

335. Ahmed H, Ramesan S, Lee L, Rezk AR, Yeo LY. On-Chip Generation of Vortical Flows for Microfluidic Centrifugation. Small Weinh Bergstr Ger. 2020 Mar;16(9):e1903605.

336. Kamel B, Ilhem K, Ali F, Abdelbaki D. 3D Simulation of Velocity Profile of Turbulent Flow in Open Channel with Complex Geometry. Phys Procedia. 2014 Jan 1;55:119–28.

337. Gandhi B, Abraham B. Investigation of Flow Profile in Open Channels using CFD. In 2010 [cited 2024 Aug 1]. Available from: https://www.semanticscholar.org/paper/Investigation-of-Flow-Profile-in-Open-Channels-CFD-Gandhi-Abraham/93226c3a8632d45019cee13b546f07ebf86432cf

338. Sabnis A, Rahimi M, Chapman C, Nguyen KT. Cytocompatibility Studies of an in situ Photopolymerized Thermoresponsive Hydrogel Nanoparticle System using Human Aortic Smooth Muscle Cells. J Biomed Mater Res A. 2009 Oct;91(1):52–9.

339. Nguyen AK, Goering PL, Reipa V, Narayan RJ. Toxicity and photosensitizing assessment of gelatin methacryloyl-based hydrogels photoinitiated with lithium phenyl-2,4,6-trimethylbenzoylphosphinate in human primary renal proximal tubule epithelial cells. Biointerphases. 2019 May 3;14(2):021007.

340. Yaralı ZB, Onak G, Karaman O. Effect of Integrin Binding Peptide on Vascularization of Scaffold-Free Microtissue Spheroids. Tissue Eng Regen Med. 2020 Oct;17(5):595–605.

341. Ouyang L, Dan Y, Shao Z, Yang S, Yang C, Liu G, et al. MMP-sensitive PEG hydrogel modified with RGD promotes bFGF, VEGF and EPC-mediated angiogenesis. Exp Ther Med. 2019 Oct;18(4):2933–41.

342. Zhou N, Ma X, Hu W, Ren P, Zhao Y, Zhang T. Effect of RGD content in poly(ethylene glycol)-crosslinked poly(methyl vinyl ether-*alt*-maleic acid) hydrogels on the expansion of ovarian cancer stem-like cells. Mater Sci Eng C. 2021 Jan 1;118:111477.

343. Bassingthwaighte JB. Blood Flow and Diffusion through Mammalian Organs. Science. 1970 Mar 6;167(923):1347–53.

344. Chan TR, Stahl PJ, Li Y, Yu SM. Collagen-Gelatin Mixtures as Wound Model, and Substrates for VEGF-Mimetic Peptide Binding and Endothelial Cell Activation. Acta Biomater. 2015 Mar;15:164–72.

345. Krüger-Genge A, Fuhrmann R, Jung F, Franke RP. Effects of different components of the extracellular matrix on endothelialization. Clin Hemorheol Microcirc. 2017 Feb 2;64(4):867–74.

346. Tran N, Garcia T, Aniqa M, Ali S, Ally A, Nauli S. Endothelial Nitric Oxide Synthase (eNOS) and the Cardiovascular System: in Physiology and in Disease States. Am J Biomed Sci Res. 2022;15(2):153–77.

347. Cheng H, Zhong W, Wang L, Zhang Q, Ma X, Wang Y, et al. Effects of shear stress on vascular endothelial functions in atherosclerosis and potential therapeutic approaches. Biomed Pharmacother. 2023 Feb 1;158:114198.

348. Zhao Y, Ren P, Li Q, Umar SA, Yang T, Dong Y, et al. Low Shear Stress Upregulates CX3CR1 Expression by Inducing VCAM-1 via the NF-κB Pathway in Vascular Endothelial Cells. Cell Biochem Biophys. 2020;78(3):383–9.

APPENDICES

APPENDIX A. GELMA SYNTHESIS PROTOCOL

1. Prepare a **0.1M carbon bicarbonate (CB) buffer** solution [Note: 1 packet in 1L diH20]
2. Prepare a 10% (w/v) **porcine gelatin solution** in 0.1M CB buffer and stir at 500rpm and 60°C. [Note: 20g of gelatin in 200mL of CB buffer]
3. Transfer the solution to a **round bottom flask** (500mL volume; 14/20 neck) and continue to stir the gelatin solution at 500rpm and 50°C.
4. Adjust the reaction pH to 9 using 0.1M **NaOH** (if too acidic) or 5N **Acetic Acid** (if too basic).
5. Add small volumes of **methacrylic anhydride** (MAA) using the sequential method based on the desired degree of functionalization.

Polymer Name	Theoretical DoM (%)	MAA (µL) per 1g Gelatin	Synthesis Method	Buffer Solution	MAA (µL) per 200mL Reaction	Total MAA (µL) per addition (5x)
GelMA35	35%	25 ± 2.8	Sequential	0.1M CB	500µL	100µL
GelMA50	50%	36 ± 4.1	Sequential	0.1M CB	720µL	144µL
GelMA60	60%	43 ± 4.9	Sequential	0.1M CB	864µL	172µL
GelMA65	65%	47 ± 5.3	Sequential	0.1M CB	940µL	188µL
GelMA75	75%	54 ± 6.4	Sequential	0.1M CB	1080µL	216µL
GelMA80	80%	58 ± 6.5	Sequential	0.1M CB	1160µL	232µL
GelMA100	100%	1000 (excess)	One-Pot	0.25M CB	20mL	-

6. Adjust the reaction pH to 9 using 0.1M NaOH between each addition of MAA.
7. Repeat steps 3 and 4 every hour until the entire desired volume of MAA is added.
8. After the last MAA addition, let the reaction complete overnight at 40°C.

9. Terminate the reaction by adding small amounts of **5N acetic acid** to titrate the reaction to a pH of 7.4.
10. Transfer the GelMA solution to porous **membrane dialysis tubes** (MWCO= 14kDa) and dialyze the GelMA against deionized water for 3 days. [Note: Change water bath once a day]
11. For 100% DoM of GelMA, add 0.1mL of MAA per gram of gelatin solution to batch reaction. [Note: Prepare 10% (w/v) porcine gelatin solution in 0.25M CB buffer at pH=9, stir for one hour at 500rpm at 50°C]

APPENDIX B. *SQUIGGLE* CHANNEL DESIGN AND DIMENSIONS

Squiggle Channel Design and Geometry

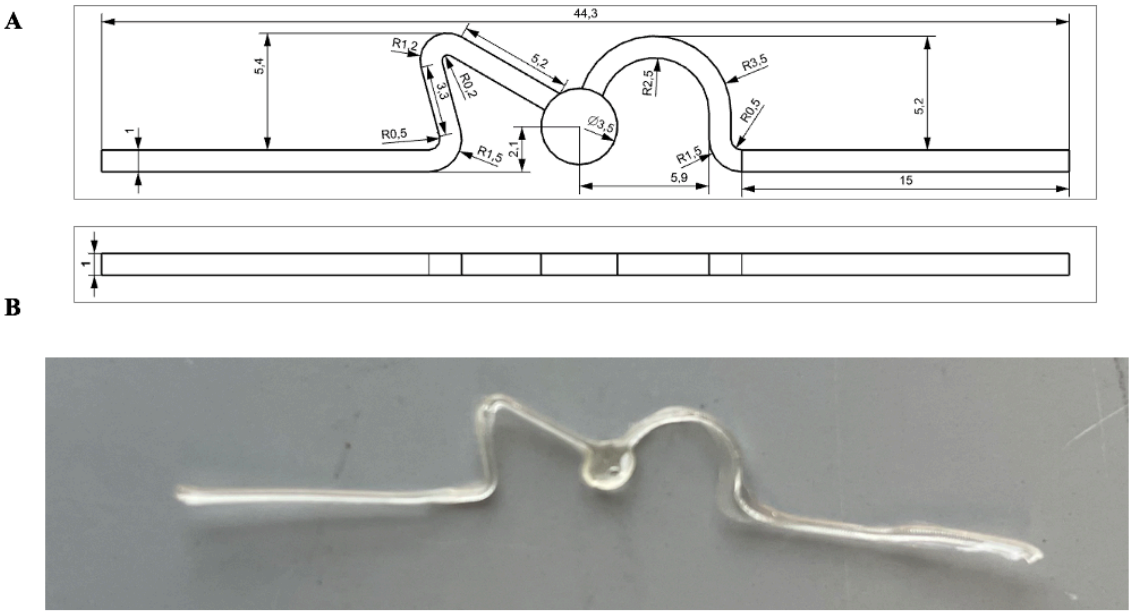

A. Sketch and dimensions of the ***Squiggle*** channel created with Siemens NX software.

B. Optical image of the dehydrated ***Squiggle*** channel made with 20% (w/v) gelatin.

APPENDIX C. MACRO-PERFUSION BIOREACTOR PROTOCOL

Step 1: Sterilization of Materials and Checklist

Macro-perfusion bioreactor parts per device

Materials	Sterilization Process	Qty	Notes
Silicone Insert	Autoclave	1	Sterilize in autoclavable plant containers
MPB Case Bottom	70% Ethanol	1	In BSC, sterilize by completely submerging case bottom in 70% ethanol for 1 minute and set to dry (for 10 minutes) before use
MPB Case Cover	Autoclave	1	Sterilize in autoclavable plant containers
Hex Aligner	70% Ethanol	1	Sterilize separately by completely submerging case bottom in 70% ethanol for 1 minute and set to dry (for 10 minutes). Attach to MPB case bottom once aligner has dried
16G x 1¼" Catheters	Pre-sterilized	2	Commercially available at TERUMO®
MPB Clamp Tops	Autoclave	2	Assemble with clamp bottom prior to autoclaving
MPB Clamp Bottom	Autoclave	1	Assemble with clamp tops prior to autoclaving
Hex Nuts	Autoclave	4	Sterilize in autoclavable plant containers
Wing Nuts	Autoclave	6	Sterilize in autoclavable plant containers
Luer Caps	Autoclave		Sterilize in autoclavable plant containers
Squiggle	Autoclave	1	20% (w/v) gelatin should be autoclaved and stored at 37°C until use. *Squiggle* molds should be stored at 37°C prior to casting. Dehydrate *Squiggle* channels at 4°C for a week. Extract *Squiggle* channels from molds in BSC. Store dehydrated *Squiggle* channels in 4°C until use.
Tray	70% Ethanol	1	Include magnetic strip tapes to secure materials placed on the tray
M3 Hex Screwdriver	Autoclave	1	Keep in BSC after opening
Forceps (large)	Autoclave	1	Keep in BSC after opening
Tweezer	Autoclave	2	Keep in BSC after opening
Paper Towels	Autoclave	10	Keep in BSC after opening
Gloves	Autoclave	1 Box	Keep in BSC after opening

**Note: Clean all autoclavable materials with 70% ethanol prior to autoclave packaging.*

Passive clearing parts per device

Materials	Sterilization Process	Qty	Notes
Masterflex® Precision Pump Tubing	Autoclave	2	Commercially available from Cole-Parmer Instrument Co. Autoclave with assembly
Clearing Reservoir	Autoclave	2	Autoclave with assembly
Masterflex® Female to Male Luer Lock Valves	Autoclave	2	Commercially available from Cole-Parmer Instrument Co. Autoclave with assembly
Masterflex® Female to Female Luer Lock Connector	Autoclave	1	Commercially available from Cole-Parmer Instrument Co. Autoclave with assembly
Masterflex® Luer Hose Barb to Luer Lock	Autoclave	1	Commercially available from Cole-Parmer Instrument Co. Autoclave with assembly
Clearing Caps	Autoclave	2	Autoclave with assembly
Printed Reservoir Holders	70% Ethanol	2	Sterilize separately by completely submerging case bottom in 70% ethanol for 1 minute and set to dry (for 10 minutes).
Acrodisc® 32mm Syringe Filters	Pre-sterilized	2	Commercially available from Pall Corporation Need 1 filter per cap
Gibco® 1X PBS	Pre-sterilized	1	Commercially available from VWR International Need 70mL per device (50mL for inlet, 20mL for outlet)

**Note: Assemble the entire clearing system (without 1X PBS and Syringe Filters) prior to sterilization.*

Biological materials per device

Materials	Sterilization Process	Qty	Notes
GFP-HUVEC	Pre-sterilized	2	Commercially available at Angio-Proteomie
Endothelial Growth Media	Pre-sterilized	2	Commercially available at Angio-Proteomie
Vascular Media	Pre-sterilized	2	Commercially available at PromoCell EGM2 Kit (C-22211 and C-39211) – only include HCS, Ang-1, and VEGFA supplements Include 1%P/S in
6%GelMA60	UV Stimulation	1	Break apart GelMA into fine pieces prior to sterilization

0.5% LAP	Syringe Filtration	2	Prep a working solution of LAP, sterilize via syringe filtration, and use to reconstitute sterilized GelMA

Perfusion system parts per experiment

Materials	Sterilization Process	Qty	Notes
Masterflex® Peristaltic Pump	70% Ethanol	1	Wipe down with 70% Ethanol thoroughly and store in large incubator
Masterflex® Precision Pump Tubing	Autoclave	1	Commercially available from Cole-Parmer Instrument Co. Autoclave with assembly
Masterflex® Tygon® Tubing (Size 14)	Autoclave	1	Commercially available from Cole-Parmer Instrument Co. Autoclave with assembly
Dampener	Autoclave	1	Perfuse with 70% Ethanol prior to autoclaving Autoclave with assembly
Perfusion Reservoir	Autoclave	1	Autoclave with assembly
Perfusion Cap	Autoclave	1	Autoclave with assembly
Acrodisc® 32mm Syringe Filters	Pre-sterilized	1	Commercially available from Pall Corporation Need 1 filter per cap
Printed Reservoir Holders	70% Ethanol	1	Sterilize separately by completely submerging case bottom in 70% ethanol for 1 minute and set to dry (for 10 minutes).

**Note: Assemble the entire perfusion system (without Pump and Syringe Filters) prior to sterilization.*

Step 2: GelMA Casting in Macro-Perfusion Bioreactor with "Squiggle" Channel

Non-Biological Work		
Step No.	**Item**	**Notes**
1	Sterilize all materials and prep MPB device (without Squiggle and GelMA) 1-3 days before experiment	See Step 1A for Checklist
2	Insert Silicone Mold into MPB Case Bottom	This should be done with sterile forceps, note correct alignment of catheter conduits in Case Bottom and Insert.
3	Loosely Secure the Case Bottom with the MPB Case Cover and 2 Butterfly Nuts	Does not have to be tightly secured. This step helps avoid potential contamination by preventing the user from accidentally sticking their finger in the Silicone Insert.
4	Assemble Hex Aligner with MPB Case Bottom	The closed Case can now be handled with gloves in the BSC. An M3 hex key (Allen wrench) might be needed if screw heads are misaligned
5	Insert Catheters (w/ Syringe) through MPB Case Bottom and Silicone Mold and remove syringe needles	The Catheters should be new. This device only supports the use of 16G x 1¼" syringe needles
6	Insert Hex Aligner into MPB Clamp Bottom	Handled with sterile gloves in the BSC
7	Secure Catheters w/ MPB Clamp Tops and Hex Nut screws	There should be 1 MPB Clamp Top and 2 Hex Nut screws for each side. Fasten Hex Nuts securely but do not overtighten. Catheters should not be able to rotate freely
8	Secure the end of each Catheter with a Luer Cap	The system is now closed, place in sterilize packaging, and store at 4°C until use.
Biological Work		
9	Remove MPB Case Cover from MPB device	Be sure to place the MPB Case Cover on its backside to avoid contamination
10	Insert dehydrated *Squiggle* into Catheters	Use sterile forceps to insert the dehydrated squiggle into catheters. Dehydrated squiggles should be stored at 4°C until use.
11	Secure dehydrated *Squiggle* with Gelatin	Sterile Gelatin should be preheated at 37°C (in the incubator) before use. Gelatin must be cooled to room temperature or until it has a viscous consistency. See Step 1 Section A for Gelatin sterilization notes.
12	Solidify Gelatin plugs at RT in BSC for 5 minutes	This is done at room temperature in BSC. Put Case Cover back on the MPB Case Bottom as Gelatin plugs are solidifying to prevent contamination.

13	Cast GelMA in MPB Case Bottom	GelMA should be reconstituted in sterile 0.5% LAP solution and placed in the water bath to dissolve. IMPORTANT: Before casting the GelMA-LAP solution, let it rest at room temperature for about 20 minutes. This is to ensure that the GelMA is slightly gelatinous (or viscous) before casting. *Squiggles* will get ruined if GelMA is too warm. If GelMA solidifies, place it in the water bath for 1-3 minutes to liquify it. See Step 1 Section C for GelMA and LAP sterilization notes.
14	UV Stimulation for 4 minutes	Place the MPB device with GelMA construct directly under the lamp and cover the lamp with foil
15	Top off the GelMA construct with Media (or 1x PBS)	Make sure you fill the remaining volume on the Case. Try to avoid bubbles but it's likely that you will not.
16	Secure MPB device with MPB Case Cover and winged nuts	Be sure to place the sterile side of the MPB Case Cover facing up. Use all 6 of the winged nuts to secure MPB case cover tightly. IMPORTANT: Do not secure catheters with Luer caps
17	Hook up the MPB device to the Passive Clearing Device	See Step 3 for detailed instructions.

**Note: MPB case, device, and system are interchangeable. MPB case bottom and MPB device bottom are interchangeable. MPB case tops and covers are interchangeable.*

Step 3: Passive Clearing Setup

Step No.	Item	Notes
1	Sterilize all materials and prep Clearing System 1-2 days before experiment	See Step 1B for Checklist
2	Place a sterile paper towel underneath the clearing device	Use large sterile forceps to transfer sterile paper towel. This is used to soak up any fluid that leaves the system and prevent sterile MPB parts from touching non-sterile surfaces.
3	Prepare Outlet Reservoir with 20mL of 1X PBS and secure it in the outlet tube rack	The Outlet Reservoir is a 50mL Conical Tube attached to tubing with a Valve at the end. This assembly should already be prepped prior to sterilization.
4	Prepare Inlet Reservoir with 45-50mL of 1X PBS and secure it in the inlet tube rack	The Inlet Reservoir is a 50mL Conical Tube attached to tubing with a Valve at the end. This assembly should already be prepped prior to sterilization.
5	Transfer MPB device to tray	The MPB device should be still in the BSC
6	Open Outlet Valve + Bead Flow + Connect it to the Outlet Catheter of the Cassette	Beading refers to the removal of air in the reservoir tubing. This is done by allowing the solution from the reservoir to fill the tubing with fluid, creating a bead (or droplet) of fluid at the end of the tubing. In this case, the bead should form at the end of the valve. This helps ensure that air bubbles are not trapped in the system, which causes damage.
7	Open Inlet Valve + Bead Flow + Connect it to the Inlet Catheter of the Cassette	Repeat beading technique for the inlet side of the Cassette. The System is now closed and can be transferred in and out the BSC.
8	Replace the old and wet paper towel (from underneath the Clearing set and MPB device) with a new and dry sterile paper towel	Use large sterile forceps to transfer sterile paper towel.
9	Transfer Clearing and MPB Assembly to the incubator for 1 hours	Keep the system on the tray as you transfer it to the BSC. This step allows the channel to dissolve.

Step 4: Lumen Endothelialization

Day 1 of Endothelialization		
Step No.	**Item**	**Notes**
1	Sterilize all materials	See Step 1C for Checklist
2	While *Squiggle* channel is clearing in the Incubator, prep HUVEC for endothelialization	Seeding density: 8-10e6 cells/ mL Approximately 0.5mL is needed to seed each side of the channel, requiring about 1mL of cell suspension per device
3	Ensure *Squiggle* channel has cleared properly in incubator	The fluid height of each reservoir should be equally leveled (about 35mL in each reservoir)
4	Transfer tray (containing the Clearing System and MPB device) from Incubator to BSC	Be careful.
5	Replace the old and wet paper towel (from underneath the Clearing set and MPB device) with a new and dry sterile paper towel	Use large sterile forceps to transfer sterile paper towel.
6	Close Inlet Valve of the Clearing system connected to the MPB device	Inlet Valve should be connected to the Inlet Catheter of the MPB device
7	Disconnect Inlet Clearing Tubing	Be careful.
8	Close Outlet Valve of the Clearing system connected to the MPB device	Outlet Valve should be connected to the Outlet Catheter of the MPB device
9	Disconnect Outlet Clearing Tubing	Be careful.
10	Remove any air bubbles that form at the connection point of each catheter	This step must occur to prevent air bubbles from entering into the *Squiggle* channel
11	Gently inject 0.5mL of cell suspension from the inlet of the catheter to the outlet (**IN to OUT**)	Avoid introducing bubbles into the channel
12	Reconnect the cell laden MPB device to the inlet and outlet of the clearing system and position **RIGHT SIDE UP**	Keep the Inlet Clearing Reservoir valve **CLOSED** and the Outlet Clearing Reservoir valve **OPEN** to allow air flow
13	Replace the old and wet paper towel (from underneath the Clearing set and MPB device) with a new and dry sterile paper towel	Use large sterile forceps to transfer sterile paper towel.

14	Transfer Clearing and cell laden MPB Assembly to the incubator for 24 hours	Keep the system on the tray as you transfer it to the BSC. This step allows the ECs to adhere to the bottom of the channel
Day 2 of Endothelialization		
15	On the next day, prep HUVEC for endothelialization	Seeding density: 8-10e6 cells/ mL Approximately 0.5mL is needed to seed each side of the channel, requiring about 1mL of cell suspension per device
16	Transfer tray (containing the Clearing System and cell laden MPB device) from Incubator to BSC	Be careful.
17	Replace non-sterile paper towel (from underneath the Clearing set and MPB device) with a new sterile paper towel	Use large sterile forceps to transfer sterile paper towel.
18	Close Outlet Valve of the Clearing system connected to the MPB device	Outlet Valve should be connected to the Outlet Catheter of the MPB device
19	Disconnect Outlet Clearing Tubing	Be careful.
20	Disconnect Inlet Clearing Tubing	Be careful.
21	Remove any air bubbles that form at the connection point of each catheter	This step must occur to prevent air bubbles from entering into the *Squiggle* channel
22	Gently inject 0.5mL of cell suspension from the outlet of the catheter to the inlet (**OUT to IN**)	Avoid introducing bubbles into the channel
23	Reconnect the cell laden MPB device to the inlet and outlet of the clearing system and position **UPSIDE DOWN**	Keep the Inlet Clearing Reservoir valve **CLOSED** and the Outlet Clearing Reservoir valve **OPEN** to allow air flow
24	Replace the old and wet paper towel (from underneath the Clearing set and MPB device) with a new and dry sterile paper towel	Use large sterile forceps to transfer sterile paper towel.
25	Transfer Clearing and cell laden MPB Assembly to the incubator for 24 hours	Keep the system on the tray as you transfer it to the BSC. This step allows the ECs to adhere to the bottom of the channel

Step 5: Perfusion System Setup

Step No.	Item	Notes
1	Sterilize all materials	See Step 1D for Checklist
2	Assemble all perfusion materials (without the cell laden MPB device) to construct the closed flow loop	This assembly should be connected prior to sterilization
3	Use the pump to prime each closed flow loop system	This should be performed in the large incubator 1-3 days in advance. Store each closed flow loop in the incubator until use.
4	Transfer the closed flow loop system (minus the pump) from the incubator to the BSC	This should be done one at a time to keep all materials at a physiological temperature. Also, use a separate tray for transferring.
5	Transfer the cell laden MPB device from the incubator to the BSC	This should be done one at a time to keep all materials at a physiological temperature
6	Replace non-sterile paper towel (from underneath the Clearing set and MPB device) with a new sterile paper towel	Use large sterile forceps to transfer sterile paper towel.
7	Close Outlet Valve of the Clearing system connected to the MPB device	Outlet Valve should be connected to the Outlet Catheter of the MPB device
8	Disconnect Outlet Clearing Tubing	Be careful.
9	Disconnect Inlet Clearing Tubing	Be careful.
10	Remove all Clearing System materials	These no longer have to be sterile
11	Transfer primed closed flow loop to MPB device tray	The primed closed loop should be on a tray and not the BSC bench
12	Remove any air bubbles that form at the connection point of each catheter	This step must occur to prevent air bubbles from entering into the *Squiggle* channel
13	Connect inlet tubing to the outlet of the MPB device	Be careful. Avoid introducing air bubbles.
14	Connect outlet tubing to the inlet of the MPB device	Be careful. Avoid introducing air bubbles.
15	Replace the old and wet paper towel (from underneath the Clearing set and MPB device) with a new and dry sterile paper towel	Use large sterile forceps to transfer sterile paper towel.
16	Transfer to entire closed flow loop to the incubator and connect to pump	Ensure the flow rate of the pump is at 0.5mL/min before you start
17	Repeat all step for each cell laden MPB device	This is important so that all materials stay at a physiological temperature for as long as possible

APPENDIX D. BIOREACTOR DESIGN AND ENGINEERED PARTS

Macro-perfusion bioreactor device: Case Bottom

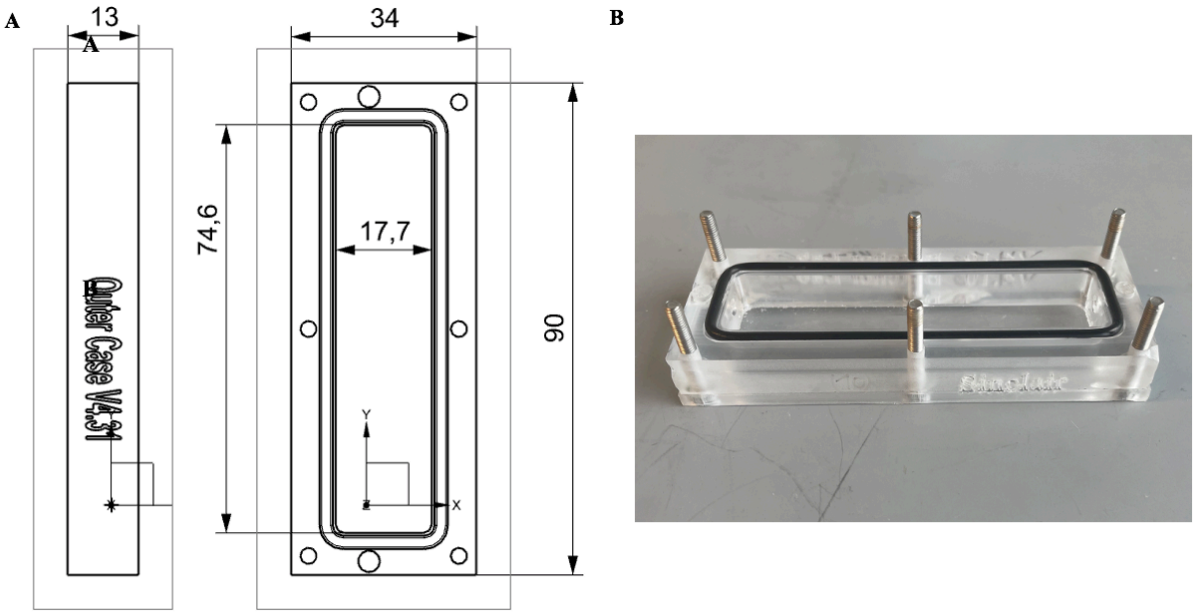

A. Sketch and dimensions of the **MPB Case Bottom** created with Siemens NX software

B. Optical image of the **MPB Case Bottom** made from polycarbonate with a black rubber O-ring gasket purchased from McMaster-Carr.

Macro-perfusion bioreactor device: Silicone Insert

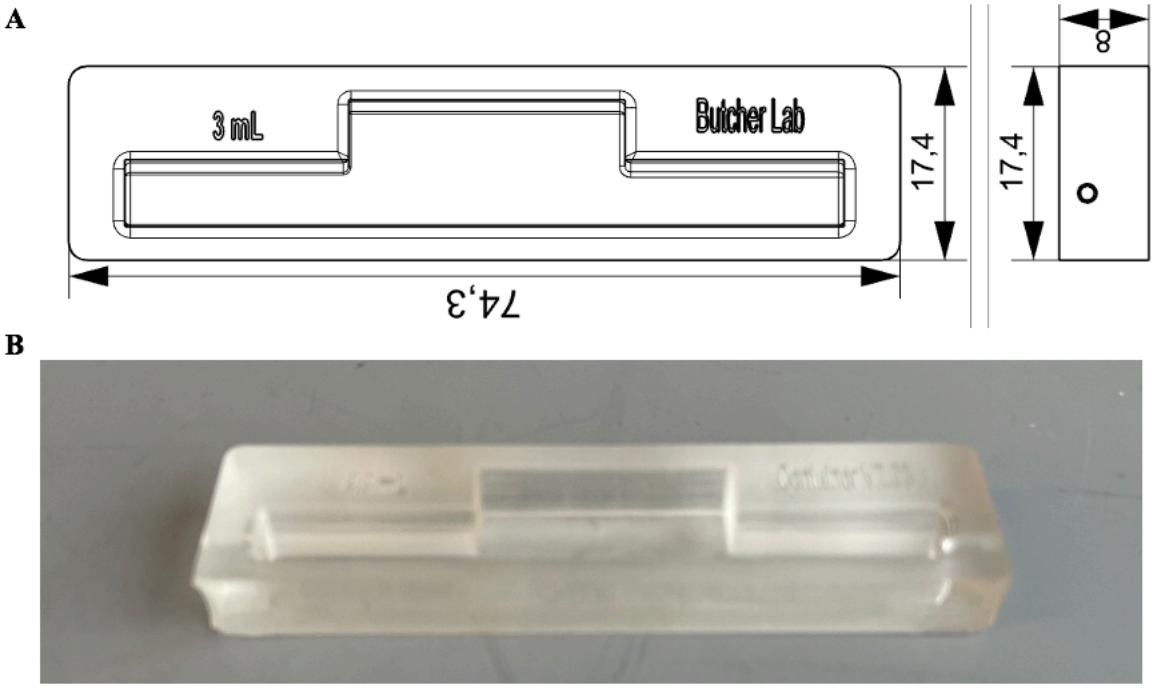

A. Sketch and dimensions of the **MPB Silicone Insert** created with Siemens NX software.

B. Optical image of the **MPB Silicone Insert** made from PDMS.

Macro-perfusion bioreactor device: Case Cover

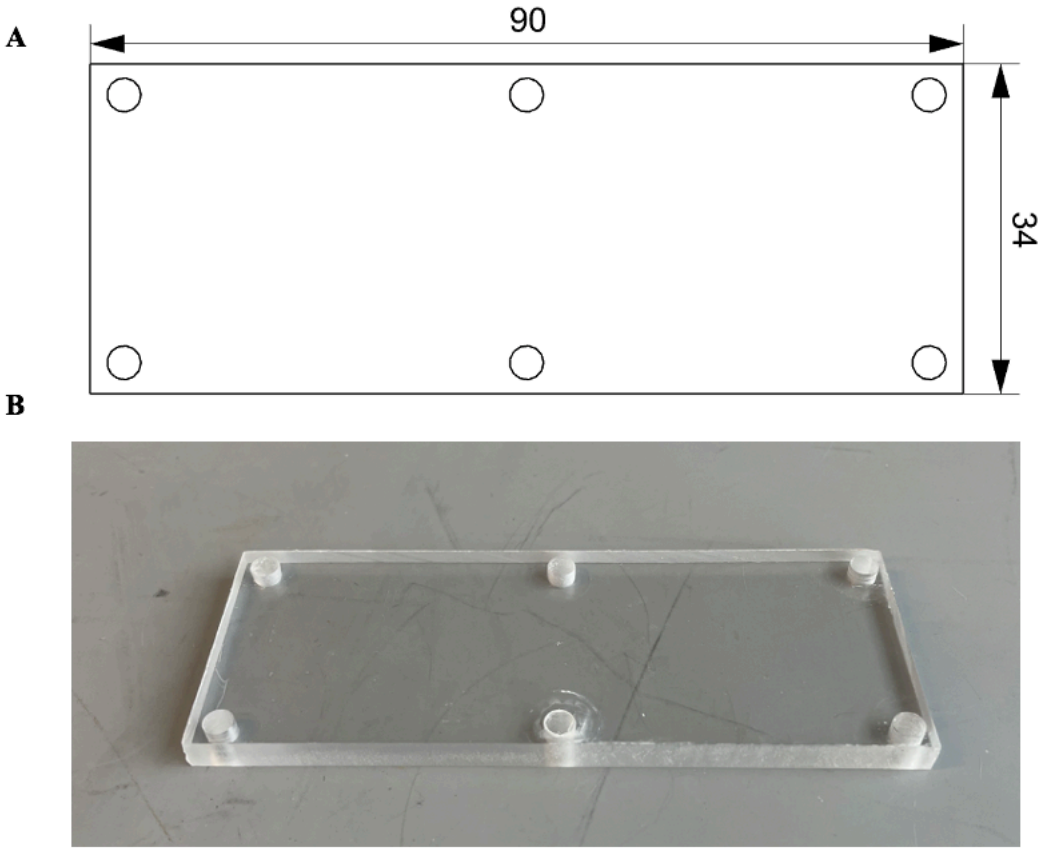

A. Sketch and dimensions of the **MPB Case Cover** created with Siemens NX software.

B. Optical image of the **MPB Case Cover** made from polycarbonate.

Macro-perfusion bioreactor device: Catheter Clamp Assembly

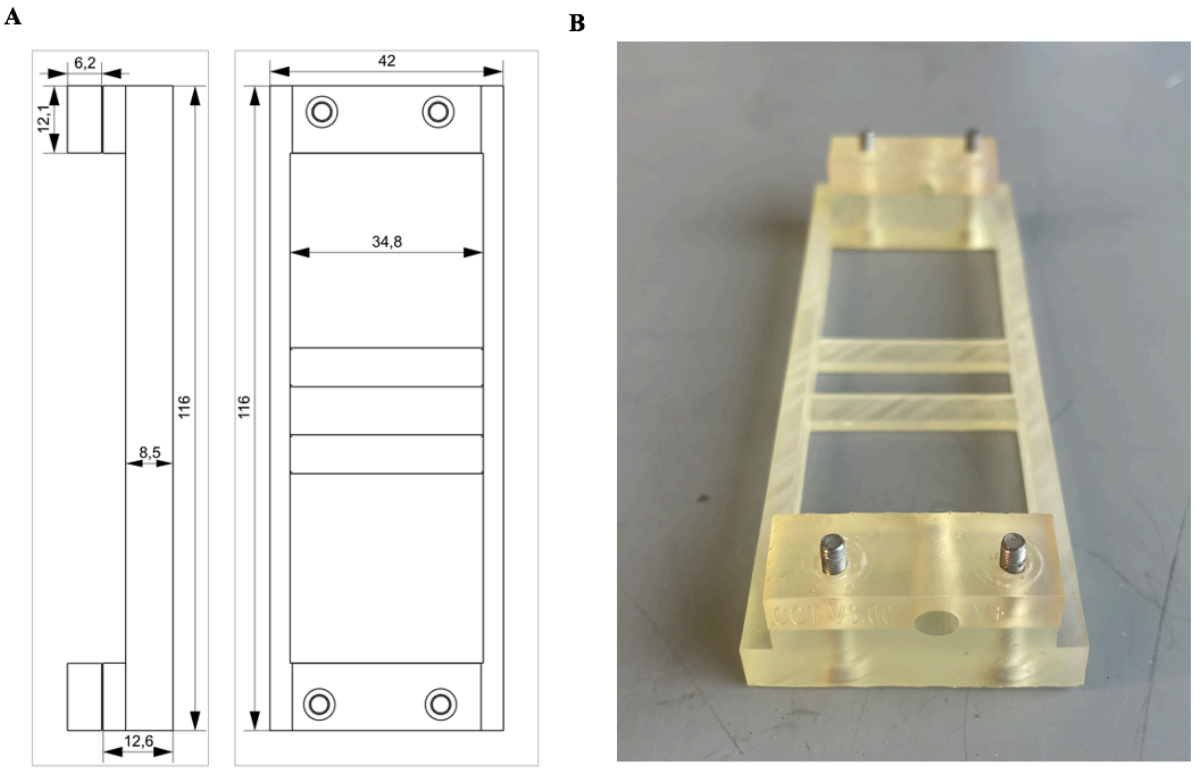

A. Sketch and dimensions of the **MPB Catheter Clamp Assembly** created with Siemens NX software.

B. Optical image of the **MPB Catheter Clamp Assembly** 3D-printed with high-temperature resin.

Macro-perfusion bioreactor device: Hex Aligner

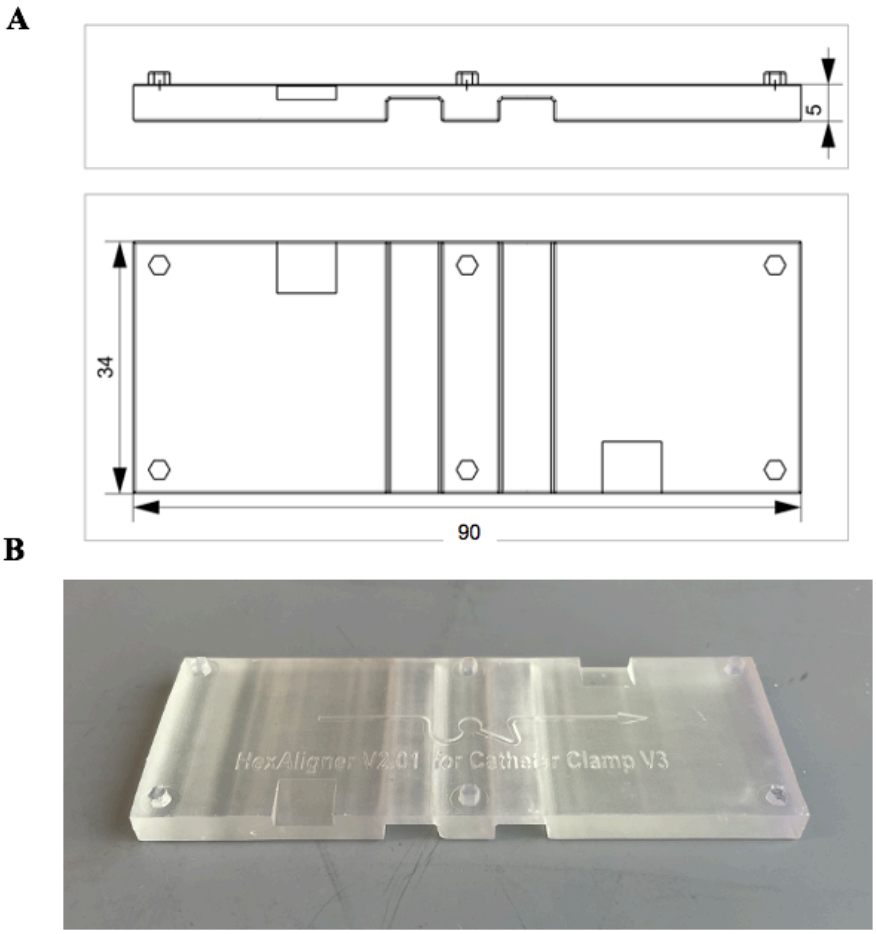

A. Sketch and dimensions of the **MPB Hex Aligner** created with Siemens NX software.

B. Optical image of the **MPB Hex Aligner** 3D-printed with high-temperature resin.

Macro-perfusion bioreactor device: Reservoir Caps

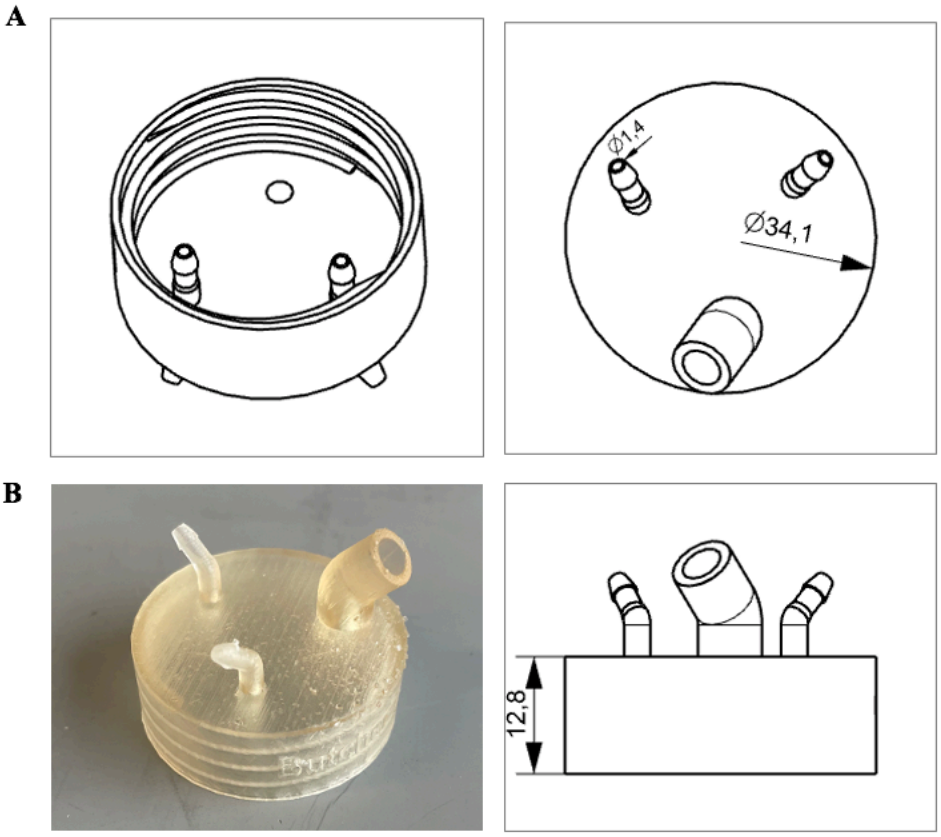

A. Sketch and dimensions of the **MPB Reservoir Cap** created with Siemens NX software.

B. Optical image of the **MPB Reservoir Cap** 3D-printed with BioMed resin.

Clearing System: Reservoir Caps

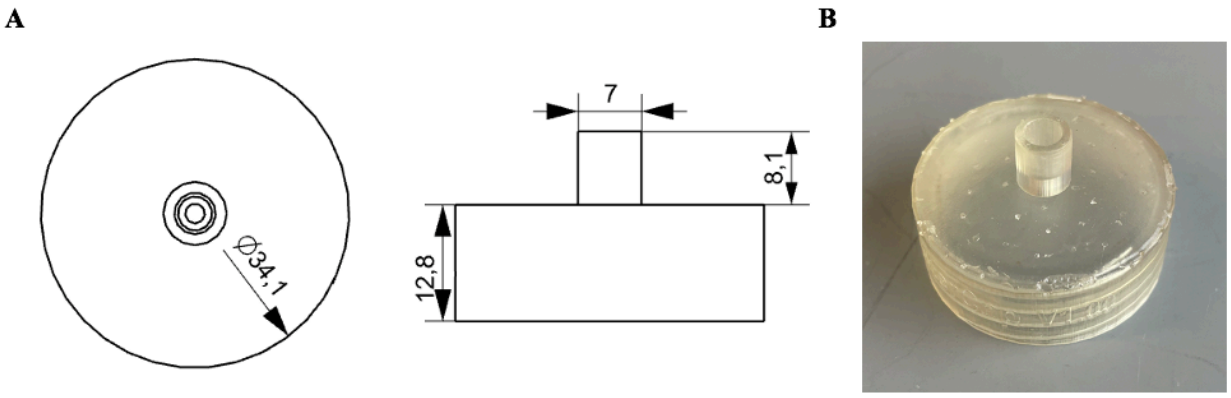

A. Sketch and dimensions of the **Clearing Reservoir Cap** created with Siemens NX software.

B. Optical image of the **Clearing Reservoir Cap** 3D-printed with BioMed resin.

Tube Holders

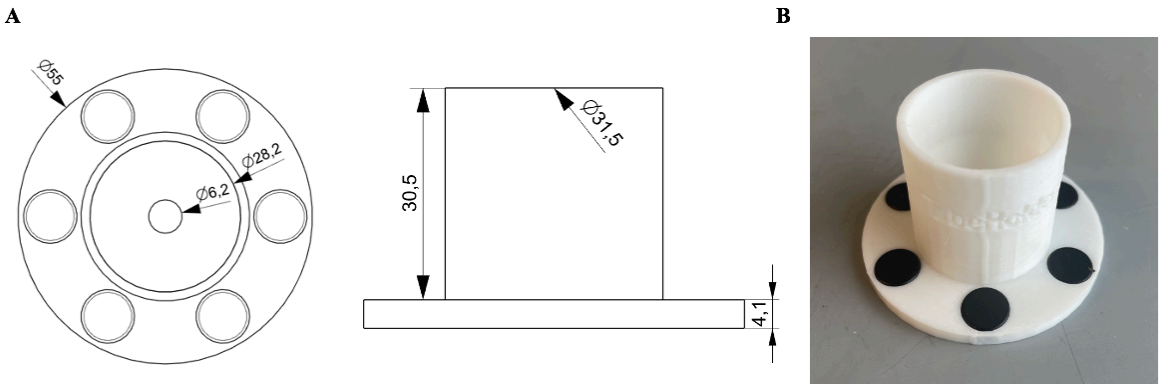

A. Sketch and dimensions of the **Tube Holders** created with Siemens NX software.

B. Optical image of the **Tube Holders** 3D-printed with PETG.

Dampener

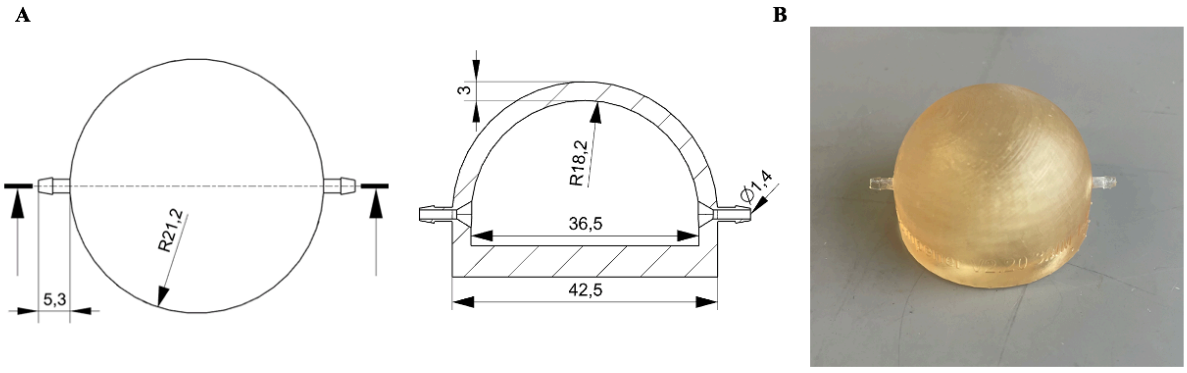

A. Sketch and dimensions of the **Dampener** created with Siemens NX software.

B. Optical image of the **Dampener** 3D-printed with BioMed resin.

APPENDIX E. RNA ISOLATION, REVERSE TRANSCRIPTION, AND POLYMERASE CHAIN REACTION PROTOCOL

RNA isolation

1. Transfer samples to labeled micro-centrifuge tubes (MCTs)
2. Digest cell laden GelMA in 200µL of 5 mg/mL (0.5% w/v) Collagenase I for 2 hours at 37ºC
3. Homogenize samples with homogenizing probes to manually break up sample
4. Continue GelMA digestion with 700µL of Tri-Reagent in 1 hour at 4ºC
5. Re-homogenize samples if necessary
6. Vortex each sample for 20s each and place on ice
7. Repeat steps 2-4 for every sample
8. Centrifuge samples down at the highest speed (17g or 13.3rpm) for 2 minutes at RT
9. Add 200µL of chloroform to each sample
10. Vortex each sample again for 20s and place on ice
11. Incubate samples on ice for 2-3 minutes
12. Centrifuge samples for 15 minutes at 4ºC and 15,000rpm
13. Recover ~200-400µL of the RNA supernatant
14. Wash samples with isopropanol supplemented with glycogen blue
15. 500µL isopropanol + 10µg glycogen blue per sample
16. Stock concentration of glycogen blue is 5µg/µL (2µL of glycogen blue per 500µL of isopropanol)
17. Store samples at -80ºC overnight or proceed to following steps

18. Incubate samples at room temperature for 10 minutes
19. Centrifuge samples at 12,000rpm for 10 minutes at 4ºC
20. Discard supernatant and re-suspend pellet in 700µL of 70% Et-OH
21. Centrifuge samples at 7,500rpm for 5 minutes at 4ºC
22. Discard supernatant and re-suspend pellet in 700µL of 70% Et-OH
23. Centrifuge samples at 7,500rpm for 5 minutes at 4ºC
24. Discard supernatant and let samples air dry under the biosafety cabinet for 3-5 minutes
25. Re-suspend pellets in 20µL RNAse Free Water under the biosafety cabinet
26. Quantify RNA concentration using the NanoDrop (Lammerding Lab)

Reverse transcription

1. Develop a chart to quantify the volume measurements reaction for each component per sample (Note: Total reaction volume should accumulate to 20µL; 260/280> 1.60):

Sample	RNA Conc. (ng/µL)	Purification (260/280)	1ug RNA Vol. (µL)	NF-H_2O Vol. (µL)	qScript Vol. (µL)	Total Vol (µL)
1	1100.5	1.91	0.91	15.09	4	20
2	998.0	1.84	1.00	15.00	4	20
3	1080.8	1.90	0.93	15.07	4	20

2. Add the appropriate volume of Nuclease-Free water to each sample's respective PCR MCT
3. Add the appropriate volume of RNA to each sample's respective PCR MCT
4. Add 4µL of the cDNA qScript solution to the cap of each sample's respective PCR MCT
5. Centrifuge each master mix solution for 5 seconds, flick each tube, and re-centrifuge samples for another 5 seconds

6. Place sample in the thermal cycler and run the **QSCRIPT protocol** for samples (Note: **stage 1:** 5 min at 25ºC; **stage 2**: 30 min at 42ºC; **stage 3:** 5 min at 85ºC; **stage 4**: indefinite at 4ºC)
7. Prepare 1:5 reaction mixture of cDNA solution to Nuclease-Free water. (Note: Add 80µL of Nuclease-Free water to each 20µL cDNA reaction mix)

Quantitative Real Time-Polymerase Chain Reaction

1. Prepare PCR template on Excel (Note: Include all relevant information on the genes, timepoints, and conditions that will be analyzed on each plate. See example below.)

Date	2/25/22		Plate	47
Gene		1	2	3
UCP-1 D14	A	D14-5%G35-1	D14-5%G35-1	D14-5%G35-1
UCP-1 D14	B	D14-5%G35-2	D14-5%G35-2	D14-5%G35-2
UCP-1 D14	C	D14-5%G35-3	D14-5%G35-3	D14-5%G35-3
	D			
	E			
UCP-1 D21	F	D21-5%G35-1	D21-5%G35-1	D21-5%G35-1
UCP-1 D21	G	D21-5%G35-2	D21-5%G35-2	D21-5%G35-2
UCP-1 D21	H	D21-5%G35-3	D21-5%G35-3	D21-5%G35-3

2. Prepare MasterMix solution for each gene and reaction. (Note: I do triplicates for each cDNA sample that I have)
    a. Each reaction should have the following components:
        i. Forward Primer (1uL per reaction)
        ii. Reverse Primer (1uL per reaction)
        iii. SBYR Green Master (10uL per reaction)

iv. Nuclease Free Water (6uL per reaction)

v. cDNA sample (2uL per reaction) **(NOTE: cDNA should not be included in your MasterMix)**

b. EXAMPLE: if you are analyzing the gene expression of 3 samples (with triplicates) this is how you should prepare your Master Mix Solution

i. 3 samples (triplicates) → 9 reactions → round up to 10 reactions

ii. For 10 reactions, add the following components to a microcentrifuge tube

1. SYBR GREEN (10uL/reaction * 10 reactions = **100uL**)
2. FORWARD PRIMER (1uL/reaction * 10 reactions = **10uL**)
3. REVERSE PRIMER (1uL/reaction * 10 reactions = **10uL**)
4. NUCLEASE FREE WATER (6uL/reaction * 10 reactions = **60uL**)
5. Total Volume should be 180uL (**DO NOT INCLUDE CDNA IN MASTERMIX)**

3. Add 18µL of MasterMix solution into each respective PCR well
4. Add 2 µL of cDNA template to each respective PCR well (Don't forget triplicates)
5. Seal PCR template with adhesive cover
6. Centrifuge PCR plate for ~30s
7. Run PCR *Express Load* program **(CFX_2StepAmp+Melt-CJS)** with following criteria

a. 40 cycles total; 20uL reactions

b. PCR Reaction Temps

i. 95ºC (30s) – Polymerase Activation and cDNA Denaturation

ii. 95ºC (5s) – Denature Temp and Duration Cycle

iii. 60ºC (30s) – Anneal Temp and Duration Cycle

c. Melt Curve Temps (w/ 0.5ºC increment)

    i. 95ºC (10s) – Denaturation Temp

    ii. 65ºC (5s)

    iii. 95ºC (5s)

APPENDIX F. LIPID AND MITOCHONDRIA IMMUNOFLUORESCENCE WHOLE MOUNT STAINING PROTCOL

Reagents

MitoTracker™ Red CMXRos (ThermoFisher; Cat No. M7512; ex:579/em:599nM)

- Storage: -20ºC
- Powder form in 50ug aliquots; reconstitute in DMSO (stock); dilute 1:1000 in 1xPBS (working)

HCS LipidTOX™ Green Neutral Stain (ThermoFisher; Cat No. H34475; ex: 495/em:505nm)

- Storage: -20ºC
- Solution form (125µL); dilute 1:200 in 1xPBS (working)

DAPI, 4′,6-diamidino-2-phenylindole (ThermoFisher; Cat No. 62248; ex:360/em:460nm)

- Storage: -20ºC
- Solution form at 1mg/mL (1mL); dilute 1:500 in 1x PBS (working)

Saponin (VWR; Cat No. 0163-100G)

- Storage: 4ºC
- Powder form (100g); reconstitute at 0.2% in 1xPBS (stock); dilute stock to 0.1% (working)

PBS, Phosphate-buffered Saline

- Storage: Room Temperature (RT)
- Solution form (10x); dilute to 1x in di-water

DMSO, Dimethyl Sulfoxide (CORNING; Cat No. 25-950-CQC)

- Storage: Room Temperature (RT)

- Solution form

MitoTrackerTM Red CMXRos Stain (Day 1)

1. Stain Live Samples with MitoTracker
    - Prepare stock solution of 1mM MitoTracker dye in DMSO as defined by the manufacturer
        - 94µL of DMSO per 50µg vial of MitoTracker
    - Prepare working solution of 1µM MitoTracker dye in 1xPBS
        - 1:1000 working solution, meaning 1µL of MitoTracker dye per 1mL of 1xPBS
    - Manufacturers guide indicates 20-500nM as the working solution, but this is specified for 2D samples, not 3D samples
    - In the same 48-well plate, submerge samples in 1mL of working solution for 3-6 hours at room temperature under slight agitation
    - Ensure your plates remained covered with foil for the remainder of staining to avoid photo-bleaching
        - Remove *MitoTracker solution* from samples in the dark
        - Wash samples in 1x PBS for 30 minutes at RT under slight agitation

2. Fix Samples in Fixative Agent
    - Prepare working solution of 4% (v/v) Paraformaldehyde

- In a 48-well plate, submerge samples in *fixative agent* for overnight at 4ºC with mild agitation
- Remove *fixative agent* from samples
- Wash samples in 1x PBS for 30 minutes at RT under slight agitation
    - Repeat step an additional two times, making a total of 3 wash steps
    - NOTE: Cover plate with foil during this entire process to prevent photobleaching!

HCS LipidTox™ Green Neutral Stain (Day 2)

1. Permeabilize Samples in Mild Detergent (Saponin)
    - Prepare stock solution of 0.2% (w/v) Saponin in 1x PBS
        a. Add 100mg of Saponin to 50mL of 1x PBS
    - Prepare working solution of 0.1% (v/v) Saponin from stock solution in 1xPBS
        a. Combine 1-part 1x PBS with 1-part 0.2% Saponin
    - In the same 48-well plate, submerge samples in *mild detergent* for one hour at room temperature under slight agitation to lyse cells
    - Remove *mild detergent* from samples
    - Wash samples in 1x PBS for 15 minutes at RT under slight agitation
        a. Repeat step an additional two times, making a total of 3 wash steps
        b. NOTE: Cover plate with foil during this entire process to prevent photobleaching!
2. HCS LipidTOX™ Green Neutral/ DAPI Co-Stain

- Prepare working solution of LipidTOX™ Green Neutral in 0.05% (v/v) Saponin at the following dilution ratio in a dark room
    a. HCS LipidTOX™ Green Neutral Lipid stain (excitation: 495nm; emission: 505nm) at 1:200 in blocking buffer (green fluorophores)
- Prepare working solution of DAPI in 0.05% (v/v) Saponin at the following dilution ratio in a dark room
    a. DAPI stain (excitation: 405nm; emission: 488nm) at 1:500 in blocking buffer (blue fluorophores)
    b. NOTE: Both stains can occur at the same time!
- In the same 48-well plate, submerge samples in 250µL of HCS LipidTOX™/ DAPI co-stain
    a. NOTE: Cover plate with foil during this entire process to prevent photobleaching!
- Stain samples overnight under mild agitation
- Perform confocal imaging for each sample

APPENDIX G. MATLAB CODE FOR DIFFUSION COEFFICIENT ANALYSIS

Diffusion Coefficient Analysis

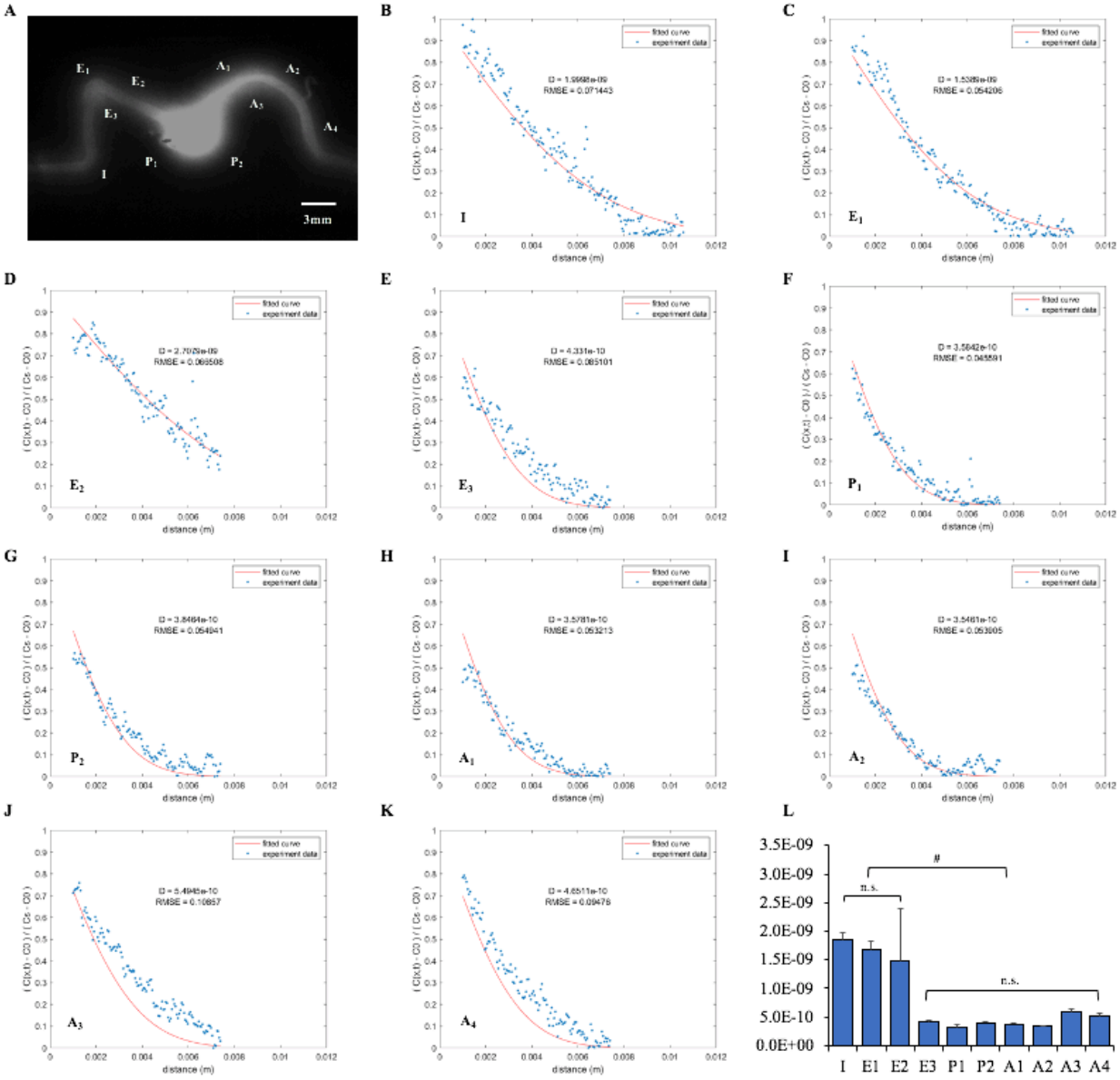

A. Diffusion of 20kD FITC-Dextran through acellular Squiggle channel after 120 minutes

B. Analysis of the diffusion coefficient at location (I) using Fick's 2nd law of diffusion

C. Analysis of the diffusion coefficient at location (E_1) using Fick's 2nd law of diffusion

D. Analysis of the diffusion coefficient at location (E_2) using Fick's 2nd law of diffusion

E. Analysis of the diffusion coefficient at location (E_3) using Fick's 2nd law of diffusion

F. Analysis of the diffusion coefficient at location (P_1) using Fick's 2nd law of diffusion

G. Analysis of the diffusion coefficient at location (P_2) using Fick's 2nd law of diffusion

H. Analysis of the diffusion coefficient at location (A_1) using Fick's 2nd law of diffusion

I. Analysis of the diffusion coefficient at location (A_2) using Fick's 2nd law of diffusion

J. Analysis of the diffusion coefficient at location (A_3) using Fick's 2nd law of diffusion

K. Analysis of the diffusion coefficient at location (A_4) using Fick's 2nd law of diffusion

L. Analysis of the diffusion coefficients at every assigned location

Fick's Second Law of Diffusion:

$$\frac{C(x,t) - C_0}{C_s - C_0} = 1 - \text{erf}\left(\frac{x}{2\sqrt{Dt}}\right)$$

C_S: Saturated concentration (pixels)

C_0: Initial concentration (pixels)

x: Distance from the lumen (m)

D: Diffusion coefficient (m^2/s)

t: time (s)

MATLAB Code

```
clear all
close all
clc

% distance in m
x_1 = readmatrix('2024-07-23_Diffusion Analysis_Steady
State_Acell_20kDa-FITC_COMBINED.xlsx', ...
    'Sheet', 'Combined-2', 'Range','A3:A184'); % input file
% C = ( C(x,t) - C0 )/( Cs - C0 )
C_1 = readmatrix('2024-07-23_Diffusion Analysis_Steady
State_Acell_20kDa-FITC_COMBINED.xlsx', ...
    'Sheet', 'Combined-2', 'Range', 'B3:J184'); % input file

% removed first 63 data points and moved x = 0
x_2 = readmatrix('2024-07-23_Diffusion Analysis_Steady
State_Acell_20kDa-FITC_COMBINED.xlsx', ...
    'Sheet', 'Combined-2', 'Range', 'A3:A124');
C_2 = readmatrix('2024-07-23_Diffusion Analysis_Steady
State_Acell_20kDa-FITC_COMBINED.xlsx', ...
    'Sheet', 'Combined-2', 'Range', 'H63:AE184');

% number of datasets
```

```
n_1 = 6;
n_2 = 24;
% Array to store coefficient estimate and RMSE
D_1 = zeros(1,n_1);
rmse_1 = zeros(1,n_1);
D_2 = zeros(1,n_2);
rmse_2 = zeros(1,n_2);

% data fitting
for i = 1:n_1

    C = C_1(:,i);
    % use custom equation, here t = 7200 s
    ft = fittype('1-erf(x/(2*sqrt(7200*D)))', 'coefficients',
'D', ...
        'independent', 'x', 'dependent', 'C');
    % erf() need real input so D cannot be zero or negative
    options = fitoptions('Method', 'NonlinearLeastSquares', ...
        'Lower', [0], 'StartPoint', [1.5E-9]);
    [mdl,gof] = fit(x_1,C,ft,options);
    % save coefficient estimates and RMSE into one array
    D_1(i) = mdl.D;
    rmse_1(i) = gof.rmse;
```

```
    % plot the fitted curve and the experiment data for
individual dataset
    figure(i)
    plot(mdl)
    xlim([0, 0.012])
    ylim([0, 1])
    % label coefficient estimate and RMSE on plot
    text(0.006, 0.700, ...
        {"D = " + num2str(D_1(i)); "RMSE = " +
num2str(rmse_1(i))}, ...
        'HorizontalAlignment', 'center');
    xlabel('distance (m)')
    ylabel('( C(x,t) - C0 ) / ( Cs - C0 )')
    hold on
    plot(x_1, C, '*', color = "#0072BD", MarkerSize = 3)
    legend('fitted curve', 'experiment data')

end

% data fitting
for i = 1:n_2

    C = C_2(:,i);
    % use custom equation, here t = 7200 s
```

```
    ft = fittype('1-erf(x/(2*sqrt(7200*D)))', 'coefficients',
'D', ...
        'independent', 'x', 'dependent', 'C');
    % erf() need real input so D cannot be zero or negative
    options = fitoptions('Method', 'NonlinearLeastSquares', ...
        'Lower', [0], 'StartPoint', [2.5E-9]);
    [mdl,gof] = fit(x_2,C,ft,options);
    % save coefficient estimates and RMSE into one array
    D_2(i) = mdl.D;
    rmse_2(i) = gof.rmse;

    % plot the fitted curve and the experiment data for
individual dataset
    figure(i + n_1)
    plot(mdl)
    xlim([0, 0.012])
    ylim([0, 1])
    % label coefficient estimate and RMSE on plot
    text(0.006, 0.700, ...
        {"D = " + num2str(D_2(i)); "RMSE = " +
num2str(rmse_2(i))}, ...
        'HorizontalAlignment', 'center');
    xlabel('distance (m)')
    ylabel('( C(x,t) - C0 ) / ( Cs - C0 )')
```

```
    hold on
    plot(x_2, C, '*', color = "#0072BD", MarkerSize = 3)
    legend('fitted curve', 'experiment data')

end


% save figures in batch mode
% https://www.mathworks.com/matlabcentral/answers/182574-save-
all-the-plots
FolderName = "C:\Users\Lenovo\Downloads\"; % output direction
FigList = findobj(allchild(0), 'flat', 'Type', 'figure');
for iFig = 1:length(FigList)
    FigHandle = FigList(iFig);
    FigName   = num2str(get(FigHandle, 'Number'));
    set(0, 'CurrentFigure', FigHandle);
    saveas(FigHandle, fullfile(FolderName, [FigName '.png']));
end


% individual fitting and plotting

% ft_C1 = fittype('1-erf(x/(2*sqrt(7200*D)))', 'coefficients',
'D', 'independent','x','dependent','C_1')
```

```
% options =
fitoptions('Method','NonlinearLeastSquares','Lower',[0]);
% [mdl_C1,gof] = fit(x,C_1,ft_C1,options)
%
% ft_C2 = fittype('1-erf(x/(2*sqrt(7200*D)))', 'coefficients',
'D', 'independent','x','dependent','C_2')
% options =
fitoptions('Method','NonlinearLeastSquares','Lower',[0]);
% [mdl_C2,gof] = fit(x,C_2,ft_C2,options)
%
% ft_C3 = fittype('1-erf(x/(2*sqrt(7200*D)))', 'coefficients',
'D', 'independent','x','dependent','C_3')
% options =
fitoptions('Method','NonlinearLeastSquares','Lower',[0]);
% [mdl_C3,gof] = fit(x,C_3,ft_C3,options)
%
%
% figure(1)
% plot(mdl_C1)
% xlabel('x')
% ylabel('C_1')
% hold on
% plot(x,C_1, '*')
% legend('fitted curve','data points')
```

```
%
% figure(2)
% plot(mdl_C2)
% xlabel('x')
% ylabel('C')
% hold on
% plot(x,C_2, '*')
% legend('fitted curve','data points')
%
% figure(3)
% plot(mdl_C3)
% xlabel('x')
% ylabel('C')
% hold on
% plot(x,C_3, '*')
% legend('fitted curve','data points')
```